Bifunctional Electrocatalysts For Rechargeable Zinc-air Batteries

by

Elaheh Davari

A thesis submitted in partial fulfillment of the requirements for the degree of

Doctor of Philosophy

in

MATERIALS ENGINEERING

Department of Chemical and Materials Engineering

University of Alberta

Abstract

With the rapid development of electrified transportation, electrochemical energy storage devices will be more important than they have ever been in human history. Lithium-ion batteries are considered as the most energy efficient candidates, due to their relatively long cycle life. However, their limited energy density, as well as the safety issues, are concerns for their long-term application. As an attractive alternative, metal-air batteries have generated interest as promising large-scale electricity storage technologies. The light-weight architecture of metal-air batteries can provide high energy density with a simple and low cost cell design. Among various types of metal-air batteries, Zn-air batteries (ZABs) and Li-air batteries have been considered as the most promising metal-air batteries. Compared with Li, Zn is a more attractive metal due to its lower cost, abundance and environmentally friendliness. However, there are several technical issues associated with the structure of ZABs, including insufficient cycling durability, low charge-discharge activity and limited power density. One of the critical issues of rechargeable ZABs is the large overpotential associated with the oxygen evolution reaction (OER) and oxygen reduction reaction (ORR) in the air cathode. Accordingly, developing novel bifunctional catalysts, which can enhance the kinetics of both OER and ORR, is one of the most critical factors to propel the ZABs to practical energy applications. Currently, the most effective bifunctional catalysts are based on precious metals (Pt-Ir based). However, the high cost and scarcity of precious metals limit their widespread use and remains a huge challenge for developing air cathodes. Therefore, it is important to develop inexpensive, stable and abundant non-precious metal catalysts in the design of ZABs.

The purpose of this work is to design and synthesize novel non-precious metal catalysts among a wide range of materials using simple techniques. Non-precious metal materials are investigated in this thesis as potential ORR/OER catalysts, including Mn-Co mixed oxides, Mn-nitride, N-doped hollow mesoporous carbon and carbon coated N-doped Fe_3O_4.

The first study is focused on the development of a mixed Mn-Co oxide. The oxides were directly deposited on a gas diffusion layer (GDL). By modifying the simple electrodeposition process, fibrous Mn oxide rods were deposited on a GDL substrate. Deposits were characterized using a variety of materials and electrochemical techniques including scanning electron microscopy (SEM), transmission electron microscopy (TEM), X-ray diffraction (XRD), X-ray energy dispersive spectroscopy (EDX), X-ray photoelectron spectroscopy (XPS), cyclic voltammetry (CV), linear sweep voltammetry (LSV) and galvanostatic charge-discharge cycling. The Mn and Co concentration were optimized to achieve the best bifunctional performance. Catalyst Mn/Co:2.5 exhibited the most positive ORR onset potential (0.076 V vs. Hg/HgO) and an OER current density of 2.28 mA cm^{-2}. A round-trip efficiency of 43.4% was obtained after 30 cycles (30 h) at 5 mA cm^{-2}.

Another approach was to develop a novel low cost bifunctional catalyst by nitridation of Mn-powder in high purity N_2 gas. Detailed phase analysis was done using TEM, electron diffraction and XRD/Rietveld techniques. For the sample heat treated for 10 h, the E_{OER}-E_{ORR} potential gap decreased by 12.6% relative to bare GDL. However, the large particle size and the presence of an insulating MnO layer and impurity phases limited the kinetics of ORR/OER in comparison with the Pt/C baseline material.

High surface area N-doped hollow mesoporous carbon (HMC) was developed collaboratively using a simple technique. Polydopamine (PDA) was used as the carbon and nitrogen source. High resolution TEM revealed both graphitic and amorphous carbon with a shell thickness of 21 nm ± 6 nm. Rechargeable ZABs showed a round-trip efficiency of 58.2% after 30 cycles (15 h) at 2 mA cm^{-2}. In a similar manner, N-doped mesoporous carbon was used as a coating for Fe_3O_4 nanorods. Fe_3O_4 nanorods were synthesized using a novel microwave assisted technique. Fe_3O_4 nanorods coated with N-doped mesoporous carbon (ND-Fe_3O_4@mC) shells were fully characterized structurally and electrochemically. Carbon shell thickness varied from 1.5 nm ± 0.2 nm to 2.2 nm ± 0.5 nm. The ORR activity and stability of ND-Fe_3O_4@mC was evaluated using CV and LSV. Among the samples, ND-Fe_3O_4@mC with a carbon shell thickness of 1.5 nm ± 0.2 nm (2 h coating) had the most positive ORR onset potential (0.024 V vs. Hg/HgO) and the highest current density (-5.24 mA cm^{-2}).

Preface

This thesis is focused on the synthesis and characterization of various non-precious metal materials as bifunctional electrocatalysts for rechargeable ZABs. The research projects summarized in Chapter 3, Chapter 4 and Appendix A are my original work.

Chapters 5 and 6 summarize the research conducted in collaboration work with Dr. Veinot's group in the Department of Chemistry at the University of Alberta. Dr. Lida Hadidi, a former PhD candidate, performed the materials selection and synthesis. She also performed part of the materials characterization for Chapters 5 and 6. The electrochemical analysis and interpretation of the results of the corresponding chapters were done solely by myself. Appendix B summarizes the collaboration work with the National Research Council - National Institute of Nanotechnology (NRC-NINT). Dr. Neda Dalili performed all the electron microscopy (SEM, TEM, FIB) and tomography analysis. The electrochemical analysis was performed primarily by Michael Clark (PhD student in our group). I was responsible for part of the electrochemical analysis, atomic absorption spectroscopy testing and sample preparation.

Versions of Chapter 3, Chapter 5 and Chapter 6 of this thesis have been published as:

Chapter 3: E. Davari, A. D. Johnson, A. Mittal, M. Xiong and D. G. Ivey, *Electrochim. Acta*, 2016, **211**, 735–743.

Chapter 5: L. Hadidi, E. Davari, M. Iqbal, T. K. Purkait and D. G. Douglas, *Nanoscale*, 2015, **7**, 1–7.

Chapter 6: L. Hadidi, E. Davari, D. G. Ivey and J. G. C. Veinot, *Nanotechnology* - doi.org/10.1088/1361-6528/aa5716

Also, Chapters 4 have been submitted to the journal of Applied Electrochemistry (ID: JACH-D-17-00038)

Dedication

To all who devoted their lives to the science and technology.

To all individuals who have struggled for their freedom.

To Shahram and Sima, who encouraged me to go on every adventure, especially this one.

Acknowledgments

I would like to gratefully acknowledge my supervisor, Dr. Douglas Ivey, for his ongoing support, feedback and encouragement from the first outline of the idea for this dissertation to the very last period. His support not only of my project, but also of me as an individual made it possible for this work to be completed. His love of teaching always inspired me and he helped me to grow as a researcher in an incalculable way.

My thanks to the members of my supervisory committee, Dr. Liu and Dr. Chen, for their guidance and thoughtful advice regarding my research. My appreciation also goes to Mr. Wei Qu and Dr. Riny Yuan from the National Research Council, Canada (NRC), for their insightful suggestions and discussions which significantly helped me with the research work. I would like to thank Dr. Lida Hadidi and Dr. Jonathan Veinot for the collaboration, guidance and suggestions as we worked on different projects.

For technical support and input, I would like to thank Dr. Anqiang He (TEM/SIMS), Dr. Shihong Xu (XPS/AES), Dr. Dimitre Karpuzov (XPS), Mrs. Diane Caird (XRD) and Dr. Andrew Locock (XRD/Reitveld analysis). I would like to thank our summer students Ms. Aliesha Johnson, Mr. Akshat Mittal and Mr. Prakhar Sharma.

Financial support from the Natural Sciences and Engineering Research Council (NSERC), the Faculty of Graduate Studies and Research (FGSR) and the Graduate Student's Association (GSA) is gratefully acknowledged. My gratitude also extends to the staff of the Department of Chemical and Materials Engineering at the University of Alberta.

I want to thank all the friends I have made over the duration of my time in Edmonton, thank you for being a part of this journey. Dr. Neda Dalili, thank you for your friendship, mentorship and guidance. Reza Nazemi, thanks for all the support and encouragement. My labmate, Ming Xiong, thanks for giving so freely of your time and making the lab such a supportive place to work. Mike Clark, thank you for being my best friend. You helped me so much through hard times with understanding. Thanks for all the proof-reading and your support.

I am grateful most of all to my family: Sima Zarrabpour, Shaharam Davari and Amirreza Davari. Mom and Dad you two are the foundation of my life. Thanks for raising me with unqualified love, the gift of freedom to choose and for your unbounded confidence in the academic path I chose. Amirreza, thanks for all the fun, laughter and endless distractions.

Table of Contents

List of Tables

List of Figures

Glossary of Terms

AAS	atomic adsorption spectroscopy
AEM	anion exchange membrane
AES	auger electron spectroscopy
ALD	atomic layer deposition
BET	Brunauer-Emmett-Teller
BF	bright field
BSE	backscattered electron
CB	carbon black
CCBC	core-corona bifunctional catalyst
CFP	carbon fiber paper
CNF	carbon nanofiber
CNT	carbon nanotube
CTAB	hexadecyltrimethylammonium bromide
CV	cyclic voltammetry
DA	dopamine
DFT	density functional theory
DI	deionized
DMSO	dimethyl sulfoxide
EDX	energy dispersive spectroscopy
EIS	electrochemical impedance spectroscopy
FTIR	fourier transform infrared
FWHM	full width half maximum
GC	glassy carbon
GDL	gas diffusion layer
GNF	graphite nanofibers
GO	graphene oxide
HAADF	high angle annular dark field
HER	hydrogen evolution reaction
HMC	hollow mesoporous carbon

HMT	hexamethylenetetramine
HOMO	highest occupied molecular orbitals
HR	high resolution
ICDD	international center diffraction data
IL	ionic liquid
JCPDS	joint committee on powder diffraction standards
K-L	Koutecky-Levich
Lcd	limiting current density
LDH	layered double hydroxide
LED	light emitting diode
LOMO	lowest occupied molecular orbitals
LSV	linear sweep voltammetry
mC	mesoporous carbon
MCNA	mesoporous carbon nanofiber array
MPL	micro-porous layer
n	number of electron transferred
NC	nanocage
ND	nitrogen doped
NP	nanoparticle
NVC	N-doped Vulcan carbon
OCV	open circuit voltage
OER	oxygen evolution reaction
Op	onset potential
oPD	o-phenylenediamine
ORR	oxygen reduction reaction
PAN	polyacrylonitrile
Pd	power density
PDA	polydopamine
PE	polyethylene
PEM	proton exchange membrane
PLD	pulsed layer deposition

PMF	phenol melamine formaldehyde
PO	polyolefin
PP	polypropylene
PPy	polypyrene
PSD	pore size distributions
PTFE	polytetrafluoroethylene
PVA	polyvinyl alcohol
RDE	rotating disk electrode
Redox	oxidation and reduction reactions
rGO	reduced graphene oxide
RHE	reversible hydrogen electrode
RRDE	rotating ring-disk electrode
RTIL	room temperature ionic liquids
SAD	selected area diffraction
Sc	specific capacity
SCE	saturated calomel electrode
SDS	sodium dodecyl sulfate
SE	secondary electron
Sed	specific energy density
SEM	scanning electron microscope
SHE	standard hydrogen electrode
SS	stainless steel
STEM	scanning transmission electron microscope
SWCNT	single walled carbon nanotube
TEM	transmission electron microscope
TEOS	tetraethoxysilane
TGA	thermogravimetric analysis
ToF-SIMS	time-of-flight secondary ion mass spectrometry
XPS	X-ray photoelectron spectroscopy
XRD	X-ray diffraction
ZAB	zinc-air battery

1 Chapter 1: Introduction

The demand for energy is increasing in modern society and finding alternatives to fossil fuels is a necessary step towards a low-carbon economy and reducing environmental pollution. According to the World Resources Institute, 61.4% of total greenhouse gas emissions come from the energy sector.[1] In recent years, renewable energy sources such as wind, hydroelectric, solar, biomass, and geothermal have been increasingly utilized. However, wind and solar power are constrained by climate conditions. Also, pumped hydroelectricity, which is one of the preferred ways of producing electrical energy, is limited by its site-specific nature and the high cost of large scale operation. Therefore, finding a safe, reliable and efficient way to store energy from these renewable and sustainable sources is an urgent need. Electrochemical conversion technologies, such as batteries with high power density, are among the key energy storage devices for the next generation of electronics and green vehicles.[2–4] Batteries are closed systems that contain all the necessary components for their operation. The oxidation and reduction reactions (redox) occur due to the potential difference between two opposite electrodes (anode and cathode) in a conductive medium (electrolyte). Therefore, batteries have always been of great interest in the electronics market, and recently the transportation sector, to reduce emissions from fossil fuels.

During the last few decades rechargeable batteries such as Pb-acid, Li-ion, redox flow, Na-S and metal-air batteries have been widely investigated.[5] Since 1990, Li-ion batteries have been implemented in electronic appliances due to their high energy efficiency, high energy density and long cycle life. However, Li-ion batteries face many challenges, such as volume change during the charge-discharge process and safety problems.[6–8]

Among various battery types, metal-air batteries, such as zinc-air batteries (ZABs), hold great promise for future energy applications. Table 1-1 summarizes the important characteristics of different rechargeable battery types. Of these common types of batteries, ZABs have the highest energy density and lowest cost. In addition, compared with fuel cells, the ZAB anode and cathode designs are less stringent and there is no need for hydrogen production and storage.[9,10]

The performance of ZAB technologies greatly depends on a pair of sluggish electrochemical reactions at the cathode, i.e., the oxygen reduction reaction (ORR) and the oxygen evolution reaction (OER). Improving the activity and stability of ORR and OER can be achieved by using precious metals as electrocatalysts. Platinum-based electrocatalysts are ORR active, but OER activity is limited due to the formation of an oxide layer at high potentials. Conversely, Ir or Ru-based electrocatalysts are effective OER catalysts, but not as active as Pt for ORR. This issue, along with their prohibitive cost and scarcity, represent a grand challenge for ZABs. Therefore, the development of a single high-performance, non-precious metal electrocatalyst with simultaneous ORR and OER activity (bifunctional) is critically needed as an alternative to precious metals. The purpose of this thesis is to develop active and stable bifunctional electrocatalysts for the air electrode of a rechargeable ZAB, which is one of the major concerns hindering the commercialization of this technology.

Table 1-1 Characteristics of various rechargeable batteries.[3]

Battery type	Zn-Mn	Pb-acid	Ni-MH	Li-ion	Zn-air
				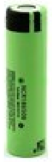	
Voltage (V)	1.5	2	1.2	3.7	1.4
Energy density (Wh kg^{-1})	150	35	75	160	470
Power density (W kg^{-1})	40	180	200	300	100
Cycle life	N/A	500 cycles	600 cycles	1000 cycles	N/A
Efficiency	N/A	75%	80%	90%	N/A
Cost	\$120/kWh	\$120/kWh	\$350/kWh	\$400/kWh	\$10/kWh
Safety	Good	Good	Medium	Poor	Good

1.1 Content of the thesis

In Chapter 1, the Introduction and contents of the thesis are provided.

Chapter 2 contains a literature review of the basic components of a ZAB and recent developments and challenges for each component of the ZAB, as well as a recently developed bifunctional electrocatalyst for primary/secondary ZABs. The review on bifunctional electrocatalysts is divided into noble metal-based, transition metal oxide-based and carbon-based materials. Also, a summary of the synthesis, electrochemical and characterization techniques is provided in this chapter.

The first objective of this work is to apply electrodeposition techniques previously developed by our research group[11,12] to deposit Mn-Co mixed oxides on a gas diffusion layer (GDL), a more practical and common substrate for ZABs than other carbon-based materials such as glassy carbon (GC). This work is covered in Chapter 3. To optimize the performance, deposition parameters are varied, using the conditions from Babakhani and Ivey's[12] work as a starting point. Mn-Co mixed oxides are characterized using a variety of techniques. The effect of changing the Mn/Co ratio in the deposition solution on ORR/OER performance is also investigated.

The second objective of this work is to develop a cost effective Mn-N catalyst using a simple technique of annealing Mn powder at 1100 °C in a N_2 atmosphere. This work is covered in Chapter 4. The synthesized Mn-N powder is fully characterized and spray-coated on GDL for ZABs. ORR and OER catalytic performance are investigated using a rotating disk electrode (RDE) apparatus.

Chapter 5 presents the synthesis of high surface area, hollow mesoporous carbon (HMC) using dopamine as a carbon precursor and nitrogen source. The HMC particles are characterized and employed as bifunctional electrocatalysts in a ZAB. Chapter 6 is an extension of the work provided in Chapter 5, where mesoporous carbon is used as a thin coating for Fe_3O_4 nanorod cores. The synthesis of Fe_3O_4 nanorods coated with a N-doped mesoporous carbon shell (ND-Fe_3O_4@mC) via a microwave assisted technique is presented. The ORR electrochemical performance of ND-Fe_3O_4@mC with different carbon shell thicknesses is evaluated.

Chapter 7 concludes the thesis and contains recommendations for future work.

Appendix A presents the preliminary results of the work done in Chapter 3, on Mn-Co oxide as bifunctional catalyst. Appendix B presents the results of work done in our group, it is not included in the main body of the thesis as it is not directly related to this work. However, the work was successful and led to a peer reviewed journal publication.

The novelty of the work presented in this thesis can be summarized as follows:

1) Mn-Co mixed oxide was directly applied on GDL by a facile anodic electrodeposition technique for the first time.

2) Manganese-nitride was synthesized via a simple route. The catalyst was applied to a ZAB for the first time and the bifunctional performance has been improved in comparison with the baseline Pt/C.

3) The HMC non-metal based catalyst was also used as a bifunctional catalyst in a rechargeble ZAB and higher stability compared with Pt/C was obtained after charge-dishcarge cycling.

4) Microwave assisted synthesis was used to develop nanostructured ND-Fe_3O_4@mC for the first time. The particles showed comparable ORR activity with Pt/C.

Several challenges still remain for the development of rechargeable ZABs. Existing gaps include the following: 1) development of a fundamental undertanding of oxygen electrocalaysis of the synthesized materials in aqueous solutions; 2) carbon (GDL) corrosion behavior during charging in highly alkaline solutions; 3) delivering high current density (>10 mA cm^{-2}) during long-term charge-discharge cycling using the fabricated non-precious metal catalysts.

2 Chapter 2: Literature review

2.1 Metal-air batteries

Metal-air batteries offer the highest theoretical energy density (Figure 2-1) among all the rechargeable battery types; this is due to the use of O_2 in air at the cathode enabling a significant reduction in cathode size and the overall weight of the batteries. During operation of a metal-air battery, the cathode consumes O_2 continuously from the air as an active material. The anode material is a metal such as Zn, Al, Mg, Li or Ca. Among all metal-air batteries, Li-air batteries have the highest theoretical specific energy of 11140 Wh kg^{-1}, which is very close to that of gasoline (12200 Wh kg^{-1}). The first successful attempt to design a rechargeable metal-air battery was a study by Abraham et al.[13] In this work, they constructed a Li-air battery composed of a Li^+ conductive organic polymer electrolyte membrane sandwiched between a thin Li metal foil anode and a thin carbon composite as the cathode (air electrode). In 2006, Li-air batteries were revised and modified by Bruce et al.[14] and their study initiated more extensive research in this field.

The properties of electrochemical metal-air cells are listed in Table 2-1. Aluminum, Mg, Li and Ca anodes have the highest specific energy. Lithium-air batteries have major limitations such as higher cost, an unstable anode which reacts with the electrolyte and safety issues.[15] For Al and Mg, fast corrosion occurs in aqueous electrolytes due to more negative electrode potentials.[2,3] Therefore, they only can be used as mechanically rechargeable metal-air batteries by refueling the system with fresh metal at the anode and electrolyte.[16]

2.2 Zinc-air batteries (ZABs)

A comparison between different properties of metal-air batteries shows that ZABs are one of the most promising metal-air systems due to two main reasons: First, Zn is an abundant metal that has been used by human culture throughout history. World Zn resources are estimated to be 1.8 gigatons, and 200 megatons were economically available in 2008.[15,17] Second, Zn is a low cost and abundant metal (Zn - US \$2/kg vs Li - US \$8/kg) which can be fully recycled.[18] Figure 2-2 shows the relationship between metal price and its relative abundance.

ZABs are composed of three main parts: a Zn anode, an alkaline electrolyte (usually concentrated KOH) and an air cathode (a carbon substrate with a catalytic layer). All the components will be further discussed in detail in the following paragraphs. There are two types of ZABs, classified into primary and secondary or rechargeable.[2,16] Primary ZABs have a long and stable storage life. A sealed battery will only experience 2% capacity decay after one year of storage. ZABs are available in many sizes and voltages (1.14, 1.4, and 3.0 V cells). Similar to other primary batteries, they may be combined in series to produce a battery with a higher voltage. Primary ZABs contain high power and energy in a small package, so they are very practical for applications where small size and high performance is critical. Typical applications include hearing aids, buoys and railroad applications.[18]

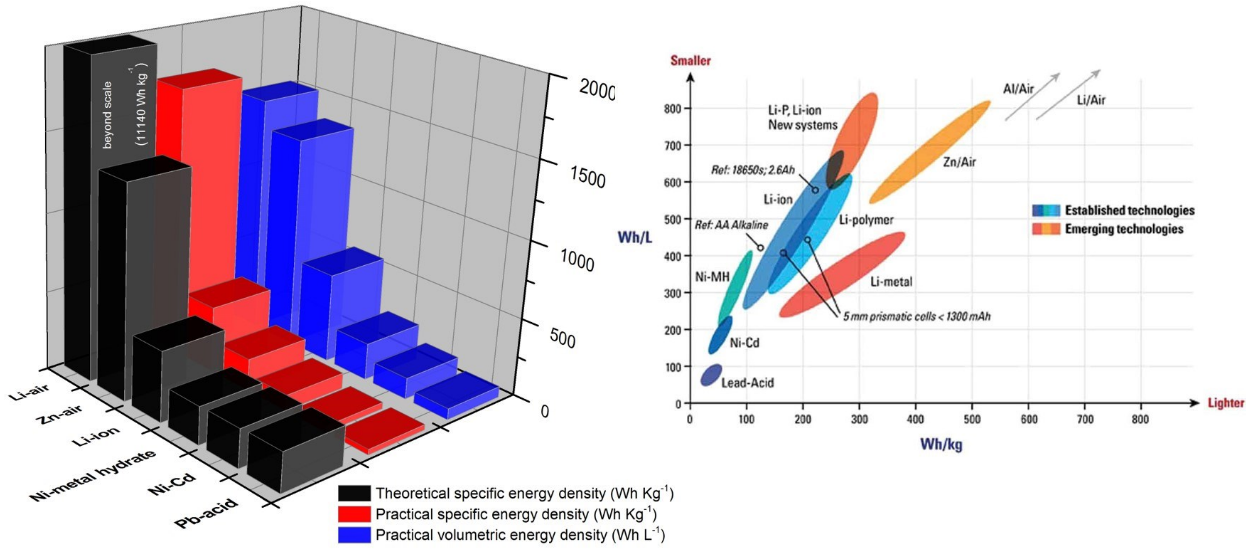

Figure 2-1 Theoretical and practical specific/volumetric energy density of various types of rechargeable batteries.[3]

ZABs can be recharged mechanically. In mechanically rechargeable Zn-air cells, the consumed Zn is physically removed from the battery and replaced with a fresh electrode. Spent Zn is processed separately at a different location back to metallic Zn. Such ZABs can be used for a grid storage application. These batteries were developed for the first time by Electric Fuel limited company and used in power military devices in the late 1960s. However, short active lifetime, intermittent operation, and also the emergence of Li batteries with easier operating systems reduced the scientific interest in developing mechanically rechargeable ZABs.[2,19]

Rechargeable ZABs, however, suffer from serious basic technological problems.[10] The main issue in the anode is low utilization efficiency due to passivation, corrosion and dendritic growth of Zn during recharge. For the cathode, on the other hand, the main problem is the sluggish and high overpotential oxygen reactions. Extensive studies have been done on ZABs, covering the challenges either of the individual components or the overall system.[9,10,15,16,20–24] As an example, Evans et al.[25,26] studied the irreversible agglomeration and shape change of the Zn-electrode in a rechargeable ZAB.

Table 2-1 Comparison of metal/air cells.[27]

Anode	Electrochemical equivalent of metal (Ah g^{-1})	Theoretical cell voltage (V)	Practical cell voltage (V)	Theoretical specific energy of the metal (kWh kg^{-1})	Valence change
Li	3.8	3.4	2.4	13.3	1
Al	2.9	2.7	1.6	8.1	3
Mg	2.2	3.0	1.4	6.8	2
Ca	1.3	3.4	2.0	4.6	2
Fe	0.9	1.2	1.0	1.2	2
Zn	0.8	1.6	1.2	1.3	2
Cd	0.4	1.2	0.8	0.6	2

Numerical modelling is a very useful tool for defining the critical design parameters for battery applications. Various numerical studies have been performed on ZABs, such as Zn electrode thickness/morphology and dissolution[28–30], gas-liquid interface movement[31,32] and the growth of O_2 bubbles during recharge.[33] Numerical methods provide a lot of valuable insights of the challenges in a ZAB system before performing time-consuming experiments. For example, a model used in a study by Deiss et al.[34] investigated the charge-discharge behavior of a ZAB. It predicted that OH^- depletion is the major limiting factor for OER overpotential at high-current discharge, and GDL pore plugging is a major limiting factor for ORR in long-term cycling. Schröder et al.[31] developed a technique to monitor the movement of the three phase boundary using a finite volume method.

Air electrode design and the reaction mechanisms are the most complex part of a rechargeable ZAB and it is by far the dominating factor affecting the performance of this system. Reactions at the cathode during discharge and charge (ORR/OER) involve complex steps and the exact mechanisms remain elusive in most cases. Normally, the integration of numerical and experimental studies is the most precise way to explain the ORR and OER mechanisms. In this regard, many studies have been dedicated to investigate the reaction mechanism and response of a diverse group of materials as electrocatalysts for ORR/OER.[23,27]

This section provides a comprehensive summary of the latest developments and studies regarding bifunctional catalysts (i.e., reversible ORR and OER) for primary and rechargeable ZABs. The operating principles and detailed mechanisms for ORR/OER are also included at the beginning of this section. Catalysts are categorized into three different groups: noble or precious metals, non-precious transition metals/transition metal oxides and carbon-based materials. This literature review bridges the gap between previous reviews dedicated to bifunctional (ORR/OER) electrocatalysts developments and ZAB performance. The review also provides a rapid snapshot of the fast-developing field of bifunctional catalysts for rechargeable ZABs over the last few years.

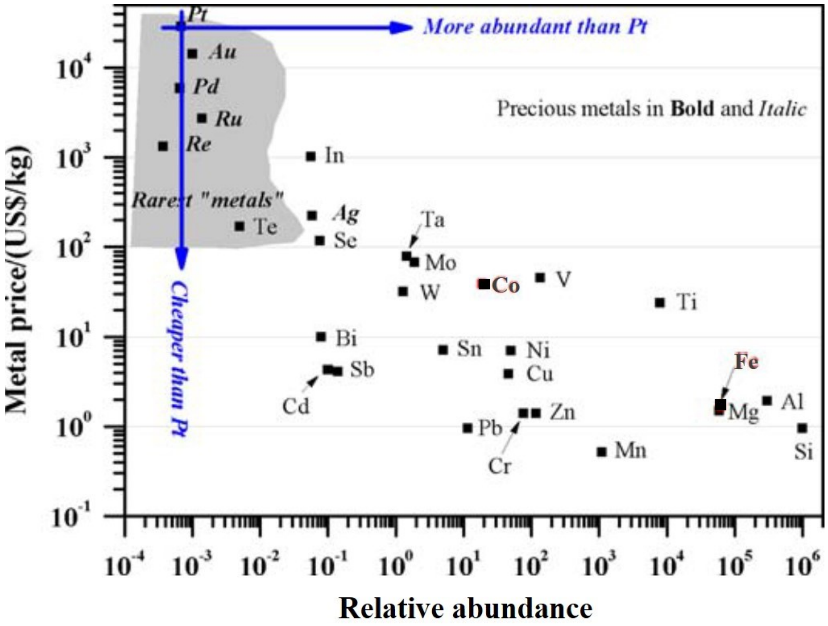

Figure 2-2 Relationship between metal prices and abundance of the chemical elements on Earth's upper crust (based on the abundance of Si with 10^6 atoms). The corresponding metal price data are from www.metalprices.com.[17]

2.2.1 Rechargeable ZAB architecture and components

The structure of a rechargeable ZABs is schematically shown in Figure 2-3, and is composed of a Zn anode, an air electrode and an alkaline electrolyte. The cathode is divided into two layers: a GDL and a catalytic layer. Upon discharge, Zn oxidizes to $Zn(OH)_4^{2-}$ at the negative electrode (Reaction 1). Supersaturation of $Zn(OH)_4^{2-}$ results the formation of ZnO which is in the form of white insulating powder (Reaction 2). On the other hand, at the positive electrode, O_2 diffuses into the GDL due to the pressure differences between the outside and inside of the cell. Oxygen is reduced at the surface of the electrocatalyst (Reaction 3).

The key process of the ZAB cathode is a three-phase reaction (gas-liquid-solid). During discharge, the catalyst (solid) accelerates the reduction of O_2 (gas) to hydroxyl ions in the electrolyte (liquid). During charge, the hydroxyl ions migrate from the cathode to the anode and Zn is electroplated from the aqueous electrolyte to complete the cell.

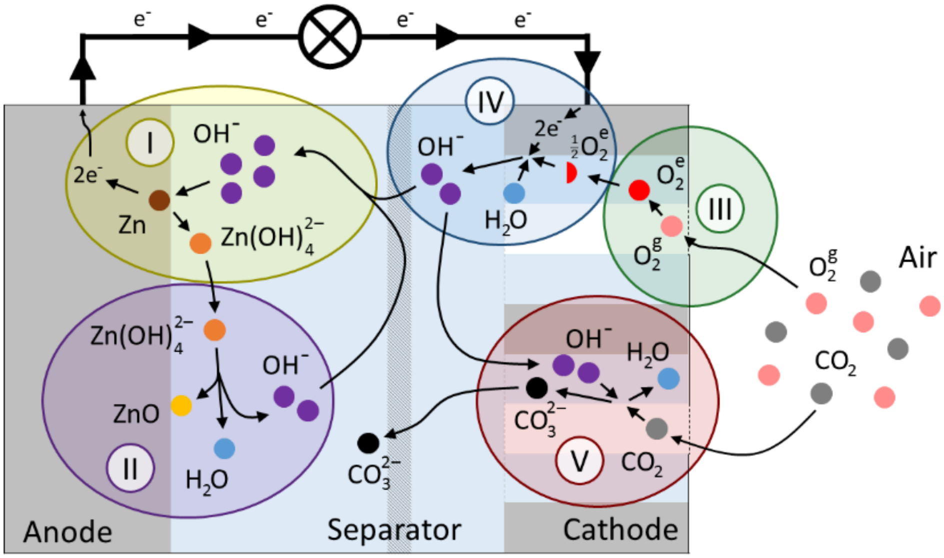

Figure 2-3 Schematic of a rechargeable ZAB and reactions.[35]

Dendritic growth of Zn occurs due to the inability of zincate ions to fully return to the same locations during recharge; this is one of the important challenges in operation of a rechargeable ZAB. Another issue that arises during cycling is the sensitivity of the highly alkaline electrolyte to CO_2 concentration from the feed air. As presented in Reaction 5, CO_2 from the feed air reacts with the KOH electrolyte to form carbonates. Carbonates precipitate and clog the pores of the air electrode and limit air access for ORR. The current challenges in developing rechargeable ZABs and the fast-growing pace of Li-ion batteries have limited attention to developing rechargeable ZABs. However, a few research groups, listed in Table 2-2, have successfully developed long cycle life secondary ZABs for commercial application.

The discharge processes in the anode and cathode of a ZAB are described by the following chemical reactions (1-5):

Anode:

$Zn_{(s)} + 4OH^-_{(aq)} \rightarrow Zn(OH)_4^{2-}{}_{(aq)} + 2e^-$ ($E° = -1.25$ V vs SHE) Reaction 1

$Zn(OH)_4^{2-}{}_{(aq)} \rightarrow ZnO_{(s)} + 2OH^-_{(aq)} + H_2O_{(aq)}$ Reaction 2

Cathode:

$O_{2(g)} + 2H_2O_{(aq)} + 4e^- \rightarrow 4OH^-_{(aq)}$ ($E° = +0.401$ V vs SHE) Reaction 3

Overall reaction: $2Zn_{(s)} + O_{2(g)} \rightarrow 2ZnO_{(s)}$ (cell potential: 1.65 V) Reaction 4

$2KOH_{(aq)} + CO_{2(g)} \rightarrow K_2CO_{3(s)} + H_2O_{(aq)}$ Reaction 5

Table 2-2 Rechargeable ZAB technology commercialization status.[21]

Company	Features and performance	Refs
Fluidic Energy	Using ionic salts plus additives as the electrolyte, coupled with nanostructured Zn as the anode	36,37
EOS	Neutral chloride electrolyte ($Zn/ZnCl_2$, NH_4Cl, H_2O/O_2); charge and discharge potentials at 2.1 V and 0.9 V; 2700 cycles with no degradation	19
Revolt	Liquid Zn slurry which flows through tubes that functions as air cathode; 200 cycles at 100 mA cm^{-2}	38–40
EDF France	Faradaic efficiency of 96% at 30 mA cm^{-2}; energy efficiency of 70%; energy density of 100 Wh kg^{-1}; cycle life of 90 cycles 15 min/cycle	41

The reversible potential for ZABs is 1.65 V (Reaction 4). However, depending on the load (applied current density), the practical voltage can drop to <1.2 V. The origin of this drop is largely due to the high overpotential at the air electrode during ORR and OER. Thus, rechargeable ZABs usually have a low round-trip energy efficiency of <55-65% (battery load: 1-50 mA cm^{-2}), which depends on the applied current density.

2.2.1.1 Zinc anode

Zinc is employed in various forms including Zn-foil, Zn-fibers or Zn-powder. Zinc is an abundant metal, relatively inexpensive and non-toxic (Figure 2-2). The specific energy density of Zn is 1084 Wh kg^{-1} and the power density demonstrated by primary ZABs is 300 Wh kg^{-1}.[42] Zinc has a low electrical resistivity of 5.95 $\mu\Omega$ cm^{-1}. Although a high Zn surface area is preferred due to the lower internal resistance and better inter-particle contact, self-corrosion of Zn electrode becomes more significant with smaller particle size.[43–46]Zinc oxidation reaction accompanied by hydrogen evolution reaction (HER) on the electrode surface will have a negative effect on zinc, electrolyte and sealing structure.[21] Many strategies have been developed to retard the HER and increase the corrosion resistance of the Zn anode. Table 2-3 summarizes the recent studies on the modification of Zn electrode during the past few years.

Another factor that limits the overall performance of ZABs is Zn dendrite growth during charge-discharge. Several reports have been published studying Zn and its the electroplating mechanism, which have investigated the effects of electrolyte concentration, concentration of OH^- and the amount of available H_2O molecules.[9] For example, it has been shown that the addition of metal oxides and hydroxides, such as Bi_2O_3, Ti_2O_3 and In_2O_3 with higher HER overpotential, to the electrolyte enhances the electronic conductivity, improves current distribution and promotes the formation of a thin, compact Zn deposit during recharge.[21]

2.2.1.2 Air electrode: gas diffusion layer (GDL)

Since 1932, after the invention of wax-treated carbon electrodes by Heise and Schumacher[47], GDL has been used as a cathode material for ZABs. Figure 2-4 shows a typical structure of an air electrode used in a ZAB. The GDL acts as an interface between the gas flow and the electrocatalyst, directing the electrolyte to the active sites. The side of the GDL facing the electrolyte is normally covered with a catalytic layer to provide a reaction zone at the three-phase boundary.[48] Typical GDLs consist of a bilayer structure including a macro-porous layer and a micro-porous layer (MPL). Mechanical properties (response to compression, bending and shear) as well as thermal and electrical properties are governed by the fibrous backing material of the GDL. The MPL facilitates catalyst deposition and improves the pore size distribution. Polytetrafluoroethylene (PTFE) loaded on both sides adjusts the degree of the hydrophobicity depending on the type of application (e.g., polymer electrolyte membrane fuel cells and metal-air batteries).[49]

GDLs are commonly fabricated by wet-laying of chopped polyacrylonitrile (PAN)-based carbon fibers; this is a highly scalable process.[50] The degree of hydrophobicity is different on either side of the GDL. The side in contact with the electrolyte contains a thin catalytic layer, which is usually spray-coated or directly deposited. This side is mildly hydrophobic with a smaller pore structure.

Table 2-3 Overview of modifications to the Zn electrode to increase the performance of ZABs.

Modification	Materials	Effects	Refs
Alloying	Hg	Improved electrical conductivity, adverse environmental problems, inhibits corrosion by 40%	2,10
	Pb, Cd, Ni, Sn, Bi	High HER overvoltage, improved discharge due to addition of an electronically conductive material, increases capacity of Zn	2,10,51,52
	7.5 wt% Ni and 2.5 wt% In	Reduced dendrite formation, raised HER overpotential	2,10,51,52
Coating	25 wt% Al_2O_3	Suppressed HER by preventing direct exposure of Zn to the electrolyte, 50% longer discharge time in 9 M KOH	53
	0.1 wt% Li_2O-$2B_2O_3$	Increased discharge capacity (1.70Ah), prevents Zn surface from facing KOH	54
	Neodymium conversion film	Stabilized the cycle life of Zn	9
	ZnO with polypyrene (PPy)	Restricts dendrite growth, superior cycle stability, stable charge voltage plateau, higher discharge voltage plateau	55
	Ni and Bi	Decreased corrosion current, decreased HER rate, shifts HER overpotential to more negative value	56
Addition of corrosion inhibitors to the electrolyte	Anions of organic, phosphoric, tartaric, succinic and citric acids	Absorbs at the sites of rapid dendrite growth, increased HER overpotential	2,9,10
	Phosphoric acid esters (GARAC RA 600)		
	Modified polyethylene glycol (PEG)		
Increasing the surface area	Fibrous	Provides 20% more capacity at high discharging currents (70 Ah), 90% material utilization at 1/7 C discharge rate	46
	3D wired sponge	Uniform deposition of discharged products, low internal resistance dendrite free discharge cycling at depth of discharge of 20%	57
Addition of binders	Na_2SiO_4	Higher conversion efficiency due to the porous nature of the silica binder, fixes metal particles, easy access to electrolyte	42
	Cross-linked polyacrylic acid polymers	Even distribution of Zn deposit, dendrite growth decreased	2,9,10,57
	2 wt % Super P carbon black	High specific discharge capacity (776 mA h g^{-1}), improved power density (20 mW cm^{-2})	45

The side in contact with the gas (e.g., pure O_2 or air) is highly hydrophobic with a larger pore size to allow gas to diffuse into the cell. Generally, carbon blacks suffer from catastrophic corrosion at very high potential during OER (>0.6 V vs Hg/HgO). Corrosion of GDL can reduce the reaction site density, leading to battery performance degradation. Therefore, increasing the corrosion resistance and porosity level and decreasing the thickness while maintaining the mechanical properties are common challenges in developing advanced GDLs.[58]

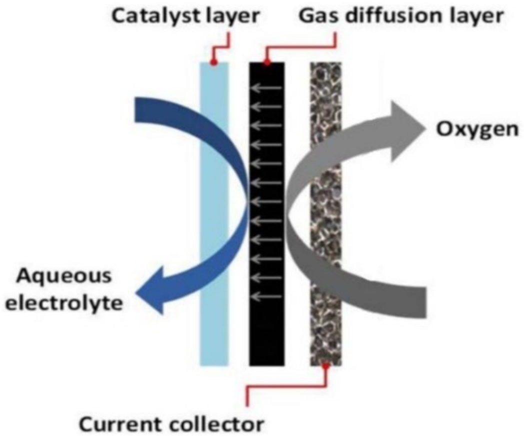

Figure 2-4 General structure of air electrode in a ZAB.[59]

Another challenge relates to the formation and maintenance of a stable three-phase boundary at the air electrode. The electrolyte may slowly flood the air electrode, leading to an increased diffusion path for O_2 into the structure and possibly the subsequent failure of the air electrode. In general, the hydrophobicity of the PTFE layer is progressively reduced in a highly alkaline solution, which results in movement of three phase reaction sites towards the back side of the GDL away from the electrocatalysts (air side). Flooding of the system results in increased ohmic resistance and a loss in the power density and efficiency. Flooding of the air electrode is also caused by carbonate by-products (Reaction 5) which clog the pores of the GDL, hindering electrolyte access to the triple-phase reaction zone. Some strategies to solve this issue are presented in Section 2.2.1.3.[21] The maximum working temperature of a ZAB is 80 °C; at this temperature the viscosity and the surface tension of the electrolyte is reduced which results in easier liquid infiltration in the GDL structure. Ventilation and cooling the battery set up reduce the risk of the liquid infiltration.[60,61]

2.2.1.3 Air electrode oxygen reaction mechanism

The main purpose of the air electrode is to facilitate OER and ORR during charge and discharge, respectively. These reactions include a series of complex reactin electron-transfer reactions. In general, there are three adsorption modes for an O_2 molecule on the surface of a metal or metal oxide catalyst: the Griffiths model, side-on mode (Yeager model) and the end-on mode (Pauling model) (Figure 2-5).[27] In the Griffiths model, the π orbitals of the O_2 molecules interact laterally with empty d-orbitals of the metal ions. The O-O bond is subsequently weakened, with an incremental increase in its length. If the interaction is sufficiently strong, it will lead to the dissociative adsorption of the O-O bond. The reactions may be followed by the reduction of the metal atom to regenerate the catalyst site. In the Pauling mode, the O_2 molecules interact with an end-on position on the electrode surface. Like the Griffiths mode, the π orbitals of O_2 molecules interact with the empty d-orbitals of the catalyst. However, only partial charge transfer occurs which results in the formation of peroxides and superoxides. The Yeager mode requires two adsorption sites with partially filled d-orbitals for bonding with π-orbitals of O_2 molecules. The adsorption mode depends on the metal/metal oxide surface and its electronic structure, which affect the nature of corresponding active sites. The original concept of active sites can be traced to the studies of Taylor and Boudart.[62] For example, preferred oxygen adsorption occurs with the side-on mode on the exposed edges of graphene nanoparticles (NPs) as opposed to adsorption on the basal plane (end-on mode), as a recent study shows.[63]

The kinetics and mechanisms of ORR/OER are a function of many experimental factors including the selection of cathode material (e.g., electrocatalysts), the electrolyte, concentration of active species (e.g., peroxides and hydroxides) and the electrode design. The mechanisms of ORR/OER in precious metals and metal oxides have been extensively studied in the last few years.[64–66] Advanced computational methods have enabled researchers to predict which catalysts will have more activity towards ORR/OER. These predictions help save time and costs in developing proper catalysts. D-band center theory, suggested by Nørskov,[67] has played an important role in studies of catalysts, and a famous volcano plot (catalyst activity vs oxygen binding energy) has been used to predict activity and selectivity of ORR/OER catalysts.

ORR multistep reactions proceed by generation of *-OH, *=O and *-OOH as intermediates, which are briefly given as following:[65]

$O_{2(g)} + 2H_2O_{(aq)} + 4e^- \rightarrow 4OH^-_{(aq)}$ ($E° = 0.40$ V vs SHE) *four-electron pathway* Reaction 6

$O_{2(g)} + 2H_2O_{(aq)} + 2e^- \rightarrow HO_2^-{}_{(aq)} + OH^-_{(aq)}$($E° = -0.07$ V vs SHE) *two-electron pathway*

Reaction 7

$HO_2^-{}_{(aq)} + H_2O_{(aq)} + 2e^- \rightarrow 3OH^-_{(aq)}$ ($E° = 0.87$ V vs SHE) Reaction 8

ORR may proceed via a four-electron pathway (Reaction 6) or a two-electron pathway on the surface of an electrocatalyst (Reaction 7). The number of electrons transferred can be obtained from rotating disk electrode (RDE) and rotating ring disck electrode (RRDE) tests, which reveal the ORR mechanism for selected materials. Recent experimental results and mathematical simulation using density functional theory (DFT) on different materials have shown that the ORR pathway is a structure sensitive reaction depending on the surface geometry, electronic structure and the O_2 adsorption sites. For example, a recent DFT study by Busch et al.[65] showed that the reversibility of ORR/OER is determined by the sequence of four coupled proton/electron transfer mechanisms as in the following (* denotes active sites):

$* + H_2O_{(aq)} \leftrightharpoons *\text{-}OH + H^+_{(aq)} + e^-$ Reaction 9

$*\text{-}OH_{(aq)} \leftrightharpoons *{=}O + H^+_{(aq)} + e^-$ Reaction 10

$*{=}O + H_2O_{(aq)} \leftrightharpoons *\text{-}OOH_{(aq)} + H^+_{(aq)} + e^-$ Reaction 11

$*\text{-}OOH_{(aq)} \leftrightharpoons * + H^+_{(aq)} + e^- + O_{2(g)}$ Reaction 12

The potential for each individual step results from the difference in binding energy of the different intermediates (i.e., *-OH, *=O and *-OOH) before and after a charge transfer. The major obstacle in finding good bifunctional catalysts is the interdependence of the binding energy of the intermediate in the first and the third electron transfer step, i.e., the *-OH and *-OOH (Reactions 9 and 12). Ideally, the energy difference between each of the four intermediates should be 1.23 eV. However, the minimum average energy for Reactions 9 and 11 is at least 1.6 eV, which results in ~0.4 V overpotential for both OER and ORR. The scaling relations between the *-OH and *-OOH binding energies prevent any compound with a single site to be both ORR and OER active. As Figure 2-6 represents, active ORR catalysts are on the top of the ORR pyramid (blue) whereas active OER catalysts are on top of the OER pyramid (green). Therefore, a bifunctional catalyst which is active towards both would fall in the forbidden region (the gap between two cross section red triangles in Figure 2-6).

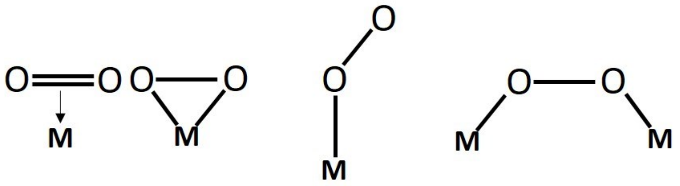

A. Griffiths model B. Pauling model C. Yeager model

Figure 2-5 Possible configuration of O_2 molecule interaction with a metal or metal oxide (M).[27]

It is now generally accepted that precious metals facilitate four-electron pathways, whereas the two-electron pathway is primarily observed in carbonaceous materials.[16] For transition metals and oxides, the surface area, specific crystal structure and the composition determine the reversibility and the oxygen reduction pathways.[16,65]

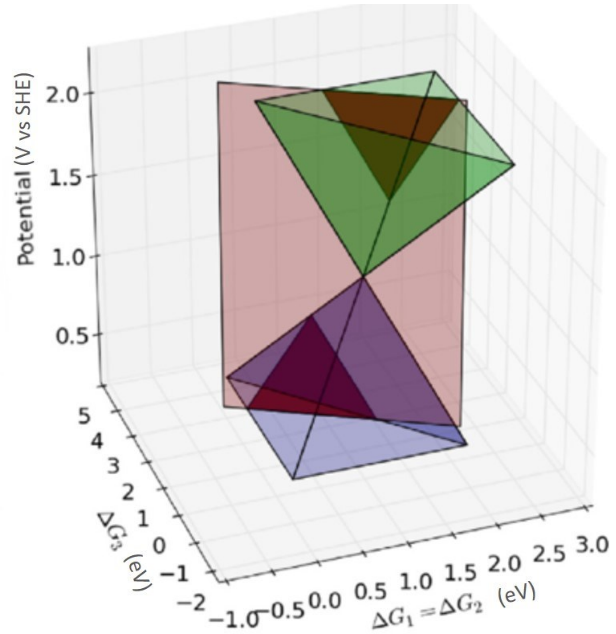

Figure 2-6 Two pyramids which depict the best achievable potential for the ORR (blue) and the potential determining step for the OER (green) as a function of the free energies for Reactions 9-11. The constraint set by the constant offset of 3.2 eV between *-OH and *-OOH is represented by the red plane. The red plane cuts the two pyramids creating two separate volcanoes for OER and ORR which are darkened.[65]

2.2.1.4 Electrolyte

Secondary ZABs utilize a highly alkaline electrolyte, typically KOH, NaOH or LiOH. KOH has a higher conductivity than NaOH (30 wt% KOH: ~0.6 S cm^{-1} [68] vs NaOH: ~0.2 S cm^{-1} [69] at room temperature).[70] Moreover, K_2CO_3, the reaction product of KOH with air (Reaction 5) has better solubility than Na_2CO_3. The concentration of KOH is optimized at 26-30 wt% (6-7 M), i.e., the highest electrical conductivity. Higher concentrations increase the viscosity and the possibility of ZnO formation (Reaction 1). Based on the Nernst equation:

$$\mathrm{E} = \mathrm{E}^{\circ} - \frac{\mathrm{RT}}{\mathrm{nF}} \ln \mathrm{Q_c}$$

where E is the cell potential (V), E° is the cell potential (V) under standard-state conditions, R is the ideal gas constant (8.314 J mol^{-1} K^{-1}), T is the absolute temperature (K), n is the number of moles of electrons transferred in the balanced equation, F is the Faraday's constant (95,484.56 C mol^{-1}), and $\mathrm{Q_c}$ is the concentration of the products divided by the concentration of the reactants in a reaction [4]. The electrode potential shifts about -0.83 V by changing the pH value of the electrolyte from 0 to 14, which significantly affects the electric field at the electrode-electrolyte interface.[2,9] An acidic medium is an inappropriate electrolyte for ZABs due to severe reaction of hydrogen ions with Zn metal. Also, some electrocatalytic materials, transition metal oxides in particular, are not stable in strongly acidic conditions.

Two major disadvantages of alkaline electrolytes are 1) carbonate precipitation (Reaction 5) which clogs the GDL pores and 2) the high sensitivity to temperature and humidity especially during long-term charge-discharge cycling.[71] To circumvent the carbonate issue, feeding purified air, employing O_2 selective permeable membranes, using CO_2 absorbents (e.g., soda lime, LiOH and LiOH-$Ca(OH)_2$) and circulating the electrolyte are effective countermeasures that have been studied. The addition of K_2CO_3 is another possibility to mitigate this negative impact. The more CO_3^{2-} ions that are present in the electrolyte, the slower the carbonation reaction (Reaction 5) rate.[72] The issue of temperature and humidity sensitivity can be resolved by strategies such as using a solid state electrolyte with an ionic conductivity of 10^{-2}-10^{-3} S cm^{-1}.[73–75] Solid-state electrolytes can be used as both an ion conducting media and a separator, simplifying the design of ZABs and increasing cycle life. Gel-type electrolytes using gelling agents such as hydroponics, polyethylene oxide, polyvinyl alcohol (PVA) and polymerized acrylate-KOH-H_2O, have been used as solid state electrolytes for ZABs.[21,57,76] As an example, an efficient, flexible ZAB has been developed by utilizing a PVA gel, which functions as both electrolyte and separator between the air electrode and Zn film. The porous gelled PVA membrane assists electrolyte accessibility to the surface of the electrode under bending conditions as well as accommodating the electrolyte by capillary forces. The ZAB was cycled 120 times under a charge-discharge rate of 150 A L^{-1} with a high volumetric energy density of 250 Wh L^{-1} and gravimetric energy density of 581 Wh kg^{-1}.[77] Another study developed lightweight functionalized cellulose nanofibers applied as a hydroxide conductive solid state electrolyte for a highly flexible rechargeable ZAB. Figure 2-7 shows a schematic diagram of the ZAB device integrated with a bandage. The device, wrapped around an index finger, powered a light emitting diode (LED) under bending conditions. High water retention and stability of natural cellulose nanofibers were observed with no power density fading under a bending condition.[78]

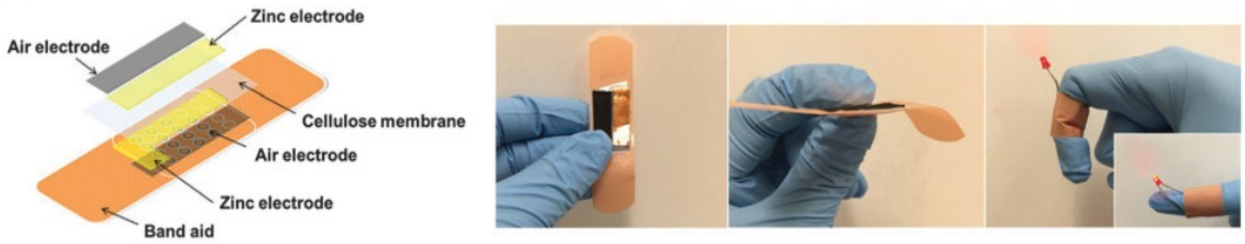

Figure 2-7 Schematic diagram of a flexible solid state ZAB device integrated with a bandage (left). The flexible device is wrapped around an index finger powers a red LED under bending condition (right).[78]

Hydrophilic or hydrophobic room temperature ionic liquids (RTILs) (non-aqueous electrolytes) have been evaluated as alternatives to aqueous electrolytes.[79–84] The benefits and drawbacks of RTILs are summarized in a recent comprehensive review by Xu et al.[85] Studies showed improved cyclability, slower corrosion rate, suppressed dendritic growth and less carbonate by-products during charge-discharge cycling.[9] However, the performance of ZABs using RTILs was inferior to batteries using KOH. There are still several challenges facing the use of RTILs and considerable work needs to be done before they are commercially viable. The challenges include, the formation of insoluble metal peroxide/superoxides when using smaller cation salts (irreversible ORR), high viscosity of RITLs (i.e., limited GDL wettability), rapid voltage drop and low maximum power density.[10,21]

2.2.1.5 Separator

Separators are fine porous structures between the Zn anode and the air cathode. They are made of non-woven polymers, such as polyethylene (PE), PVA, polyolefin (PO) and polypropylene (PP). Separators transfer the hydroxyl ions (OH^-) from the air electrode to the anode. The basic requirement for a suitable separator for ZABs includes an appropriate pore size, high ionic conductivity, high stability, high adsorption capacity and high electrical resistivity in alkaline solutions. Celgard® 5550 which is a tri-layered structure (PP/PE/PP) coated with surfactants for rapid electrolyte wetting has been commonly used as the separator in recent ZAB studies.[10,21,78] One challenge in using separators is that the porous structure of separators allows Zn^{2+} ions to migrate towards the air electrode, which will decrease the capacity of the battery. The use of anion exchange membranes, which are selective to the passage of ions, has been proposed to overcome this problem.[10,21]

2.3 Bifunctional catalysts for ZAB air electrode

As mentioned previously, a major challenge of developing a highly efficient and stable rechargeable ZAB is overcoming the slow kinetics of ORR and OER. The main function of an efficient bifunctional electrode is to promote ORR/OER in a single layered structure. Reviews on cathode electrocatalysts can be found in previous studies.[16,17,20,23,24,66,86–89] In this section, bifunctional catalyst materials are divided into three main groups: noble metals and alloys, transition metals and oxides (spinels and perovskites) and carbon-based materials. Some examples of high performance catalysts and ZABs are presented for each category.

2.3.1 Noble metals and alloys

Noble metals, such as Pt and Ir, are well-known benchmark catalysts for ORR and OER, respectively. While they offer the advantage of high catalytic activity and electrical conductivity, their high cost and scarcity are serious concerns. Noble based catalysts are normally well-dispersed on a high surface area carbon support (e.g., carbon black, carbon nanotubes (CNTs) and graphene). As shown in Figure 2-2, Platinum is one of the most expensive and least abundant metals. Three main strategies have been taken to reduce the cost of precious metal electrocatalysts, including using less expensive alternatives such as Ag, alloying with high ORR/OER active low cost metals/metal oxides or nanostructuring noble metals to minimize the mass required. Table 2-4 presents a summary of recently developed precious metal-based bifunctional electrocatalysts used in ZABs. Several examples of recent studies are provided in the next paragraphs.

Silver with only 1% of the cost of Pt is one of most cost effective precious metals. Silver-based catalysts are usually coupled with MnO_2 and carbon supports (e.g., single walled carbon nanotubes (SWCNTs) and carbon blacks) as ORR/OER active composites.[90,91]

Rechargeable ZABs with only 10 wt% Ag/C (Ag particles size of 25.9 nm) as the electrocatalyst demonstrated a power density of 34 mW cm^{-2} at 35 °C.[92] Although the electrocatalytic results were not compared with Pt/C, it was shown the power density increased to 72 mW cm^{-2} at 80 °C, which is closer to the ZAB operating temperature. In a different study, a novel GDL was designed using Ag-NPs supported on SWCNTs as a cathode of a ZAB. The weight and thickness of the GDL was reduced to 0.005 mg cm^{-3} and 0.05 mm, respectively, for AgNP-SWCNTs vs 0.79 mg cm^{-3} and 0.49 mm for conventional carbon-based electrodes with comparable performance.[93] It was also shown that Ag-based catalysts had better OER (i.e., more negative OER onset potential) performance compared with Pt/C in highly alkaline electrolytes. The low OER performance of Pt/C was attributed to the accumulation of oxygenated species, which cover the surface and decrease the active surface area.[94]

Alloying precious metals with non-precious metals such as Cu and Pb is also one of the strategies to reduce the cost and increase the long-term stability of ZABs.[95–98] For example, structurally ordered Pd_3Pb/C catalysts exhibit ~2-4 times higher mass activity relative to the traditional baseline Pt/C catalyst. The activity enhancement of Pd_3Pb/C originates from the higher number of active sites created by varying the Pd-Pd bond distance and modification of the electron configuration. The corresponding ZAB exhibited excellent long-term stability with only a 0.14 V overpotential increase after 560 h of cycling.[96]

Table 2-4 Summary of secondary/primary ZAB batteries and bifunctional electrocatalyst characteristics for recently studied noble metals and alloys

Catalyst material	Secondary (S)/Primary(P) ZAB battery characteristics	ORR and OER catalyst characteristics	Refs
10 wt%Ag/C	(P) Pd: 34 mW cm^{-2} at 35 °C	n=4 larger particles, n=2 smaller particles	92
Ag-Cu	(S) E_{charge}: 2.04 V; $E_{discharge}$: 1.1 V; efficiency: 53.09% (P) Pd: 85.8 mW cm^{-2} at 100 mA cm^{-2}; Sc: 72 mAh g^{-1}	ORR_{Op}: -0.19 V, OER_{Op}: 0.55 V vs SCE, n=3.9	99
NPAg-SWNT	(P) SC: 515 mAh g^{-1}; Sed: 300 Wh kg^{-1}	ND	93
Ordered Pd_3Pb/C-$NiCo_2O_4$	(S) E_{charge}-$E_{discharge}$: 0.72 V (first cycle); 0.86 V (135th cycle); 4h/cycle at 10 mA cm^{-2} (P) Sc: 574 mAh g^{-1}; Sed: ~710 Wh kg^{-1} at 10 mA cm^{-2}	ORR_{op}: 1.03 V vs RHE $ORR_{E1/2}$: 0.92 V vs RHE ORR_{Lcd}: -6.5 mA cm^{-2} at 1600 rpm n=4	96
CuPt-nanocaged	(P) 253.8 mA cm^{-2} at 1 V; Sc: 560 mAh g^{-1}; Sed: 728 Wh kg^{-1} at 20 mA cm^{-2}	ORR_{Op}: 0.95 V vs RHE ORR_{Lcd}: -6.25 mA cm^{-2}	95
RuO_2-MCNA	(S) initial E_{charge}: <1.9 V and $E_{discharge}$: ~1.25 V at 4 mA cm^{-2}; 100 cycles at 1200s/cycle	$ORR_{E1/2}$: 0.8 V vs RHE n=~4	100
AgCu-nanoalloys	(S) E_{charge}: 2.2 V $E_{discharge}$: 1.08 at 10 mA cm^{-2}; +0.01 V increase after 200 cycles (P) Pd: 86.3 mW cm^{-2}; discharge current: 60 mA cm^{-2} at 1 V	ORR_{Lcd}: 5.9 mA cm^{-2}, n=3.9	97
AgCu	(S) Efficiency: 56.4% at 20 mA cm^{-2}; 4h/cycle (P) Pd: 86.5 mW cm^{-2} at 100 mA cm^{-2}	ORR_{Op}:-0.15 V vs SCE ORR_{Lcd}: -25.6 mA cm^{-2} at 0.8 V	99

*Op: Onset potential
*Lcd: Limiting current density
*$E_{1/2}$: Half-wave potential
*Pd: Power density
*Sc: Specific capacity
*Sed: Specific energy density
*n: Number of electron transferred
*SWNT: Single wall carbon nanotube
*MCNA: Mesoporous carbon nanofiber array

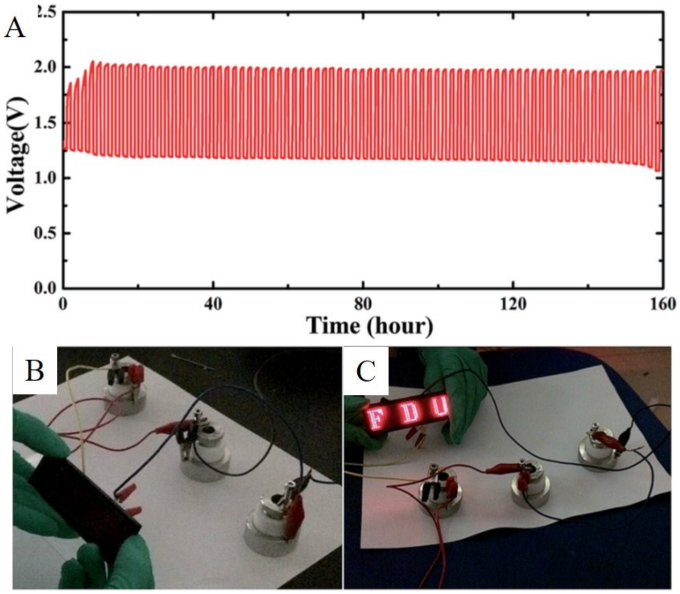

Figure 2-8 (A) Charge-discharge cycling curves of a ZAB with RuO_2-coated MCNA catalyst (current density of 4 mA cm^{-2} and 1 h/cycle) (B,C) images of an LED before and after being driven by three ZABs in series.[100]

In another study, CuPt-nanocages (NCs), an intermetallic structure, with particle size of ~20 nm were prepared by a solvothermal method. Open faceted hollow geometric CuPt-NCs with an ordered atomic arrangement provided facile O_2 molecular accessibility and high numbers of active sites within the structure. Applying CuPt-NCs in a ZAB led to a superior specific capacity and energy density (560 mAh g_{Zn}^{-1} and 728 Wh kg_{Zn}^{-1}, at a discharge rate of 20 mA cm^{-2}), in comparison with the performance of a system with Pt/C as the cathode (480 mAh g_{Zn}^{-1} and 624 Wh kg_{Zn}^{-1}, at a discharge rate of 20 mA cm^{-2}).[95] Recently, dendrite shaped Ag-Cu catalysts developed by a galvanic displacement reaction were suggested as an active bifunctional catalyst. A facile preparation technique, carbon-free structure and high stability were touted as advantages of this catalyst.[99] Also, DFT analysis on a similar catalyst (Ag-Cu nanoalloy), fabricated using pulsed layer deposition (PLD), showed an increase in oxygen adsorption energy from -0.86 eV for pure Ag clusters to -1.36 eV for AgCu (Cu-shell) clusters. This facilitates the thermodynamics of ORR by lowering the adsorption energy.[97,98]Coating the carbon support with precious metals/metal oxides has been reported in a recent report. Using a crab shell template, RuO_2-coated with ordered mesoporous carbon nanofiber arrays (MCNA) were developed. Figure 2-8 shows a ~3.7 V LED powered by three ZAB cells, using a RuO_2-coated MCNA catalyst, connected in series. The uniform RuO_2 coating provides efficient ORR/OER active sites and long cycle life (160 h at 4 mA cm^{-2}) in a rechargeable ZAB.[100]

2.3.2 Transition metal oxides

Compared with precious metals, non-precious metal catalysts are more desirable for applications such as fuel cells and batteries due to their abundance and low cost. Among them, transition metal oxides have been extensively investigated in the form of single, binary or ternary oxides. Figure 2-9 summarizes the ORR catalytic process for transition metal-oxides. Based on this theory, the competition between O_2^{2-}/OH^- displacement (Step 1) and OH^- regeneration (Step 4) on surface of the transition-metal ions determines the rate-limiting steps for ORR in alkaline solutions.[101]

2.3.2.1 Single/binary transition metal oxides/hydroxides

MnO_x is the most common candidate among all the single transition metal oxide based catalysts. MnO_x catalysts are low cost and abundant, with minimal environmental impact.[102–107] The bifunctional activity of MnO_x based catalysts depends on the crystal structure, oxidation states and surface area. For example, MnO_2 has many polymorphic forms with different properties, including α- (cryptomelane), β- (rutile), γ- (manganite) and δ- (vernadite) types. It has been shown in several studies that the catalytic activity of polymorphic MnO_2 is in the sequence of $\beta\text{-}MnO_2 < \lambda\text{-}MnO_2 < \gamma\text{-}MnO_2 < \alpha\text{-}MnO_2 \sim \delta\ MnO_2$.[108–111] As stated in a study by Cao et al.[112], the ORR activity of polymorphic MnO_2 is attributed to the crystal structure. For crystalline phases, each crystallographic orientation provides certain energies for O_2 dissociation. However, it was shown that MnO_x with amorphous structures are also active towards ORR due to the large concentration of defects in the lattice. According to this speculation, amorphous/monocrystalline MnO_x has also been investigated in several reports.[113–115] For example, poorly crystalline/amorphous-bifunctional MnO_2 catalysts were grown on carbon paper using a simple immersion process in a study by Sumboja et al.[116] Good cycling stability up to 500 cycles and a power density as high as 108 mW cm^{-2} were achieved. In a different study, increasing the weight percentage of amorphous MnO_x up to 28% in a Ni-modified MnO_x/C composite enhanced the ORR current density with lower generation of peroxide. Further electrochemical characterization showed that the higher ORR activity of Ni-modified MnO_x/C is due to the increased amount of MnOOH from the oxidation of Mn^{2+}.[105] More specifics about the mentioned examples can be found in Table 2-5.

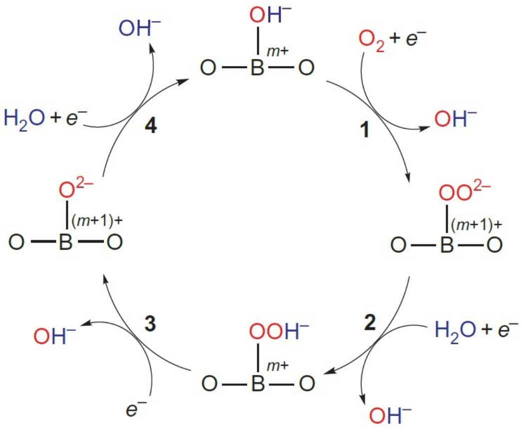

Figure 2-9 Proposed ORR mechanism on transition metal oxide catalysts in four steps. Step 1: surface oxide displacement; Step 2: surface peroxide formation; Step 3: surface oxide formation' Step 4: surface hydroxide regeneration (B= transition metal ion).[101]

The low conductivity of MnO_x catalysts is one of the factors limiting the utilization of it as an air electrode catalyst for ZABs. To overcome this problem, conductive carbon materials such as carbon black (Vulcan XC-72), CNTs and graphene are usually added to MnO_x as the catalyst support.[117] Another approach is to increase the conductivity of MnO_x by incorporating conductive elements such as Ag-NPs[118,119] or other ORR/OER active transition metal oxides catalysts such as Co_3O_4[120]; this will be further discussed in Section 2.3.2.2

Other bifunctional catalysts that have been extensively studied are transition metal oxides such as Co-oxide/hydroxide NPs supported on graphene, graphene oxide and carbon blacks.[121–126] It has been proposed, by a DFT study, that the origin of ORR reactivity of CoO_x/C relies on the gap between highest occupied molecular orbitals (HOMO) and the lowest unoccupied molecular orbitals (LOMO) of the crystalline surface of Co (II). A small gap implies low kinetic stability but high electrochemical activity to extract the electrons from the HOMO to the LOMO.[121] Using the same numerical technique, it was shown that hexagonal $Co(OH)_2$/N-doped reduced graphene oxide (rGO) nanoplates outperformed CoO and Co_3O_4 with a ΔE (energy gap between the HOMO and LOMO) of 0.87 V. This means that the Co-OH bond is neither too strong nor too weak, which results in enhanced bifunctional activity of $Co(OH)_2$.[122]

Recently, Liu et al.[127] developed highly active bifunctional catalysts, fabricated by a non-surfactant assisted hypothermal method, consisting of a non-spinel Co-Mn oxide supported by N-doped CNTs (NCNT/$Co_xMn_{1-x}O$).[127] A rechargeable ZAB with a low charge-discharge gap (0.57 V) and high stability was reported. The authors believed that graphitized nanocarbon, such as CNTs, can mitigate carbon oxidation and increase the corrosion resistance resulting in long-term stability.

One of the most interesting discoveries in this group of electrocatalysts is the development of layered double hydroxide (LDH) materials. LDHs are conducting hydroxide clay materials with the formula of $[M^{II}_{1-x}M^{III}_{x}(OH)_2]\left[(A^{n-})_{\frac{x}{n}}.mH_2O\right]$, where $M^{II}$is a divalent cation such as Ni^{2+}, $M^{III}$is a trivalent cation such as Fe^{3+} and A^{n-} is an anion such as CO_3^{2-}. Ni-Fe-CO_3^{2-}LDH has electronic and ionic conductivities of 5×10^{-3} and 6×10^{-6} S cm^{-1}, respectively. Also, the presence of CO_3^{2-} will inhibit carbonate precipitation at the triple phase boundary in a rechargeable ZAB. Various Ni-Fe mixed compounds have been synthesized and reported in the last few years.[128–130] For example, a rechargeable ZAB in a tri-electrode configuration was designed using a CoO/N-CNT hybrid as the ORR catalyst and Ni-Fe-LDH as the OER catalyst for the cathode. High ORR and OER activities were attributed to the strong coupling effect between nanoscale inorganic particles and the conducting CNT substrate. A peak power density of 265 mW cm^{-2} and a current density of ~200 mA cm^{-2} at 1 V were reported, which is a significant improvement in performance for a primary ZAB in comparison with previous reports. It is worth noting that the cathode electrocatalysts were loaded on two separate electrodes for charge (CoO/N-CNT) and discharge (Ni-Fe-LDH), respectively. Improved activity and efficiency were also confirmed for a rechargeable ZAB (~65% at 20 mA cm^{-2}) using a tri-electrode configuration. No significant voltage change and no obvious degradation were discerned during both the charge and discharge segments after 200 h cycling at 20 mA cm^{-2} in this configuration.[129] Ni-Fe-LDH was also used as an anion exchange membrane (AEM)-type electrode to prevent the formation of K_2CO_3 (Reaction 5).[130] The AEM was placed at the interface between the alkaline electrolyte and catalyst layer of the air electrode. Applying an AEM suppressed the permeation of K^+ cations from the electrolyte into the air electrode and inhibited the formation of carbonate. The other advantage of Ni-Fe-LDH is its ability to sense the external electric field through a color change.

Table 2-5 Summary of secondary/primary ZAB batteries and bifunctional electrocatalyst characteristics for recently studied single/binary transition metal oxides/hydroxides.

Catalyst material	Secondary (S)/primary (P) battery characteristics	ORR and OER catalyst characteristics	Refs
MnO_x nanowire-Ketjenblack Carbon	(P) Pd: ~190 mW cm^{-2}	ORR_{op}: -0.05 V vs Hg/HgO ORR_{Lcd}: -7.5 mA cm^{-2} at 3200 rpm	113
MnO_2-Ag NP	(S) E_{charge}: 2.6 V and $E_{discharge}$: 1.1 V at 5 mA for 90 h	ORR_{op}: -0.06 V vs Ag/AgCl ORR_{Lcd}: -1.9 mA cm^{-2}, OER_{cd}=11.61 mA cm^{-2} average n=3.7	118
NiFe LDH/CNT-CoO/N-CNT	(S) E_{charge}: 1.95 V and $E_{discharge}$: 1.25 V at 20 $mAcm^{-2}$ for 200 h; efficiency: ~65% (P) Pd: 265 mW cm^{-2}; current density at 1 V: 200 mA cm^{-2}; Sc: ~ 570 mAh g^{-1}; Sed: 700 Wh Kg^{-1}	N/A	129
NCNT/CoO-NiO-NiCo	(S) E_{charge}-$E_{discharge}$= 0.75 V at 20 mA cm^{-2}; 600 s/cycle for 100 cycles (P) Sc: 545 mAh g^{-1}; Sed: 615 Wh kg^{-1} at 35 mA cm^{-2}	ORR_{op}:0.97 V, E_{OER}: 0.27 V vs RHE at 10 mA cm^{-2}, n=3.85	131
rGO–IL/Mn_3O_4	(P) Pd: 120 mW cm^{-2} at 200 mA cm^{-2}	ORR_{op}:-0.1 V Hg/HgO, ORR_{Lcd}: -0.22 mA at -0.45 V, Average n: 3.5	117
$Co(OH)_2$-N-rGO	(S) E_{charge}-$E_{discharge}$= 1.2-1.3 V at 15 mA cm^{-2} for 50 h; efficiency: 46%	$\Delta E_{OER-ORR}$=0.87 V n: ~3.6 E_{OER}: Vat 10 mA cm^{-2}: 1.68 V E_{ORR} at -3 mA cm^{-2}: 0.66 vs RHE	122
CoO_x/XC-N	(P) Pd: 110 mW cm^{-2} at 160 mA cm^{-2}	ORR_{op}: 0.86 V vs RHE n=~3.7	121
NCNT/$Co_xMn_{1-x}O$	(S) E_{charge}-$E_{discharge}$= 1.18 V at 50 mA cm^{-2}; E_{charge}-$E_{discharge}$= 0.57 V at 7 mA cm^{-2} (P) Sc: 581 mAh g^{-1}; Sed: 695 Wh kg^{-1} at 7 mA cm^{-2}	ORR_{op}: 0.086 V vs RHE, ORR_{Lcd}:: -5.5 , OER_{cd} at 0.3 V vs RHE: 4.6 mA cm^{-2}	127
MnO_2-NCNT	(S)E_{charge}-$E_{discharge}$ =1.6 V at 10 mA cm^{-2} 300 s/cycle	ORR_{cd}=-4 mA cm^{-2} at -0.8 V vs Ag/AgCl, OER_{cd}: ~39 mA cm^{-2}	110
Ni-MnO_x/C	(S) $E_{discharge}$: 0.96 V at 100 mA cm^{-2} (P) Pd: 122 mW cm^{-2}	ORR_{op}: -0.063 V vs Hg/HgO ORR_{cd}: 0.94 mA, n=~3.82	105
MnO_2/C-NiO/NiOOH	(S) Faradiac efficiency: 96% at 30 mA cm^{-2}; energy efficiency: 70% Sed: 100 Wh kg^{-1} cycle life: 90 cycles at 15 s/cycle (P) Sc: 819.8 mAh g^{-1}	N/A	41
N-NiFe-LDH	(P) Pd: 0.55 mW cm^{-2} at 0.65 V	E_{OER}: 0.23 V vs Ag/AgCl at 10 mA cm^{-2}	132
CuFe	(P) Pd: 212 mW cm^{-2}	n~3.7-3.9	133
MnO_2	(S) E_{charge}: 2.04 V $E_{discharge}$: 1.27 V at $charge_{Cd}$: 7.5 mA cm^{-2} at 4 h/cycle and $discharge_{Cd}$: 15 mA cm^{-2} at 2 h/cycle	ND	116

*Op: Onset potential, Lcd: Limiting current density, Pd: Power density, Sc: Specific capacity, Sed: Specific energy density, N/A: Not applicable, n: Number of electrons transferred
*NP: Nanoparticle, LDH: Layered double hydroxide, CNT: Carbon nanotube, GO: Graphene oxide, rGO: Reduced graphene oxide, IL: Ionic liquid

In a recent study by Chen et al.[132], a N-doped Ni-Fe-LDH film was prepared by a facile one-step chemical bath deposition method. Nickel and Fe salts were used as precursors and hexamethylenetetramine (HMT, $C_6H_{12}N_4$) was used as the structural template as well as the nitrogen source. Nickel foam was used as the substrate. A well-crystallized 3-dimensional microporous nanolayer composed of numerous thin nanolayers (~0.8 nm) was vertically grown on a framework. As shown in Figure 2-10, the pristine color of Ni-Fe-LDH is gray silver, which changed to dark black during the OER process for a potential scan from 0 to 1 V vs RHE (reversible hydrogen electrode). Interestingly, the color can recover to the original state during the reverse scan from 1 to 0 V. The origin of the color change corresponded to the oxidation of Ni species following the equation: $Ni(OH)_2 + OH^- \rightarrow NiOOH + H_2O + e^-$ at ~0.45 V during charge and the reverse reaction at ~0.25 V during discharge.[132]

Nickel- and Co-based bifunctional electrocatalysts (stand alone metallic or NiCo/oxide-hydroxides) have attracted considerable attention due to their high electrical conductivity.[131,134] A NiCo alloy coupled with a small fraction of their oxides (NCNT/CoO-NiO-NiCo) exhibited excellent bifunctional activity and stability for ORR-OER in primary and rechargeable ZABs (Table 2-5). Under ambient air conditions, the primary ZAB showed a high energy density of 615 Wh kg_{zn}^{-1} at a current density of 20 mA cm^{-2}, due to the synergistic effect between the monometallic Co- (ORR active) and Ni-based (OER active) electrocatalysts.[135]

Furthermore, Co and Fe and their oxides have also been reported to have high bifunctional activity.[136] Copper-Fe-NP alloys encapsulated within graphitic carbon layers are highly active and durable ORR catalysts. DFT calculations revealed a complex ORR mechanism and a possible synergistic effect due to the alloying. The results showed that the $CuFe_{inner}$ surface facilitated ORR at a lower overpotential. Also, high resolution transmission electron microscopy (HRTEM) after 1000 continuous cycles showed no change in the crystal structure of the pristine CuFe particles, whereas the graphitic carbon layers were completely transformed into amorphous carbon. It is mentioned in this study that the carbon layer increased the corrosion resistance and acted like a protective layer for the catalysts.[133]

Other transition metal oxides have also been the subject of several studies for ZAB applications. For example, Magneli phase materials such as Ti_nO_{2n-1} ($4<n<10$) have been explored as electrode materials due to their high electrical conductivity (1000 S cm^{-1}) and corrosion resistance in aggressively alkaline/acidic solutions.[137] TiO_2 (anatase) is formed by one-step vapor hydrolysis of

$TiCl_4$. Anatase showed a small polarization of 8 mV at 150 mA cm^{-2} and the catalyst showed steady performance during discharge (1.05 V).[138]

The above examples, as well as the summary provided in Table 2-5, indicate that transition metal-based electrocatalysts have potential to achieve widespread practical application in ZABs.

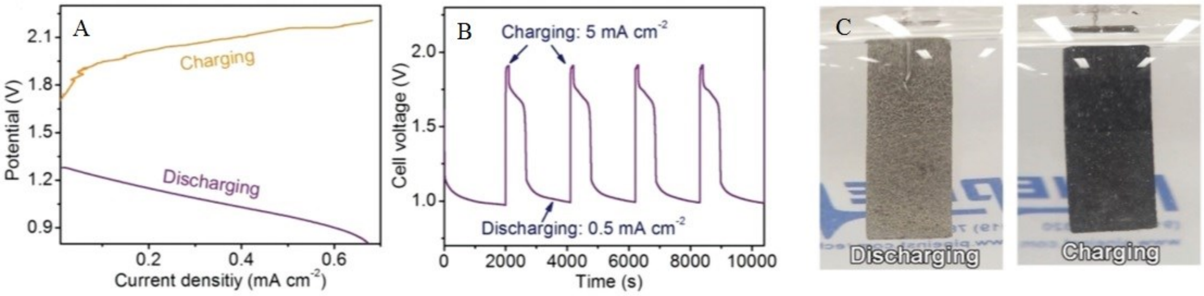

Figure 2-10 (A) Charge and discharge polarization (V-i) curves at 5 mV s^{-1}; (B) cycling performance of the battery at a charging current density of 5 mA cm^{-2} for 200 s and discharging current density of 0.5 mA cm^{-2} for 2000 s; C) optical images during charging and discharging processes.[132]

2.3.2.2 Spinels

Spinels with the structure of AB_2X_4 (A,B = metal, X = chalcogen) have attracted a great deal of attention as bifunctional catalysts. The spinel structure is built around a closely packed array of O^{2-} ions, with A^{2+} and B^{3+} cations occupying parts or all of the tetrahedral and octahedral positions, respectively. Among the various spinel types, MnCo-based spinels such as $MnCo_2O_4$, Co_2MnO_4 and $Co_3O_4/CoMnO_4$ are the most intriguing spinel-based composite oxides. They have many advantages such as low cost, low toxicity and multiple valences.[139–146] Traditional ceramic synthesis routes for spinel structured materials generally follow solid state reaction of oxides, nitrates or carbonates. Solid state reactions consume energy and offer limited control over the shape and size of the synthesized products; this is one of the major challenges in developing high surface area spinel-based electrocatalyst materials.

Recently, a low temperature technique was developed to fabricate Co-Mn-O spinel using NaH_2PO_2 and $NaBH_4$ as strong reducing agents. Two nanocrystalline $Co_xMn_{3-x}O_4$ spinels, CoMnO-P (tetragonal) and CoMnO-B (cubic), were synthesized using NaH_2PO_2 and $NaBH_4$ as reductants, respectively. Since the synthesis route was at low temperature (180 °C), the product featured small particle sizes and high specific surface areas (80-100 m^2 g^{-1}). Both DFT and experimental analysis demonstrated the phase dependence of ORR and OER activities for the corresponding spinel structures. The effect was attributed to the different oxygen binding ability on the surface of each phase. CoMnO-B outperformed CoMnO-P in ORR and since OER is the reverse process, CoMnO-P demonstrated higher OER activity.[147]

Due to the lower electrical conductivity of most spinel structures, integration of spinels with nanocarbon supports provides a more conducting network and facilitates charge transfer during ORR and OER. Moreover, nanocarbon materials enhance the dispersion uniformity for the metal-oxide, prevent agglomeration of the metal-oxide particles and provide additional accessible surface area.[143,148]

Hybrid spinel based bifunctional catalysts and carbon based materials such as N-doped rGO, CNTs, carbon nanofibers and carbon black have been recently studied and the activity was attributed to the synergistic coupling of nanocarbons and oxide materials.[149] The following are a few examples showing the effects of the addition of conductive nanocarbon supports to spinel structures.

Prabu et al.[139,150] investigated several groups of spinel based materials as bifunctional air electrodes for ZABs, such as 1-dimensional $NiCo_2O_4$[151], $CoMn_2O_4$/rGO and $CoMn_2O_4$/N-rGO. Strong coupling between Co_2MnO_4 and rGO can provide a notable improvement in electrochemical activity with high stability. The details of secondary and primary ZABs for this group are summarized in Table 2-6.

A highly stable bifunctional catalyst was developed using NH_3-treated N-doped macro/meso-porous carbon as the ORR active component. Co_3O_4 was directly grown on Ni foam acted active as the OER component.[152] The ORR and OER catalysts were decoupled in a ZAB set up similar to the tri-electrode design studied by Li et al.[152] The ZAB was cycled for 800 h at a current density of 10 mA cm^{-2} with only a 4.5% decrease in voltaic efficiency (60% efficiency after 800 h of cycling) (Figure 2-11). The performance of the battery was unprecedented in terms of the cycle life for all spinel-based bifunctional catalysts reported in the last few years.

Table 2-6 Summary of secondary/primary ZAB batteries and bifunctional electrocatalyst characteristics for recently studied spinel-based electrocatalysts.

Catalyst material	Secondary (S)/primary (P) battery characteristics	ORR and OER catalyst characteristics	Refs
Co_2MnO_4-N-rGO	(S) E_{charge}-$E_{discharge}$= 1.25 V at 75 mA cm^{-2}; round-trip efficiency= 58% (1st cycle) (P) Dc: 610 mAh g^{-1}	N/A	139
Co_3O_4-NVC	(S) E_{charge}: 2.1 V and $E_{discharge:}$:1.1 V at 20 mA; (P) PD =33 mW cm^{-2} at 53 mA cm^{-2}	ORR_{op}: -0.08 V vs Ag/AgCl; ORR_{Lcd}: 4.6 mA cm^{-2} at -0.8 V, OER_{Op}: 0.55 V vs Ag/AgCl and OER_{Cd}: 30 mA cm^{-2} at 0.9 V; n= ;	153
dual phase-$MnCo_2O_4$/N-rGO	(S) E_{charge}: 2 V at CD; $E_{discharge}$: 1.25 V at 5 mA cm^{-2}	ORR_{op}: -0.09 V vs Ag/AgCl; ORR_{Lcd} 5.53 mA cm^{-2} at -0.8 V; OER_{op}: 0.59 V vs Ag/AgCl, OER_{Cd}: 10.85 mA cm^{-2} at 0.8 V; n= 4	143
$NiCo_2O_4$-CNT	(S) E_{charge}-$E_{discharge}$= 0.75 V at 510 mA cm^{-2} (P) Pd: 320 mW cm^{-2} at 210 mA cm^{-2} (1 V)	ORR_{op}: 0.934 V vs RHE; ORR_{Lcd}: 7.2 mA cm^{-2} at 0.2; OER_{Cd}: 16 mA cm^{-2} at 1.7 V vs RHE	148
Co_3O_4 NC/N-CNT	(S) E_{charge}: 2.16 V and $E_{discharge}$: 1.14 V at 20 mA cm^{-2}	ORR_{op}: -0.044 V vs SCE; ORR_{Lcd}: 3.55 mA cm^{-2}; OER_{Cd}: 20 mA cm^{-2} at 0.802 V vs SCE	154
Co_3O_4 nanodisks	(S) E_{charge}: 2.2 V and $E_{discharge}$: 1 V at 50 mA	N/A	155
Co_3O_4 nanowires	(S) E_{charge}: 2 V at and $E_{discharge}$: 0.98 V at 50 mA	N/A	156
Spherical Co_3O_4/NGr-24h	(P) Pd: 190 mA cm^{-2}; Sc: 590 mAh g$^{-1}{}_{Zn}$	ORR_{op}: 0.03 V vs Hg/HgO n= 3.7	157
$MnCoFeO_4$-NrGO	(S) E_{charge}-$E_{discharge}$= ~1.2 V	ORR_{op}: 0.91 V vs RHE; n= 3.8; E_{OER}-E_{ORR}= 0.93 V	158
MnO_2/Co_3O_4	(S) E_{charge}-$E_{discharge}$= ~1 V at 15 mA cm^{-2}; +5% after 60 cycles (P) Pd: 33 mA cm^{-2} at 50 mA cm^{-2}	ORR_{op}: 1.05 V vs RHE; ORR_{Lcd}: 3.4 mA cm^{-2}; OER_{Cd}: 2.2 mA cm^{-2} at 1.8 V vs RHE	141
CoMnO-P	(P) Sed: 255 Wh kg^{-1} at 20 mA	ORR_{op}: -0.08 V vs Hg/HgO; ORR_{Lcd}: -43.2 mA mg^{-1}; n= 3.7	147
MnO_x-Co_3O_4/C	(P) Pd: 97 mW cm^{-2} at 0.97 V	ORR_{op}: 0.73 V vs RHE; ORR_{Lcd}: 21.8 mA mg^{-1}	159
Co NP-CNF	(S) E_{charge}-$E_{discharge}$= 0.85 V at 20 mA cm^{-2}; +0.1 V change after 55 cycles 1 h/cycle (P): Pd: 125 mW cm^{-2} at 81 mA cm^{-2}	E_{OER}: 0.64 V at 2 mA cm^{-2} vs Ag/AgCl; $E_{1/2}$ ORR: -0.188 V; n= 4	149
Cubic-$CoMn_2O_4$/C	(S) Discharge potential change -8.5% after 155 cycles at 400 s/cycle (P) Sc: ~500 mAh g^{-1}; Sed: ~650 Wh kg^{-1} at 10 mA cm^{-2} ,	ORR_{op}: 0.95 V vs RHE; ORR_{Lcd}:- 5.7 mA cm^{-2}; n= 3.91	160
NiO-Co_3O_4 Co/Ni:9/1	(P) Pd: 100.1 mW cm^{-2} at 148.3 mA cm^{-2}; discharge capacity: 579.5 mAh g^{-1} at 50 mA cm^{-2}	N/A	161

*Op: Onset potential, Lcd: Limiting current density; Pd: Power density; Sc: Specific capacity; Sed: Specific energy density; N/A: Not applicable; n: Number of electrons transferred; $E_{1/2}$: Half-wave potential

*N-rGO: N-doped reduced graphene oxide; NP: nanoparticles; CNF: Carbon nanofibers; NVC: N-doped Vulcan carbon; CNT: Carbon nanotube

The bifunctional activity of Fe_3O_4 based spinels have also been well-studied.[158] Manganese and Co were co-substituted in a spinel structure of Fe_3O_4 NPs and integrated with N-doped-rGO ($MnCoFeO_4$-NrGO). The catalyst was prepared using a hypothermal technique and showed high stability under ZAB conditions for 16.7 hours. Enhanced electronic conductivity of the cubic spinel Fe_3O_4 by doping with Mn and Co, as well as the coupling of $MnCoFeO_4$ with N-rGO nanosheets, improved the cyclability of the $MnCoFeO_4$-NPs.[158] Another hypothermal technique was used in a different study to develop Co_3O_4 NPs with various morphologies such as cubic, blunt edge cubic and spherical particles. The catalyst was supported on N-doped graphene.

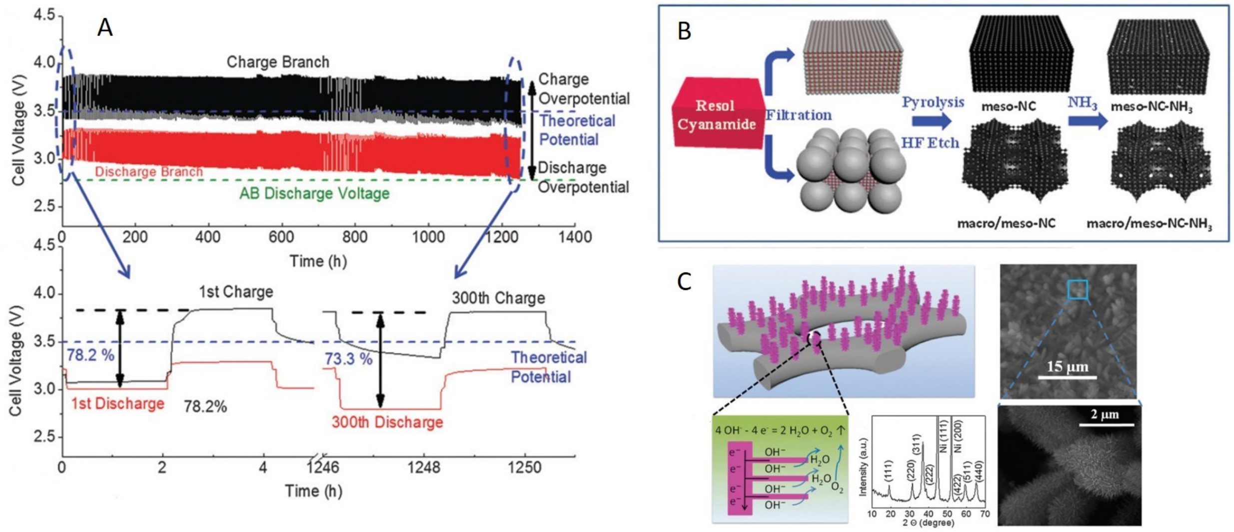

Figure 2-11 (A) Discharge and charge voltage profiles of ZAB with developed hierarchical structure. Co_3O_4 was directly grown on Ni foam catalyst at a current density of 10 mA cm^{-2}. (B) Schematic illustration of the synthesis route for macro/meso-NC-NH_3. (C) Schematic representation of Co_3O_4 microtrepangs grown on Ni-foam and OH^- splitting on the branches of Co_3O_4 microtrepangs (XRD pattern showing the pure spinel-type Co_3O_4).[158]

Rotating ring-disk electrode (RRDE) results showed that spherical Co_3O_4 significantly outperformed the other tested morphologies, with performance close to that of Pt/C. Calculated specific capacity and power density were reported as ~590 mAh g_{Zn}^{-1} and 190 mA cm^{-2}, respectively. [157]

The recent work of Lee et al.[155,156] was focused on Co_3O_4 spinel nanocrystals (nanodisks and nanowires). A lower current density decay rate at 1 V vs saturated calomel electrode (SCE) was observed after 1000 cycles for Co_3O_4 nanocapsules/N-doped-CNTs vs Co_3O_4 nanocapsule/Vulcan carbon. This was attributed to the higher stability of N-doped-CNTs and strong coupling between N-doped-CNTs and Co_3O_4 nanocapsules.[154] In a different study, a power density of 33 mW cm^{-2} was achieved using N-doped Vulcan carbon/Co_3O_4 at a current density of 53 mA cm^{-2}. However, the ZAB malfunctioned after 15 days of cycling (discharged at a constant current of 20 mA over 4 h and then charged at a constant current of 10 mA over 8 h). The malfunction was attributed to the partial loss of electrolyte, catalyst detachment from the air electrode, and the corrosion of carbon black.[153]

Yuan et al.[162] prepared a non-carbon Ni and Co based spinel ($Ni_xCo_{2-x}O_4$) using a sol-gel technique. Low ORR/OER overpotentials and an electron transfer number of four were reported. The non-carbon based catalyst reached a maximum current density of 56 mA cm^{-2} during discharge and 62 mA cm^{-2} during charge. Also, more complex spinel-type electrocatalysts, such as $LaMn_{2-x}Co_xO_4$, $LaMn_{2-x}Fe_xO_4$ and $LiMn_{2-x}Co_{x-2}Fe_{x-2}O_4$, were also investigated. They were synthesized by an improved citric precursor method. $LaMn_{1.6}Co_{0.4}O_4$ was found to be the most active compound towards OER and ORR with an energy efficiency of 60-70% at 100 mA cm^{-2}.[163]

A summary of ZAB performance of the spinel based catalysts mentioned above, as well as other recent studies on this group of materials, can be found in Table 2-6.

2.3.2.3 Perovskites

Perovskites are a group of transition metal oxides with a chemical formula ABO_3, where A is a rare-earth metal and B is a transition metal.[164] Perovskites are fabricated by thermal decomposition of nitrates, acetates and carbonates at temperatures between 600 and 900 ºC. Similar to spinel-based materials, the traditional synthesis routes limit the practicality of perovskites-based bifunctional catalysts due to their large particles sizes and low mass activity.[164,165] Recent studies addressed this problem by using different strategies, such as an electrospinning technique, which will be discussed later in this section.

Perovskites are more stable and corrosion resistant when compared with spinels (AB_2O_4). Partial substitution of other cations in A and B sites enhances the electrical conductivity, chemical stability, oxygen adsorption properties and catalytic activities. Mixing perovskites with high surface area carbon black, graphene and/or CNTs helps to overcome the relatively low electrical conductivity of these structures. It has been noted in several studies that the ORR activity of perovskites is mostly attributed to the B site cations compared with the A site ones.[101,166]

Furthermore, simulation studies on this category of materials suggest that there is a correlation between the doping and catalytic activity due to modification of the electronic structure, as opposed to morphological variations. In fact, the 3d-electron number of B site ions (anti-bonding electron occupation of B-O) can influence B-O_2 interaction strength. Further studies on various La-based perovskites (Figure 2-12) showed that the intrinsic ORR activity as a function of e_g-orbital filling of B ions produces a volcano shape plot with a voltage span of 0.25 V. Transition metal oxide perovskites with an e_g-filling of slightly below one showed the highest ORR activity, whereas perovskites with an e_g value occupancy slightly above one was a better OER catalyst.[101] The influence of the ratio between A and B site cations has the subject of many studies. CNTs and α-MnO_2 nanorods were integrated in a $LaNiO_3$ perovskite. The study showed the ratio ranges of x:y from 1:1 to 3:2 and w:z from 1:2 to 3:2 for $[(a\text{-}MnO_2)_x (LaNiO_3)_y]_w/(CNTs)_z$ (where x and y represent molar ratios and w and z represent weight ratios)) result in the highest conductivity and bifunctional activity for these catalysts.[167] The bifunctional activity of $La_{0.7}Sr_{0.3}Co_{1-x}Fe_xO_3$ (x= 0.1-0.4) has also been investigated, using cyclic voltammetry (CV) and linear sweep voltammetry (LSV). It was shown that a composition of $La_{0.7}Sr_{0.3}Co_{0.7}Fe_{0.3}O_3$ is the best catalyst in this family. According to anodic and cathode polarization curves, the smallest potential gap (0.82 V) at 100 mA cm^{-2} was achieved using $La_{0.7}Sr_{0.3}Co_{1-x}Fe_xO_3$.[168]

Perovskites can be doped with a wide range of aliovalent cations, which results in different catalytic properties. Cation doping increases the ability to catalyze ORR and the concentration of the dopant plays a very important role.[169] For example, studies on Ca and Co doping of $LaMnO_3$ perovskites suggest increased ORR activity when Mn^{3+} is replaced by Ca^{2+} or Co^{2+} ions. This effect is explained by the creation of a large number of oxygen vacancies which facilitate the diffusion of O_2 within the crystal structure.[170–172]

Lanthanum-based perovskites have received significant attention as active bifunctional catalysts.[173–177]. Among all La-based perovskites, research has primarily focused on the composition of $La_{1-x}A_xMO_{3-\delta}$ (where A = Ca, Sr, Mn, Co or Ba and M = Co, Ni, Mn, Fe or Ir). Some examples of recent studies on this group of electrocatalysts are provided in the next paragraphs. Also, Table 2-7 summarizes in more detail the battery and catalytic characteristics of perovskite based electrocatalysts.

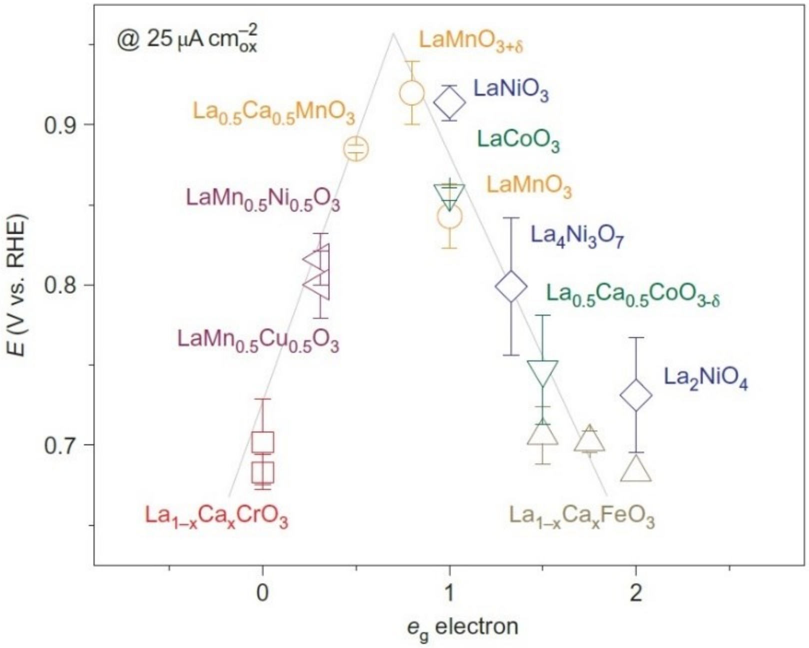

Figure 2-12 Role of e_g electrons on ORR activity of La-based perovskite oxides.[101]

$LaNiO_3$ is a highly OER active catalyst, while CNTs show excellent ORR activity. Nitrogen-doped CNT/$LaNiO_3$ is referred to as core-corona bifunctional catalyst (CCBC). Excellent charge-discharge stability and activity were achieved with a hybrid material of $LaNiO_3$ (core) and N-doped CNTs (corona) in a rechargeable ZAB. After a full range of degradation tests (long-term charge-discharge cycling), CCBC-2 fabricated using 2 ml of precursor has 3 and 13 times greater ORR and OER current, respectively, compared with state-of-the-art Pt/C.[178] Perovskite based $La_{1-x}Ca_xCoO_3$ ($0.2 < x < 0.4$) (LCCO) catalysts were prepared by a citrate method. The partial substitution of La^{3+} by Ca^{2+} (B site cation) increased the BET (Brunauer-Emmett-Teller) surface area as well as the bifunctional activity. The optimum Ca-doping concentration for $LaCoO_3$ was evaluated as x= 0.1 ($La_{0.9}Ca_{0.1}CoO_3$) due to its higher homogeneity in the material and higher current density.[179]

Due to severe carbon corrosion in ZABs, the carbon substrate was replaced by $LaNiO_3$ in a recent study. $LaNiO_3$ is an active perovskite for OER. $LaMnO_3$ was loaded on a $LaNiO_3$ substrate as an active ORR catalyst using a reverse micelle method. The $LaMnO_3$/$LaNiO_3$ composite showed improved bifunctional activity and stability over that of a carbon-based $LaMnO_3$ catalyst.[166]

Table 2-7 Summary of secondary/primary ZAB batteries and bifunctional electrocatalyst characteristics for recently studied perovskite-based electrocatalysts.

Catalyst material	Secondary (S)/primary (P) battery characteristics	ORR and OER catalyst characteristics	Refs
$LaNiO_3$-NCNT	(S) $E_{discharge}$: 0.94 V; E_{charge}: 2.33 V after 12 h at 24.5 A g^{-1}	ORR_{Lcd}: -3.00 mA cm^{-2} at -0.3 V; OER_{Cd}= 20.5 mA cm^{-2} at 1 V vs Ag/AgCl	178
α-MnO_2-$LaNiO_3$/CNTs	(S) Pd: 55.1 mA cm^{-2} at 81 mA cm^{-2}; $E_{discharge}$: 1.191 V; E_{charge}: 2.048 V after 12 h C-D at 24.5 A g^{-1}	n~ 4	167
$La_{0.7}Sr_{0.3}Co_{0.7}Fe_{0.3}O_3$	(S) E_{charge}-$E_{discharge}$= 0.82V at 100 mA cm^{-2}	N/A	168
$LaMnO_3$/$LaNiO_3$	(S) ORR_{op}: 900-1000 mV more positive $LaNiO_3$ electrode at 300 mA cm^{-2}	N/A	166
$La_{0.9}Ca_{0.1}CoO_3$	(S) E_{charge}-$E_{discharge}$= 0.89V at 50 mAcm^{-2}	N/A	179
LMCO/NCNT	(S) E_{charge}= 2.2 V and $E_{discharge}$= 1 V at 18 mA cm^{-2}	ORR_{op} : -0.11 V SCE and OER_{Cd}: 27 mA cm^{-2}	180
$LaNiO_3$ NP-NCNT	(S) E_{charge}= 2.05 V and $E_{discharge}$= 0.94 V at 50 mA	N/A	181
$La_{0.7}Sr_{0.3}MnO_3$	(S) E_{charge}-$E_{discharge}$= 1.06 V at 100 mAcm^{-2}	N/A	182
La_2NiO_4 doped with Sr^{2+} and Ca^{2+}	(S) E_{charge}-$E_{discharge}$= 1.51 V at 75 mAcm^{-2}	ORR_{op}: 0.91 V vs RHE and OER_{Cd}: 27 mA cm^{-2}	169
$LaMn_{0.9}Co_{0.1}O_3$-graphene	(P) Initial $E_{discharge}$: 1.186 V at 20 mA cm^{-2}	ORR_{Lcd}: -4.5 mA cm^{-2}; n= 3.872	170
$La_{0.7}(Ba_{0.5}Sr_{0.5})_{0.3}Co_{0.8}Fe_{0.2}O_{3-\delta}$	(S) Initial E_{charge}-$E_{discharge}$= 0.75 V; final E_{charge}-$E_{discharge}$= 1 V at 10.5 mA cm^{-2}; 5 min/cycle for 100 cycles	ORR_{op}: 0.72 V vs RHE; ORR_{Lcd}: -5.9 mA cm^{-2}; OER overpotential at 10 mA cm^{-2}: 370 mV	183
$La(Co_{0.71}Ni_{0.25})_{0.96}O_{3-\delta}$	(S) Initial E_{charge}-$E_{discharge}$= 0.791 V at 5 A g^{-1}; battery efficiency: 67.8% (P) Discharge capacity: 705 mAh g^{-1}; Sed: 710 mWh g^{-1}	OER overpotential at 10 mA cm^{-2}: 324 mV	184
$LaMnO_3$	(S) Initial E_{charge}-$E_{discharge}$= 1.63 V at 25 mA cm^{-2}; 600 s/cycle (P) Sed: 885 Wh kg^{-1} at 25 mA cm^{-2}; discharge voltage of 1.18 V	N/A	173
$La_{0.8}Ca_{0.2}MnO_3$	(S) Initial E_{charge}-$E_{discharge}$= 1.15 V; final E_{charge}-$E_{discharge}$= 1 V at 50 mA cm^{-2}; (P) Pd: 98 mW cm^{-2} at 168.5 mA cm^{-2}	N/A	172
$LaTi_{0.65}Fe_{0.35}O_{3-\delta}$	(S) Initial E_{charge}-$E_{discharge}$= 0.57 V; final E_{charge}-$E_{discharge}$= 0.83 V at 5 A g^{-1}; 5 min/cycle for 60 cycles; round-trip efficiency before and after: 69% vs 59%; (P) Sc: 440 mAh g^{-1}; flat discharge: 1.16 V for 12 h	ORR_{op}: 0.92 V vs RHE, n= 4	185
$LaCoO_3$ and $LaMnO_3$	(S) E_{charge}: 2.1 V; $E_{discharge}$: 1.22 V after 150 cycles (P) Pd: 70-77 mW cm^{-2} at 140 mA cm^{-2}	N/A	177

*Op: Onset potential; Lcd: Limiting current density; Pd: Power density; Sc: Specific capacity; Sed: Specific energy density; N/A: Not applicable; n: Number of electron transferred
*CNT: carbon nanotube; NP: Nanoparticle, LDH: Layered double hydrioxide
*LMCO: Lanthanum manganese cobalt oxide

As previously mentioned, making perovskite nanoparticles through traditional synthesis routes is a great challenge. Recently, 50 nm particle size $La_{0.7}(Ba_{0.5}Sr_{0.5})_{0.3}Co_{0.8}Fe_{0.2}O_{3-\delta}$ was synthesized through a complex polymerization method. Rhombohedral $LaCoO_3$ nanoparticles were incorporated on the surface of $Ba_{0.5}Sr_{0.50}Co_{0.8}Fe_{0.2}O_{3-\delta}$. A five-fold increase in OER current density was observed in comparison with the IrO_2 baseline.[183] Another alternative to traditional synthesis routes is electrospinning. Electrospinning is a simple technique, which has recently used to develop nanosized perovskites. PAN acted as a source of porous carbon with high nitrogen content, apart from being an electrospinning medium.[184,185] Also, the process is simple and low cost to prepare one dimensional interconnected structures such as nanotubes, nanofibers and nanobelts. Electrospinning was used in a recent study by Vignesh et al.[184] for synthesis of $La(Co_{0.71}Ni_{0.25})_{0.96}O_{3-\delta}$ NPs. The particles had a nanotubular structure based on SEM observations, with outer and inner diameters of 100−150 and 50−70 nm, respectively. The OER overpotential was 324 mV at 10 mA cm^{-2}, which is 56 mV more negative than baseline IrO_2. Eectrochemical analysis indicated the presence of Ni in octahedral sites, which alter e_g-filling (< 1) and weaken the bonding strength of OH^- species on the perovskite structure, leading to good OER activity.

The above examples of mixed transition metals oxides (spinels and perovskites) show that the rich defect properties of this group of electrocatalyst materials make their structures flexible and adaptable for developing advanced air electrodes for future rechargeable ZAB.

2.3.3 Carbon-based (bifunctional catalyst/catalyst support)

Great efforts have been devoted to the development of efficient and durable metal-free carbon based electrocatalyst materials. Carbon materials provide a balance between catalytic activity, electrical conductivity, surface area and cost. However, the reported performance of traditional carbon materials is still inferior to baseline Pt/C catalysts due to the corrosion susceptibility of carbon during OER and insufficient performance at higher loads. Several reviews have been published about carbon-based metal-free catalysts for ORR/OER, presenting the challenges, critical issues and perspectives.[186,187] Table 2-8 presents highlights of the bifunctional activity of recently developed carbon-based electrocatalysts examined in this review.

Bifunctional catalytic activity has been studied in various carbon-based materials, such as carbon black, graphene/GOs[188,189], graphene quantum dots[190], CNTs[191] and nanodiamond.[192] In general, tightly packed carbon bonds in graphitic carbon (hybridized sp^2 orbital), such as graphene nanosheets and CNTs, are more stable than conventionally used carbon black due to the higher number of active sites and corrosion resistance.

Two important factors determine the performance of carbon-based electrocatalysts, i.e., surface functionality and surface area. Carbon blacks (e.g., Vulcan XC-72) are the most common catalyst support for ZAB applications. A study by Eom et al.[193] investigated the effect of carbon black types with different surface areas. It was shown that the air cathodes consisting of mesoporous and macrospores carbon blacks such as Darco G-60 N have the highest power density (353 mW cm^{-2}) at 0.71 V. However, the calculated BET surface area of Darco G-60 N was lower compared with other types of carbon blacks (e.g., Vulcan XC-72). This indicates that high surface area is not the only factor affecting catalytic performance. In general, mesoporous/microporous carbon is a desirable ORR active electrocatalyst because it provides numerous active sites for favorable and efficient mass transport during charge-discharge cycling.[194] Another important factor is optimizing the degree of hydrophobicity of mesoporous/microporous carbon particles for catalyst supports. A large thickness of hydrophobic carbon layers as a catalyst support may block the electrolyte, limit the mobility of Zn ions and increase the overall interfacial resistance.[191] A study on the effect of the surface area of Ketjenblack vs graphitized and activated Vulcan XC-72 as the catalyst support for $La_{0.6}Ca_{0.4}CoO_3$ bifunctional catalysts showed that Ketjenblack ED-600JD, with the highest surface area (1300 m^2 g^{-1}), has the best ORR activity with a potential of -0.2 V vs Hg/HgO at 100 mA cm^{-2}. It was suggested that homogenously dispersed, high surface area carbon supports provide shorter diffusion pathways for peroxide ions resulting in smaller total resistance.[195]

Recent studies have been highly focused on doping nitrogen into pristine graphene, graphene oxide and CNTs. N-doping of these carbon structures creates pyrrolic, pyridinic and graphitic C-N bonds which increase the number of active sites.[196–198] It was found that charge delocalization in N-doped carbon facilitates the Yeager model for oxygen chemisorption over the Pauling model, which could effectively weaken the O-O bond (Figure 2-4).[187] Nitrogen is an n-type carbon dopant, meaning that N donates electrons to carbon and creates an uneven charge distribution. Also, N-doped carbon materials are more disordered than their undoped analogues.[199] For example, novel, highly active mesoporous N-doped carbon based ORR catalysts were developed using a hard templating synthesis technique (polymerization of o-phenylenediamine (oPD)) in the presence of a silica colloid. The process was followed by the pyrolysis of the oPD/silica composite at high temperature. The resulting high surface area (1280 m^2 g^{-1}) catalyst, denoted as microporous/mesoporous pyrolyzed-oPD, showed a remarkable ORR onset potential of 0.85 V vs RHE and stability of up to 100 h in a ZAB. It was found that the catalytic activity of pyrolyzed-oPD derived catalysts was largely influenced by NH_3 activation time (N-doping time). The ORR activity improved with increasing N-doping time, plateauing after 15 min. Based on quantum theory calculations, quaternary nitrogen in the graphene planes reduces the energy barrier for oxygen adsorption by inducing a non-uniform electron distribution in short C-N bonds. Therefore, the dissociation and adsorption of oxygen was facilitated.[188] In a different study, eggplant-derived 2D mesoporous carbon microsheets with high surface area (1051 m^2 g^{-1}) were fabricated by simple carbonization and activation steps. The catalyst was applied in a rechargeable ZAB to evaluate its bifunctional activity. The results showed high stability for 62 h after charge-discharge cycling at 5 mA cm^{-2}.[200]

In another study, N-doped hydrophobic Ketjenblack carbon was derived from gelatin and tested in a ZAB cell at 25 and 50 mA cm^{-2}. The peak power density of the cell was 5.3% higher than the Pt/C baseline.

Furthermore, doping a second heteroatom such as B, S or P also can modulate the electronic properties and surface polarities for further improvement of carbon-based electrocatalytic activity.[189,196,199,201–204] The reason for enhanced ORR activity after doping with heteroatoms is described as partial positive charge remaining on the heteroatom centers, which act as active sites for O-O dissociation. Three-dimensional N-P-co-doped mesoporous nanocarbon foam was synthesized in a one-step process involving the pyrolysis of a polyaniline aerogel in the presence of phytic acid. The electron transfer number obtained after RRDE testing was 3.85 with a small ratio of peroxide species (<8%). The bifunctional activity of the catalysts was evaluated in primary and rechargeable ZABs. The primary ZAB was operated with no significant discharge potential drop after 30 h at 5 mA cm^{-2}. Integrating two Zn-air button cell batteries in series generated an open circuit potential of ~2.8 V to power LEDs. First-principle DFT calculations were performed to investigate the possible active sites on the doped structures, providing a minimum ORR overpotential. In most cases, OER and ORR occurred near the edge of the graphene basal plane. Based on volcano plots for ORR, N-doped sites showed lower overpotential (0.44 V) in comparison with P-doped (0.47 V) and N-P-co-doped sites (0.47 V). On the other hand, N-P-co-doped graphene was identified as the most OER active with the lowest overpotential of 0.39 V.[66]

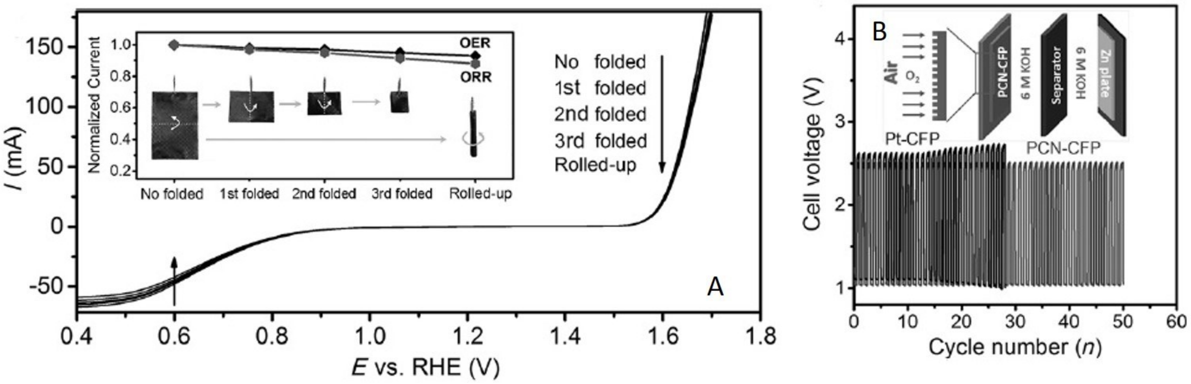

Figure 2-13 (A) LSV currents for PCN-CFP in different folded and rolled up forms. (B) Charge-discharge cycling curves using PCN-CFP and Pt-CFP directly as the air electrode (inset: ZAB configuration schematic).[205]

Dopamine (DA) is also used as a carbon and N-doping source in the development of active ORR/OER carbon based electrocatalysts. DA can be readily self-polymerized at room temperature to form polydopamine (PDA) on a substrate. Also, DA possesses OH^- chelating groups, which can contain metal ions during polymerization and form metal/PDA composites.

Very recently, researchers designed a material with a 3-dimensional, carbon-based architecture as a flexible electrode for wearable electronics.[191,201,205] High mechanical integrity and cycling stability were observed in P-doped graphitic-C_3N_4 directly grown on carbon-fiber paper (PCN-CFP) prepared through a hypothermal process. Different folded and rolled-up forms of the air-electrode were studied using ORR/OER polarization testing, as shown in Figure 2-13. LSV curves of the folded PCN-CFP before and after 3000 cycles exhibited negligible current loss. The highly rolled up structure preserved 87.8% and 92.7% of the initial ORR and OER currents, respectively.[201] Also, ZABs based on nonporous carbon nanofiber films (NCNFs) were integrated in series to power commercial light emitting diodes (LED, 3V) worn on a human hand, demonstrating the possibility of ZABs as a flexible power source in wearable optoelectronics.[205]

.

Table 2-8 Summary of secondary/primary ZAB battery and bifunctional electrocatalyst characteristics for recently studied carbon-based materials.

Catalyst materials	Secondary (S)/Primary(P) battery characteristics	ORR and OER catalyst characteristics	Refs
Meso/micro-PoPD	(P) Sc: 630 mAh g^{-1} works for 100 h	ORR$_{op}$: 0.84 V vs RHE ORR$_{E1/2}$: 0.85; n= 3.97	188
Eggplant derived 2D carbon sheets	(S) E$_{discharge}$: 1.23 V at 5 mA cm^{-2} (P) Sc: 669 mAh g^{-1}	ORR$_{op}$: 0.069 V vs Ag/AgCl; ORR$_{Lcd}$: -6.09 mA cm^{-2} at 0.65 V vs Ag/AgCl; n= 4	206
N/P doped mesoporous carbon	(S) Pd: 55 mWcm^{-2}; stable operation for 240 h at 2 mA cm^{-2} (P) Sc: 735 mAh g^{-1}, Sed: 835 Wh g^{-1}	N/A	196
ND-hollow mesoporous carbon	(S) E$_{charge}$: 2.13 V; E$_{discharge}$: 1.24 V at 2 mA cm^{-2}	ORR$_{op}$: -0.05 V vs Hg/HgO; ORR$_{Lcd}$: -4.95 at -0.7 V; n=4	66
Fe and N-doped graphene nanosheets	(P) Pd: 61 mW cm^{-2}	ORR$_{op}$: -0.023 V vs SCE; n= 3.79 to 3.99	198
N-doped gelatin with Ketjenblack carbon	(P) Pd: 193 mW cm^{-2}	n= 3.7-3.85	199
N-doped carbon fibers like	(P) Pd: 194 mW cm^{-2}	Kinetic current: 6.85 mA cm^{-2} at -0.15 V; n= 3.7-3.8; peroxide yield: 13% at -0.4 V vs Hg/HgO	207
Graphene oxide and PMF	(P) Pd: 70 mW cm^{-2} at 100 mA cm^{-2}; Sc: 400 mAg^{-1}	ORR$_{op}$: -0.1 V vs SCE; n=3.4-3.8	189
N-doped CNT	(P) Pd: 69.5 mWcm^{-2} at 78.6 mA cm^{-2}	N/A	204
SWCNT	(P) Discharge capacity: 375 mAh g^{-1} at 0.25 mA	N/A	191
Co-PDA-C	(S) E$_{charge}$: 2.15 V E$_{discharge}$: 1.21 V at 2 mA cm^{-2}; +0.23 V increase in gap after 500 h	ORR$_{pp}$: 0.783 V vs RHE; ORR$_{E1/2}$: 0.767 V; E$_{OER}$: 1.601 V at 2 mA cm^{-2} vs RHE; n~ 4	208
N-D dope nondiamond	(S) E$_{charge:}$: 2.4 V E$_{discharge}$: 1 V at 16 mA cm^{-2} 300 s/cycle (P) Pd: 24.8 mW cm^{-2}	ORR$_{pp}$: -0.02 V vs SCE; ORR$_{op}$: -0.05 V; ORR$_{E1/2}$: -0.18 V; n~ 3.96	192
PCN–CFP	(S) E$_{charge}$: 2.46 V; E$_{discharge}$: 1.05 V at 10 mA cm^{-2}, 5 min/cycle	ORR$_{op}$: 0.94 V vs RHE; OER$_{op}$: 1.53 V vs RHE	201
Macro/meso-NC-NH$_3$	(S) E$_{charge}$-E$_{discharge}$= 0.7 V at 10 mA cm^{-2}; 200 cycles at 4h/cycle	ORR$_{Lcd}$: -6.6 mA cm^{-2} at -0.4 V SCE	208
NCNF	(S) Initial E$_{charge}$: 1.93 V; E$_{discharge}$: 1.20 V at 10 mA cm^{-2}; 5 min/cycle in air (P) Pd: 185 mW cm^{-2}; Sed: 776 Wh kg^{-1}; Sc: 626 mAh g^{-1}	ORR$_{op}$: 0.97 V vs RHE; ORR$_{Lcd}$: -4.7 mA cm^{-2} at 1600 rpm; n= 4; OER$_{op}$: 1.84 V	205
Graphene quantum dots	(P) Pd: 70 mW cm^{-2} at 100 mA cm^{-2}	ORR$_{op}$: -0.13 V vs Ag/AgCl;	190

*Op: Onset potential; Lcd: Limiting current density; Pd: Power density; Sc: Specific capacity; Sed: Specific energy density; N/A: Not applicable, n: Number of electrons transferred

*E$_{1/2}$: Half-wave potential

*PoPD: Pyrolyzed o-phenylenediamine; ND: N-doped; PMF: Phenol–melamine–formaldehyde; SWCNT: single wall carbon nanotube; PDA: Polydopamine; PCN: P-doped graphitic-C$_3$N$_4$; CFP: Carbon-fiber paper; Macro/meso-NC-NH$_3$: NH$_3$-activated N-doped macro/mesoporous carbon; NCNF: Nanoporous carbon nanofiber film

2.4 Progress and outlook

This review has highlighted recent progress in the design and electrochemistry of bifunctional electrocatalysts for primary/secondary ZABs. To sum up, there are still major challenges that exist in this field. However, promising progress has been made in the area of ZABs over the past few decades. The number of publications dedicated to secondary/primary ZABs derived from Scopus and Google Scholar databases is summarized in Figure 2-14, which shows that the number of scientific reports, journal papers and patents has increased by ~80% since 1996.

In general, it is much easier to handle secondary ZABs relative to other metal-air batteries such as Li-air batteries.[209,210] All the components of ZABs are moderately stable towards moisture and all the reactions can be carried out under ambient air conditions. Therefore, the manufacturing process for ZABs is less stringent and cheaper than Li-air batteries. Although there has been progress, many aspects of ZABs are not fully understood and extensive investigation is still required in this field.

Rechargeable ZABs can be used in a bi-electrode or tri-electrode configurations, which will dramatically affect the cycle life of the battery. Bi-electrodes are structurally compact with limited cycle life. The catalytic layer is normally a multilayered structure, wherein the hydrophilic side of the GDL (facing the electrolyte) is used for OER catalysts and the ORR catalysts are oriented towards the air side. Using N-doped graphene and CNTs can improve the electrical conductivity of the air electrode. Also, as previously discussed in Section 2.3.2.1, catalysts such as Ni-Fe-CO_3^{2-} LDH can prevent carbonate precipitation on the air electrode. However, there is also a high probability of the catalyst detachment from GDL during recharge at high potentials due to the generation of O_2 bubbles. Based on the summarized data in Tables (2-4)-(2-8), a bifunctional electrode in this configuration generally has a low cycle life (<100 h) with a lower operating rate (<50 mA cm^{-2}).

The tri-electrode mode, on the other hand, is structurally complex but it can significantly improve the battery's cycle life. Some examples are provided in Sections 2.3.2.1 and 2.3.2.2. Since the charging process does not occur on the third electrode, O_2 bubbling will not damage the ORR catalysts. Also, the third electrode is usually a Ni or Ni alloy foil, which is a suitable OER catalyst. Furthermore, carbon corrosion will be avoided because the air electrode operates at lower potential. As a result, the performance of the ZAB is mainly determined by the stability and activity of the applied ORR catalyst.[21,129]

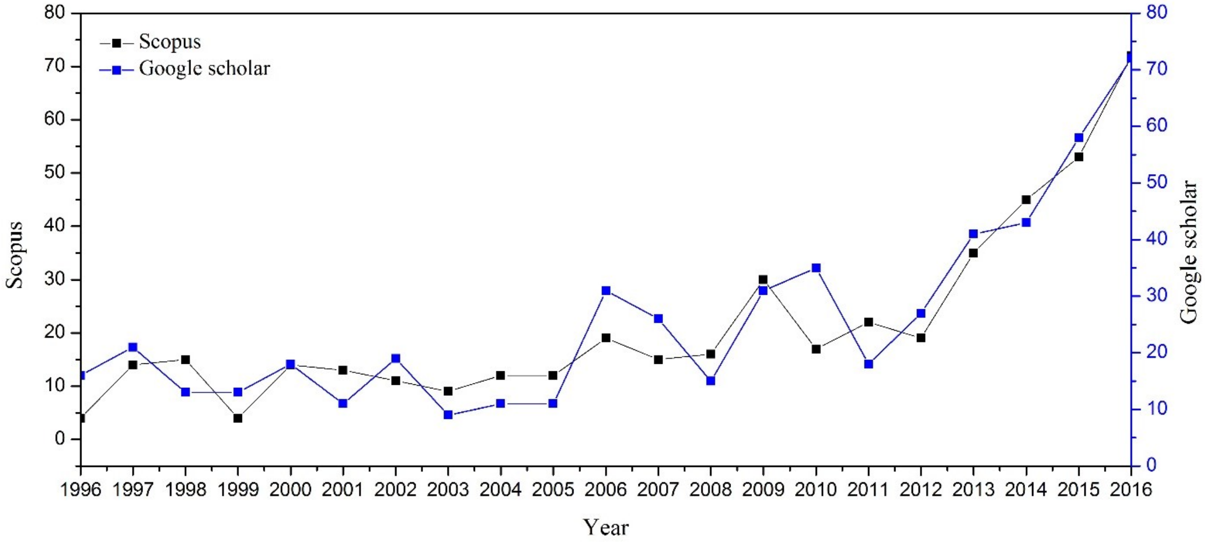

Figure 2-14 The number of publication addressing the challenges in primary/secondary batteries between 1996 and 2016. (The numbers are provided from the Scopus and Google Scholar databases).

Amendola et al.[19] investigated a horizontal configuration for rechargeable ZABs. As shown in Figure 2-15, the air electrode is at the top and Zn is at the bottom of the cell. The electrolyte is contained and sealed by the frame. An airflow tunnel is also provided between the Zn and the air cathode. In this specific configuration, gravity helps in settling the discharge product as an even layer on the Zn electrode so there may be no need for a separator. This configuration is suitable for stationary devices requiring a large amount of energy density. The battery cycle life is reported as 2700 cycles with no performance degradation.

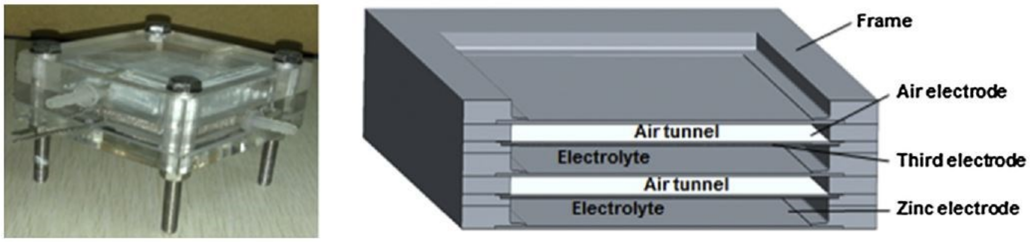

Figure 2-15 The structure of a rechargeable ZAB arranged in a horizontal configuration.[19,44]

Furthermore, using a flowing electrolyte as opposed to a static electrolyte is another design modification to prevent the rapid growth of the dendrites by removing the discharge product over time. Moreover, heat and gas bubbles generated are removed, which would eventually increase the charge/discharge rate of the battery.[21]

In summary, although the Zn anode, separator and electrolyte were not emphasized in this review, it is critical to develop a rational design considering the challenges for each component of a rechargeable ZAB structure. The performance of ZABs is highly affected by durability and activity of innovative bifunctional electrocatalysts, the degree of hydrophobicity/hydrophilicity in GDL, viscosity, conductivity and composition of the electrolyte and the Zn anode's utilization efficiency. A possible technological solution to overcoming the power limitation of ZABs is to use a hybrid system with supercapacitors, which can deliver high power on demand. Finally, overcoming the remaining challenges will doubtlessly require ongoing research efforts form different disciplines.

2.5 Materials characterization techniques

This section discusses the materials characterization techniques, which are utilized in this thesis. Materials characterization was mainly used to reveal and understand the morphology, crystal structures, oxidation states and thermogravimetric properties of the materials developed in this study.

2.5.1 Scanning electron microscopy

Scanning electron microscopy is a versatile technique used for the observation of the morphology of materials. The specimen is irradiated with a fine electron beam (electron probe) and the topography of the surface can be observed by two-dimensional scanning of the electron probe over the surface. Since SEM operation involves the movement and detection of electrons, a high vacuum (10^{-6} to 10^{-9} torr) is required. The resolution of an SEM depends on the source (the electron gun). Field emission SEMs, with lower energy spread and much higher brightness (~10^{8} A cm^{-2} sr at 20 kV), have resolution of better than 1 nm. However, they are more expensive and better vacuums are normally required (<10^{-9} torr).

An SEM consists of two main components, the column and control console. The column includes the electron gun, lenses, apertures, scan (deflection) coils and detectors. The console has a viewing screen, knobs/buttons and computer control. To image in an SEM, the sample must be conductive. Non-conductive samples may need to be coated with conductive materials, such as carbon or Au.

A number of interactions occur after the electron beam hits the sample. Secondary electrons (SE) are emitted when the electron beam interacts with the electron cloud and knocks out electrons from the inner/outer atomic shells. SEs are fairly low energy electrons (2-5 eV) and generally give information about the topography of a sample; i.e., features closer to the detector will be brighter. Backscattered electron (BSE) are emitted when the incident beam collides with the nucleus of the sample. BSEs are quite high energy (1-20 keV) and provide atomic number contract (Z-contrast). Furthermore, information about the composition of a sample can also be obtained through X-ray spectroscopy, using an energy dispersive X-ray (EDX) spectrometer which measures the number and energy of the X-rays emitted from a specimen. The energies of the X-rays are characteristic of the element generating the X-rays and correspond to the difference in energy between two shells of the emitting element. The EDX spectrum is presented as X-ray intensity vs the X-ray energy.[211]

2.5.2 Transmission electron microscopy

Transmission electron microscopy (TEM) is one of the most powerful tools used for characterization. The main parts of the microscope column are the electron source (gun), electron optics (lenses) and the imaging system (detectors). In a conventional TEM, a thin specimen is irradiated with an electron beam. The electrons transmitted through the specimen are used for imaging. The accelerating voltage is 100-200 kV in a routine instrument. TEM analysis allows for high resolution imaging; some instruments are capable of resolution of the order of 50 pm. The main limitation associated with TEM is sample preparation. The samples must be electron transparent, which means samples should be no more than ~200 nm thick.

The scattering processes experienced by electrons during their passage through the specimen determines the kind of information obtained. Elastic scattering involves no energy loss and can give rise to diffraction patterns. Inelastic interactions between primary electrons and sample electrons cause absorption and scattering effects, leading to a spatial variation in the intensity of the transmitted electrons. In TEM one can switch between imaging the sample and viewing its diffraction pattern by changing the strength of the intermediate lens.[212]

2.5.3 X-ray diffraction

Powder X-ray diffraction (XRD) is useful analytical technique primarily used for phase identification of materials. XRD provides information about the phases and the spacing between the lattice planes. The types of the samples suitable for XRD analysis include inorganic materials, organic materials, polymers, metals and there composites in powder or thin film forms. X-ray diffractometers consist of three basic elements: an X-ray tube, a sample holder and an X-ray detector. The geometry of an X-ray diffractometer is such that the sample rotates in the path of a collimated X-ray beam at an angle of θ while the X-ray detector is mounted on an arm to collect the diffracted X-rays and rotates at an angle of 2θ. X-rays are generated in a cathode ray tube by heating a filament to produce electrons. When electrons have sufficient energy to dislodge the inner shell electrons of the target material (Cu, Fe, Mo or Cr), characteristic X-rays are produced. An X-ray spectrum consists of several components, the most common being K_α and K_β X-rays. K_α X-rays are made up of $K_{\alpha 1}$ and $K_{\alpha 2}$ X-rays, which are close in wavelength. Monochromatic X-rays needed for diffraction are generated by filtering the X-rays using a foil or crystal monochromators. A typical diffraction pattern consists of a plot of reflected intensities vs the detector angle 2θ or θ, depending on the goniometer configuration. The 2θ values for the peaks depend on the wavelength of the anode material of the X-ray tube. It is customary to characterize a peak position by the interplanar d-spacings that correspond to the (hkl) planes that caused the reflection. The d-spacing is a function of 2θ according to Bragg's law.

$$\lambda = 2d\sin\theta$$

where λ is the wavelength of the K_α of the target material. Knowing the d-spacing and the corresponding Miller indices (hkl), the structure of the unknown materials can be identified. The International Center Diffraction Data (ICDD), formerly known as the Joint Committee on Powder Diffraction Standards (JCPDS), is the organization that maintains the database of inorganic and organic materials. The database is available from diffraction equipment manufacturers or from ICDD directly.[213]

2.5.4 X-ray photoelectron spectroscopy (XPS)

X-ray photoelectron spectroscopy (XPS) is a technique providing surface compositional information, electronic states, bond type and valence of the elements. To perform XPS, the sample is bombarded with a beam of X-rays that has a narrow energy range. These X-rays are absorbed by the electrons associated with the atoms in the sample and some of the electrons are then ejected from the sample surface; the electrons are called photoelectrons. Photoelectrons are low energy and their escape depth is about 10 nm (near the surface region of a sample). The energy of the ejected electrons is measured and this gives information on the atomic species and the types of bonds present in the sample. Based on the law of energy conservation, photoemission is described by the following equation:

$$E_k = h\nu - E_B$$

where h is the Planck's constant, v is the frequency of the X-ray photon, E_k is the kinetic energy measured by electron energy analyzer scanning the kinetic energy spectrum and E_B represents the electron binding energy of the i-th level. By counting the number of electrons at different binding energies, an energy spectrum can be precisely produced via a pattern with intensity vs binding energy. The specific binding energy of the electron acts as the blue print to identify the composition of the sample with the intensity corresponding to the quantity of the element. High resolution (HR)-XPS can be achieved using an additional monochromator in the XPS system to reduce energy width dispersion. Additionally, lower spectral background and the elimination of the unwanted X-rays can also be accomplished. The detection limit for the XPS is usually in the parts per thousand range. However, higher resolution can be obtained with extended signal collection time.[214]

2.5.5 Time-of-flight secondary ion mass spectrometry (ToF-SIMS)

Time-of-flight secondary ion mass spectrometry (ToF-SIMS) is a surface-sensitive analytical method used to analyze the composition of solid surfaces and thin films. A pulsed ion beam (Cs or Ga) is used to dislodge chemical species on the surface. The particles are removed from atomic monolayers on the surface; these are secondary ions typically called fragments. The fragments are then accelerated into a "flight tube" and their mass is determined by measuring the exact time at which they reach the detector (i.e., time-of-flight). Three operational modes are available with ToF-SIMS: surface spectroscopy, surface imaging and depth profiling. Under typical operating conditions, the results from ToF-SIMS analysis include a mass spectrum that surveys all atomic masses over a range of 0-10,000 atomic mass units, maps of any mass of interest on a sub-micron scale and depth profiles through removal of surface layers by sputtering with an ion beam.[215]

2.5.6 Auger electron spectroscopy

Auger electron spectroscopy (AES) is a surface-sensitive analytical technique that utilizes a high-energy electron beam as an excitation source. Atoms that are excited by the electron beam can subsequently relax, leading to the emission of Auger electrons. When an atom is probed by a beam of electrons, a core state electron can be removed leaving behind a hole. As this is an unstable state, the core hole can be filled by an outer shell electron, whereby the electron moving to the lower energy level loses an amount of energy equal to the difference in orbital binding energies. The transition energy can be coupled to a second outer shell electron, which will be emitted from the atom if the transferred energy is greater than the orbital binding energy. The kinetic energies of the emitted Auger electrons are characteristic of the elements present within the top 3-10 nm of the sample according to the following equation:

$$\mathrm{E_{kin}} = \mathrm{E_{core\ state}} - \mathrm{E_B} - \mathrm{E_C}$$

where $\mathrm{E_{core\ state}}$, $\mathrm{E_B}$, and $\mathrm{E_C}$ are the core level, first outer shell and second outer shell electron binding energies, measured by Auger electron detectors. Auger electrons have energies ranges from 50 eV to 3 keV with a short mean free pass in solids. The small escape depth of Auger electrons makes this technique surface sensitive. Semi-quantitative analysis of a sample is dependent on measuring the yield of Auger electrons. The electron yield depends on critical parameters such as electron-impact cross section and fluorescence yield. One of the most common limitations encountered with Auger spectroscopy is charging effects for non-conducting samples. Charging can result SEs being unable to escape from the surface creating a net positive charge at the surface.

2.5.7 Brunauer-Emmett-Teller (BET) analysis

Brunauer-Emmett-Teller (BET) analysis, which is based on the Langmuir isotherm theory for monolayer adsorption, was developed in 1938 by Stephen Brunauer, Paul Hugh Emmett and Edward Teller.[216] BET analysis is useful for obtaining structural information of the catalyst and its support, especially when the material is porous. Typically, the physical adsorption of non-corrosive gas molecules (N_2, Ar, CO_2, etc.) onto the surface of a solid material is utilized to measure the specific surface area, average pore volume and pore size distribution of the sample. The theory works based on several assumptions, which are from Langmuir isotherm theory: 1) Adsorption occurs only on well defined sites of the sample. 2) There is no interaction between each adsorption layer. 3) Adsorption occurs as a monolayer and each layer is treated as a Langmuir monolayer. Based on the above assumptions, the following BET equation has been used:

$$\frac{1}{\nu[\left(\frac{\mathrm{p_0}}{\mathrm{p}}\right) - 1]} = \frac{\mathrm{c} - 1}{\nu_{\mathrm{m}}\mathrm{c}}\left(\frac{\mathrm{p_0}}{\mathrm{p}}\right) + \frac{1}{\nu_{\mathrm{m}}\mathrm{c}}$$

where p and p_0 are the equilibrium and saturation pressure of the adsorbates at the temperature of adsorption, ν is the adsorbed gas quantity and ν_m is the monolayer adsorbed gas quantity. c is the BET constant, which is defined as:

$$c = \exp(\frac{E_1 - E_L}{RT})$$

where E_1 is the heat of adsorption for the first layer and E_L is the heat of adsorption for the next layers. By adjusting the pressure, the equation can be modified and plotted as a linear relationship. An intercept and a slope from the plot provides the volume of adsorbed gas in the monolayer (ν_m). Then ν_m is utilized to calculate the specific surface area according to the following equations:

$$S_{total} = \frac{(\nu_m Ns)}{V} S_{BET} = \frac{S_{total}}{\alpha}$$

where N is the Avogadro's number, s is the adsorption cross section of the adsorbing species and α is the mass of solid sample or adsorbent.[216]

2.5.8 Thermogravimetric analysis (TGA)

Thermogravimetric analysis (TGA) is a technique to measure the changes in physical and chemical properties of a material as a function of temperature. TGA can provide information about vaporization, sublimation, adsorption/desorption, chemisorption and solid-gas reactions. A TGA instrument consists of a suspended sample pan which is connected by a microgram balance arm to a tare pan. The TGA instrument tracks the change in weight of the sample via a microgram balance. Temperature is monitored via a thermocouple. TGA can also track the change in the weight as a function of time. Data is graphed as weight percent or time vs temperature (°C).[217]

2.5.9 Fourier transform infrared (FTIR) spectroscopy

FTIR provides a way to identify the presence of certain functional groups in a molecule by producing an infrared absorption spectrum. The spectrum is a profile of the sample, a distinctive molecular fingerprint that can be used to screen and scan samples for many different components. FTIR is an effective analytical instrument for detecting functional groups and characterizing covalent bonding information.

An FTIR spectrometer consists of a light source, monochromator, slit, beamsplitter, detector and an analog recorder. The source generates light across the spectrum of interest. The monochromator (e.g., a salt prism or grating with finely spaced lines) separates the source radiation into its different wavelengths. The slit selects the collection of wavelengths that pass through the sample at any given time. In a double beam operation, a beam splitter separates the incident beam in two; half goes to the sample and half to the reference. The sample absorbs light according to its chemical properties. The detector collects the radiation that passes through the sample and compares its energy to that going through the reference. The detector puts out an electrical signal, which is normally sent directly to an analog recorder. A link between the monochromator and the detector allows the user to record energy as a function of frequency or wavelength.

To improve the resolution, it is necessary to narrow the slit and decrease the sensitivity. Secondly, it is possible to run multiple scans to build up signal-to-noise ratio. Finally, the instrument needs to be calibrated repetitively due to misalignment between the analog connection and the monochromator.[218]

2.5.9.1 Raman Spectroscopy

Raman spectroscopy is an alternative, and often complimentary, way to observe the vibrational, rotational and other low-frequency modes in a material. In Raman spectroscopy, the sample is illuminated with a monochromatic beam, typically by some type of laser. The laser light interacts with molecular vibrations and phonons, resulting in the energy of the laser photons being shifted up or down. The shift in energy provides information about the vibration modes in the system.

The Raman effect occurs when the electromagnetic radiation interacts with the polarizable electron density and the bonds of a molecule. It is a form of inelastic light scattering, a photon (electromagnetic radiation of a specific wavelength) excites the molecule from either the ground or excited state. This results a so-called virtual state for the molecule for a short period of time before an inelastically scattered photon occurs. During the inelastic scattering, the photon can be either relaxed either in a lower (Stokes) or higher (anti-Stokes) energy level of the incoming photon. In fact, the Raman effect is due to inelastic scattering and should not be confused with fluorescence or phosphoresecne where the molecule is in an excited state, emits a photon of energy and returns to the ground electronic state. Raman scattering is an example of inelastic scattering because the energy and momentum transfer between the photons and the molecules during the interaction results in a difference in energy between the incident and scattered photons. This is contrasted with infrared absorption, where the energy of the single absorbed photon matches this difference in energy (between those same two states).

There are many reasons to prefer Raman spectroscopy over infrared spectroscopy. First of all, many bands that are weak in the infrared spectrum are among the strongest bands in the Raman spectrum, such as S-S and C=C stretching bands. Secondly, some Raman bands are found at very low characteristic frequencies, such as those for monosubstituted aromatic compounds.[219]

2.6 Electrochemical characterization techniques

In addition to the above microstructural characterization methods, electrochemical measurements are required to evaluate the performance of the synthesized catalysts. The following sections include half-cell testing via RDE and rechargeable ZAB cycling tests.

2.6.1 Half-cell electrochemical analysis

The performance of a developed catalyst is evaluated using half-cell electrochemical tests. Half-cell electrochemical analysis, including current-voltage (CV) and linear sweep voltammetry (LSV), is carried out using a rotating disk electrode (RDE) set-up.

2.6.1.1 Linear sweep voltammetry (LSV)

Linear sweep voltammetry (LSV) can identify unknown species and determine the concentration of solutions. Typically, a fixed potential range is employed and the voltage is scanned from a lower limit (E_i) to an upper limit, as shown in Figure 2-16. The slope of the potential vs time graph is called the scan rate and can range from mV/s to 10^6 V/s. The characteristics of LSV depend on several factors, including the rate of the electron transfer reactions, the chemical reactivity of the electroactive species and the scan rate. In a typical LSV measurement, the current response is plotted as a function of the voltage. The equation below gives an example of a reduction occurring at the surface of the working electrode.

$O + e^- \leftrightarrow R$

Assuming E_i is the reduction potential of O in a standard condition, as the voltage is swept from E_i to E, a current begins to flow and [O]=[R] (concentration of the redox species) at the surface when $E = E_i$. As the molecules on the surface of the working electrode are reduced, they move away from the surface and new molecules come into contact with the surface of the working electrode. The flow of electrons into or out of the electrode causes the current. In fact, the current is a direct measure of the rate at which electrons are being exchanged through the electrode-electrolyte interface. When this rate becomes higher than the rate at which the oxidizing or reducing species can diffuse from the bulk of the electrolyte to the surface of the electrode, the current reaches a plateau or exhibits a peak.

There are some instances where linear sweep voltammetry is more useful than other techniques such as cyclic voltammetry. For example, in cases where the reaction is irreversible cyclic voltammetry will not give any additional data.[4]

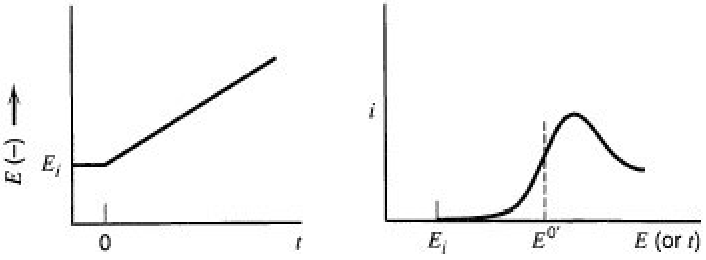

Figure 2-16 Linear potential sweep starting at E_i, resulting in a current density-potential (i-E) curve.[4]

2.6.1.2 Cyclic voltammetry (CV)

Cyclic voltammetry (CV) is the most widely used technique for acquiring qualitative information about the electrochemical reactions. It offers rapid identification of redox potentials of the electroactive species. A typical electrode reaction involves the transfer of charge between an electrode and a species in the solution. The electrode reaction is usually referred to as electrolysis, which typically involves a series of steps.

CV is very similar to LSV. In this case the voltage is swept between two values (E_λ and E) at a fixed rate; however, when the voltage reaches E_λ the scan is reversed and the voltage is swept back to E (Figure 2-17). The forward sweep produces an identical response to that seen for the LSV experiment. The current flow in reverse is from the solution species back to the electrode and, therefore, occurs in an opposite sense to the forward step, but otherwise the behavior can be explained in an identical manner.[4]

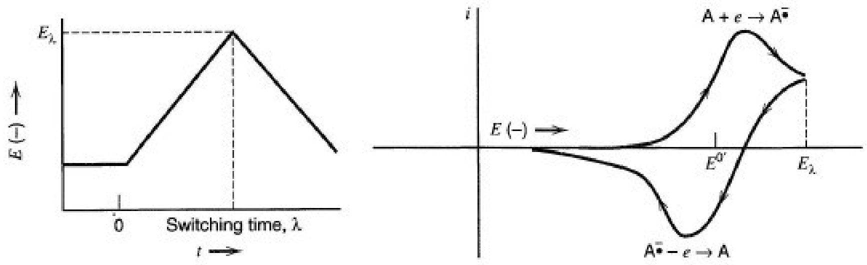

Figure 2-17 Cyclic potential sweep, resulting in a cyclic voltammogram.[4]

2.6.1.3 Rotating disk electrode

Rotating disk electrode (RDE) voltammetry is employed to test different sets of electrochemical methods introduced above, such as CV and LSV. Figure 2-18 shows a typical RDE set up. Electrolyte (0.1-9 M KOH or NaOH) is contained in a three-neck flask. The electrolyte is purged for 30 min with either O_2 or an inert gas (N_2 or Ar), depending on the purpose of the voltammetry. The working electrode is a 5 mm diameter electrode (glassy carbon (GC), Au ot Pt) held by Teflon where the half-cell reaction occurs. Teflon is hydrophobic, which helps to retain the catalytic ink during coating. The electrode is rotated with a control speed. A reference electrode is used to standardize the other half of the cell. Widely used reference electrodes in alkaline solutions are Hg/HgO with a potential of 0.098 V vs saturated hydrogen electrode (SHE), the saturated calomel electrode (SCE) ($Hg/Hg_2Cl_2/KCl$ saturated in water) with a potential of 0.242 V vs SHE and Ag/AgCl with a potential of 0.197 V vs SHE. Pure Pt wire/coil/foil is used as the counter electrode. All three electrodes (working, counter and reference) are connected to a potentiostat that controls the RDE system by adjusting the voltage/current of the working electrode. A catalyst ink is prepared prior to RDE voltammetry. The ink is a solution containing different proportions of a binder such as Nafion, isopropanol, and the catalyst powder. Then, the mixture is sonicated to obtain a uniform dispersion. The catalyst ink is drop-coated on the surface of the GC of the RDE with a desired amount of catalyst loading.

The RDE is connected to a vertical rod, which is rotated at various speeds using a controller. Rotation generates a flow of electrolyte, which is triggered by convection, and allows for mass transport of the active species such as hydroxide ions. A series of experimental data such as LSV curves are obtained using a variety of RDE rotation speeds.

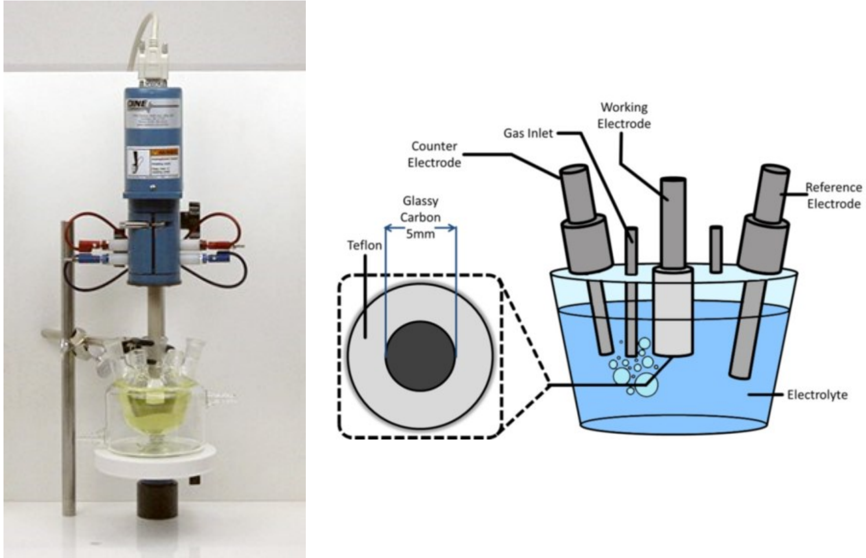

Figure 2-18 Schematic of an RDE voltammetry setup and the RDE electrode.[59,220]

Catalytic activity toward ORR is normally recorded from 0.1 to -0.8 V vs Hg/HgO at scan rate of 5-10 mV s^{-1} with an O_2 saturated electrolyte under a series of rotating electrode speeds (100, 400, 900, 1600 and 2500 rpm). The ORR polarization curves are corrected by subtracting background currents by the same test procedures obtained with N_2/Ar saturated electrolyte to remove the ORR capacitive current. The electrochemical performance of OER is evaluated from 0 to 0.8 V vs Hg/HgO at a scan rate of 5-10 mV s^{-1} with N_2/Ar saturated electrolyte. Normally, Pt/C and Ir/C precious metal-based bifunctional active materials are employed as ORR and OER baseline materials, respectively.

A typical ORR polarization curve is shown in Figure 2-19. Three regions are defined on the polarization curve. Region A corresponds to the initial step of the electrochemical reaction and contains the ORR onset potential where due to the insignificant overpotential the reaction is under kinetic controlled. ORR activity of a catalyst can be measured by its onset potential and limiting current. Region B corresponds to a mixed control region, where a kinetic controlled part and a mass transport limiting part are combined and a half-wave potential is included in the mixed region. The slope of the pseudo-linear region depends on the catalytic reaction rate of the developed catalyst. Region C corresponds to the mass transport limited region and includes the limiting current where the mass transport of the active species is maximized, but the reaction kinetics are much faster than the rate of mass transport. A higher limiting current for the catalyst means higher ORR activity. The mass transport limiting current density depends on mass loading and the rotation speed.[59]

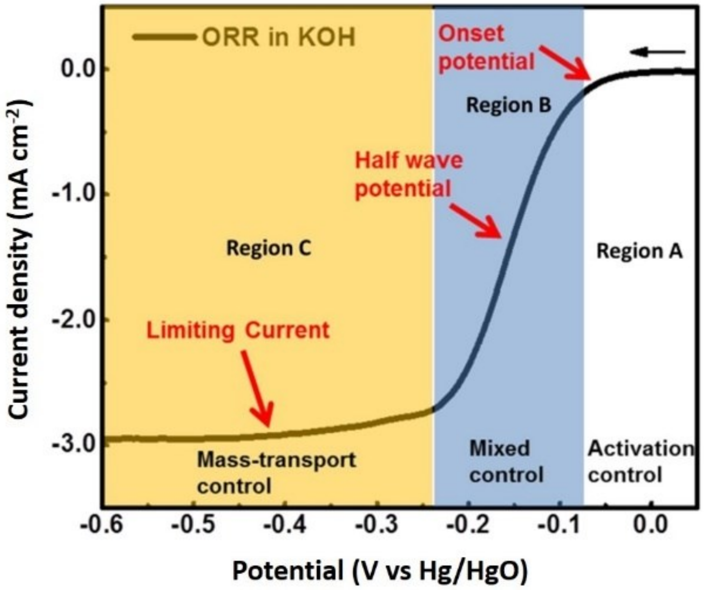

Figure 2-19 Typical ORR polarization curve in KOH electrolyte.[59]

From the ORR polarization curves obtained at the different rotation speeds, it is possible to study the reaction kinetics and mechanisms of the developed catalyst via a Koutecky-Levich (K-L) equation.

$$\frac{1}{\mathrm{i}} = \frac{1}{\mathrm{i_k}} + \frac{1}{\mathrm{i_l}} = \frac{1}{\mathrm{i_k}} + \frac{1}{\mathrm{B}\omega^{0.5}}$$

$$\mathrm{i_k} = \mathrm{nFAkC_{O_2}}$$

$$\mathrm{B} = 0.62\mathrm{nAFC_{O_2}}\,\nu^{-1/6}\mathrm{D}_0^{2/3}$$

where the observed current i is related to the kinetic current $\mathrm{i_k}$ and the limiting current $\mathrm{i_l}$. n is the number of electrons transferred per O_2 molecule, F is the Faraday constant (96,485 C mol^{-1}), $\mathrm{C_{O_2}}$ is the saturated concentration of O_2 in the electrolyte (1.2 × 10^{-6} mol cm^{-3}), $\mathrm{D_0}$ is the diffusion coefficient of O_2 (1.9 × 10^{-5} cm^2 s^{-1}) in 0.1 M KOH and ν is the kinematic viscosity of 0.1 M KOH (0.01 cm^2 s^{-1}).[66] The ideal number of electrons transferred should be close to 4.0, which corresponds to a four-electron reduction pathway during the cathodic reaction.

2.6.2 ZAB performance

In order to consolidate the electrochemical results from the above half-cell tests, the applicability of a developed electrochemical catalyst is investigated using a rechargeable ZAB. Figure 2-20 shows the components of ZAB used in this work. The air electrode is prepared either by the direct deposition of the catalyst onto a GDL or by spray-coating the catalyst ink using an air brush. Galvanodynamic discharging and charging is a versatile technique to study the discharge and charge behaviour of the catalyst. The test is conducted over a range of current densities, from 0 to 100 mA cm^{-2}. During discharge, the applied current is changing from 0 A up to a desired value at a fixed current rate (mA s^{-1}), and simultaneously the battery potential decreases from its open circuit voltage (OCV). During charge, on the other hand, the current increases from 0 A to a desired value at the same current rate and the battery potential increases from the OCV. Polarization curves during charge-discharge process are obtained from this technique and utilized for verifying overpotentials. The overpotential is related to the catalytic oxygen reactions (ORR and OER) and resistances of the developed catalysts.

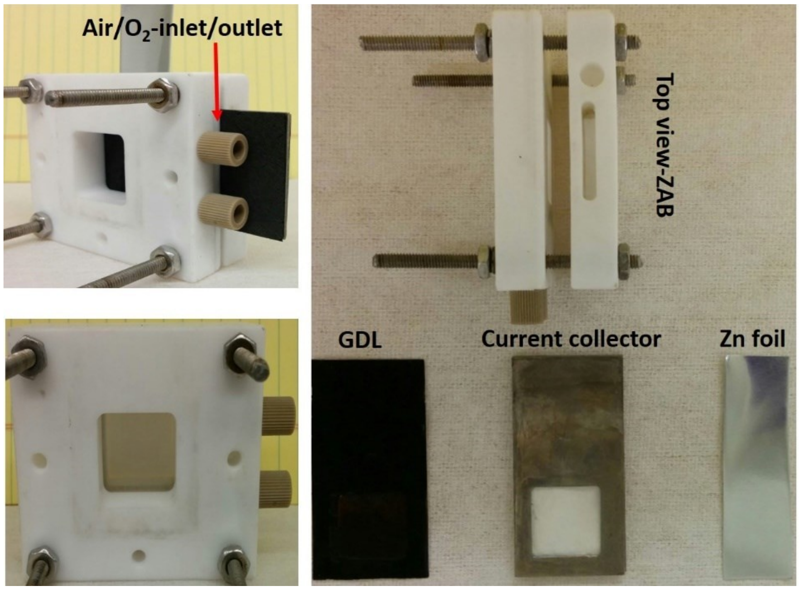

Figure 2-20 The components of a ZAB used in this work.

Galvanostatic cycle testing is a common technique to evaluate the overpotential between charge and discharge voltages and the continuous cycle life without severe enlargement of the overpotential. The battery potential profiles, during the cycling tests, are obtained by applying repeated discharge/charge processes with a fixed current and a fixed amount of cycle time. Pulsed cycling is applied to evaluate the battery's rechargeability by interchanging the polarity in short intervals for extended cycling to measure the cycling capabilities of the battery. The activity of the catalyst is determined by the overpotential between the discharge potential and the charge potential, where typically a low overpotential signifies high activity toward oxygen reactions. Also, the durability of the catalyst is determined by the degree of the retention of the battery potential over several cycles.

3 Chapter 3: Manganese-cobalt mixed oxide film as a bifunctional catalyst for rechargeable Zn-air batteries

Preliminary results for this Chapter have been published in the Materials Research Society Proceedings and are included in the Appendix.

E. Davari and D. G. Ivey, Mn-Co oxide/PEDOT as a bifunctional electrocatalyst for oxygen evolution/reduction reactions, *MRS Proceedings*, 2015, **1777**, 1-6.

A version of this Chapter has been published in the journal Electrochimica Acta:

E. Davari, A. D. Johnson, A. Mittal, M. Xiong and D. G. Ivey, Mn-Co mixed oxide film as a bifunctional catalyst for rechargeable Zn-air batteries, *Electrochim. Acta*, 2016, **211**, 735–743.

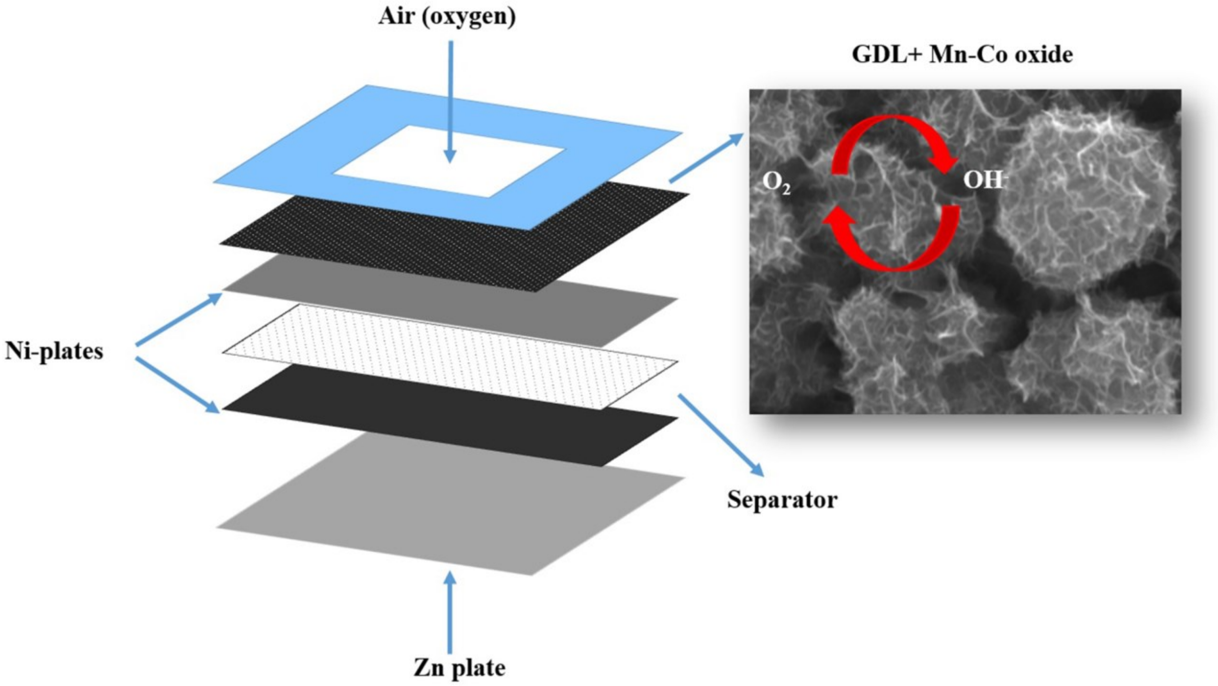

3.1 Introduction

Many researchers believe that metal-air batteries will become, in the near future, one of the most efficient and reliable energy storage devices. Metal-air batteries have advantages, such as higher energy density, lower operation risk and a more environmentally benign nature, compared with traditional Li-ion batteries. In metal-air batteries, the cathode consumes oxygen from air as a reactant rather than storing heavy materials within the cell, as in other battery types such as Li-ion batteries. Among metal-air batteries, ZABs possess cost, safety and technology advantages over Li-air, Al-air and Mg-air batteries.[9,10,16,27,129,130,167,178,221,222] Despite the promising features and technical progress, there are several major challenges associated with ZABs. The most critical challenge limiting the practical use of this technology is the sluggish ORR and OER kinetics. Therefore, bifunctional air electrodes play key roles for the development of electrically rechargeable ZABs.[27,222] Traditionally, Pt and Ir/Ru and their alloys have been employed as bifunctional catalysts due to their relatively low overpotentials and high current densities. However, Pt- and Ir/Ru-based catalysts suffer from low stability, high cost and limited natural supply for practical application. These problems can be addressed by developing new, non-precious metal bifunctional electrocatalysts. The catalysts need to have relatively high activity, similar to precious metals, in addition to long term stability.[22,129,147]

Non-precious metal catalysts, such as transition metal-oxides[158,160], carbon-based materials[143,223–225], perovskites and spinel oxides[178,223], have been investigated widely as less expensive alternatives to Pt- and Ir/Ru-based catalysts. Composite metal oxides incorporating two or more transition metal elements into one oxide framework have been studied extensively in the context of non-precious metal bifunctional electrocatalysts during the last few years.[140,143,158,160,224–228] In mixed valence transition metal-oxide based catalysts, intimate electrical and chemical coupling between the oxides results in structural and electrochemical stability as well as good electrical conductivity. Additionally, high abundance, facile preparation techniques and outstanding redox stability in aqueous solutions make them a promising candidate for large-scale applications such as hybrid vehicles.[139,143] Given this background, MnO_x is presently being considered as one of the most promising non-precious metal ORR electrocatalysts in alkaline solutions due to its high stability against corrosion and relatively high catalytic activity.[20,229,230] Additionally, Co-oxides and hydroxides have been widely studied as electrocatalysts for OER.[231–233] The combination of Mn-oxide and Co-oxide electrocatalysts has also been reported in many studies.[139,141,150] Zhang et al. described the excellent electrocatalytic activity of dual phase spinel $MnCo_2O_4$/nanocarbon hybrid catalysts for OER and ORR with activity comparable to Pt/C.[143] Wang et al. reported a nanocomposite of well dispersed OER active Co_3O_4 and ORR active Co_2MnO_4 as an active bifunctional catalyst.[140] Zhao et al. synthesized stable and active spinel Mn-Co oxide in N-doped carbon nanotubes for reversible oxygen electrodes.[228] Theoretical calculations using DFT have also confirmed the bifunctional activity of Co-Mn-O spinels.[147]

Recently, Liu et al[127] have developed highly active bifunctional catalysts, fabricated by a non-surfactant assisted hypothermal method, consisting of non-spinel Co-Mn oxide supported by N-doped CNT (N-doped CNT/$Co_xMn_{1-x}O$). The OER activity of the catalyst outperforms IrO_2 nanoparticles. A current density of 4.6 mA cm^{-2} is generated at 0.3 V overpotential. NCNT/$Co_xMn_{1-x}O$ has an ORR onset potential as high as 0.96 V, which is comparable to that of Pt/C. A rechargeable durable ZAB with a low charge-discharge gap (0.57 V) and high stability is reported. Although the authors have shown that graphitized nanocarbons, such as CNTs, can mitigate carbon oxidation and corrosion, incorporating CNTs increases the production cost for large-scale applications. In another recent study, Sumboja et al.[116] have directly grown nanosized-bifunctional MnO_2 catalysts on carbon paper using a simple immersion process. The catalyst has low contact resistance at the air cathode/electrolyte interface. Good cycling stability up to 500 cycles and a power density as high as 108 mW cm^{-2} were achieved.

Electrodeposition is one of the most promising binder and template-free techniques for fabrication of Mn and Co oxides. The thin-film preparation with electrodeposition can be divided into galvanostatic, potentiostat (PS), pulsed current, pulsed potential, and CV techniques according to the different styles of applied voltage or current.

The overall process for Mn or Co oxide electrodeposition can be described by the following equation:

$$(x)M^{m+}_{(aq)} + (y)H_2O_{(aq)} \rightarrow M_xO_{y(s)} + (2y)H^{+}_{(aq)} + 2(y-x)\bar{e} \qquad (M = Co, Mn)$$

The general steps in the mechanism that have been proposed typically involve electrochemical oxidation of $M^{m+}_{(aq)}$, followed by precipitation of the solid phase, which subsequently dehydrates to form Mn-oxide or Co-oxide ($M_xO_{y(s)}$). However, there is controversy concerning the exact mechanisms of Mn and Co electrodeposition.[234] More details about the nucleation and growth of Mn-oxide during anodic electrodeposition can be found in the work by Clark and Ivey.[11]

Herein, we report on a hybrid material composed of Mn oxide and Co oxide as a highly active and stable bifunctional electrocatalyst, which is directly grown on commercial carbon paper via anodic electrodeposition. The process is a simple, template-free method done at moderate temperatures and is similar to the processes used in our group[11,12,235] to fabricate Mn oxide for supercapacitor applications. Furthermore, a catalyst directly grown on the air cathode improves adhesion and lowers the risk of catalyst detachment during cycling, relative to catalysts that are physically attached to the air electrode. In addition, anodic electrodeposition at moderate temperatures (60 °C) does not require high cost facilities and can be scaled up easily. The deposit morphology consists of free standing fibrous rods, composed of a mixed Mn-Co oxide, which is distributed uniformly across the carbon paper without blocking the porosity that is crucial for oxygen transport. Our study shows that mixed Mn-Co oxide is a reliable catalyst for the air electrode to improve the cycle life and performance of ZABs.

3.2 Experimental methods

3.2.1 Chemicals and reagents

All chemicals were of reagent grade and used without further purification. All solutions were prepared with deionized (DI) water. A solution consisting of 0.01 M Mn-acetate ($Mn(CH_3COO)_2$), 0.02 M ammonium-acetate ($C_2H_4O_2.NH_3$) and 10 wt% dimethyl sulfoxide (DMSO) ($(CH_3)_2SO$) was used for Mn-oxide deposition. Co-oxide deposition was done using 0.01 M Co-acetate ($Co(CH_3COO)_2$), 0.02 M ammonium-acetate ($C_2H_4O_2.NH_3$) and 10% dimethyl sulfoxide (DMSO) ($(CH_3)_2SO$).

3.2.2 Electrodeposition

The oxides were electrodeposited using a two electrode cell configuration (Figure 3-1) onto commercially pure stainless steel (SS) (grade 304) foil for the catalyst study. For the battery study, electrodeposition was done in a similar manner on anodized GDL (SGL 39 BC, 20% PTFE) with a working area of 5 cm^2.

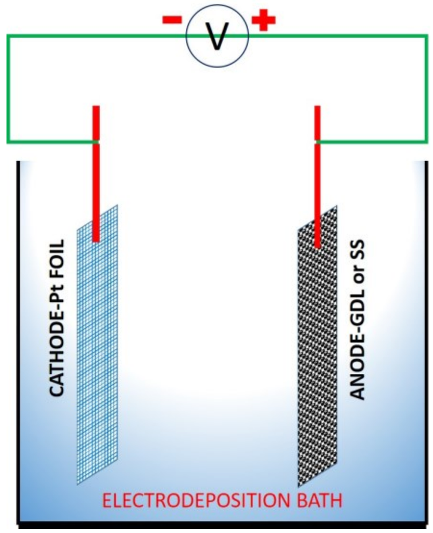

Figure 3-1 A schematic of the anodic electrodeposition process.

Before deposition, the SS foil was washed in (DI) water for 15 min in an ultrasonic bath and then dried in air. The electrochemical cell included an anodic SS substrate centered between two parallel Pt meshes. The deposition solution temperature was maintained at 60 ºC using a hot plate and agitated continuously during deposition with a magnetically driven Teflon® coated stirring bar at a speed of 300 rpm. Galvanostatic control with a current density of 5 mA cm^{-2} was applied using a power source. Mn oxide and Co oxide were deposited sequentially (Mn oxide first) at various times ranging from 1 to 5 min. After electrodeposition the substrate was rinsed with DI water and dried in air at 100 ºC for 1 h to remove residual water.

3.2.3 Half-cell electrochemical analysis

Electrochemical half-cell testing included CV and LSV using a RDE setup (Pine Instruments Co., AFMSRCE) and was performed using a potentiostat (Bio-logic® SP-300) with a typical three electrode system. The sequentially deposited oxide films were scraped off from the SS electrodes and mechanically mixed with carbon black (CB) (catalyst:carbon = 1:1.5) to overcome electronic conductivity limitations. It is important to note that the ratio of the catalyst to CB is consistent with the baseline (40 wt% catalyst - 60 wt% CB). The catalyst ink was prepared by blending 20 mg of the catalyst and the conductive carbon mixture with 0.2 ml of 0.5 wt% Nafion (5% w/w in water and 1-propanol dispersion, ≥0.92 meq g^{-1} exchange capacity) and 0.7 ml of isopropanol solution. After ultrasonication for 45 min, 5 µL of the ink was drop-coated on a 5 mm diameter GC disk as a working electrode to reach a mass loading of 0.1 mg cm^{-2}. The electrode was dried for 1 h under a 20 W lamp. The working electrode was immersed in a glass cell containing Ar- or O_2-saturated KOH (0.1 M or 6 M) aqueous electrolyte. A Pt coil and Hg/HgO (1 M NaOH, 0.098 V vs. NHE at 25 °C) served as the counter and reference electrodes, respectively (Figure 2-18). To remove any capacitive contribution during evaluation of the ORR-OER activity, background currents were obtained under an Ar-saturated environment by sweeping the potential from 0.2 to -0.7 V vs. Hg/HgO at a scan rate of 10 mV s^{-1}. The working electrode was immersed in the electrolyte for 30 min before each test. ORR activity was measured by sweeping the potential from -0.7 to 0.2 V vs. Hg/HgO at a scan rate of 10 mV s^{-1}. For OER measurements, the potential range was 0 to 0.7 V vs. Hg/HgO with a rotation speed of 1600 rpm. The ORR onset potential is defined as the potential at which the current density is 10% of the current density at a potential of -0.4 V[200], i.e., where the current density reaches the diffusion limited value. The OER onset potential was determined by the intersection of the tangent line with the background before the anodic current reached 50 μA. The number of electrons transferred during ORR was calculated using K-L equations:

$$1/i = 1/i_k + 1/i_l \qquad \text{Equation 1}$$

$$i_l = B\omega^{1/2} \qquad \text{Equation 2}$$

$$B = 0.62nFAv^{-1/6}C_o(D_o)^{2/3} \qquad \text{Equation 3}$$

where i is the measured current density, i_k is the kinetic current density, i_l is the limiting diffusion current density, ω is the angular velocity, n is the number of electrons transferred, F is the Faraday constant (96,485 C mol^{-1}), ν is the kinematic viscosity (0.01 cm^2 s^{-1}), C_o is the bulk concentration of oxygen (1.2×10^{-6} mol L^{-3}) and D_o is the diffusion coefficient of oxygen (1.9 cm^2 s^{-1}) in the 0.1 M KOH solution.[236]

3.2.4 ZAB testing

In order to evaluate the catalyst performance in a ZAB, the oxides were sequentially electrodeposited (Mn oxide first) onto an anodized GDL with an active area of 5 cm^2 and dried at 100 ºC for 1 h. The oxide performance was compared with GDL coated with Pt-Ru catalyst. The Pt-Ru catalyst material was dispersed into an isopropanol:nafion:PTFE (25 g:0.5 g:1 g) mixture at a catalyst concentration of 19.4 mg mL^{-1}. The ink was then air brush sprayed onto the GDL (5 cm^2), to achieve a loading of 1 mg cm^{-2}, and dried at 300 ºC for 1 h. A polished Zn plate and two layers of fast flow rate membrane (Fisherbrand P8) were used as the Zn electrode and separator, respectively. The electrolyte used in the ZAB was 6 M KOH with 2% ZnO dissolved to form zincate ions. Rechargeable ZABs were tested in a laboratory-built electrochemical cell (Figure 2-20). The gap between the anode and cathode was approximately 1.0 cm. The battery charge-discharge voltages were measured by galvanodynamic methods, scaling the current from 0 to 50 mA cm^{-2} at a rate of 5 mA s^{-1}. Charge-discharge pulse cycling was tested by the recurrent galvanic pulse method using an applied current of 25 mA with each cycle consisting of a 30 min discharge followed by a 30 min charge for 30 cycles.

3.2.5 Materials characterization

Electrodeposited samples were characterized using XRD. Patterns were recorded at a scan rate of $1° min^{-1}$ on a Rigaku Ultima diffractometer with CuKα radiation (λ= 0.154051 nm). The samples were prepared by scraping off deposits from the SS substrate. The morphology and the composition of the Mn-Co oxides were investigated using a Tescan Vega-3 SEM operated at 20 kV and equipped with an EDX detector with an ultra-thin window (UTW). Higher resolution microstructural characterization was done using a Philips CM20 FEG TEM/STEM operated at 200 kV and equipped with an UTW X-ray detector. The electron transparent samples for TEM analysis were prepared by scraping some of the deposit from the SS substrate and then ultrasonically dispersing the residue in isopropanol for 20 min. One or two drops of the suspension were deposited onto holey carbon-coated Cu grids. After isopropanol evaporation, samples were ready for TEM analysis. Chemical state analysis was carried out by XPS using a Kratos AXIS Ultra X-ray photoelectron spectrometer. A monochromatic Al source (λ = 8.34 Å), operating at 210 W with a pass energy of 20 eV and a step of 0.1 eV, was utilized. All XPS spectra were calibrated using the C 1s peak at 285 eV. CASA XPS Version 2.3.13 software was used to accomplish background subtraction and curve fitting. In order to confirm the intermixing of Mn and Co oxide during the electrodeposition, AES was performed using a JAMP 9500F instrument equipped with a hemispherical analyzer AES with 7 channeltron detectors. AES was performed on Mn-Co oxides rods were deposited on an Au-coated Si-wafer substrate (2mm × 2mm). Prior to AES, the tops of the rods were sputtered using a focused ion beam (FIB) (Ga^+ ions) perpendicular to the growth direction. AES was performed on several regions including the edges and the center of the particles.

3.3 Results and discussion

3.3.1 Microstructural characterizations

In this study, time controlled sequential electrodepositions (Mn oxide first) were carried out to optimize the catalytic activity of the Mn-Co oxides by systematically changing the ratio of Mn and Co. Table 3-1 summarizes the deposition conditions and nomenclature for each sample.

Table 3-1 Summary of the time-controlled electrodepositions of Mn-Co oxides.

Sample*	Deposition time Mn-oxide (min)	Deposition time Co-oxide (min)	Temperature (°C)	Rotation speed (rpm)
Mn/Co:1	1	5	60	300
Mn/Co:1.1	3	5	60	300
Mn/Co:2.5	5	5	60	300
Mn/Co:3.4	5	3	60	300
Mn/Co:4.2	5	1	60	300

* The nomenclature is based on the Mn/Co ratio determined from EDX analysis in Figure 3-3.

Cross section and plan view SEM images for different deposition times are shown in Figure 3-2. In all cases, the as-deposited material consists of fibrous, rod-like structures (about 5-10 µm long and 2-5 µm in diameter), which are orientated perpendicular to the surface and distributed uniformly across the substrate. In general, fine particles are prone to agglomeration in electrochemical processes[237]; therefore, the rods fabricated in this work, with moderate size and high surface area, could be an advantage for long-term performance of the catalyst.

Overall compositional analysis of the as-deposited samples was done using EDX spectroscopy of plan view samples in the SEM. Several areas, 10 µm by 10 µm in size, were analyzed. The average Mn and Co compositions, as well as the Mn/Co ratios, are summarized in Figures 3-3(A-B). The relative amount of Mn/Co in the deposits increases with increasing Mn oxide deposition time. Manganese and Co were uniformly distributed across the surface, as shown by X-ray mapping of several deposit areas. An example for the as deposited Mn/Co:2.5 sample is shown in Figure 3-4.

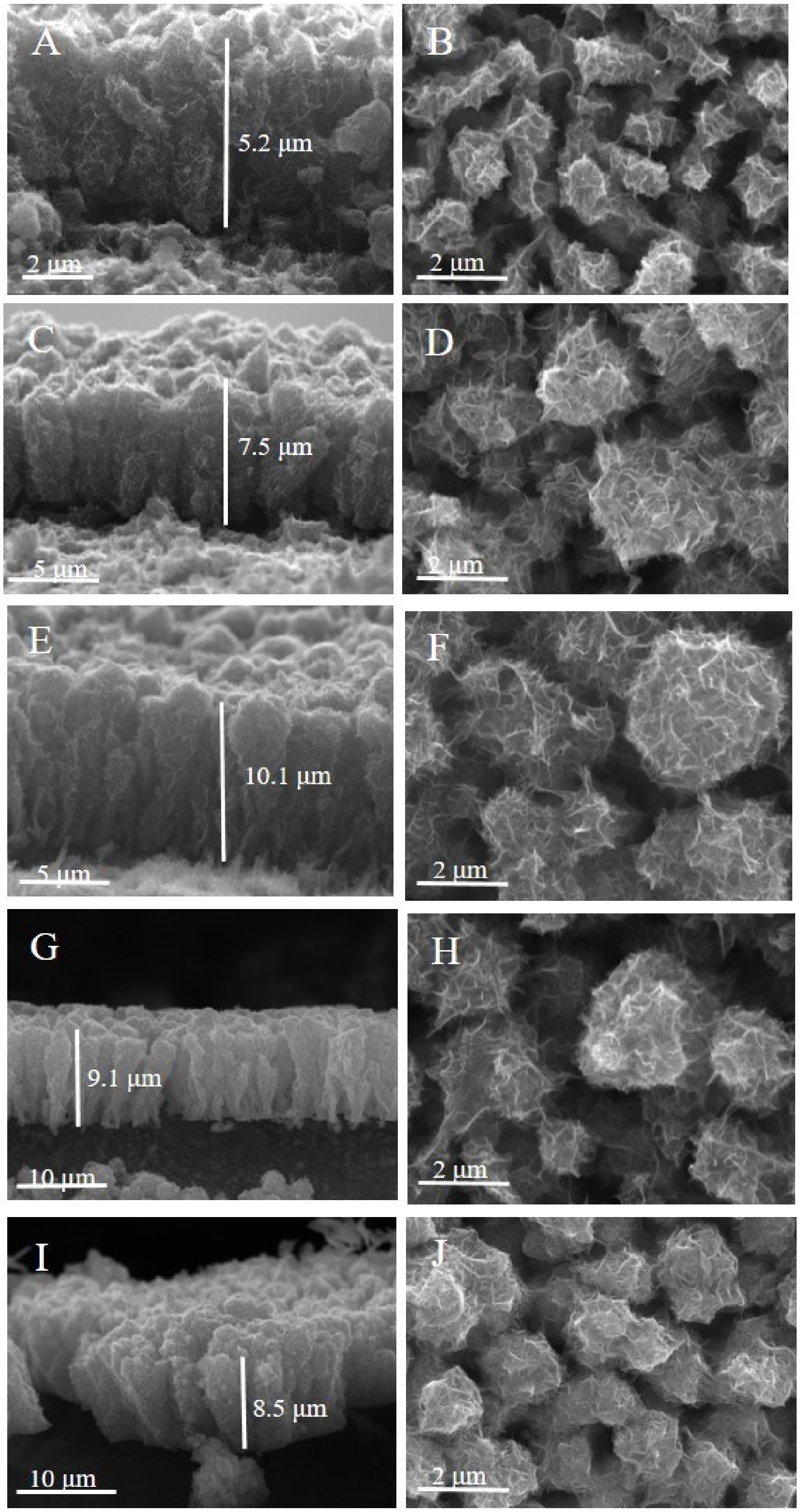

Figure 3-2 SEM SE cross section and plan view images of Mn-Co oxide deposits prepared at various deposition times. (A, B) Mn/Co:1; (C, D) Mn/Co:1.1; (E, F) Mn/Co:2.5; (G, H) Mn/Co:3.4; (I, J) Mn/Co: 4.2.

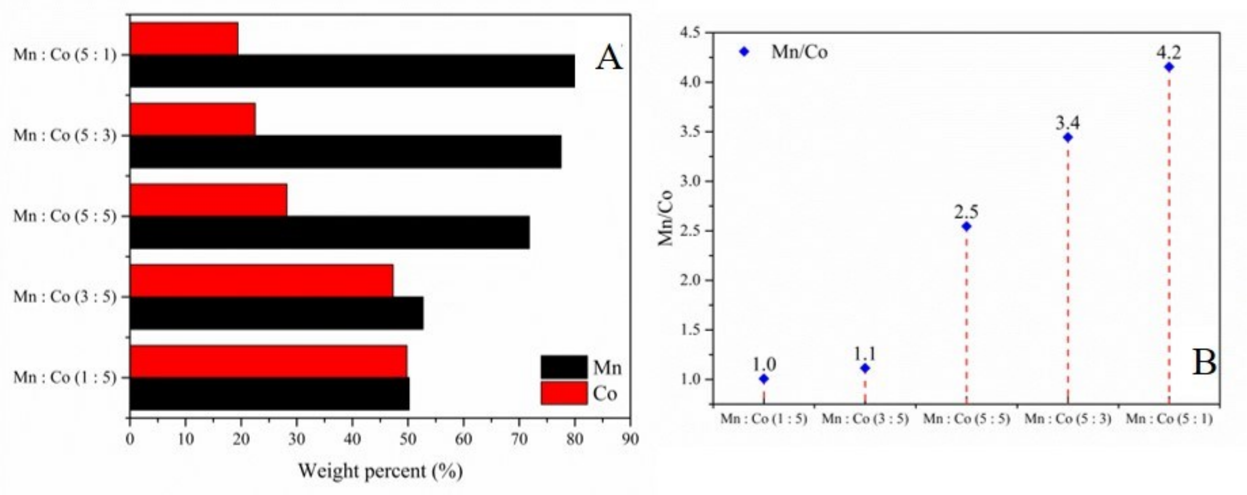

Figure 3-3 (A) Mn and Co composition analysis for the time-controlled electrodepositions. (B) Plot of Mn/Co ratio for the as-deposited samples.

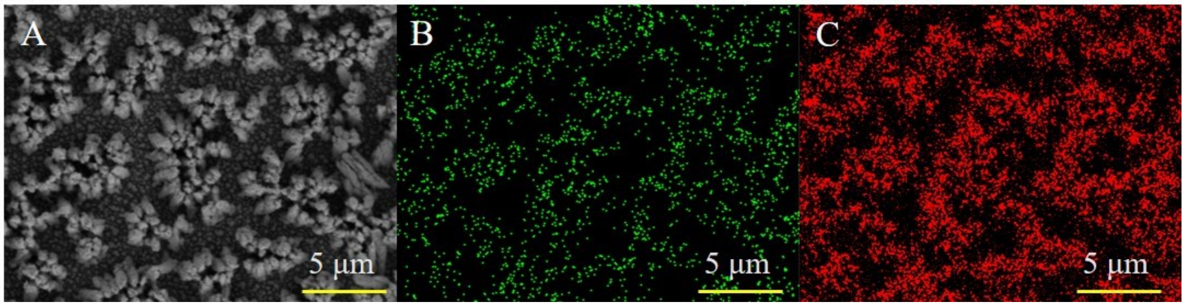

Figure 3-4 (A) SEM SE image of a Mn/Co:2.5 on a GC substrate. EDX elemental maps showing (B) Co and (C) Mn.

The as deposited Mn/Co:2.5 oxide sample had the best electrochemical performance (discussed later in this Chapter), so it was examined in more detail by XRD, TEM, AES and XPS. An XRD pattern was obtained of the material electrodeposited on the SS substrate (Figure 3-5). Broad peaks are visible and are an indication of the nanocrystalline nature of the deposit. Attempts were made to index the peaks to known Mn oxides, Co oxides and mixed oxides. The best agreement was with a single phase, $Mn_7O_{13}.5H_2O$ (birnessite - JCPDS card #23-1239)[238]; the peaks were indexed to the (110), (221), (060), (252), (128), (183), (457) and (641) planes of birnessite. Even though the Mn oxide and Co oxide layers were deposited separately, a single phase appears to have formed.

A TEM sample was prepared of the Mn/Co:2.5 sample. A bright field (BF) image of part of a rod is shown in Figure 3-6(A). The rod is composed of thin sheets (~5 nm in thickness). The SAD pattern in Figure 3-6(B) shows at least three diffuse rings, which indicate the nanocrystalline nature of the deposit. The d-spacings of the rings are ~0.249, 0.206 and 0.146 nm, respectively. These can be indexed to the (060)/(252) (which have similar d-spacings), (128) and (457) planes of $Mn_7O_{13}.5H_2O$ (birnessite). These results are in agreement with the XRD results in Figure 3-5.

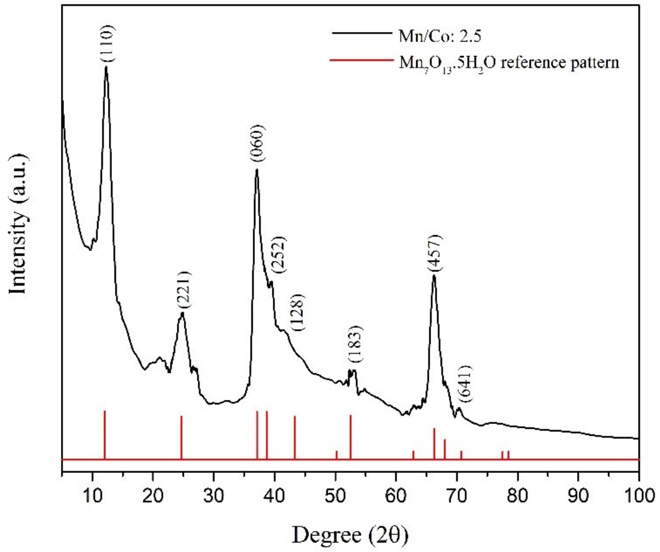

Figure 3-5 XRD pattern for as-deposited Mn-Co oxide and the reference pattern for birnessite $Mn_7O_{13}.5H_2O$ (JCPDS No. 23-1239).

X-ray line scans were performed on TEM samples to examine the distribution of Mn and Co; an example is shown in Figures 3-6(C-D). Mn and Co are uniformly distributed throughout the particles, i.e., the Mn and Co line scans follow the same trend. The combined diffraction and X-ray microanalysis results indicate that a single phase (birnessite) in present in the as-deposited material, which means that Mn and Co interdiffusion has occurred during deposition. No individual Mn oxide or Co oxide phases were detected.

To further investigate the interdiffusion of Mn and Co oxides, AES was performed on several areas as shown in Figure 3-7(A). Since Mn and Co oxide are deposited sequentially, it was suspected that Co oxide may only deposit on the surface of the rods. In this case, AES would show higher concentration of Co on the edge of the particles compared to the center. However, Figure 3-7(B) shows that the AES spectra obtained from the edge and center of rods have very similar trends, indicating that Mn and Co are homogenously dispersed throughout the rods. This provides further evidence of the interdiffusion of Mn and Co during the electrodeposition process.

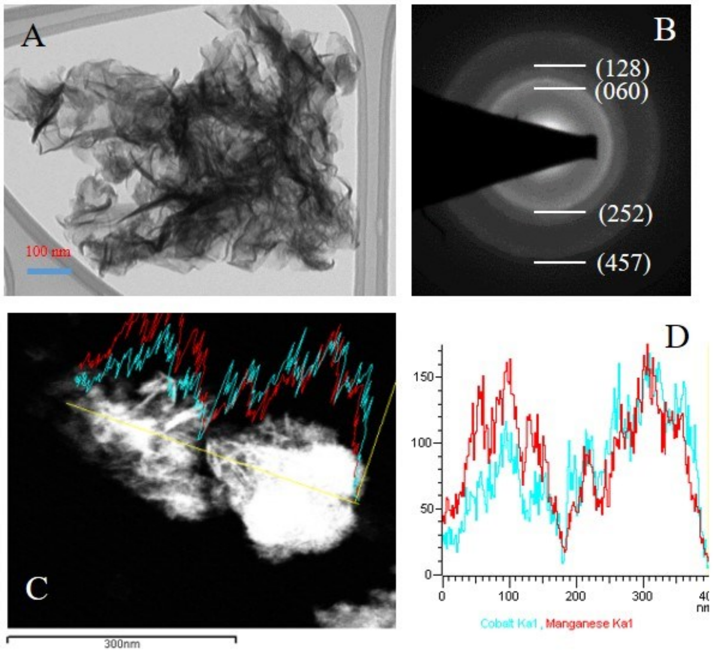

Figure 3-6 (A) TEM BF image of a Mn-Co oxide rod, (B) SAD pattern from the area in (A) and (C, D) high angle annular dark field (HAADF) image and corresponding X-ray line scan along part of a Mn-Co oxide rod.

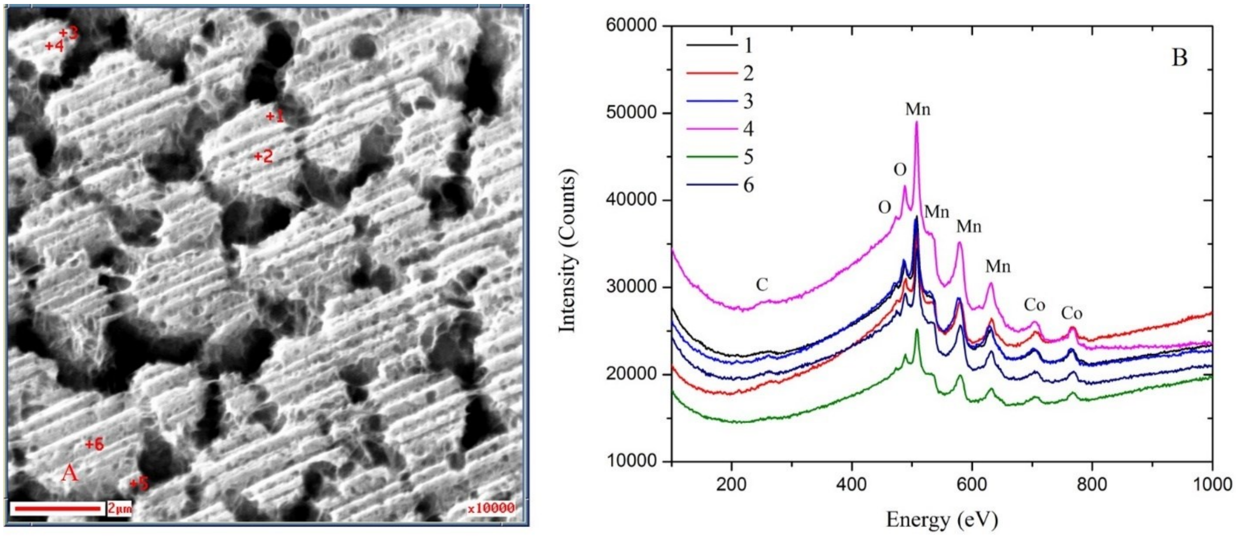

Figure 3-7 (A) SE image from Mn/Co:2.5 sample (the streaks are due to curtaining during FIB sputtering), (B) AES spectra from six different areas shown in A.

The likelihood of diffusion of Co ions into the Mn oxide structure at 60 °C can be estimated. Since the diffusion coefficients for Co^{2+} or Co^{3+} in the MnO_x structure were not available in the current database, the diffusion data for Co^{2+} in Co_xO[239] was used as a reasonable approximation. The temperature dependence of the diffusion coefficients is:

$$D = D_0 \exp(\frac{-Q_d}{RT}) \qquad \text{Equation 4}$$

where D_0 is the frequency factor ($m^2\ s^{-1}$), Q_d is the activation energy for diffusion ($J\ mol^{-1}$), R is the gas constant ($8.314\ J\ mol^{-1}\ K^{-1}$) and T is the absolute temperature (K).[240]

D_0 and Q_d for Co^{2+} in Co_xO at 1100-1400 °C are $4.08 \times 10^{-7}\ m^2\ s^{-1}$ and $150.2\ kJ\ mol^{-1}$[239], respectively. As such, the diffusion coefficient at 60 °C is estimated as $\sim 8 \times 10^{-19}\ m^2\ s^{-1}$. The diffusion time can be estimated using the following equation:

$$t = {x^2}/{D} \qquad \text{Equation 5}$$

where x is the diffusion distance (m) and t is the time required for the diffusion process to happen (s). Assuming a diffusion distance of 0.5 μm (diameter of the rods is 2-5 μm), the calculated interdiffusion time for Co^{2+} in Co_xO is ~87 h at 60 °C, which shows that Co^{2+} interdiffusion into the Mn oxide structure is feasible. It should be noted that this calculation approximates the rod shape as solid cylinders. In reality the rods are fibrous and porous, providing short paths for Co diffusion into the bulk. Because of this effect, the time for Co diffusion is likely to be significantly shorter than the calculated time of 87 h.

XPS was employed to investigate the surface chemical state of the synthesized Mn-Co mixed oxide. Mn 3s and Mn 2p spectra are shown in Figure 3-8(A-B). The Mn 3s spectrum (Figure 3-8(A)) shows two peaks at 84.7 eV and 89.6 eV. The Mn 3s peak splitting is 4.7 eV, which corresponds to a mixed valence state of Mn^{3+} and Mn^{4+}[141,236]. The Co 2p spectrum (Figure 3-8(B)) shows two pairs of spin-orbit doublets and shakeup satellites revealing the coexistence of Co^{2+} and Co^{3+}[141]. Additionally, the O 1s spectrum for as deposited Mn-Co oxide exhibits two features (Figure 3-8(C)). The intense peak, located at 529.7 eV, corresponds to lattice oxygen bonding with Mn and Co. The peak shoulder, located at 531.3 eV, can be assigned to adsorbed oxygen as hydroxyl OH^- ions on the surface.[241]

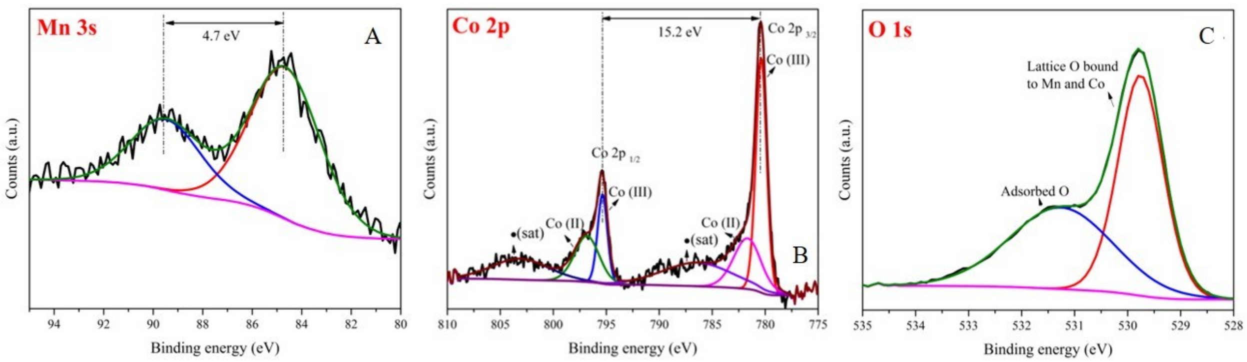

Figure 3-8 XPS spectra for (A) Mn 3s, (B) Co 2p and (C) O 1s from the as-deposited Mn/Co:2.5 sample.

Based on the XRD and SAD results, a single Mn-Co oxide phase is synthesized after sequential anodic electrodeposition. The oxide contains Co^{2+} and Co^{3+} ions, as well as Mn^{3+} and Mn^{4+} ions; the Co ions appear to partially substitute for Mn ions in the birnessite structure generating a phase with a composition corresponding to $(Mn,Co)_7O_{13}.5H_2O$. Although the exact mechanism associated with mixed oxide formation is not clear, the uniform dispersion of Mn and Co oxide (see the EDX line scan in Figure 3-6(D) and AES spectra Figure 3-7(B)) shows that interdiffusion of Co oxide in Mn oxide occurs during the second electrodeposition step at 60 °C. Similar intermixing of Mn and Co was reported in an earlier study on supercapacitors by Nakayama et al. [242], where anodic electrodeposition (at 70 ºC) using an electrolyte consisting of 2 mM $MnSO_4.5H_2O$, 50 mM $Et_4NCL(Et=C_2H_5)$ and $CoSO_4.7H_2O$ produced a layered, Mn-oxide birnessite phase containing Co^{2+} ions. The introduction of Co^{2+} ions did not generate any new XRD peaks; however, peak broadening in the XRD pattern is attributed to Co ions in the birnessite framework. A significant increase in the specific capacitance and cycling ability was obtained with Co doped birnessite.[242]

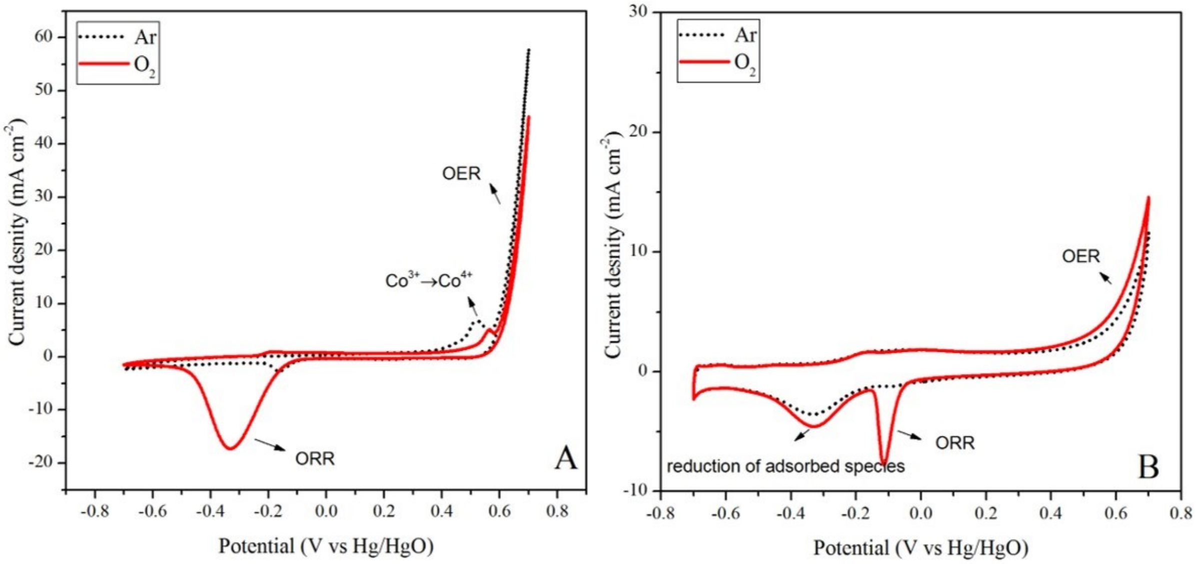

Figure 3-9 CV curves for (A) Mn/Co:2.5-CB oxide and (B) Pt-Ru/CB in O_2-saturated (red line) and Ar-saturated (blue line) 6 M KOH with a sweep rate of 10 mV s^{-1}.

3.3.2 Electrochemical characterization

Thin-film RDE CV and LSV techniques were performed to characterize the catalytic performance of the oxides for ORR and OER and the results were compared with Pt-Ru/CB as the baseline. CV was performed for all the samples presented in Table 3-2 and the sample with the best ORR-OER performance is presented here. Figure 3-9 shows the thin-film RDE CV curves measured for the ORR/OER performance of Mn/Co:2.5-CB, as well as Pt-Ru/CB, in an alkaline electrolyte (6 M KOH) saturated with Ar or O_2. The potential is scanned in the range of -0.7 to 0.7 V (vs Hg/HgO) with a scan rate of 10 mV s^{-1}. CV results reveal that the ORR onset potential for Mn/Co:2.5-CB is only 105 mV more negative (-0.10 V) than the baseline catalyst. Furthermore, the OER potential for Mn/Co:2.5-CB is only 100 mV more positive (0.51 V) in comparison with Pt-Ru/CB. The peak observed at -0.33 V for Pt-Ru/CB CV corresponds to adsorbed species at the Pt-Ru/CB electrode.[243] Also, the peak at ~0.5 V for Mn-Co/CB corresponds to the oxidation of Co^{2+} to Co^{3+}.[4] However, the ORR/OER peak current density in the O_2-saturated electrolyte is almost three times higher than that for Pt-Ru/CB with similar mass loading. RDE measurements were employed to assess the ORR and OER kinetics of the catalysts (Figure 3-10). The optimum catalyst composition was also evaluated by comparing the onset potentials and the ORR/OER current densities for different samples (Table 3-2 and Figure 3-11). The tests were reproducible; each sample was tested

3 times. The ORR current density increases as the amount of Mn oxide in the mixed Mn-Co oxide increases, up to the composition corresponding to Mn/Co:2.5-CB, after which the current density levels off.

Table 3-2 Summary of the ORR/OER catalytic activity at a rotation rate of 1600 rpm and a scan rate of 10 mV s^{-1}.

Sample	E_{ORR} (V)	i_{ORR} (mA cm^{-2}) at E=-0.7 V	E_{OER} (V)	i_{OER} (mA cm^{-2}) at E=0.7 V	E_{OER} - E_{ORR} (V)
Mn/Co:1-CB	-0.084	-3.80	0.220	6.10	0.304
Mn/Co:1.1-CB	0.026	-5.10	0.464	1.72	0.438
Mn/Co:2.5-CB	0.076	-6.20	0.322	2.28	0.246
Mn/Co:3.4-CB	0.030	-5.52	0.515	0.61	0.485
Mn/Co:4.2-CB	0.032	-5.79	0.526	0.39	0.494
Pt-Ru/CB	0.140	-5.29	0.309	3.98	0.169

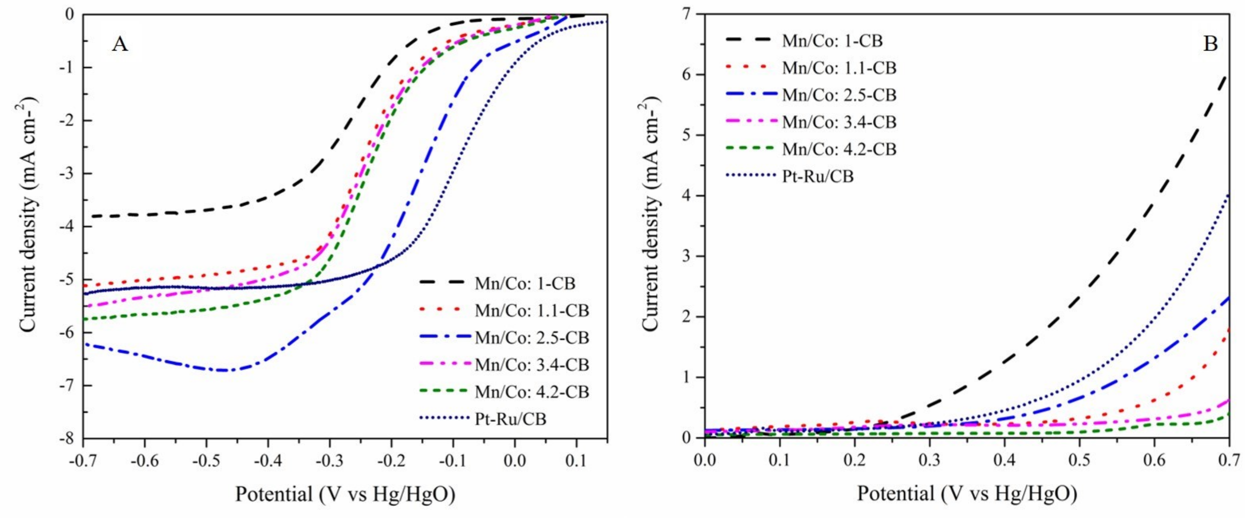

Figure 3-10 (A) LSV ORR curves for Mn/Co:1-CB, Mn/Co:1.1-CB, Mn/Co:2.5-CB, Mn/Co:3.4-CB, Mn/Co:4.2-CB and Pt-Ru/CB on RDE electrodes in O_2-saturated 0.1 M KOH solution, at a rotation speed of 1600 rpm with a sweep rate of 10 mV s^{-1}. (B) LSV OER curves for Mn/Co:1-CB, Mn/Co:2.5-CB, Mn/Co:3.4-CB, Mn/Co:4.2-CB and Pt-Ru/CB on RDE electrodes in Ar-saturated 0.1 M KOH solution, at a rotation speed of 1600 rpm with a sweep rate of 10 mV s^{-1}.

A similar trend is seen for the ORR onset potential. The onset potential increases (more positive) up to the composition corresponding to Mn/Co:2.5-CB, then it drops and then levels off. Lowering the amount of Mn oxide (increasing the amount of Co oxide) in the mixed Mn-Co oxide generally increases the OER performance (increases the current density and decreases the OER onset potential). The Mn/Co:1.1-CB sample is an exception; it has a higher onset potential and lower current density for OER compared with the Mn/Co:2.5-CB sample. It may be due to higher OER activity of Co-oxide which results increase in the These results are consistent with the literature.

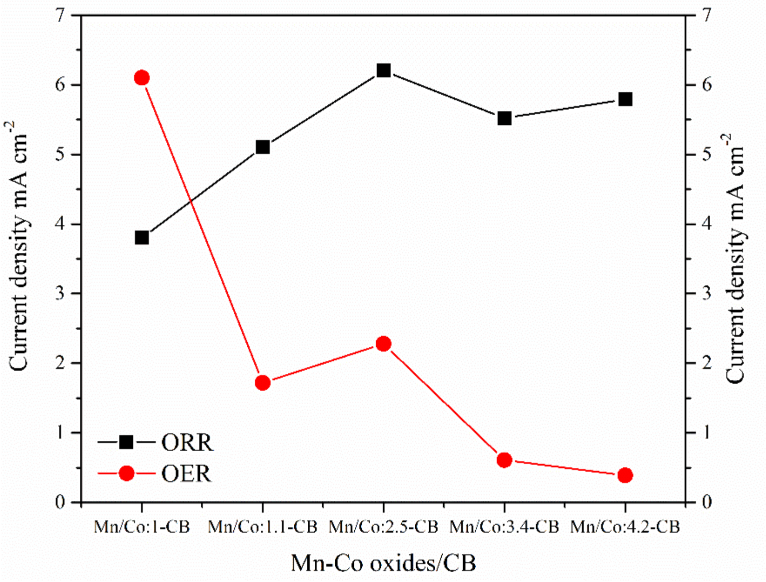

Figure 3-11 Comparison of LSV ORR and OER current densities for various Mn-Co oxide-CB samples at 1600 rpm.

Rios et al.[226] investigated electrodes produced from Co and Mn spinel type oxide powders ($Mn_xCo_{3-x}O_4$, $0 \leq x \leq 1$). They reported that Mn oxide is an ORR active catalyst, while Co oxide improves the OER performance. In addition, Mn oxide strongly inhibits the oxidation of OH^-, which is the rate determining step for OER.[146] Mn/Co:2.5-CB has the highest ORR activity and has the second best OER activity among all the Mn-Co oxide samples. Mn/Co:2.5-CB outperforms Pt-Ru/CB in terms of ORR current density, while its OER performance is similar to that of Pt-Ru/CB. Mn/Co:2.5 has the best combined performance of the Mn-Co oxides, since its ORR/OER overpotential (E_{OER} - E_{ORR}) is the lowest (0.246 V) (Table 3-2). Also, the ORR onset potential of this sample (0.076 V) is more positive than that for $Co_xMn_{3-x}O_4$ spinel nanoparticles (0.019 V)[147] and is comparable with the potential reported for Co_3O_4 nanoparticle-modified MnO_2 nanotubes (0.176 V).[141] A summary of ORR/OER activity for Mn/Co:2.5-CB and other Mn-Co oxide based catalysts from the literature is presented in Table 3-3.

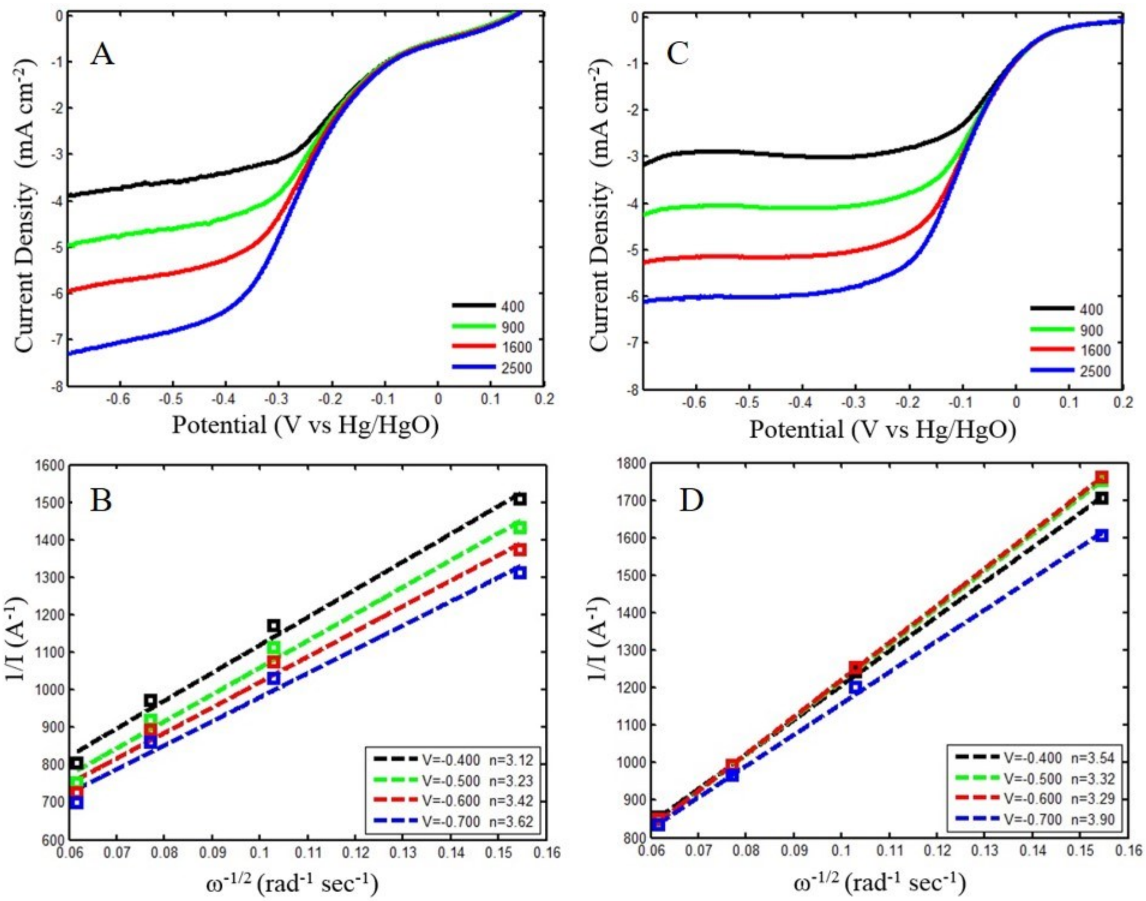

Figure 3-12 (A) LSV plots for Mn/Co:2.5-CB on RDE in O_2-saturated 0.1 M KOH with a sweep rate of 10 mV s^{-1}. (B) K-L plots obtained from (a) at different potentials. (C) LSV plots for Pt-Ru/CB on RDE in O_2-saturated 0.1 M KOH with a sweep rate of 10 mV s^{-1}. (D) K-L plots obtained from (D) at different potentials.

The ORR kinetics was also evaluated for the Mn/Co:2.5-CB and Pt-Ru/CB samples from a set of voltammetry profiles collected on rotating electrodes (Figures 3-12(A-B)). The current density increased with increasing rotational rate (ω) as a result of faster oxygen flux to the surface of the electrode. The current densities at different rotation speeds were used to construct K-L plots, where the number of electrons transferred per O_2 molecule (n) and the kinetic current density (i_k) were determined from the slope and intercept of the fitted linear line, respectively. As shown in Figures 3-12(A-B), the average n value in the potential range of -0.4 V to -0.7 V is 3.34 for Mn/Co:2.5-CB. This high value for n indicates good selectivity towards the four-electron pathway (Equation 8), which is similar to ORR catalyzed by commercial Pt-Ru/CB. The ORR activity of transition metal oxide based catalysts proceeds through multistep reactions. First, a peroxide intermediate forms from the adsorbed O_2 on the active sites (Equation 6). This is followed by further reduction or decomposition to OH^- ions leading to a four-electron reduction process (Equations 7 and 8).[27,143]

$O_{2(g)} + H_2O_{(aq)} + 2e \rightarrow HO_2^-{}_{(aq)} + OH^-{}_{(aq)}$ Equation 6

$2HO_2^-{}_{(aq)} \rightarrow 2OH^-{}_{(aq)} + O_{2(g)}$ Equation 7

$O_{2(g)} + 2H_2O_{(aq)} + 4e \rightarrow 4OH^-{}_{(aq)}$ Equation 8

Table 3-3 Comparison of Mn/Co:2.5-CB with various non-precious metal catalysts in the recent literature, as bifunctional catalysts in ZABs.

Refs	Materials	ORR onset potential (V)	i_{ORR} at -0.7 V (mA cm^{-2})	OER onset potential (V)	i_{OER} at 0.7 V (mA cm^{-2})	Catalyst loading (mg cm^{-2})
This work	Mn/Co:2.5-CB	0.076	-6.20	0.322	2.20	0.100
244	MnO_x nanowires	-0.500	-1.70	ND	ND	ND
141	MnO_2-Co_3O_4	0.176	3.40	ND	1.30	0.100
150	N-doped $CoMn_2O_4$	-0.004	-9.00	ND	10.00	ND
146	Mn-Co oxide nanofibres	-0.174	0.02	0.676	0.09	0.005
160	Mn-Co oxide	0.106	-5.70	ND	10.50	0.054
140	Co_3O_4-Co_2MnO_4	0.116	-5.10	0.621	10.00	ND
158	Mn-Co doped Fe_3O_4	0.036	-5.00	ND	ND	ND
127	NCNT/$Co_xMn_{1-x}O$	0.086	-5.50	ND	10.00	0.210

In general, on the basis of molecular orbital theory, the s and p orbitals of the oxygen molecules should overlap with the d-orbital of a metal ion to break the O=O bond. Since each surface configuration provides a certain energy for breaking the O=O bond, fibrous nanocrystalline Mn-Co oxide particles potentially provide more active sites with a high density of defects that allow oxygen adsorption in all potential surface configurations. It has also been reported in previous studies[113] that amorphous MnO_x structures provide more active sites for ORR. Furthermore, a uniform distribution of Co and Mn oxides results in fast Mn and Co cation exchange to facilitate ORR and OER.[64,245] However, more theoretical and experimental characterization on the electronic structures of the catalyst is required to unravel the detailed mechanism of the ORR/OER process on Mn-Co oxide composite electrodes.

The mass transport corrected kinetic current density i_k was applied to construct Tafel plots (Figure 3-13). Tafel slopes at low overpotentials for Mn/Co:2.5-CB and Pt-Ru/CB are close to theoretical values of -2.303 RT/F = -59 mV decade^{-1}, where R is the universal gas constant, F is the Faraday constant and T is the absolute temperature (300 K). The comparable Tafel behavior for both ORR and OER shows a similar reaction pathway and rate-determining step for the catalysts, which is consistent with reported results for other Mn-Co oxide based bifunctional catalysts.[143,225] These results suggest that the high activity of Mn/Co:2.5-CB for ORR may be due to the coexistence and synergistic effects of Mn oxide and Co oxide. As shown in Figure 3-14, there is improved ORR activity (Figure 3-14(A)) for the combined Mn oxide/Co oxide (Mn/Co:2.5-CB) relative to Mn oxide alone. The OER activity (Figure 3-14(B)) is improved for Mn/Co:2.5-CB compared with only Mn oxide alone. The overall bifunctional performance is superior for Mn/Co:2.5-CB compared with either Mn oxide or Co oxide.

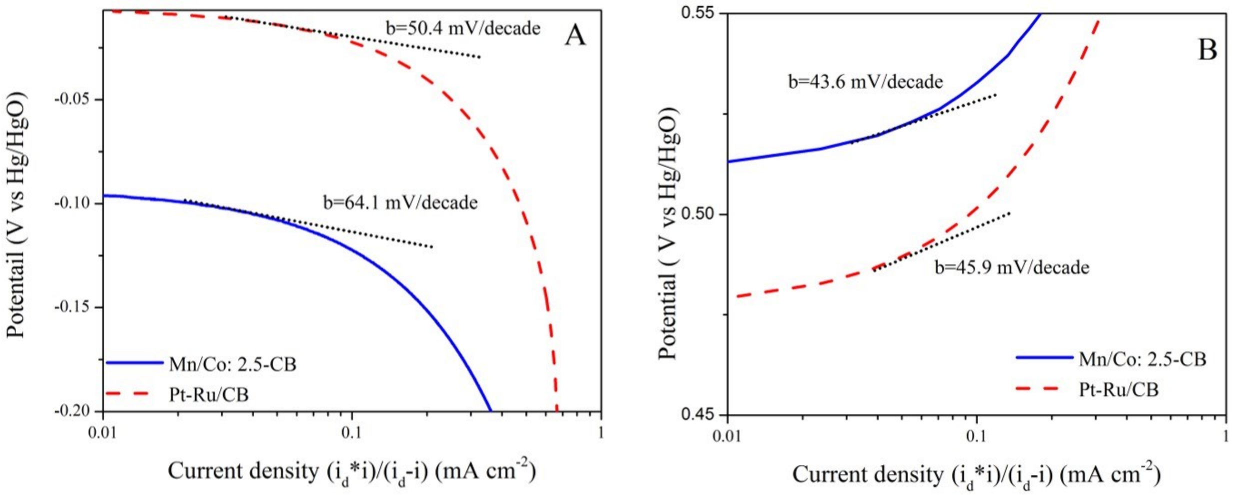

Figure 3-13 . (A) Tafel plots for Mn/Co:2.5-CB and Pt-Ru/CB derived from ORR voltammograms at 1600 rpm. (B) Tafel plots for Mn/Co:2.5-CB and Pt-Ru/CB derived from OER voltammograms at 1600 rpm.

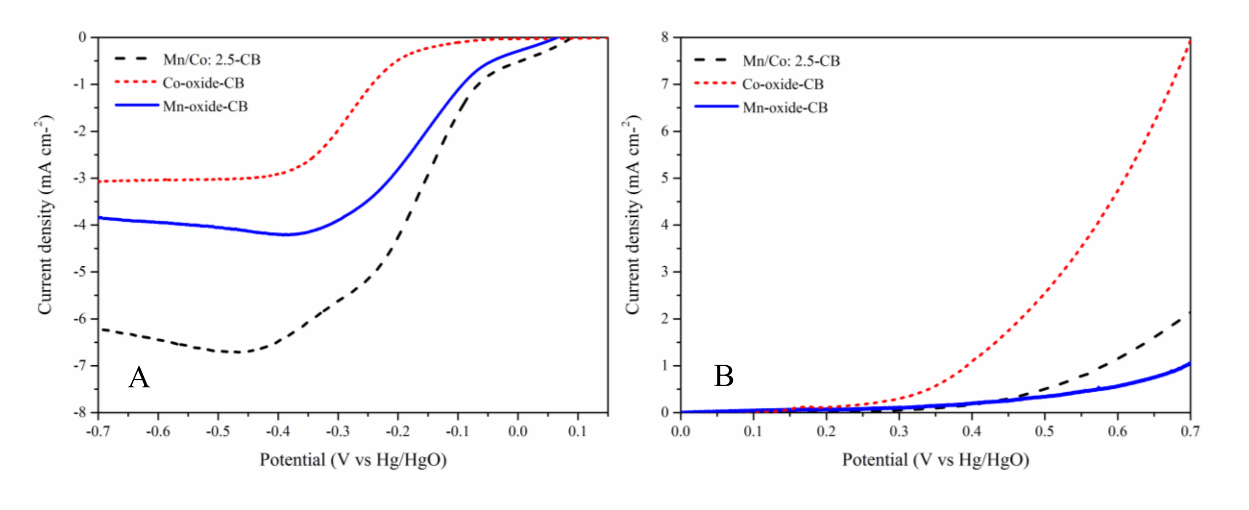

Figure 3-14 Comparison of LSV curves for (A) ORR and (B) OER for Mn/Co:2.5-CB, Co-oxide/CB and Mn-oxide-CB at 1600 rpm in 0.1 M KOH.

RDE measurements for bifunctional activity of the catalyst are not sufficient to predict performance of the catalyst, due to the low concentration of the electrolyte (0.1 M KOH) utilized, compared with the concentration usually employed in practical ZABs (6 M KOH). Therefore, it is necessary to evaluate the bifunctional activity in a full cell. The laboratory fabricated ZAB consists of an air electrode (GDL with deposited catalyst), a separator, a current collector and a Zn anode. During the charge-discharge process, the Zn/Zn^{2+} redox reaction and oxygen reduction/evolution occur on the anode and cathode, respectively. In this case, oxygen reduces via four electron transfer (based on K-L plot results) and the hydroxide ions react with Zn^{2+} to form zincate ions ($Zn(OH)_4^{2-}$). Zincate is soluble, but can be further dehydrated to ZnO, which is a white insulating powder and makes the rechargeability of ZABs more challenging. Other parasitic reactions also occur in rechargeable ZABs. For example, Zn metal could react with KOH at more negative potentials leading to hydrogen evolution and GDL corrosion. Furthermore, extended oxygen evolution during charging can damage the surface of the electrode and catalyst.[246] Therefore, the structural stability and long term bifunctional performance of the catalyst were examined through charge-discharge cycling in 6 M KOH.

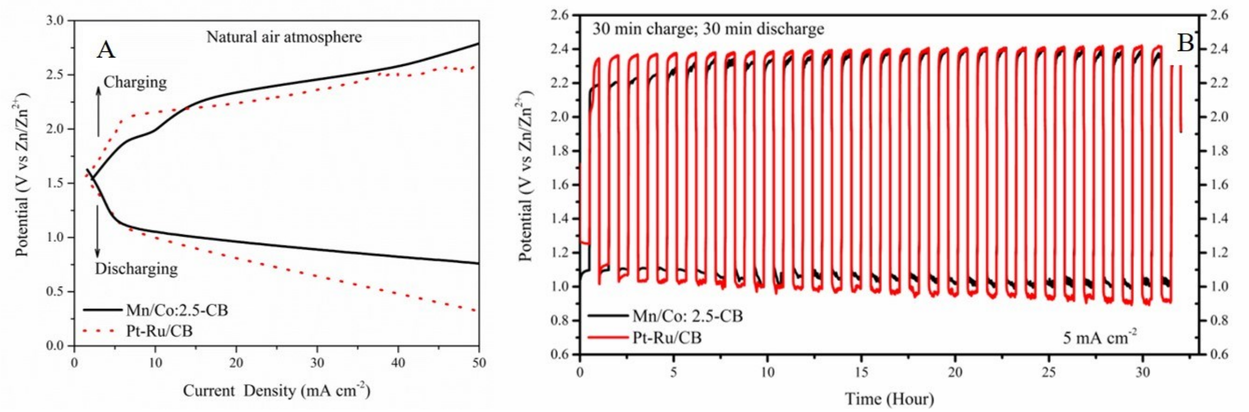

Figure 3-15 (A) Galvanodynamic discharge and charge polarization curves for Mn-Co:2.5-CB and Pt-Ru/CB consuming air under ambient conditions. (B) Galvanostatic pulse cycling of Mn/Co:2.5-CB and Pt-Ru/CB under ambient air conditions at a current density of 5 mA cm^{-2} for intervals of 1 h per cycle.

The Mn/Co:2.5-CB catalyst was evaluated as the air electrode by a galvanodynamic method (Figure 3-15 (A)). The results show that the open circuit potential is very close to that for Pt-Ru/CB (1.53 V). The charging performance of the catalyst is similar to the baseline catalyst and discharging out performs the Pt-Ru/CB catalyst. Galvanostatic charge-discharge experiments were also performed by discharging and charging (30 min for each cycle) for 30 h at 5 mA cm^{-2} (Figure 3-15(B)). Using the Mn/Co:2.5-CB catalyst as the air electrode, the initial potential gap between charge and discharge was about 1.09 V. The battery performance is similar to the results reported[116] (Table 3-4) in an earlier study using a similar technique for growing Mn-mixed oxide on carbon paper. The discharge potential dropped from 1.27 V to 1.19 V and the charge potential rose from 2.04 to 2.19 V, as measured after the 1st and 15th cycles, giving a 6.7% and 6.8% change in discharge and charge potentials, respectively.[116]For Mn/Co:2.5-CB in this work, after almost 30 cycles (30 h), the discharge potential decreased from 1.10 to 1 V and the charge potential increased form 2.18 V to 2.35 V, which gives 9% and 7.7% changes, respectively. The round-trip efficiency of the Mn/Co:2.5-CB catalyst is approximately 50.2% for the first cycle and decreases to 43.4% after 30 cycles. The round-trip efficiency dropped from 57.7% to 38.3% for baseline Pt-Ru/CB after 30 cycles. As mentioned above, in a ZAB performance degradation is not just limited to the air electrode. Corrosion of the carbon based-GDL during OER and Zn stripping and plating during charging and discharging also determine the overall performance and efficiency of the battery. Table 3-4 compares the ZAB battery performance of Mn/Co:2.5-CB with other recently reported catalyst materials. The long-term stability and activity of the Mn-Co oxide bifunctional catalyst shows that this structure outperforms the Pt-Ru/CB catalyst for both ORR and OER with a smaller charge-discharge potential gap after 30 h of cycling (1.33 V vs 1.48 V), which is promising for development of the air electrode for ZABs.

Table 3-4 Comparison of rechargeable ZAB with Mn/Co:2.5-CB as the ORR/OER catalyst with various non-precious metal catalysts in the recent literature.

Refs	**Materials**	**Initial charge potential (V)**	**Initial discharge potential (V)**	**Mass loading (mg cm^{-2})**
This work	Mn/Co:2.5-CB	2.19	1.10	1
This work	Pt-Ru/CB	2.20	1.23	1
247	a-MnO_2-$LaNiO_3$/CNTs	1.95	1.20	ND
116	MnO_2	2.04	1.27	1±0.1
150	$CoMn_2O_4$-N-doped-garphene	1.80	1.10	ND
206	Eggplant-derived microporous carbon sheets	2.20	1.23	ND

3.4 Summary

A facile route has been developed to synthesize high surface area Mn-Co oxide bifunctional catalysts directly grown on commercial carbon substrates using low-cost raw materials at mild temperature and ambient atmosphere. The catalyst demonstrates high activity towards ORR in 6 M KOH, exhibiting only 105 mV more negative onset potential, and higher kinetic current density, than the baseline Pt-Ru/C catalyst. In addition, Mn-Co oxide exhibits comparable catalytic activity at the optimized composition relative to Pt-Ru/CB. The catalyst has a smaller Tafel slope of 43.7 mV decade^{-1} for OER than that for Pt-Ru/C. A ZAB based on Mn-Co oxide electrodeposited on GDL demonstrates high stability during 30 h of charge/discharge cycling. The good performance of the catalyst is attributed to the mixed Mn oxide/Co oxide, which provides enhanced ORR and OER activity as well as a high density of defects as oxygen adsorption and desorption active sites. This approach opens up new avenues for developing other catalytic materials using transition metal oxides for future advanced energy conversion technologies.

4 Chapter 4: Synthesis and electrochemical performance of manganese nitride as an oxygen reduction and oxygen evolution catalyst for Zn-air secondary batteries

A version of this Chapter has been submitted to the journal of ACS Applied Materials and Interfaces.

E. Davari and D. G. Ivey, Synthesis and electrochemical performance of manganese nitride as an oxygen reduction and oxygen evolution catalyst for Zn-air secondary batteries, *Journal of Applied Electrochemistry,* **submission ID: JACH-D-17-00038**.

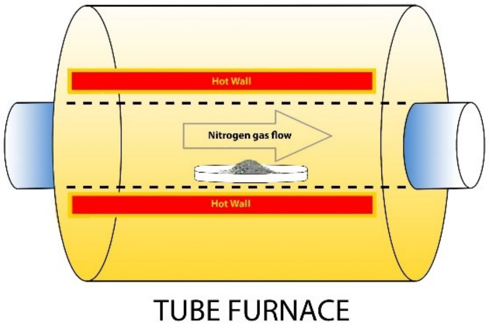

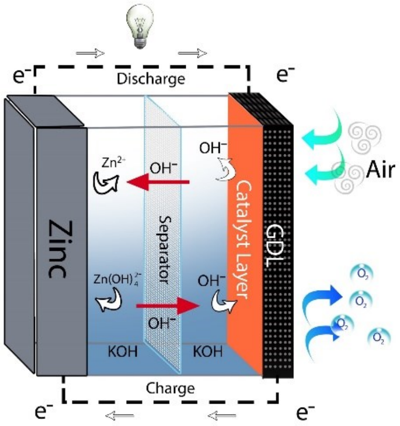

4.1 Introduction

During the past few decades, rechargeable metal-air battery technology has made significant progress towards commercialization. However, much more research needs to be done in many aspects of this promising alternative energy storage device in order to compete against traditional Li-ion batteries. Of the various types of metal-air batteries, ZABs have received broad attention due to their low cost, safe operation and environmentally friendly nature.[2,3,9,22] One of the most crucial factors limiting the performance of rechargeable ZABs is the slow kinetics of ORR and OER at the air electrode. In general, ORR can proceed either through a two-step, two-electron process with the formation of hydrogen peroxide ions as the intermediate or a more desirable four-electron process.[27,221,222] The most efficient bifunctional electrocatalysts are Pt and Ir/Ru and their alloys. However, their high cost and scarcity have motivated the development of non-precious metal electrocatalysts.[89] Non-precious metal catalysts, such as transition metal oxides (spinels and perovskites)[114,115,225,248,249], carbon-based materials[66,200,250–252] and metal-nitrides[253–259] have been investigated widely as less expensive alternatives to Pt- and Ir/Ru-based catalysts.

The interest in the M_xN_y (M= Mn, Fe, Ni, Co, W, Mo, Ti) transition metal nitrides is increasing due to their unique electronic and magnetic properties. Nitrides are categorized in three different groups, based on the electronegativity difference between nitrogen and the metal and the atomic radius size, as: 1) interstitial nitrides, 2) covalent nitrides and 3) intermediate nitrides. Late transition metals (Group VII and VIII), including Mn-N, form nitrides with an intermediate structure similar to intermediate carbides.[260] Metal nitrides have potential applications as magnetic recording materials, spin carriers in spintronics[261] and catalysts used for batteries and water splitting.[262–265] Carbon supported tungsten nitride (W_2N/C) was investigated in a proton exchange membrane (PEM) fuel cell setup, where significant activity and stability after 100 h of operation was observed.[266] Xia et al[262] demonstrated the catalytic activity of carbon supported molybdenum nitride (MoN/C) catalysts, synthesized using an ammonia heat treatment procedure. The effective reduction of oxygen by a four-electron pathway to produce water was reported. Titanium nitride (TiN) and oxynitrides (TiO_xN_y) have recently been investigated as electrocatalysts and catalyst support materials, particularly for ORR [257–259,263,264,267–269]. ORR active $TiC_{0.21}N_{0.01}O_{1.88}$ catalysts were synthesized in a study by Chisaka et al.[264] It was shown that ORR active sites were created in the rutile-TiO_2 lattice. The oxygen defects on the reduced rutile (110) plane were reported to be active towards the dissociation of oxygen adsorbed on the surface.[265] The study by Ohinishi et al.[263] suggested that the surface of TiN was partially oxidized after exposure to air and the active sites for ORR could be oxygen vacancies, which presumably facilitate the adsorption of oxygen molecules. Nonetheless, the ORR activity and the role of the amount of nitrogen in metal nitrides/oxynitrides has not been extensively studied.

Previous studies on Mn-N based materials as active ORR catalysts[270,271] have led to our interest in synthesizing manganese nitride (Mn-N) as a potential bifunctional catalyst in ZABs for the first time. Manganese nitrides have unique magnetic properties. There are four stable phases (ε, η, ζ and θ) in the Mn–N binary system. The ε phase (Mn_4N) has a face centered cubic (fcc) structure with 18-22 at.% nitrogen. The ζ phase ($Mn_6N_{2.58}$) has a hexagonal closed packed (hcp) structure with 8-36 at.% nitrogen. The η (Mn_3N_2) and θ phases (MnN) form face centered tetragonal (fct) structures with 38-41 at.% and 46-49 at.% nitrogen, respectively. θ, η and ζ are antiferromagnetic, while ε is a ferromagnetic compound.[272,273] Due to the diversity in the number of phases and their magnetic properties, Mn-nitrides have potential applications in spintronics.[274,275] They can be prepared by reacting N_2 or NH_3 with Mn powder at high temperatures.[272,273,276,277] Other methods, such as reactive sputtering[277] and molecular beam epitaxy,[274] have also been studied.

Herein, a mixture of two Mn-N phases, the ε phase (Mn_4N) and ζ phase ($Mn_6N_{2.58}$), has been synthesized by annealing Mn powder in 99.998% N_2 at 1100 °C. The bifunctional activity of CB supported Mn-N (Mn-N/CB) was tested using CV and LSV techniques. Although Mn-N powder is coarse, i.e., micron size particles, the bifunctional activity is comparable to the baseline nanopowder Pt/C and superior to MnO commercial catalysts in alkaline media. Furthermore, Mn-N/CB shows excellent stability during repeated charge-discharge cycling in a ZAB.

4.2 Experimental

4.2.1 Chemicals and synthesis method

Manganese metal flakes were obtained from Acros Organics with purity of 99+%. The powder (40 mesh = 400 μm) was manually ground using a pestle and mortar and passed through a 63 μm SS sieve (No. 230). The powder was placed in a SiO_2 crucible and then into a tube furnace (Lindberg/Blue M). Before nitridation, N_2 gas was passed through the tube for 15 min. Afterwards, three different samples were prepared by heating the Mn powder to 1100 °C at a heating rate of 5 °C min^{-1} for 4 h, 10 h and 30 h with a continual supply of pure N_2 gas (99.998%). The samples are hereafter referred to as Mn-N-4, Mn-N-10 and Mn-N-30 (the last number represents the annealing time). After reaction, the furnace was shut off, allowing the temperature to slowly decrease (cooling rate was ~5°C min^{-1}) to room temperature. The flow of forming gas was maintained during cooling to minimize oxidation of the nitride powder.

4.2.2 Materials characterization

Phase analysis was done using XRD. XRD patterns were recorded at a scan rate of 1° min^{-1} on a Rigaku Geigerflex 2173 system with CoK$_\alpha$ radiation (λ= 0.178797 nm) as the source. Phase quantification was done through Rietveld refinement of the XRD data using General Structure Analysis System (GSAS-EXPEGUI) software. The morphology and composition of the sample were investigated using a Tescan Vega-3 SEM and a JEOL 2010 TEM. Details about SEM and TEM operation and sample preparation are provided in Section 3.2.5. It was suspected that there would be some oxidation during Mn nitride fabrication, so composition depth profiling was performed with a time-of-flight, secondary ion mass spectrometer (TOF-SIMS - ION-TOF GmbH). The analytical Bi$^+$ ion source was operated at 25 kV with Cs$^+$ ions as the sputter source. Secondary ions were collected from a 150 µm × 150 µm area.

4.2.3 Electrochemical half-cell testing

Electrochemical half-cell testing included CV and LSV, using a RDE setup (Pine Instruments Co., AFMSRCE). These tests were performed using a potentiostat (Bio-logic® SP-300) with a typical three electrode system. The catalyst ink and the GC electrode (working electrode) preparation methods can be found in Section 3.2.3. The baseline catalyst used in this study was 40 wt% Pt/C. The ORR onset potential was determined as the potential corresponding to a current density of 25 µA cm^{-2}. Section 3.2.3 includes the specifics of the half-cell set up (reference and counter electrodes) and the details for calculation of the number of electrons transferred (K-L plots).

The stability of the catalyst for ORR and OER was investigated by extended cycling in an O_2-saturated electrolyte. CV tests were performed from -0.7 to 0.7 V vs. Hg/HgO for 1500 cycles. CV testing was perfomed at a higher scan speed (100 mV s^{-1}) due to the long term nature of the experiment (~12 h). In an effort to minimize error caused by the resistance of the electrolyte (iR), corrections were made for all experiments using Equation 1:

$$E_{true} = E_{measured} - iR_u \qquad \text{Equation 1}$$

where i is the cell current and R_u is the uncompensated resistance (determined from electrochemical impedance spectroscopy (EIS) measurements). $E_{measured}$ is the measured potential and E_{true} is the iR-corrected potential.

4.2.4 ZAB electrochemical analysis

The working electrode, catalyst ink and ZAB set-up were prepared using the same techniques discussed for the preparation of the 40 wt% Pt-Ru catalyst in Section 3.2.4. In this study, a surfactant coated, microporous monolayer PP membrane (Celgrad® 5550) was used as the separator between the two Ni plates (current collectors) in the ZAB set up. Galvanostatic charge-discharge cycling was done at various current densities in a 6 M KOH electrolyte. Long-term charge-discharge cycling was done using an applied current of 35 mA (7.5 mA cm^{-2}), with each cycle consisting of 30 min discharge followed by 30 min charge for 14 cycles (14 h).

4.3 Results and discussion

4.3.1 Microstructural characterizations

The morphology of nitrided Mn (Mn-N) particles was analyzed using SEM plan view secondary electron (SE) imaging. Since the morphology was very similar for all Mn-N samples prepared, images are only presented for Mn-N-10 (Figure 4-1). Irregular shaped particles with different sizes (<100 µm) were observed. Every particle consists of several grains with an average grain size of ~1.7 µm. Grain and particle size were determined using image processing software.

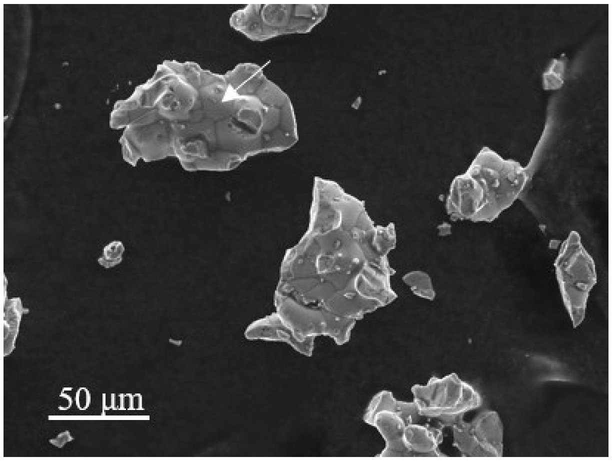

Figure 4-1 SEM SE image of Mn-N-10 sample (the arrow points to an individual grain).

SEM/EDX mapping was performed on the same sample. Elemental maps for Mn, O, N and Si are shown in Figure 4-2(B-E). Si was chosen, in addition to the other elements, because of suspected contamination from the silica crucible. Manganese and N are uniformly distributed throughout the sample, suggesting that Mn nitride formation has been successful. Oxygen is also present everywhere, but is more concentrated in Si-rich regions. This will be discussed in subsequent paragraphs.

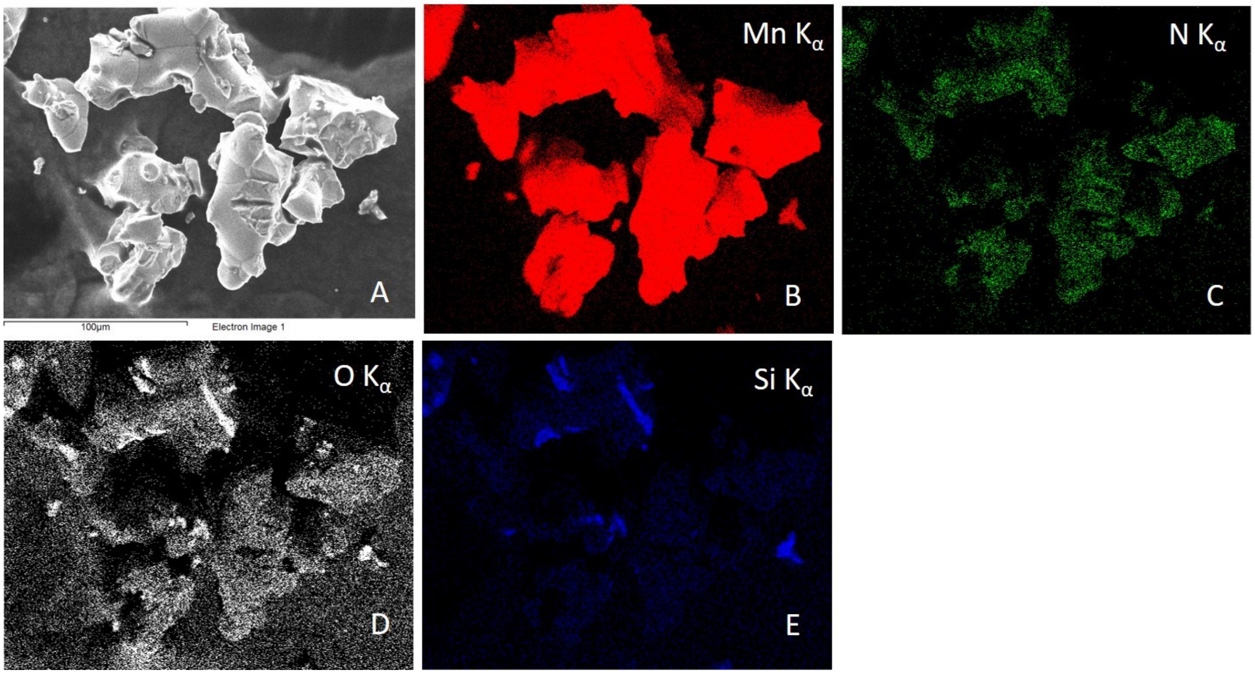

Figure 4-2 (A) SEM SE image of the Mn-N-10 sample. (B-E) EDX elemental maps showing Mn, N, O and Si distributions.

Figure 4-3 shows an XRD pattern for the ground Mn powder, prior to annealing, along with patterns from the three Mn-N samples annealed for 4 h, 10 h and 30 h. The metallic Mn pattern was indexed to α-Mn (JCPDS card #32-0637) with a space group of $I\bar{4}3m$. The calculated lattice parameter is a=0.891 nm, which is close to the nominal value. The peaks from the XRD patterns for the annealed samples can be ascribed to five separate phases, i.e., cubic Mn_4N (JCPDS card #089-3704), hexagonal $Mn_6N_{2.58}$ (JCPDS card #071-0200), orthorhombic $MnSiN_2$ (JCPDS card #083-1967), cubic MnO (JCPDS card #007-0230) and orthorhombic Mn_2SiO_4 (JCPDS card #019-0788). Clearly some impurity phases formed during annealing. MnO is likely due to reaction with residual oxygen in the furnace; qualitatively, the amount increases significantly for the 30 h anneal.

Mn_2SiO_4 and $MnSiN_2$ are due to reaction between the sample and SiO_2 crucible during nitridation. Only small amounts of Mn_2SiO_4 were found for the shorter annealing times; $MnSiN_2$ was only detected for the Mn-N-30 sample (30 h anneal).

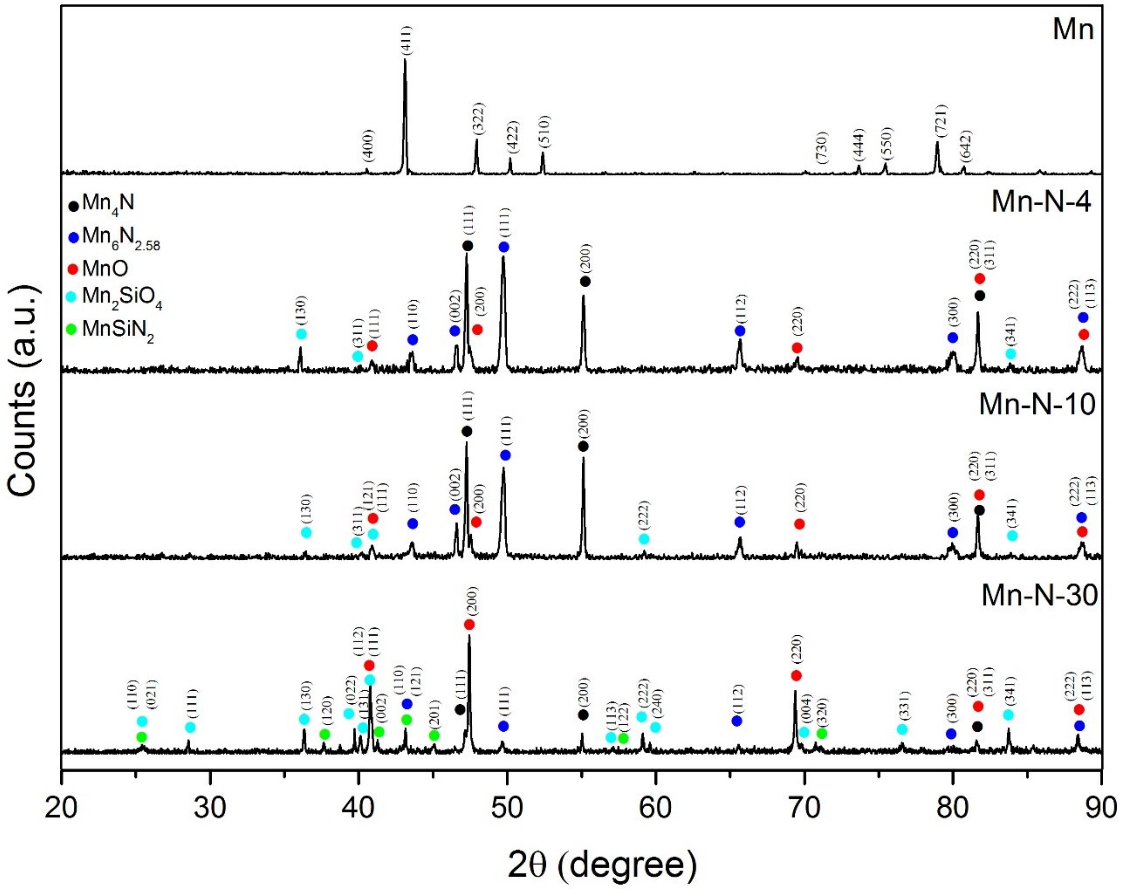

Figure 4-3 XRD patterns for Mn powder, Mn-N-4, Mn-N-10 and Mn-N-30 samples.

Phase quantification for the annealed sample was performed using Rietveld-based fitting. Four phases, Mn_4N, $Mn_6N_{2.58}$, MnO and $MnSiO_4$, were used for Rietveld refinement of the Mn-N-4 and Mn-N-10 samples. The same four phases, plus $MnSiN_2$, were used for refinement of the Mn-N-30 sample. The observed XRD patterns and the calculated XRD patterns, as well as the difference (between observed and calculated) plots, are shown for the three samples in Figure 4-4. The fit between the observed and calculated diffraction patterns is quite good with $\chi^2 = 2.1$-2.7 for all patterns. χ^2 is the reliability factor, which provides a measure of the fit; the closer χ^2 is to zero the better the fit. Tables 4-1, 4-2 and 4-3 summarize the quantification results, showing calculated lattice parameters and densities of each phase after refinement. The amount of nitride phases (Mn_4N and $Mn_6N_{2.58}$) for Mn-N-4 and Mn-N-10 is significantly higher than for Mn-N-30 (~75-

77% vs. ~8%). The amounts of MnO, Mn_2SiO_4 and $MnSiN_2$ are quite high for Mn-N-30, which is due to the long annealing time (30 h) and contact time with the silica boat and any residual oxygen in the tube furnace. The calculated densities and lattice parameters of the phases (Tables 4-2 and 4-3) show a reasonable match with standards derived from the Powder Diffraction Database.

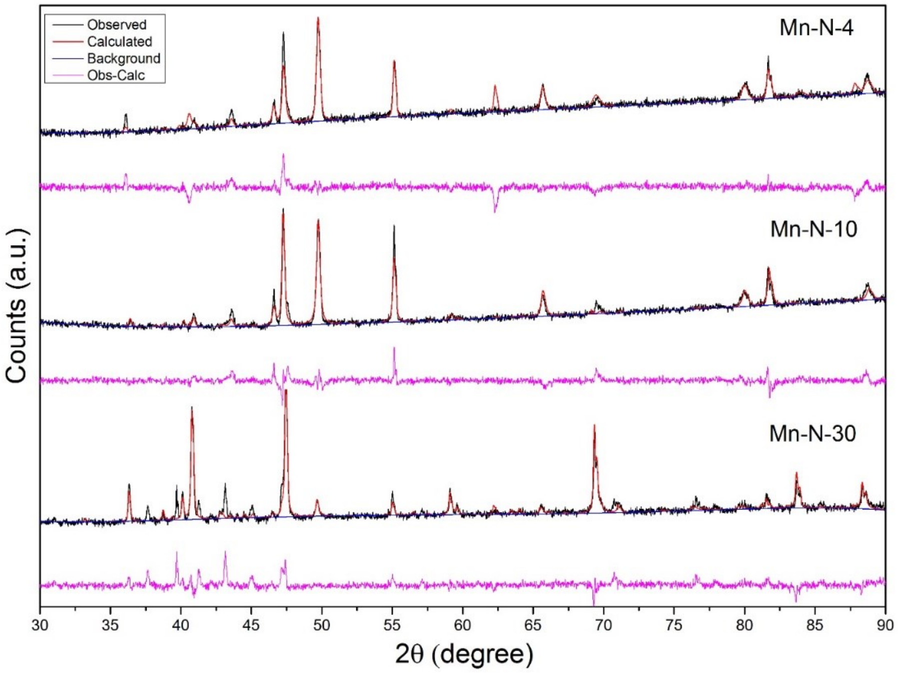

Figure 4-4 Rietveld refinement plots for Mn-N-4, Mn-N-10 and Mn-N-30 samples. The experimental and calculated intensity data are plotted as black and red lines, respectively, and the difference plot (I_{exp}-I_{cal}) is shown below (magenta line).

Table 4-1 Phase quantification for Mn-N-4, Mn-N-10 and Mn-N-30 using Rietveld analysis.

	Phase fraction (wt.%)		
	Mn-N-4	**Mn-N-10**	**Mn-N-30**
Mn_4N	**52.7**	**47.1**	**5.8**
$Mn_6N_{2.58}$	**24.3**	**27.6**	**2.4**
MnO	**15.7**	**19.5**	**38.2**
Mn_2SiO_4	**7.2**	**5.8**	**30.4**
$MnSiN_2$	**NA***	**NA**	**23.2**

*Not applicable

Table 4-2 Calculated lattice parameters and standard values for Mn-N-4, Mn-N-10 and Mn-N-30 using Rietveld analysis.

	Lattice parameters (nm)			
	Mn-N-4	Mn-N-10	Mn-N-30	Database values (nm)*
MnO	a= 0.442	a= 0.445	a= 0.444	a= 0.444
Mn_4N	a= 0.387	a= 0.387	a= 0.387	a= 0.384
$Mn_6N_{2.58}$	a= 0.482 c= 0.453	a= 0.482 c=0.452	a= 0.482 c= 0.452	a= 0.489 c= 0.455
Mn_2SiO_4	a= 0.622 b= 0.107 c= 0.490	a= 0.6.23 b= 0.10.7 c= 0.489	a= 0.626 b= 0.106 c= 0.49	a= 0.622 b= 0.105 c= 0.487
$MnSiN_2$	NA	NA	a= 0.526 b= 0.651 c= 0.507	a= 0.524 b= 0.651 c= 0.507

*These values were obtained from the Powder Diffraction Database.

Table 4-3 Calculated (Rietveld analysis) and reference phase densities for Mn-N-4, Mn-N-10 and Mn-N-30.

	Phase densities (g cm^{-3})			
	Mn-N-4	Mn-N-10	Mn-N-30	Standard values* (g cm^{-3})
MnO	5.4	5.3	5.3	5.3
Mn_4N	6.6	6.7	6.6	6.8
$Mn_6N_{2.58}$	7.5	7.5	6.6	6.4
Mn_2SiO_4	4.1	4.1	4.1	4.1
$MnSiN_2$	NA	NA	4.2	4.2

*These values obtained from the Powder Diffraction Database; NA: not applicable.

Further microstructural characterization was done using TEM analysis. A TEM sample was prepared from the Mn-N-10; this sample was chosen, as it exhibited the best overall electrochemical performance as discussed later in this chapter. BF images from two different nitride particles are shown in Figure 4-5. The particles are <800 nm in size. Selected area diffraction (SAD) patterns and EDX spectra were taken from the regions indicated. The EDX spectra (Figure 4-5(E-F)) indicate the presence of both O and N, as well as Mn. This is more clear from the insets showing expanded views of the low energy range. The O peak forms as a shoulder on the Mn L peak. The SAD patterns in Figures 4-5 (C-D) are both spot patterns, which indicate a single phase and single crystals. The implication, then, is that Mn has formed a ternary phase with O and N during annealing; however, the diffraction patterns could not be indexed to any known Mn oxynitrides. In addition, no Mn oxynitrides were identified in the XRD analysis. The diffraction patterns in Figure 4-5(C-D) could be indexed to the two nitrides identified through XRD, i.e., Mn_4N (zone axis = [001]) and $Mn_6N_{2.58}$ (zone axis = $[1\bar{1}0]$), respectively. SAD patterns were obtained (not shown here) from other particles containing Mn, O and N, and these could be indexed to the same two nitrides as well.

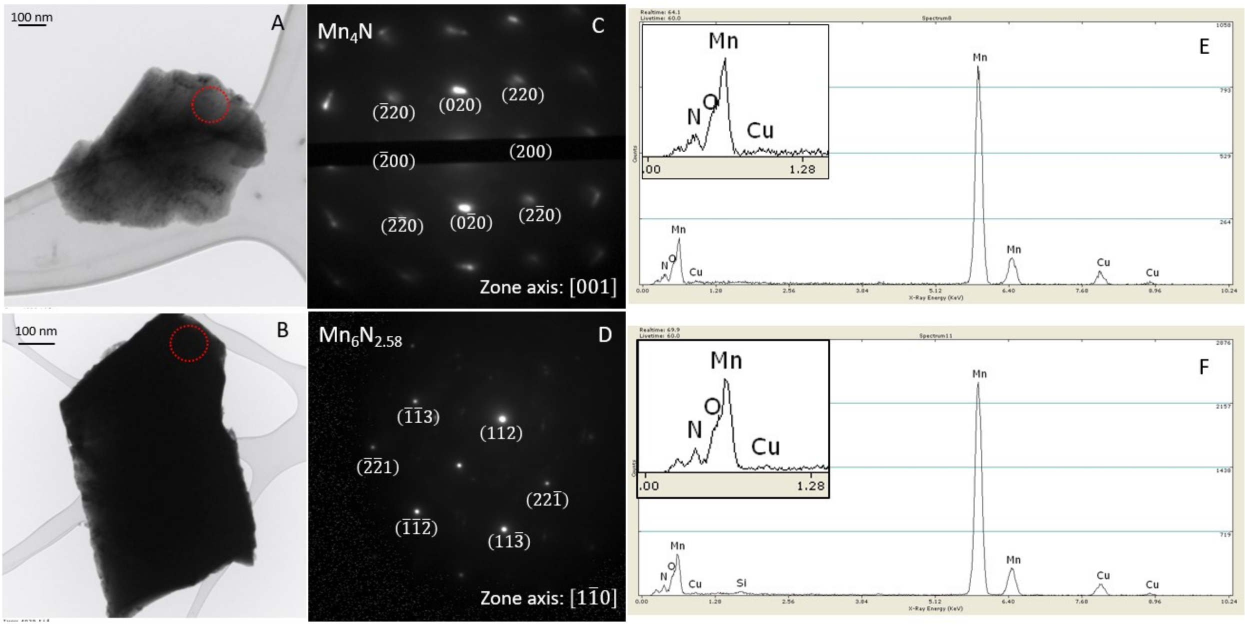

Figure 4-5 (A, B) TEM bright field (BF) images from two separate particles of Mn-N-10. (C, D) SAD patterns from the respective circled regions in A and B. (E, F) EDX spectra from the same regions as the SAD patterns in C and D (insets represent magnified O/N region.

In an attempt to explain the apparent conflicting results, the crystal structures for Mn_4N, $Mn_6N_{2.58}$ and MnO were examined and compared. These structures are shown in Figure 4-6. MnO has a cubic, NaCl-type structure, with Mn occupying the fcc positions and O occupying all the octahedral sites (Figure 4-6(A)). Mn_4N also has a cubic structure; in fact, the two structures are quite similar. Mn also occupies fcc positions, like MnO, but N is only located in the central octahedral site (½, ½, ½) (Figure 4-6(B)). The lattice parameters for the two pure phases are 0.445 nm for MnO and 0.385 nm for Mn_4N. It is conceivable that Mn_4N, which formed from Mn and N_2 gas, was partially oxidized during annealing and subsequent cooling to room temperature. Residual oxygen in the furnace likely diffused into the Mn_4N lattice structure, filling some of the vacant octahedral sites.

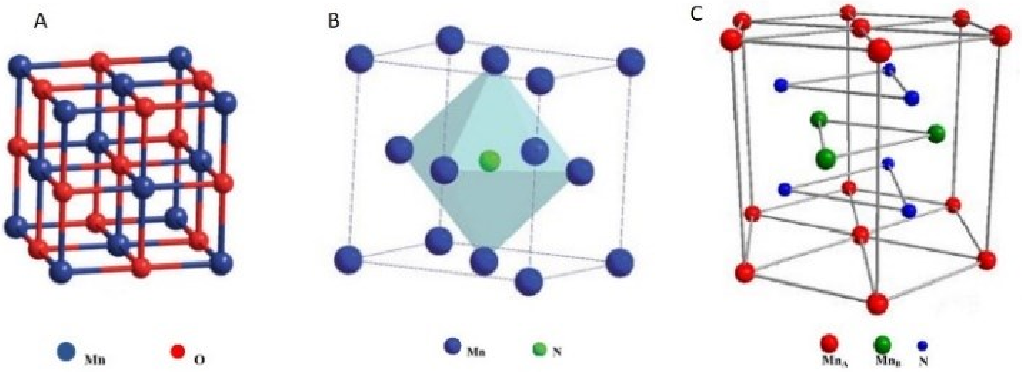

Figure 4-6 Crystal structures for A) MnO[225], B) Mn_4N[278] and C) $Mn_6N_{2.58}$.[279]

If O is indeed incorporated into the octahedral sites of Mn_4N, the effect on the lattice needs to be considered. There are two ways to calculate the size of the octahedral sites. One way is by assuming that the Mn atoms are in contact along <110> directions. This gives a Mn atom size of 0.136 nm (which is close to the size usually given for neutral Mn of ~0.140 nm[280]), based on a lattice parameter of 0.385 nm, and an octahedral site radius of 0.0565 nm. The atomic radius for N is ~0.065 nm[280], which is larger than the interstitial site. The other way of calculating the octahedral site size is to assume that Mn and N atoms are in contact along the <001> direction through the center of the cell and use the value of 0.065 nm for the N radius. In this case, the Mn radius is 0.128 nm and the interstitial site radius is equal to 0.065 nm. The actual case is likely somewhere between the two extremes, i.e., the octahedral sites have a radius between 0.0565 nm and 0.065 nm. Interestingly, the atomic radius of O is ~0.060 nm[280], which is within the range of the interstitial site size. As such, it is conceivable that limited amounts of oxygen could be accommodated by the Mn_4N lattice, without having much effect on the lattice parameter. Therefore, the Mn_4N phase detected by XRD is effectively a pseudobinary phase, i.e., $Mn_4(N_{1-x}O_x)$ with $0 \le x \le 1$, with approximately the same lattice parameter as Mn_4N. This explains the oxygen detected in the TEM EDX spectra for Mn-N-10 particles, where the electron diffraction patterns were indexed to Mn_4N (Figure 4-5C and 4E).

At some critical concentration of oxygen incorporated in Mn_4N, the structure would essentially change to that for MnO (Figure 4-6(A)). This is related to changes in the bonding between Mn and O; moving away from metallic/covalent in nature towards more ionic. Assuming that Mn and O are in their ionic forms, i.e., Mn^{2+} and O^{2-}, and that the ionic radius for O^{2-} is ~0.140 nm[281], the Mn^{2+} ion radius can be calculated. For the MnO structure, the ions are in contact along <001> directions, so the Mn^{2+} ions have a radius of 0.0825 nm. The ionic radius for Mn^{2+} is often given as 0.070 nm[281], which is relatively close to the calculated value. The discrepancy is likely due to the fact that the bonding in MnO is not entirely ionic. The phase is a pseudobinary corresponding to $Mn(O_xN_{1-x})$ with $0 \leq x \leq 1$, and contains large amounts of oxygen, but still some nitrogen. The lattice parameter would be close to that of MnO. This phase was not detected by TEM analysis of the Mn-N-10 sample, but this may just be a sampling phenomenon. The Mn-N-10 sample has ~20% MnO, based on the Rietveld analysis of the XRD pattern, but the volume of material examined in the TEM is extremely small relative to the overall sample volume.

A similar argument can be made regarding $Mn_6N_{2.58}$. $Mn_6N_{2.58}$ has a hexagonal structure (Figure 4-6(C)), with Mn occupying the hcp positions and N occupying some of the octahedral positions (<50% are filled; if all were filled, the Mn/N ratio would be 1 instead of 2.33). As with Mn_4N, some O could go into vacant interstitial positions or even replace N in the positions. This has, in fact, been reported by Meng et al.[279], who have shown doping of $Mn_6N_{2.58}$ with O, with amounts up to ~14 at%, forming the pseudobinary phase $Mn_2(N_{0.74}O_{0.12})$. They confirmed, through XPS, that oxygen partially substituted for nitrogen in the octahedral positions and did not form a separate Mn oxide phase. Using the above arguments, the XRD and TEM results can be reconciled. The three major phases are Mn_4N, $Mn_6N_{2.58}$ and MnO, although none of these phases are pure, containing both N and O.

To further corroborate the discussion in the preceding paragraphs, SIMS depth profiles were performed on the Mn-N-10 sample (Figure 4-7). During depth profiling, a pulsed primary ion beam was used to desorb ionized species from the surface. The resulting ions were accelerated into a mass spectrometer, where they were analyzed by measuring the time to travel from the surface of the sample to the detector. A relatively large region was sampled (~150 μm by 150 μm), with MnO^- and MnN^- fragments sputtered from the surface to identify regions containing O and N, respectively. Figures 4-7(A-B) show the MnO^- and MnN^- images from the surface, prior to sputtering. Clearly, O is present everywhere across the surface, as is N but in lower concentration. It was possible to isolate SIMS data from specific particles (e.g., Figures 4-7(C-D)) and to extract depth profiles from those particles. The depth profiles for MnN^- and MnO^-, shown in Figure 4-7(E), are from the particles shown in Figure 4-7(C-D). The surface is O-rich and N-deficient, with the O concentration decreasing and N concentration increasing with increasing depth up to a depth of ~40 nm from the surface. This depth is approximate and was estimated from the sputtering rate. The concentrations for both O and N then level off at deeper depths from the surface. The oxidation of the particle surfaces agrees with our previous discussion based on the XRD and TEM results.

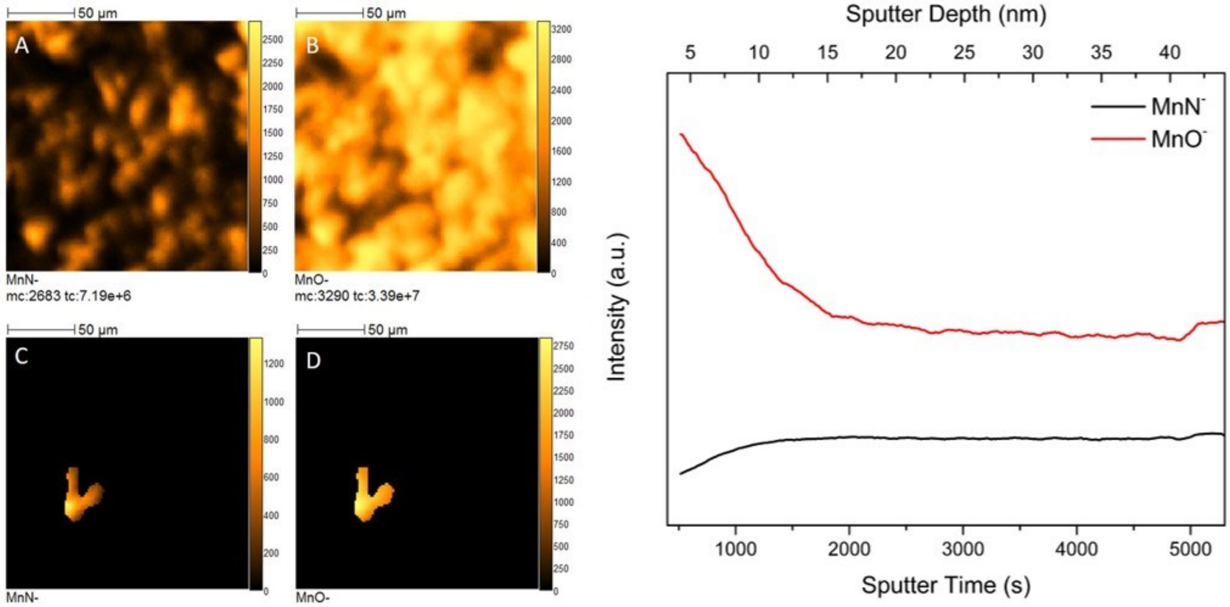

Figure 4-7 (A, B) Representative SIMS MnN^- and MnO^- images from Mn- N-10. The depth profile in (E) is from the particle shown in C and D.

In addition, previous literature on the Mn-N system report the formation of a thin MnO layer on Mn-N.[272,273,282] Vempaire et al[49] used plasma-based ion implantation to synthesize Mn_4N by implanting nitrogen in Mn layers deposited by sputtering assisted multi-dipolar microwave plasma. After implantation, according to XRD and XPS analysis, a thin layer of MnO (~20 nm) formed. Zi et al[39] detected trace amounts of MnO, which they ascribed to the oxide impurities in the precursor and relatively poor vacuum before nitridation.[273]

4.3.2 Electrochemical cahractrizations

To investigate the catalytic performance of the Mn-N samples, CV and LSV were used. CB (Vulcan XC-72) was added as a support material to increase the conductivity of the catalyst (Mn-N/CB). CV curves were recorded in both Ar- and O_2-saturated 0.1 M KOH from -0.7 V to 0.7 V vs. Hg/HgO (Figure 4-8). ORR peaks are located at -0.142 V, -0.136 V and -0.212 V vs. Hg/HgO for Mn-N-4/CB, Mn-N-10/CB and Mn-N-30/CB, respectively. The sharp peak present at 0.7 V vs. Hg/HgO for all the samples represents OER for both O_2- and Ar-saturated 0.1 M KOH. Well-defined CV peaks for both OER and ORR demonstrate the bifunctional activity of Mn-N/CB. Also, according to the CV curves, Mn-N-10/CB has the most positive ORR peak potential of the three samples.

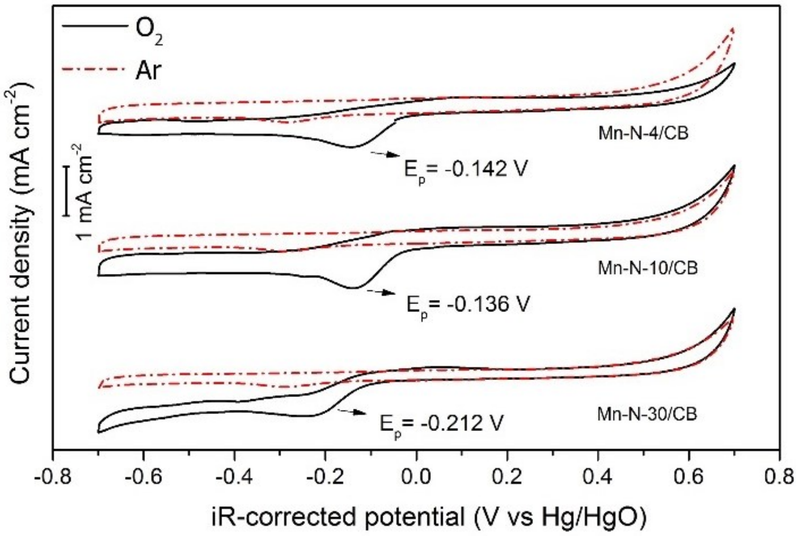

Figure 4-8 CV curves for Mn-N-4/CB, Mn-N-10/CB and Mn-N-30/CB in both O_2- and Ar-saturated 0.1 M KOH at a scan speed of 10 mV s^{-1}.

To further study the ORR-OER catalytic activity, LSV curves were obtained at 1600 rpm using an RDE set-up. As discussed earlier in the chapter, the surfaces of the particles are oxygen-rich with some nitrogen, i.e., mostly MnO. Therefore, it is of interest to determine whether the catalytic activity is due to the presence of MnO or if nitrogen plays a role. Since no commercially pure Mn nitride powder was available, comparison was only made between the as-fabricated material and commercially available MnO (≥99.99% purity - purchased from Sigma-Aldrich). MnO was the binary oxide detected through XRD analysis. LSV curves for 40 wt% Pt/C were also obtained as a baseline catalyst for comparison.

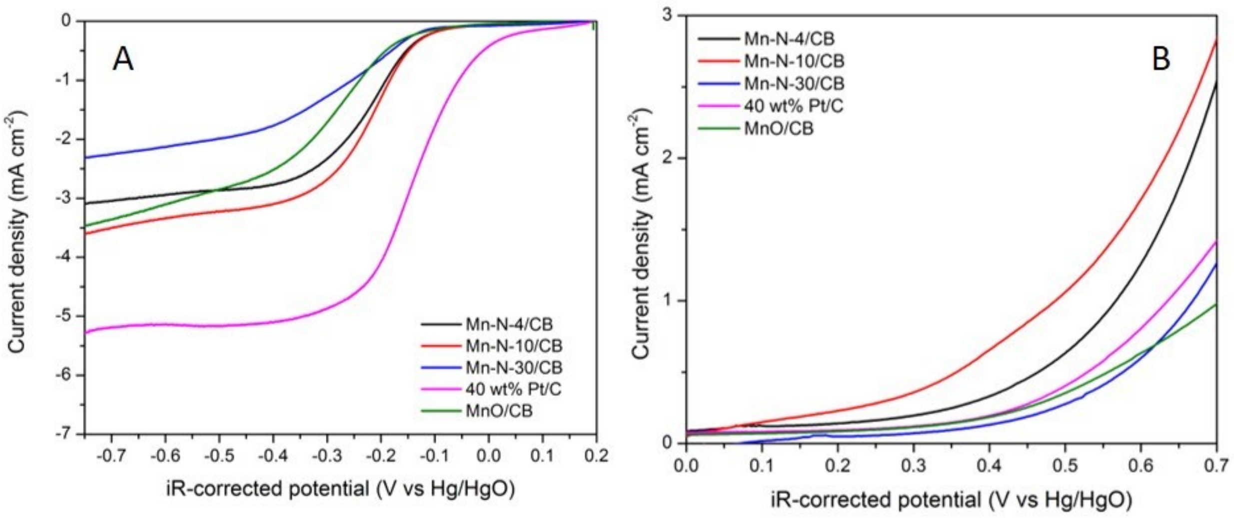

Figure 4-9 (A) ORR LSV curves for Mn-N-4/CB, Mn-N-10/CB, Mn-N-30/CB, Pt/C and MnO/CB samples in O_2-saturated 0.1 M KOH. (B) OER LSV curves for Mn-N-4/CB, Mn-N-10/CB, Mn-N-30/CB, Pt/C and MnO/CB samples in Ar-saturated 0.1 M KOH. The tests were done at 1600 rpm and a scan speed of 10 mV s^{-1}.

Table 4-4 Summary of oxygen electrode ORR-OER performance.

Samples	**ORR onset potential (V vs Hg/HgO)**	**ORR current density at -0.7 V (mA cm^{-2})**	**OER current density at 0.7 V (mA cm^{-2})**	**Average n**
Mn-N-4/CB	-0.078	-3.04	2.51	3.33
Mn-N-10/CB	-0.038	-3.52	2.81	3.62
Mn-N-30/CB	-0.173	-2.25	0.96	3.22
MnO/CB	-0.091	-3.37	1.24	2.98
Pt/C	0.119	-5.19	1.39	3.68

As shown in Figure 4-9(A) and summarized in Table 4-4, the ORR onset potential for Mn-N-10/CB is the most positive among the Mn-N/CB samples, which is consistent with the CV results. Also, Mn-N-10/CB shows a slightly higher ORR current density and more positive onset potential than MnO/CB. The ORR onset potential for Mn-N-10/CB is only 157 mV more negative than the baseline catalyst (Pt/C). These results are comparable with those recently reported for Mn-oxynitride, which has ~100 mV more negative onset potential than Pt/C.[270] The limiting current density, which is another important factor for assessing catalyst performance, is also compared in Table 4-4. For Mn-N-10/CB, the limiting current density is higher (3.52 mA cm^{-2}) than that for

MnO (3.37 mA cm^{-2}), Mn-N-4/CB (3.04 mA cm^{-2}) and Mn-N-30/CB (2.25 mA cm^{-2}). The limiting current density for Mn-N-10/CB is also higher than that previously reported for the Mn-oxynitride ORR catalyst[270] in O_2-satuarted 1 M KOH solution (~2 mA cm^{-2}). The ORR performance of Mn-N-10/CB still, however, falls short of the performance for Pt/C. However, the OER current density was also obtained at 0.7 V vs. Hg/HgO for all samples; Mn-N-10/CB had the highest current density (Figure 4-9(B)).

The OER and ORR combined results show good bifunctional performance for Mn-N-10/CB with lower overpotential for ORR and OER compared with the other Mn-N/CB samples. The relatively poor OER performance for the Pt/C catalyst is explained in the study by Reier et al.[283] During OER a poorly conductive Pt oxide species covers the surface of the catalyst. Therefore, the electrons released during OER have to tunnel through the oxide layer resulting in a lower current density, which is dependent on the oxide layer thickness. As reported in earlier studies[22,267], MnO suffers from limited electronic conductivity, large volume change and rapid capacity decay upon cycling, so its relatively poor ORR-OER performance is not unexpected. The high concentration of MnO (~50%), along with the $MnSiO_4$/$MnSiN_2$ impurities phase (~40%), is responsible for the inferior bifunctional performance for Mn-N-30/CB vs. Mn-N-4/CB and Mn-N-10/CB. The poorer ORR performance for Mn-N-4/CB and Mn-N-10/CB relative to the baseline catalyst (Pt/C) may be due to the surface oxide, which is a poor electronic conductor and inhibits electron transport.[269] Furthermore, it is worth noting that bifunctional catalytic performance is highly influenced by the surface area. The Mn-N/CB catalyst studied here has a much larger particle size (several microns) (Figure 4-1) than the nanoscale Pt/C catalyst. Therefore, ORR performance may be improved by limiting the amount of MnO formation (i.e., increasing the N/O ratio at the surface), which requires better vacuum control during nitridation of Mn powder, and reducing the catalyst particle size.

Further electrochemical analysis was performed for all samples using LSV measurements and corresponding K-L plots at different rotation speeds (Figure 4-10). The average electron transfer number (n) was calculated from the K-L plots and the results are shown in Table 4-4. The electron transfer number is close to 4 for the nitride-rich samples (Mn-N-4/CB and Mn-N-10/CB), but lower for MnO and Mn-N-30/CB (with a higher amount of MnO and other impurities). The results show that the presence of nitrogen improves the ORR kinetics. All CV and LSV tests were reproducible; each sample was tested 3 times.

The stability of Mn-N-10/CB (the best Mn-N catalyst) was assessed, and compared with Pt/C, through extended cycling up to 12 h. The initial CV curves for Mn-N-10/CB and Pt/C, as well as the CV curves at 500 and 1500 cycles, are shown in Figure 4-11. The ORR current density, at -0.4 V for Pt/C and Mn-N-10/CB (Figure 4-11(A)) drops 10.1% and 3.3%, respectively. The larger current density drop for Pt/C may be due to agglomeration of Pt particles and the formation of an oxide layer during cycling, as previously mentioned.

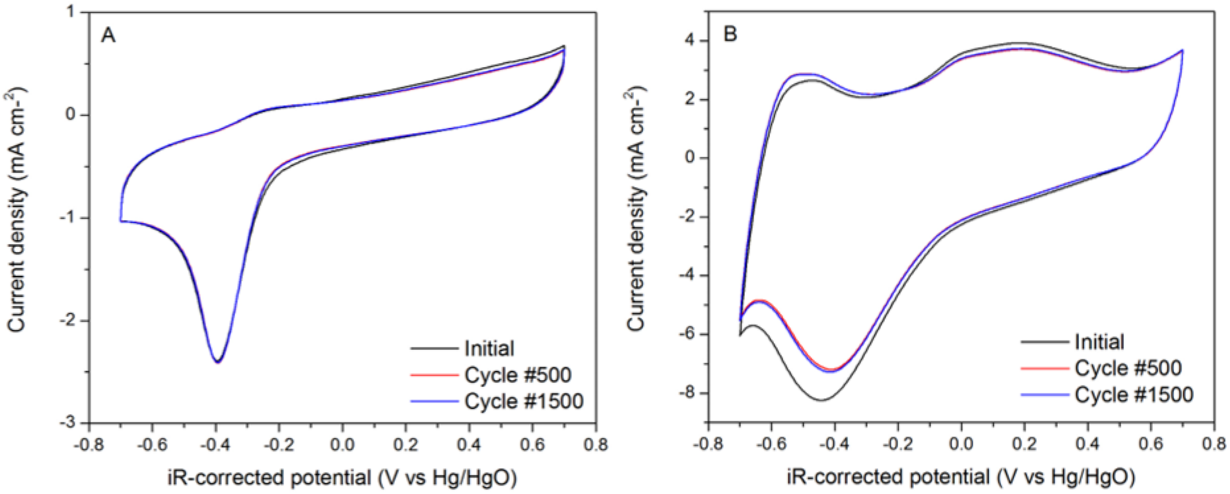

Figure 4-10 Long term cycling performance for (A) Mn-N-10/CB and (B) Pt/C catalysts. The CV tests were performed at a rate of 100 mV s^{-1} from -0.7 V to 0.7 V vs. Hg/HgO in O_2-saturated 0.1 M KOH.

Mn-N-10/CB shows excellent stability during long-term cycling, with only a 3.3% drop in current density. Although the current density for Pt/C is almost four times higher than that for Mn-N-10/CB, its poor stability during extended cycling is a disadvantage as a catalyst for energy storage applications.The OER current density at 0.7 V for both catalysts (Figure 4-11) decreases by less than 1% and 5.5% for Pt/C and Mn-N-10/CB, respectively. Although Pt/C has slightly better OER stability than Mn-N-10/CB, Mn-N-10/CB has better ORR stability and better combined bifunctional stability. The small decrease in OER/ORR current densities for Mn-N-10/CB may be due to the low surface area and possible electrochemical oxidation to MnO. Similar behavior was reported for partially oxidized TiN-based catalysts. Repeated cycling involves imposing oxidizing potentials on the TiN nanoparticles electrode surface and leads to the formation of oxide and oxynitride components which tend to dissolve in acidic solution.[269]

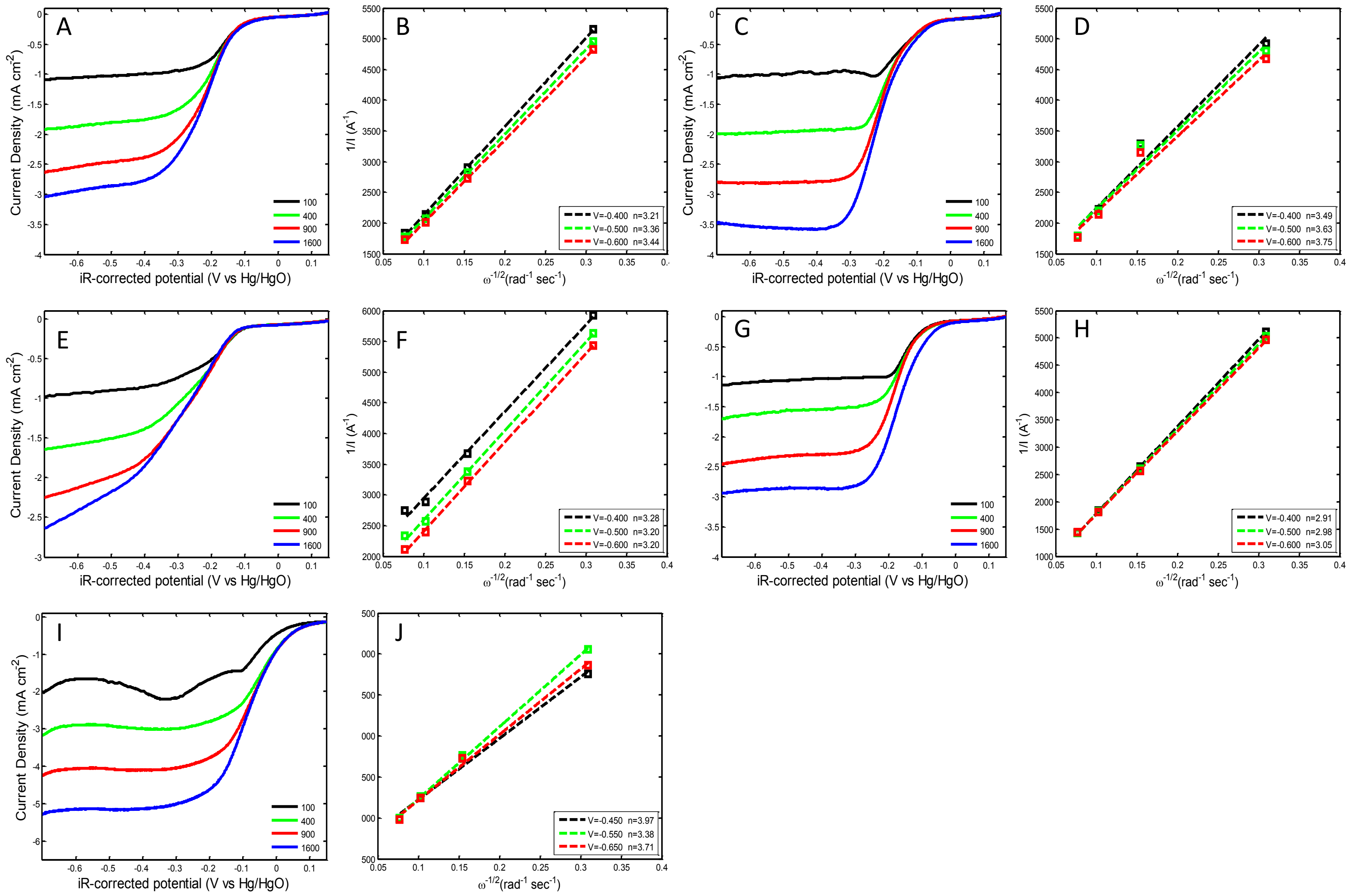

Figure 4-11 (A, C, E, G, I) ORR LSV curves for Mn-N-4/CB, Mn-N-10/CB, Mn-N-30/CB, Pt/C and MnO/CB samples in O_2-saturated 0.1 M KOH, at various rotation speeds (100-1600 rpm) and a scan speed of 10 mV s^{-1}. (B, D, F, H, J) Corresponding K-L plots for Mn-N-4/CB, Mn-N-10/CB, Mn-N-30/CB, Pt/C and MnO/CB samples. The number of electrons transferred was calculated at -0.4 V, -0.5 V and -0.6 V vs. Hg/HgO.

RDE measurements are useful for characterizing the intrinsic activity of Mn-N/CB towards ORR and OER; however, it is of practical significance to characterize the bifunctional activity of the catalyst in an actual ZAB in a highly alkaline electrolyte (6 M KOH). Separate ZABs with Mn-N-10/CB, Pt/C and bare GDL as the cathode catalysts were prepared. Galvanostatic charge-discharge experiments were performed at different current densities for all the samples (Figure 4-12(A)). Mn-N-10/CB, spray coated onto bare GDL, decreases the E_{OER}-E_{ORR} potential gap by 12.6% relative to bare GDL.

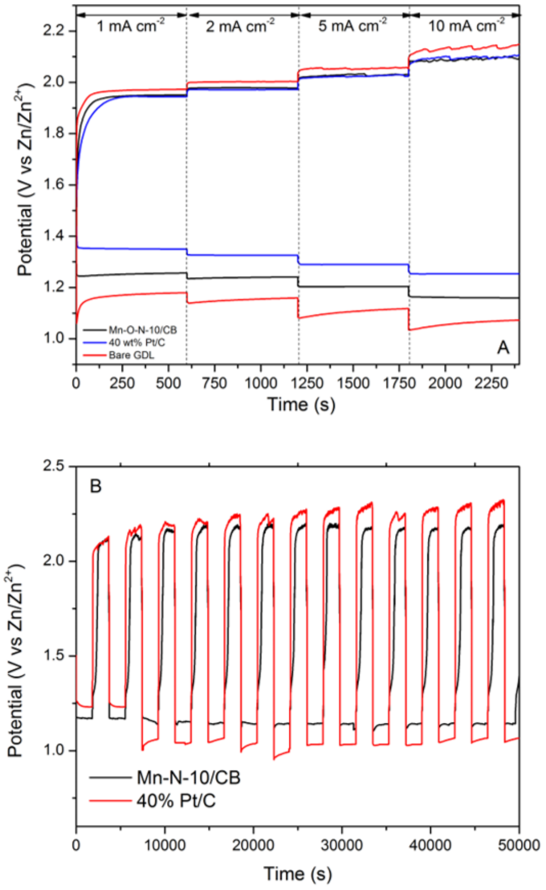

Figure 4-12 (A) Charge-discharge rate performance of Mn-N-10/CB, Pt/C and bare GDL at 1 mA cm^{-2}, 2 mA cm^{-2}, 5 mA cm^{-2} and 10 mA cm^{-2}. (B) Galvanostatic charge-discharge performance for Mn-N-10/CB and Pt/C at 7.5 mA cm^{-2} (35 mA) for 14 cycles (1 h/cycle).

The potential gap is reduced more (23.8%) with Pt/C as the cathode catalyst. The poorer short-term performance of Mn-N-10/CB, relative to Pt/C, may be due to its lower surface area (much larger particle size). Although the short-term performance of Pt/C is better than that of Mn-N-10/CB, long-term stability tests reveal better performance for Mn-N-10/CB (Figure 4-12(B)).

During the first few cycles, Pt/C has a higher efficiency than Mn-N-10/CB (58.57% vs. 55.57%); however, the efficiency drops by 18% after 2 cycles whereas the efficiency of Mn-N-10/CB drops by only 5.8% after 14 cycles. The efficiency drop for Mn-N-10/CB occurs within the first three cycles and then remains constant over the next 11 cycles, demonstrating good stability over the limited cycle range.

4.4 Summary

For the first time, Mn nitride is investigated as a potential bifunctional catalyst for rechargeable ZABs. Mn nitride was synthesized by nitridation of Mn powder in N_2 gas at 1100°C for 4 to 30 h. The resultant particles were irregular in shape with a range of sizes up to 100 µm. XRD and electron microscopy were utilized to characterize the Mn nitride particles. Two nitride phases, Mn_4N and $Mn_6N_{2.58}$, as well as MnO and impurity phases (Mn_2SiO_4 and $MnSiN_2$), were identified. The impurity phases formed as a result of reaction with the silica crucible, but the amounts were low in samples annealed for 10 h or less. The nitride and oxide phases were not pure, with the former containing some oxygen and the latter some nitrogen. The nitride phases were the majority phases for the samples annealed for 10 h or less. Depth profiles through the particles, performed by secondary ion mass spectroscopy, revealed an oxygen-rich surface and nitrogen-rich bulk. As an electrocatalyst, the sample annealed for 10 h (Mn-N-10/CB) showed the best performance with an ORR onset potential of -0.038 V vs. Hg/HgO, as well as good ORR/OER stability for at least 1500 cycles in 0.1 M KOH. The ORR electrocatalytic activity was not as good as baseline Pt/C, but the stability was better; the efficiency only dropped by 5.8% after 14 charge-discharge cycles compared with an 18% drop for Pt/C. Catalytic performance may be improved by reducing the particle size and tuning the N/O ratio on the surface.

5 Chapter 5: Spherical nitrogen-doped hollow mesoporous carbon as an efficient bifunctional electrocatalyst for Zn-air batteries

A version of this Chapter has been published in the journal of Nanoscale:

L. Hadidi, **E. Davari**, M. Iqbal, T. K. Purkait, D. G. Ivey and J. V. Veinot, Spherical nitrogen-doped hollow mesoporous carbon as an efficient bifunctional electrocatalyst for Zn-air batteries, *Nanoscale*, 2015, **7**, 20547-20556.

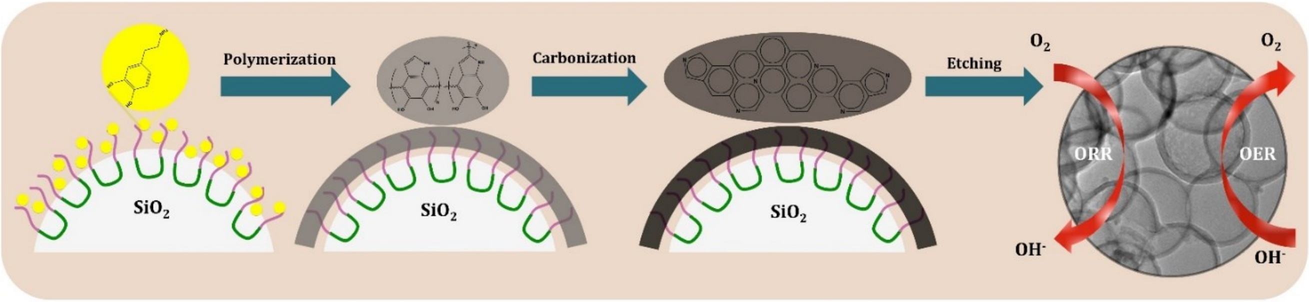

5.1 Introduction

Energy storage systems play key roles in energy management because they mitigate the mismatch rate between energy supply and energy demand.[3] Of the available electrical storage technologies, secondary electrochemical batteries are one of the most reliable and efficient devices. Lithium-ion batteries have so far dominated the market; however, their low theoretical energy density (~ 400 Wh kg^{-1}) is insufficient to meet the demands of large-scale applications such as electric automobiles. Metal-air batteries, such as ZABs, offer a promising alternative boasting theoretical energy densities up to 1084 Wh kg^{-1}. ZABs generate electricity by way of redox reactions involving Zn metal and oxygen found in air.[5,10,16] Despite their benefits, a major hurdle for metal-air batteries is developing highly active bifunctional electrocatalysts that facilitate ORR/OER at the battery "air breathing" cathode. Currently, the most efficient ORR and OER catalysts are based upon Pt and Ir, respectively.[16] These noble metals are scarce and costly; clearly, the development of cost-effective precious metal-free bifunctional electrocatalysts is of paramount importance to the advancement and wide scale use of metal-air batteries.[9,22,23]

Carbon is a good electrocatalyst; it is electronically conductive, straightforward to modify, easily separated from catalytic metals, abundant and cost effective. Many carbon systems, including porous carbon[188,200,284], graphite nanofibers (GNFs) and CNTs[285,286], have been explored as catalysts for ORR and oxidation of small organic molecules (e.g., alcohol and ether).[287] Despite the potential of these materials, there is continued interest in developing durable cost-effective catalysts exhibiting high activity. Porous carbon has received substantial attention because of its high surface area and physicochemical properties (e.g., electronic conductivity, thermal conductivity, chemical stability and low density).[288] As a result, its potential applications are far reaching and include support materials for catalytic processes, sorbents for separation processes, gas storage and purification, as well as electrode materials for batteries, fuel cells and supercapacitors.[289] Porosity is one of the most important attributes of these carbon materials because it dictates surface area and facilitates mass transport.[290] Mesoporous carbon (mC) is often preferred for electrochemical applications because of its comparatively high surface area and efficient ion mass transport.[290] Mesoporous carbon is commonly prepared using templating methods.[291–293] Soft templates, such as surfactants, self-assemble and guide the formation of carbon, which is generated from a subsequent carbonization reaction. Precursors have been demonstrated; examples include acetonitrile, polyvinylchloride, acetylene, anthracene, sucrose, glucose and furfuryl alcohol, among others.[9,200,292–311]

Doping of carbon nanostructures with N can induce/improve favorable properties (e.g., catalytic activity and conductivity).[312–315] Of particular note here, nanostructures of N-doped carbon frequently exhibit enhanced bifunctional catalytic activity without and with metals.[315–318] Although the exact catalytic mechanism is still debatable, N within carbon nanostructures influences catalytic properties because N decreases the band gap and facilitates higher electron (charge) mobility that lowers the work function at the carbon/liquid (gas) interface.[312] Doping carbon nanostructures with N can be achieved during synthesis (in-situ) or following preparation via post treatment with N-containing species (e.g., N_2 and NH_3).[287] For example, hollow carbon spheres with a metallic core (e.g., Pt, Co and Fe) were prepared using PDA.[251,252,319–323] PDA is a biomimetic adhesive polymer and an excellent carbon source that affords N-doping directly.[324] Solid sub-micrometer carbon spheres fabricated using PDA showed excellent thermal stability and ORR catalytic activity without any change in the morphology.[325] In this chapter, a facile method that generates high surface area N-doped HMC is presented. Well-defined carbon shells with abundant N-doped active sites demonstrate comparable ORR/OER catalytic activity to that of the commercial 40 wt% Pt/C catalyst, which is the baseline material. Despite being metal-free, the presented materials exhibit a high electron transfer number (~ 4) and high ORR durability when compared with baseline catalyst. Furthermore, ZAB performance of metal-free N-doped HMC outperforms the Pt/C catalyst over repeated charge-discharge cycling. In addition, N-doped HMC synthesized in this study could act as a general building block for fabricating other transition metal-HMC hybrid materials as bifunctional electrocatalysts for metal-air batteries.

5.2 Experimental

5.2.1 Materials

Dopamine hydrochloride, pluronic F127, tris-(hydroxymethyl) amino-methane, hexadecyltrimethylammonium bromide (CTAB) (≥99%) and tetraethoxysilane (TEOS) (≥99%) were purchased from Sigma-Aldrich and used as received. Pt/C (40%), Nafion solution (5% w/w in water) and 1-propanol (99.99%) were purchased from Alfa Aesar. Potassium hydroxide was purchased from Fisher and used as received.

5.2.2 Preparation of Stöber silica spheres

Spherical silica particles were prepared using the Stöber method and TEOS as the silica source, as previously reported.[319] For a typical synthesis, 40 mL of 0.2 M TEOS was added to a mixed solution of 50% ethanol (80 mL) and ammonium hydroxide (28%, 4 mL) and then stirred for 3 h at ambient temperature. The solution was centrifuged three times at 10000 rpm for 30 min to collect the particles.

5.2.3 Synthesis of silica@mC particles

For a typical synthesis, 15 mg of Stöber silica (170 ± 10%), 7.5 mg of triblock copolymer pluronic F127 and 4.5 mg of 2-amino-2-hydroxymethyl-propane-1,3-diol (tris) were dispersed/dissolved in 4 mL of deionized water. Subsequently, dopamine hydrochloride (15 mg) was added and the mixture was stirred at room temperature for 24 h. The resulting PDA coated silica particles were collected by centrifugation at a speed of 10000 rpm for 30 min. The particles were washed three times using ethanol (25 mL) and then dried under vacuum. The resulting black powder was placed in a quartz boat in a tube furnace and heated to 400 °C (heating rate of 1 °C min^{-1}) and held for 2 h. The temperature was then raised (heating rate of 5 °C min^{-1}) to 800 °C and held for 3 h; this was followed by cooling to room temperature.[320] All heating and cooling were performed under a flowing Ar atmosphere.

5.2.4 Synthesis of hollow mesoporous carbon particles (HMC)

As-synthesized silica@mC particles (~ 0.2 g) were placed in a PET beaker. Water (2 mL), ethanol (2 mL) and aqueous 49% HF (2 mL) were subsequently added sequentially and the mixture was stirred for 1 h at room temperature. The particles were recovered via vacuum filtration and washed with water (60 mL) and ethanol (60 mL). The resulting black powder was finally dried under vacuum. The HMC product (0.05 mg) was characterized using TEM and SEM, Raman and infrared (IR) spectroscopy, XPS and N adsorption/desorption measurements.

5.2.5 Preparation of polydopamine beads (PDA)

Dopamine (0.3 mg mL^{-1}) was dissolved in Tris-HCl buffer (10 mM and pH = 8.8) and the resulting solution was stirred for 12 h.[319] The black suspension was centrifuged at 14000 rpm for 30 min. The clear supernatant was decanted and discarded. The black precipitate was washed three times in water (60 mL) with sonication followed by recovery by centrifugation. Finally, the sample was dried under vacuum and heated in an Ar atmosphere in a tube furnace, as outlined for the silica@mC particles (Section 5.2.3).

5.2.6 Electrochemical measurements

All electrochemical measurements were performed using a Bio-Logic SP-300 potentiostat/galvanostat. CV and LSV half-cell experiments were performed using RDE (Pine Instruments Co, AFMSRCE). Details of the CV and LSV tests, the electrochemical set up (reference and counter electrodes) and the catalyst ink preparation are explained in Section 3.2.3. The ZAB was assembled with a laboratory made Zn-air cell using an air cathode with HMC or commercial Pt/C (40% Pt) as the catalyst. The battery performance was evaluated at ambient air conditions without introducing an additional O_2 source. Polished Zn plate was used as the anode and 6 M KOH (containing 2% ZnO to facilitate the reversible Zn electrochemical reactions by forming zincate ions) was used as the electrolyte. The current density used for battery testing was normalized to the geometric surface area of the catalyst film. Charge-discharge pulse cycling was tested by the recurrent the galvanic pulse method using an applied current of 10 mA with each cycle consisting of 5 min discharge followed by 5 min charge. All electrochemical were done in tripicate and yielded reproducible results.

5.2.7 Materials characterization

FTIR was performed on a Nicolet Magna 750 IR spectrometer by drop coating an ethanol dispersion of particles on a piece of Si wafer.

Conventional TEM was performed using a JEOL 2010 TEM equipped with a LaB_6 thermionic emission filament operated at an accelerating voltage of 200 kV. TEM sample preparation is explained in Section 3.2.5. HR-TEM images were acquired using a Hitachi-9500 TEM operated at an accelerating voltage of 300 kV and processed using Image J software (Version 1.48v). SEM analysis was carried out with a JEOL 6301F field emission SEM at an acceleration voltage of 5 kV. Samples were prepared by drop casting samples of choice from dilute ethanol suspensions onto a clean Si (100) wafer.

XPS was performed using a Kratos Axis Ultra instrument with a monochromatic Al Kα source (λ = 8.34 Å) with an energy hν = 1486.6 eV. Survey spectra were collected with an analyzer pass energy of 160 eV and a step size of 0.3 eV. For high-resolution spectra, the pass energy was 20 eV and the step size was 0.1 eV with a dwell time of 200 ms. The base pressure in the sample analytical chamber was lower than 1×10^{-9} torr. Binding energies were calibrated by using the C 1s peak as a reference (284.6 eV). CASA XPS Version 2.3.13 software was used to accomplish the background subtraction and curve fitting.

Nitrogen adsorption–desorption isotherms were measured at -196 °C with a Quantachrome Autosorb-1 adsorption analyzer. Prior to adsorption measurements, samples were degassed at 250 °C under vacuum for 2 h. The data were analyzed using BET theory. The specific surface area was determined from the linear portion of the BET data and the total pore volume was calculated from the amount adsorbed at a relative pressure of about $P/P_o = 0.995$. The pore size distributions (PSDs) were obtained using the DFT method. Raman spectra of the particles were measured with a Renishaw inVia Raman microscope. The excitation wavelength was 514 nm. Samples were prepared by mounting the powder on Al foil.

5.3 Results and discussion

5.3.1 Microstructural charactrizations

HMC, silica@mC and PDA beads were prepared using straightforward DA polymerization followed by carbonization. The resulting structures were fully characterized and evaluated as bifunctional electrocatalysts in alkaline solutions. Stöber silica particles, used in the present study as templates in the formation of silica@mC, were prepared by exploiting standard sol-gel processing. As-synthesized Stöber silica particles (diameter = 170 nm ± 10%) were coated with dopamine and triblock copolymer PEO-PPO-PEO (F127); this layer was polymerized under basic conditions.[326] Finally, the polymer layer was carbonized upon heating in Ar at 400 °C for 2 h and at 800 °C for 3 h.

Figure 5-1 shows representative SEM secondary electron (SE) images of coated Stöber silica particles before and after carbonization. After heating at 800 °C (Figures 5-1(B-D)) the particle structure remains intact. The shell thickness after carbonization is ~21 nm ± 6 nm. Etching with alcoholic HF acid provided a convenient method for removing the silica template.

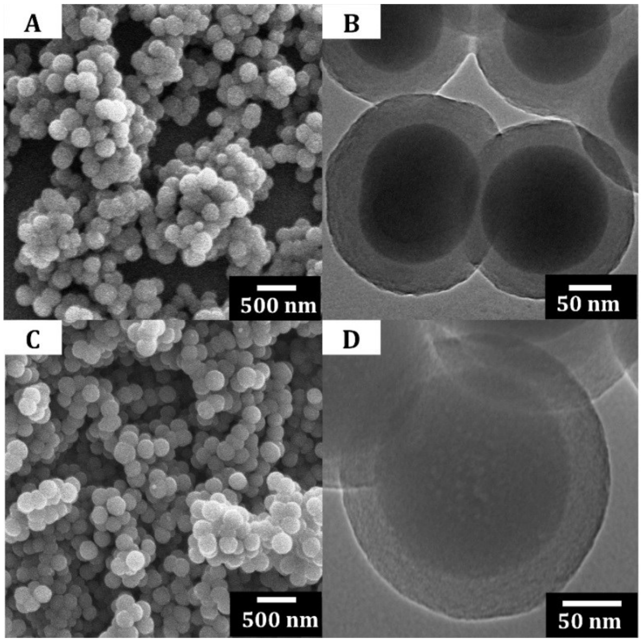

Figure 5-1 SEM SE images of coated silica before (A) and after (C) carbonization. TEM BF images of carbon-coated silica before (B) and after (D) carbonization.

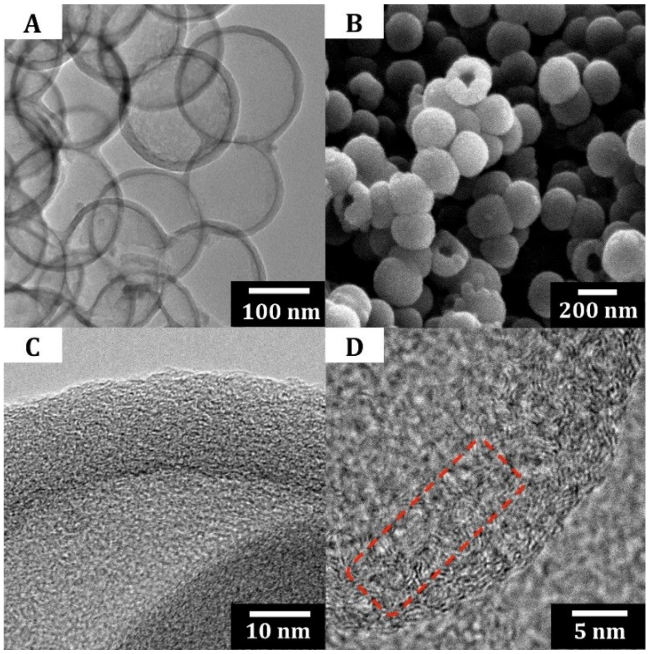

Figure 5-2 (A) TEM BF image of HMC. (B) SEM SE image of HMC. (C) and (D) HR-TEM images of HMC.

Consistent with a porous structure, one hour of etching provided hollow uniformly shaped hollow mesoporous spheres (Figures 5-2(A-B)) bearing a trace of silica (identified using EDX and XPS techniques) (Figures 5-3 and 5-4). TEM EDX spectrum is shown in Figure 5-3; the Cu signal in the EDX spectrum arises from the sample support. Evaluation of the carbon shells using HR-TEM revealed graphitic (Figures 5-2(C-D)) and amorphous domains. PDA beads (d = 121 µm ± 34 µm; Figure 5-5) were also prepared via oxidative polymerization of dopamine in a Tris-HCl buffer solution.[326,327] Carbonization was achieved using the same conditions as for HMC.

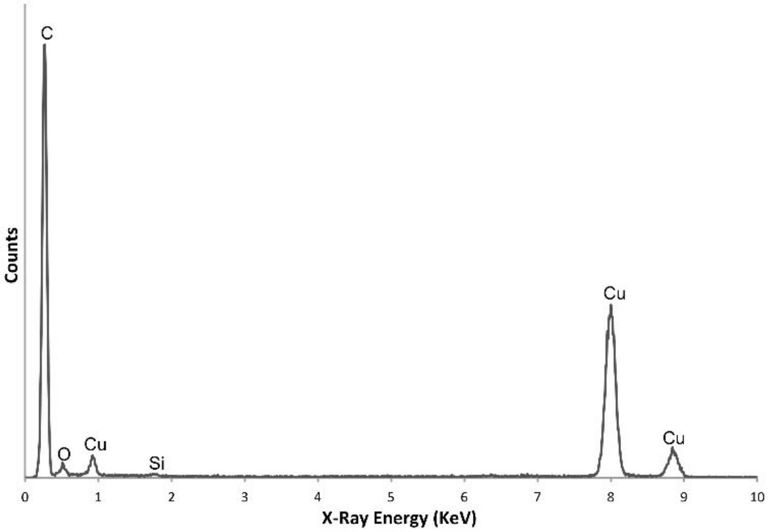

Figure 5-3 TEM EDX spectrum for HMC.

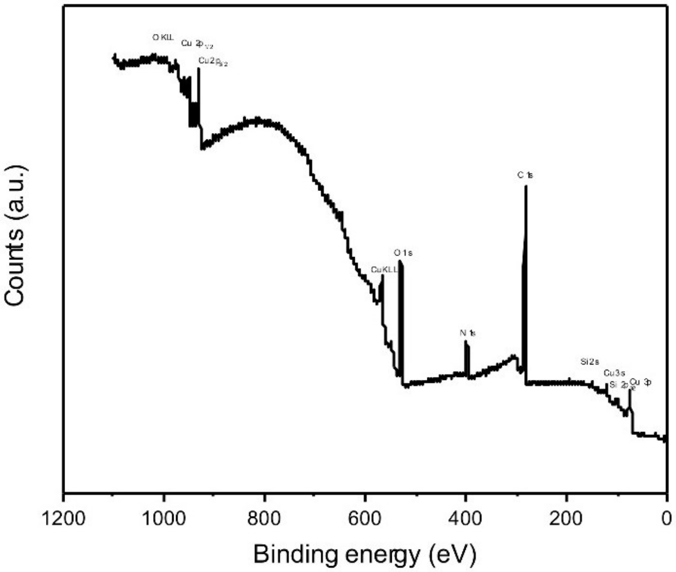

Figure 5-4 XPS survey spectrum of HMC.

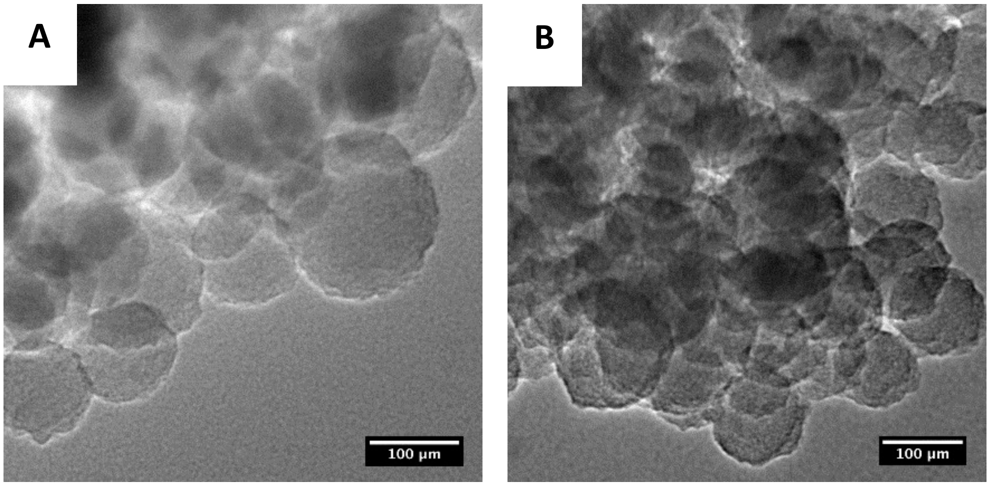

Figure 5-5 TEM BF images of polydopamine beads (A, B).

The present carbonaceous materials were further characterized using XPS, FTIR and Raman spectroscopy (Figures 5-6 and 5-7). The N 1s XPS spectra provide insight into the environment of the N atoms in silica@mC, HMC and PDA beads. Representative spectra for silica@mC and HMC are shown in Figure 5-7; peak deconvolution indicates two components centered at 398.2 and 400.3 eV, corresponding to pyridinic N and pyrrolic N (Figure 5-8), respectively. Similar analysis of PDA beads shows pyrrolic N with only minor contributions from pyridinic N approaching the sensitivity limits of the XPS method. Speciation of the N content in silica@mC, HMC and PDA beads is summarized in Table 5-1. The survey XPS spectrum showed no evidence of metals at the sensitivity of this method. The Cu signal observed in the spectrum arises from the sample substrate (Figure 5-4).

FTIR spectra for PDA beads, silica@ mC and HMC are shown in Figure 5-6(A). The PDA beads spectrum shows absorption at 2921 cm^{-1}, which is assigned to C-H stretching modes, and a feature at 1431 cm^{-1} arising from heterocyclic stretching (C-N bonds).[326] The peak at 1161 cm^{-1} is the result of heterocyclic N-H in-plane deformation breathing.[326] In addition, a feature associated with C-N bending is found at ~1500 cm^{-1} and appears to be merged with the heterocyclic stretching feature at 1431 cm^{-1}.[326] The IR spectrum for silica@mC shows a strong band at 1103 cm^{-1}, which is assigned to the Si-O-Si stretching mode. As expected, this feature is not obvious after HF etching (HMC). A feature associated with C-N bending is observed for silica@mC and HMC at ~1570 cm^{-1}.

The Raman spectra for silica@mC, HMC and PDA beads (Figure 5-6(B)) show two features at 1331 and 1578 cm^{-1} that correspond to the D band and G band, respectively. The D band arises from the A_{1g} breathing mode from sp^3 carbon components, while the G band corresponds to in-plane stretching of bonds involving sp^2 carbon atoms.[326] Based upon these observations and the HR-TEM data (Figures 5-2), we conclude that all the present materials contain a mixture of graphitic and amorphous carbon.

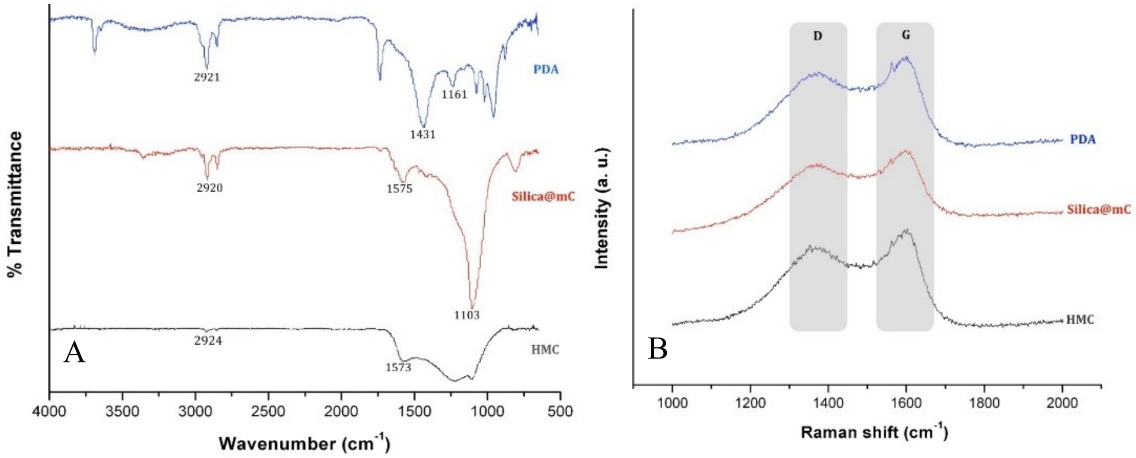

Figure 5-6 (A) FTIR spectra and (B) Raman spectra for PDA beads, Silica@mC and HMC.

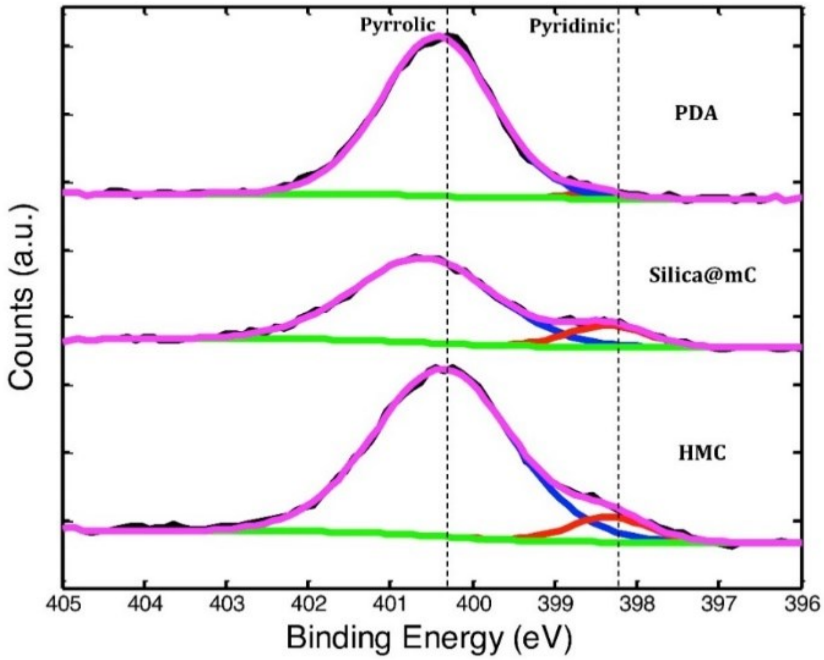

Figure 5-7 Representative high-resolution XPS spectra of N 1s for PDA beads, silica@mC and HMC.

Table 5-1 Relative atomic ratios of nitrogen species for HMC, silica@mC and PDA beads.

Catalyst	N content (at%)	Pyridinic N (at %)	Pyrrolic N (at%)
HMC	7.08	0.58	6.5
Silica@mC	4.34	0.56	3.8
PDA beads	4.9	0.08	4.81

Table 5-2 Textural properties of HMC, silica@mC and PDA beads.

Catalyst	BET surface area ($m^2 g^{-1}$)	Pore diameter (nm)	Pore volume ($cm^3 g^{-1}$)
HMC	340	30	2.5
Silica@mC	22	50	0.28
PDA beads	45	10	0.1

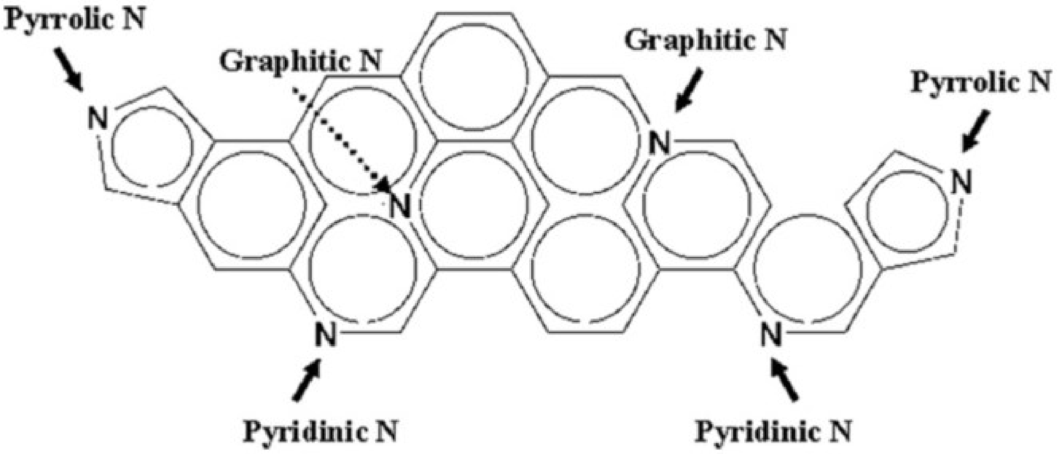

Figure 5-8 Bonding configurations for nitrogen atoms in N-doped carbon materials.[328]

Nitrogen sorption analysis was used to evaluate the specific surface area, pore volume and average pore diameter of the silica@mC, HMC and PDA beads. The corresponding isotherms (Figures 5-9(A-C)) show a distinct hysteresis loop at high relative pressure, consistent with mesoporous materials as defined by IUPAC.51. Analysis of HMC indicates it possesses porosity consisting of uniformly sized mesopores (~30 nm). Silica@mC and PDA beads show pore sizes of about 50 nm and 10 nm, respectively. Of the three materials, HMC exhibits the highest BET surface area (i.e., 340 m^2 g^{-1}) and pore volume (2.5 cm^3 g^{-1}) followed by silica@mC and then PDA beads (Table 5-2).

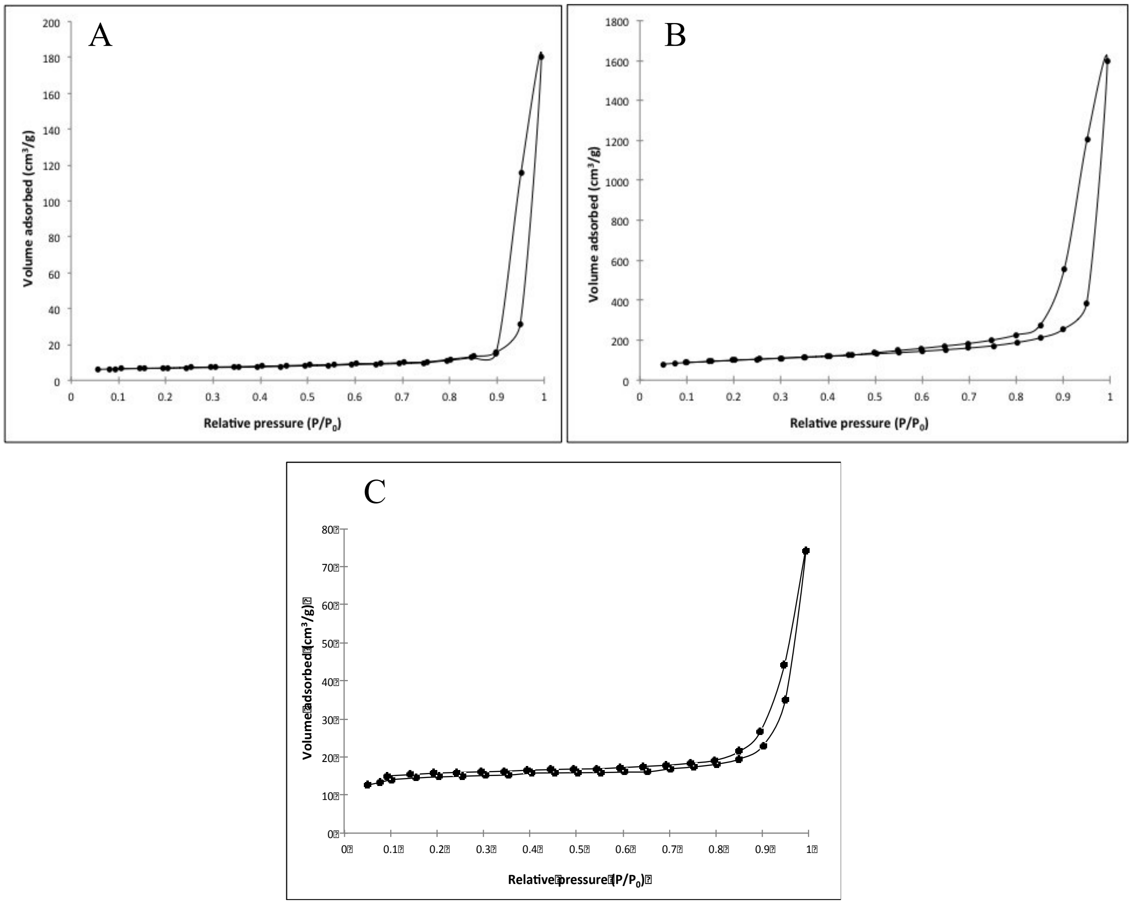

Figure 5-9 Nitrogen adsorption-desorption isotherms for A) HMC, B) silica@mC spheres and C) PDA beads.

5.3.2 Electrochemical charactrizations

The ORR catalytic activity of HMC was explored using a conventional three-electrode system within Ar- or O_2-saturated 0.1 M KOH as the electrolyte. CV experiments were performed after removal of dissolved oxygen from the solution. The CV curve for HMC (Figure 5-10) shows a featureless capacitive current in the Ar-saturated electrolyte. After purging the electrolyte solution with O_2, an irreversible cathodic current at -0.23 V, indicative of ORR occurring at the HMC surface, appears.

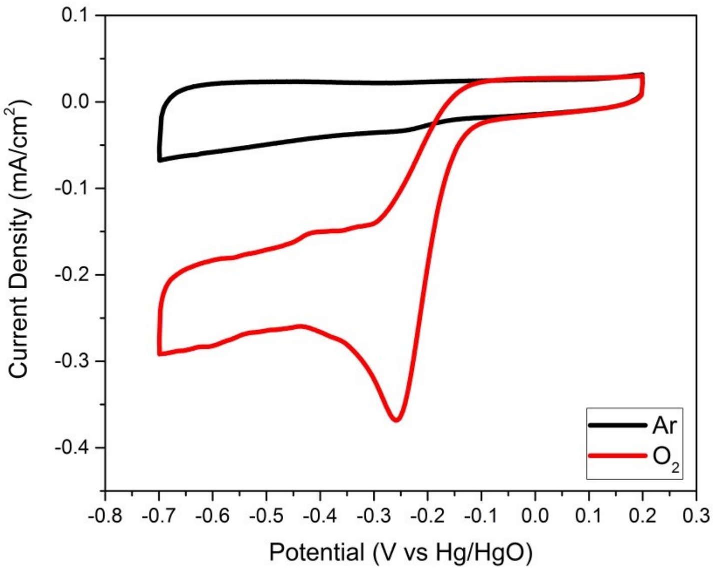

Figure 5-10 CV curves for HMC in Ar- (black trace) and O_2- (red trace) saturated 0.1 M KOH with a scan rate of 10 mV s^{-1}.

To evaluate the ORR performance of HMC, LSV was conducted from -0.8 to 0.05 V vs. Hg/HgO using predefined electrode rotation rates (400, 900, 1600 and 2500 rpm) and a scan rate of 10 mV s^{-1} in O_2-saturated 0.1 M KOH solution (Figure 5-11(A-B)). The results for silica@mC and PDA beads are shown in Figure 5-11 (C-F). The ORR polarization curve for HMC can be divided into three regions: (i) kinetically controlled (ca. -0.1 to -0.3 V), (ii) kinetic-diffusion controlled (-0.3 to -0.6 V) and (iii) mass transfer controlled (less than -0.6 V). The limiting current density increases with oxygen flux to the electrode surface. Consistent with first-order kinetics of ORR with respect to the concentration of dissolved O_2, the K-L plots for HMC (Figure 5-11(B)) show linear relationships for I^{-1} as a function of $(\omega)^{-1/2}$.

Oxidation-reduction in alkaline solutions proceeds by a direct two-electron or a four-electron pathway (Reactions 1 and 2). Applying the K-L relationships to the present systems yields the number of electrons transferred (n) as ~4 for the potentials investigated. The details regarding the number of electrons transferred and the K-L equation can be found in Section 3.2.2.

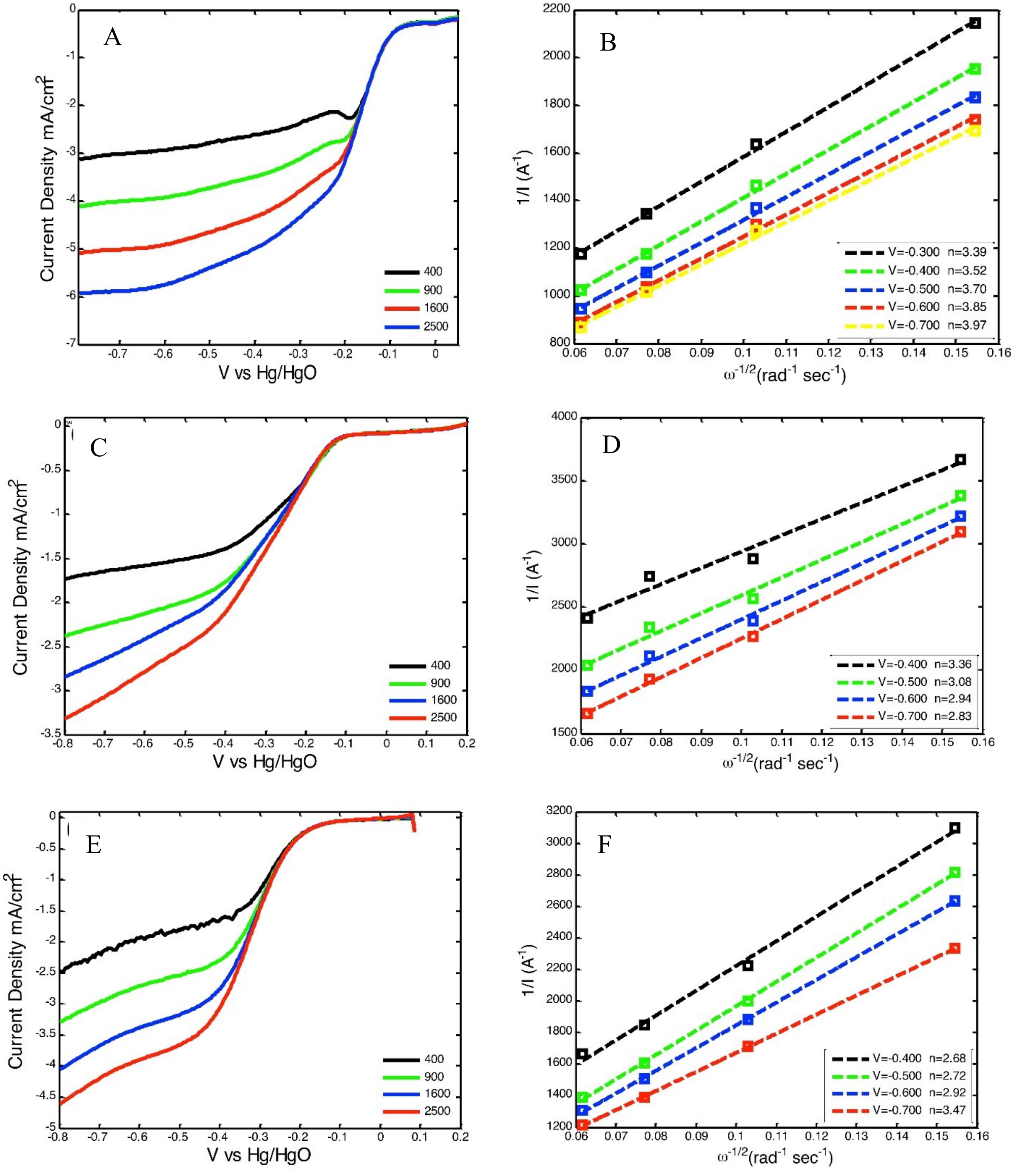

Figure 5-11 . ORR LSV curves in an O_2-saturated 0.1 M KOH solution at indicated rotational rates and a scan rate of 10 mV s^{-1} for (A) HMC, (C) silica@mC and (E) PDA beads. K-L plots in the potential range of -0.3 to -0.7 V vs. Hg/HgO for (B) HMC, (D) silica@mC and and (F) PDA beads.

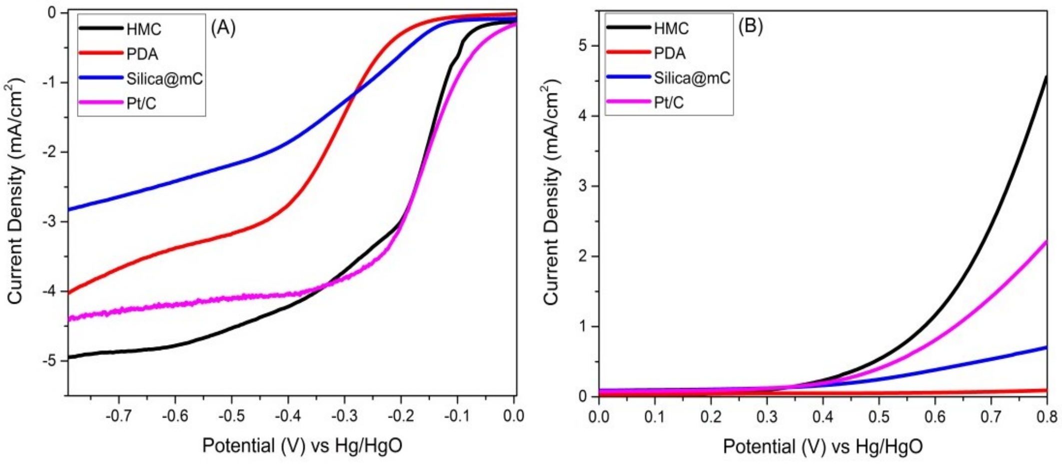

Figure 5-12 (A) ORR LSV curves for HMC, silica@mC, PDA beads and Pt/C in an O_2-saturated 0.1 M KOH solution at 1600 rpm. (B) OER LSV curves for HMC, silica@mC, PDA beads and Pt/C in 0.1 M KOH solution at 1600 rpm.

The number of electrons transferred increases at more negative potentials, which indicates the further reduction of hydrogen peroxide (Reaction 3) to hydroxide in this potential range. These results indicate the electrocatalytic process of HMC proceeds via the four-electron mechanism and is appropriate for ORR.[222]

$O_{2(g)} + 2H_2O_{(aq)} + 4e^- \rightarrow 4OH^-_{(aq)}$ (E° = 0.40 V vs SHE) Reaction 1
$O_{2(g)} + H_2O_{(aq)} + 2e^- \rightarrow HO_2^-{}_{(aq)} + OH^-_{(aq)}$ (E° = -0.07 V vs SHE) Reaction 2
$HO_2^-{}_{(aq)} + H_2O_{(aq)} + 2e^- \rightarrow 3OH^-_{(aq)}$ (E° = 0.87 V vs SHE) Reaction 3

The ORR LSV curves for the candidate catalysts, obtained at 1600 rpm, are shown in Figure 5-12(A). The catalysts were initially cycled 40 times at 10 mV s^{-1} in 0.1 M KOH O_2-saturated electrolyte in order to stabilize the system. HMC shows the highest ORR kinetic-limiting current density (-4.95 mA cm^{-2}) of the carbon-based catalysts investigated. This value exceeds the current density for Pt/C (-4.39 mA cm^{-2}), which is the benchmark catalyst for ORR. The ORR onset potential for HMC (-0.055 V) is the most positive of the catalysts studied in this work and is ~54 mV more negative than the ORR onset potential for commercial 40% Pt/C (0.001 V). The ORR onset potential and current density of the HMC particles is superior to that of other mesoporous carbons (-0.06 V and 1.7 mA cm^{-2}).[329] The half-wave potential ($E_{1/2}$) (the potential where the current density reaches half the limiting current), provides insight into the capability of catalysts to decrease the ORR overpotential. The $E_{1/2}$ for HMC is only 170 mV more negative than that of 40% Pt/C. From this data, HMC exhibits excellent electrocatalytic activity.

The catalytic activity of cycled HMC for OER was tested using LSV. Figure 5-12(B) shows a large anodic current due to the oxidation of water. Clearly the OER activity of the present HMC is superior to that of the other carbon-based materials and the 40% Pt/C material. Table 5-3 summarizes the bifunctional oxygen activity of HMC, silica@mC and PDA beads. To assess the overall oxygen catalytic activity, the difference between the ORR and OER onset potentials was tabulated. A smaller difference indicates better catalytic behavior for the bifunctional electrode. Based upon this metric, HMC particles have an onset potential difference of 420 mV, which compares favorably with the 40% Pt/C material.[330] In addition, a summary of the ORR activity in 0.1 M KOH for HMC and other carbon based electrocatalysts is presented in the Table 5-4. The ORR activity of metal-free N-doped HMC is comparable to that of other carbon-based ORR catalysts.

Table 5-3 Oxygen electrode catalyst activities.

Catalyst	**ORR onset (V)**	**j_l (mAcm^{-2})**	**n at -0.7V**	**OER onset (V)**	**j_l (mAcm^{-2})**	**E_{OER}-E_{ORR} (V)**
HMC	-0.055	-4.95	3.97	0.365	4.53	0.228
Silica@mC	-0.112	-2.85	2.83	0.373	0.68	0.367
PDA beads	-0.165	-4.05	3.47	0.463	0.08	0.628
Pt/C	0.001	-4.39	4.00	0.430	2.18	0.219

*Note: i_l: limiting current density; n: number of electrons transferred; $E_{½}$: half-wave potential.

ORR-OER bifunctional catalytic activity depends upon the surface area and N content of the structure.[329] According to the data summarized in Table 5-1, the present HMC has the highest N content of the samples investigated. The N bonding environment (e.g., pyridinic, pyrrolic and graphitic) influences catalytic activity; the literature suggests that the proportion of pyridinic and pyrrolic N play key roles.[317,328–331] Still, conflicting reports exist regarding the precise relationship between catalytic activity and N speciation.[328] Comparison of HMC, silica@mC and PDA beads shows differences in specific surface area, pore size, pore volume and N speciation. The specific surface area of HMC is the highest (340 m^2 g^{-1}) of the studied structures (Table 5-1). Furthermore, the pore volume of HMC particles is an order of magnitude higher than that of both silica@mC and PDA beads, which is consistent with the electrochemical performance of HMC. The mesoporous nature of HMC provides more active sites for ORR and OER. These factors, along with the type of N doping, contribute to the different electrochemical performances. Therefore, the synergistic effect of high surface area and N doping improve the bifunctional electrocatalytic activity of HMC.

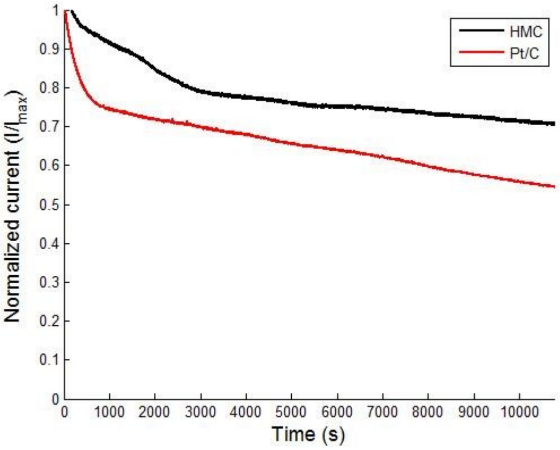

Figure 5-13 Chronoamperometric responses for ORR for HMC and Pt/C catalysts at -0.2 V vs. Hg/HgO in O_2-saturated 0.1 M KOH solution at a rotation rate of 1600 rpm.

The short-term durability of HMC was evaluated by chronoamperometry at a constant potential of -0.2 V vs. Hg/HgO for 3 h in O_2-staurated 0.1 M KOH at 1600 rpm. The chronoamperometric results are shown in Figure 5-13. The HMC catalyst exhibits higher relative current over time than 40% Pt/C. After 3 h, 40% Pt/C retained 54.7% of the initial current, whereas HMC retained 70.1% of its initial current. This shows the good stability of the HMC in addition to its promising bifunctional activity. The gradual decay of the reduction current may be due to insufficient gas flux or slow catalyst removal from the electrode surface during testing. Activity degradation of 40% Pt/C catalysts in alkaline solutions has been observed previously and it is attributed to the dissolution or aggregation of Pt nanoparticles.[16] The stability of HMC was confirmed by extended cycling of the catalysts. This is shown in Figure 5-14 where HMC has been exposed to repeated potential cycles from -0.8 to 0.7 V vs. Hg/ HgO in O_2-saturated electrolyte at 100 mV s^{-1}. After 1000 cycles, only minimal changes to ORR kinetics are observed. In fact there is a slight increase in the magnitude of the current density with cycling. The good stability is attributed to the nature of the HMC active sites, which are N doped, and the corrosion resistant nature of the HMC particles. The high stability and rapid kinetics may arise from the high surface area and multiple active sites for oxygen adsorption.[332]

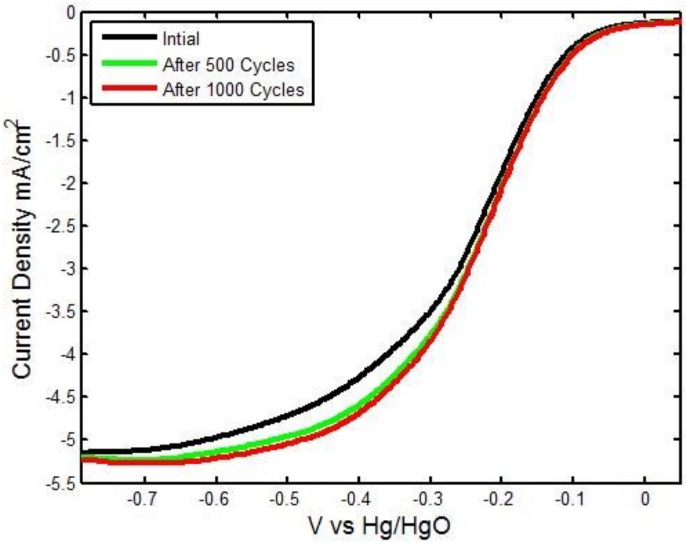

Figure 5-14 LSV ORR curves measured during cycling of HMC in O_2-saturated 0.1 M KOH at 1600 rpm (potential range -0.8 to 0.7 V vs. Hg/HgO at 100 mV s^{-1}).

Table 5-4 Comparison of the ORR activity of HMC with various non-precious metal catalysts in the recent literature.

Refs	Materials	ORR onset potential (V)	ORR peak potential (V)	Limiting current density at 1600 rpm (mA cm^{-2})	Mass loading (mg cm^{-2})
This study	Nitrogen doped-HMC	-0.050	-0.230	4.95	0.1
252	Fe/N/C hollow nanospheres	ND	-0.070	ND	0.2
323	Co-nanoparticles in N-doped carbon	-0.040	-0.140	5.29	0.2
333	N-doped graphene	-0.319	-0.389	2.42	ND
325	N-rich PDA based carbon	-0.001	-0.120	ND	ND
334	P-doped ordered mesoporous carbons	-0.060	ND	1.70	0.7
200	Eggplant-derived microporous carbon sheets	-0.003	-0.120	2.45	ND
188	N-doped hierarchically porous carbon	ND	-0.140	4.32	0.5
335	$NiCo_2S_4$	-0.050	-0.120	4.30	0.7

Notes: ND: Not determined; all the potentials have been converted to Hg/HgO reference.

RDE measurements are generally insufficient in their prediction of the performance of the catalyst, because the KOH concentration (0.1 M KOH) is much lower than the concentration usually used in a battery system (6 M KOH). Therefore, it is necessary to characterize the bifunctional activity under conditions that approach those of a "real world" ZAB. A ZAB typically consists of a Zn electrode, a separator and an air cathode. The ZAB investigated here was fabricated using a polished Zn plate anode, 6 M KOH with 2 wt% ZnO electrolyte and HMC or 40 wt% Pt/C as the active material in the air electrode. Galvanostatic charge-discharge at a current density of 2 mA cm^{-2} gave a discharge voltage of 1.24 V and a charge voltage of 2.05 V during the initial stage for HMC (Figure 5-15(A)). The charge-discharge potential gap for HMC increased from 0.85 to 0.89 V (~10%) after 100 cycles. For the Pt/C based air cathode ZAB, the initial potential gap is smaller compared with HMC (0.65 V vs. 0.85 V). However, the potential gap for Pt/C increases to 1.05 V (~60%) after 100 cycles (Figure 5-15(B)). This clearly shows the HMC is a more stable catalyst than Pt/C in highly alkaline electrolytes. The charge and discharge potentials after 30 cycles are compared with other bifunctional catalysts in Table 5-5, which highlights the superior performance and stability of HMC. These results will open new avenues to develop cost effective and high performance metal free electrocatalysts applied in advanced energy storage devices.

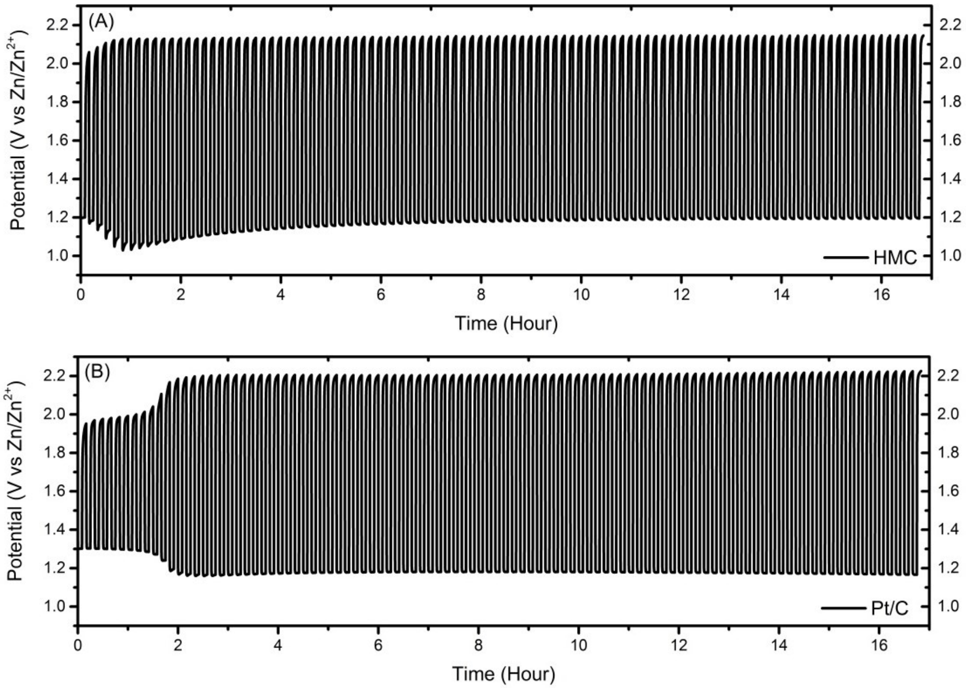

Figure 5-15 ZAB cycling test data for (A) HMC-based ZAB at 2 mA cm^{-2} and (B) Pt/C-based ZAB at 2 mA cm^{-2}. One cycle includes 5 min of charge followed by 5 min discharge.

Table 5-5 Comparison of the rechargeable ZAB performance of HMC with various non-precious metal catalysts in the recent literatures.

Refs	Materials	Charge potential (V)	Discharge potential (V)	Mass loading (mg cm^{-2})
This study	Nitrogen doped-HMC	2.13	1.24	1.00
This study	Pt/C	2.20	1.15	1.00
336	N and P co-doped mesoporous nanocarbon	~2.50	~0.95	0.50
200	Eggplant-derived microporous carbon sheets	~2.20	1.23	ND

Notes: ND: Not determined

5.4 Summary

The synthesis and characterization of N-doped carbon mesostructures obtained from the carbonization of polymerized dopamine have been reported. N-doped HMC exhibits high ORR and OER activities as well as superior stability in alkaline electrolytes when compared with baseline Pt/C catalysts. The unique structures of the porous shell provide abundant active sites for oxygen adsorption and desorption and facilitate the diffusion of reactants during the catalytic processes. More importantly, when used as a bifunctional catalyst to construct the air electrode for ZAB, N-doped HMC outperforms the baseline Pt/C counterpart. The high surface area and N-doped active sites boost the limiting current and long-term stability. As a result, HMC is a promising high performance alternative to precious metal bifunctional electrocatalysts in ZABs.

6 Chapter 6: Microwave-assisted synthesis and prototype oxygen reduction electrocatalyst application of N-doped carbon-coated Fe_3O_4 nanorods

A version of this Chapter has been published in the journal of Nanotechnology:

L. Hadidi, **E. Davari**, D. G. Ivey and J. G. C. Veinot, Microwave-assisted synthesis and prototype oxygen reduction electrocatalyst application of N-doped carbon-coated Fe_3O_4 nanorods, *Nanotechnology* - doi.org/10.1088/1361-6528/aa5716

6.1 Introduction

The development of high performance electrocatalysts for ORR is an essential aspect of research aimed at establishing efficient fuel cells and metal-air batteries.[16,337] Pt-based catalysts are very effective in promoting ORR, however, high cost and limited availability present challenges for their widespread practical application.[89,221,246,336] Much effort has been expended toward establishing affordable, alternative precious metal-free electrocatalysts.[338] In particular, because of their low cost, abundance and environmental compatibility, non-precious transition metals[114,127,339] and metal oxides (e.g., spinels and perovskites)[115,146,225,340], as well as N-doped carbons[194,200], have garnered attention. Recently, focus has turned to carbon-supported Fe_3O_4 nanocrystals; Fe_3O_4 possesses an inverse spinel (Fd3m) structure and a comparatively high electrical conductivity ($200\ \Omega^{-1}\ cm^{-1}$ vs. $\sim 10\ \Omega^{-1}\ cm^{-1}$ for MnO_2).[341,342] The inverse spinel structure also provides redox active surface sites capable of O_2 adsorption, which are crucial to the ORR process.[341,343] Reports also indicate that Fe_3O_4 is resistant to chemical degradation in alkaline conditions.[344] Tuning the catalyst surfaces with heteroatom-doped carbon is an effective strategy for improving conductivity and electrocatalytic activity by lowering the ORR activation energy.[153,339,345–348] In this context, one approach toward improving the ORR activity of transition metal oxide nanocrystals has been to coat them with mesoporous carbon containing pyrrolic and pyridinic nitrogen active sites (Figure 5-8).[349–352] Jiang et al. fabricated B-doped and N-doped graphene incorporated in spherical Co_3O_4 nanoparticles as ORR catalysts. The catalyst exhibits high stability and activity when used as cathode catalysts in a ZAB.[353] Detailed electrochemical analysis of these promising systems suggested a coupling effect between electrochemically active Co_3O_4 and heteroatom doped carbon that exhibits strong interactions with the adsorbed O_2 species. Similarly, nanoscale Fe_3O_4 nanoparticles grown on porous carbon black have been employed as ORR catalysts in direct methanol fuel cell applications and exhibit better stability than baseline Pt-C catalysts.[354]

Microwave irradiation heating is a clean, cost effective and rapid method that provides homogeneous heating. As a result, microwave heating enhances reaction rates and product yield compared with conventional heating.[355,356] In this work, we demonstrate a new straightforward and rapid microwave-based approach that generates well-defined α-Fe_2O_3 nanorods and the subsequent solution-based coating of these nanorods with PDA(α-Fe_2O_3@PDA). Heating the PDA coated nanorods leads to a new hybrid catalyst consisting of Fe_3O_4 nanorods coated with N-doped mesoporous carbon (ND-Fe_3O_4@mC). The resulting ND-Fe_3O_4@mC hybrid with various carbon shell thicknesses was also investigated as an ORR catalyst. The results suggest improved ORR electrochemical activity for the ND-Fe_3O_4 nanorods with shorter carbon coating time.

6.2 Experimental

6.2.1 Chemicals

Iron (III) chloride hexahydrate (99.9%) and sodium hydroxide (98.8%) were purchased from Fisher. Dopamine hydrochloride, pluronic F127 and tris-(hydroxymethyl) amino-methane were purchased from Sigma-Aldrich. Pt-C (40%), Nafion solution (5% w/w in water) and 1-propanol (99.99%) were purchased from Alfa Aesar. Carbon black (CB) (Vulcan XC-72) was purchased from CABOT. KOH was purchased from Fisher. All reagents were used as received unless otherwise specified. High purity O_2 (99.993%) and Ar (99.998%) were obtained from Praxair.

6.2.2 Synthesis of α-Fe_2O_3 nanorods

Aqueous NaOH solution (9 mL; 6.0 M) was slowly added to aqueous $FeCl_3 \cdot 6H_2O$ (10 mL; 2.0 M) with stirring. Additional DI water (~1 mL) was added to the solution and the orange mixture was stirred for 15 min at room temperature. Subsequently, the solution (6 mL) was transferred to a microwave reactor vial. The vial was sealed and transferred to a Biotage Initiator microwave synthesizer that was programmed to heat the sample at 150 °C for 60 min. Following the reaction, a crude product mixture appeared which was a red precipitate. The crude nanorods were isolated by centrifuging (10,000 rpm; 20 min) and purified through three redispersion/centrifugation cycles using DI water and ethanol. The final red product was isolated, dried in vacuo at room temperature, characterized and stored in air until needed.

6.2.3 Synthesis of ND-Fe_3O_4@mC

Coating α-Fe_2O_3 with N-doped carbon was achieved by combining purified α-Fe_2O_3 nanorods (50 mg) with triblock copolymer pluronic F127 (25 mg). Subsequently, 2-amino-2-hydroxymethyl-propane-1,3-diol (tris) (15 mg) was added and the mixture was dispersed/dissolved in deionized water (12.5 ml). Dopamine hydrochloride (50 mg) was then added and the mixture was stirred at room temperature for 2, 4 and 12 h. The resulting polydopamine coated α-Fe_2O_3 nanorods (α-Fe_2O_3@PDA) were collected by centrifugation at 10,000 rpm for 0.5 h, washed using ethanol

(3×25 mL) and dried in vacuo. The resulting dark grey powder was placed in a quartz boat, transferred to a standard Lindberg Blue tube furnace and heated to 400 °C (heating rate of 5 °C min^{-1}) in a flowing Ar atmosphere where it remained for 3 h followed by cooling to room temperature. The samples are denoted as ND-Fe_3O_4@mC-2, ND-Fe_3O_4@mC-4 and ND-Fe_3O_4@mC-12, indicating different coating times of 2, 4 and 12 h, respectively.

6.2.4 Preparation of “Bare” Fe_3O_4 nanorods

20 mg of ND-Fe_3O_4@mC-2 was heated at 300 °C for 30 min under air atmosphere (heating rate of 10 °C min^{-1}) to remove the carbon coating. The resulting material was characterized using HR-TEM, XRD and TGA.

6.2.5 Preparation of hollow carbon nanorods

10 mg of ND-Fe_3O_4@mC-2 were treated with 6 M HCl to dissolve the Fe_3O_4 core to obtain hollow carbon nanorods. The resultant material was characterized using HR-TEM.

6.2.6 Electrochemical measurements

Electrochemical properties of the nanomaterials were evaluated using a conventional three-electrode assembly with a Bio-logic potentiostat (SP-300) and RDE (Pine Instruments Co, AFMSRCE. Details of CV and LSV tests, the electrochemical set up (reference and counter electrodes) and the catalyst ink preparation are explained in Section 3.2.3.

Catalyst stability was evaluated using repetitive CV cycling for 5000 cycles at a scan rate of 100 mV s^{-1} from -0.7 V to 0.2 V *vs.* Hg/HgO. In order to standardize the comparison, the ORR onset potential was set at the potential at which the cathodic current density reached 25 μA cm^{-2} at 1600 rpm for O_2 saturated LSV curves. In an effort to minimize error caused by the resistance of the electrolyte, iR corrections were made for all experiments. Details of this process can be found in Section 4.2.3. The electrochemical measurements were perfomed in triplicate and the results were reproducible.

6.2.7 Materials characterization

TEM and EDX analysis were performed using a JEOL 2010 transmission electron microscope equipped with a LaB_6 thermionic emission filament operated at an accelerating voltage of 200 kV. Details of TEM specimen preparation are explained in Section 3.2.5. HR-TEM images were acquired using a Hitachi-9500 TEM, operated at an accelerating voltage of 300 kV; images were processed using ImageJ software (Version 1.46r).[357] Samples were prepared by drop casting dilute ethanol suspensions of the sample of choice onto holey carbon-coated copper grids (400 mesh).

XPS analyses were performed using a Kratos Axis Ultra instrument operating in energy spectrum mode at 210 W. Samples were prepared by drop coating a solution of prepared materials onto a Cu foil substrate to yield thin films. The base and operating chamber pressures were maintained at 10^{-7} Pa. A monochromatic Al Kα source (λ = 8.34 Å) was used to irradiate the samples and the spectra were obtained with an electron take-off angle of 90 °. To minimize sample charging, a charge neutralizer filament was used when required. Survey spectra were collected using an elliptical spot with major and minor axis lengths of 2 and 1 mm, respectively, and 160 eV pass energy with a step size of 0.33 eV. CasaXPS software (VAMAS) was used to interpret high-resolution spectra. All spectra were internally calibrated to the C 1s emission (284.8 eV). After calibration, a Shirley-type background was applied to remove most of the extrinsic loss structure. The FWHM for all the fitted peaks was maintained below 1.2 eV.

Nitrogen adsorption-desorption isotherms were measured at -196 °C with a Quantachrome Autosorb-1 adsorption analyzer. Prior to adsorption measurements, samples were degassed at 250 °C under vacuum for 2 h. The data were analyzed using BET theory.[356] The specific surface area was determined from the linear portion of the BET plot and the total pore volume was calculated from the amount adsorbed at a relative pressure of about $P/P_o = 0.995$.

TGA was performed using a Mettler Toledo Star TGA/DSC system. The Fe_3O_4@mC samples were placed in a Pt pan and heated in a N_2 atmosphere from 30 to 800 °C at 10 °C min^{-1}. XRD was performed using a Rigaku Geigerflex 2173 diffractometer equipped with a Co Kα radiation source (λ = 1.78 Å). Samples were mounted on a silicon plate inside an aluminum holder. Raman spectra were collected using a Renishaw inVia Raman microscope. The excitation wavelength was 514 nm. Samples were prepared by mounting the sample of choice on Al foil.

6.3 Results and discussion

6.3.1 Microstructural characterizations

Nitrogen-doped carbon coated nanorods (i.e., ND-Fe_3O_4@mC) were prepared using a new convenient microwave assisted hydrothermal method (Figure 6-1). Briefly, α-Fe_2O_3 precursor nanorods were prepared upon slow addition of an aqueous solution of NaOH solution to an aqueous $FeCl_3 \cdot 6H_2O$ solution with stirring. The resulting solution was heated in a microwave reactor to 150 °C for one hour.

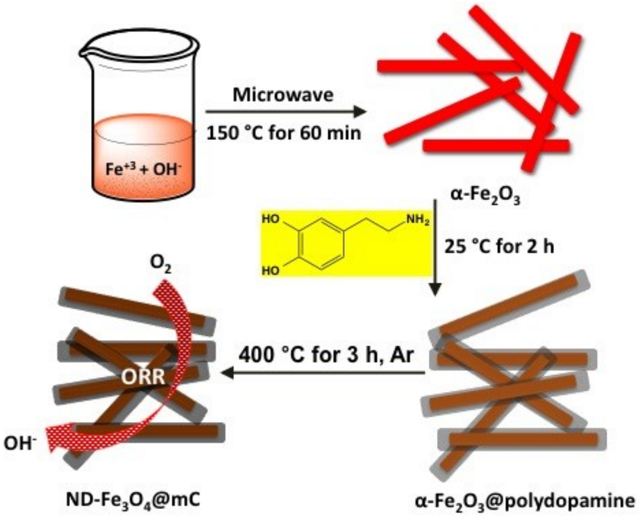

Figure 6-1 Preparation of ND-Fe_3O_4@mC nanorods.

The resulting red precursor α-Fe_2O_3 nanorods were purified upon repeated washing with water/ethanol followed by drying in vacuo at room temperature. The purified α-Fe_2O_3 nanorods were coated with dopamine-derived nitrogen-doped mesoporous carbon using a modified procedure from the literature.[194] The resulting dark grey powder consisting of nanorods was collected by centrifugation, repeatedly washed with ethanol, dried at room temperature in vacuo and subsequently heated to 400 °C for 3 h under Ar followed by cooling to room temperature. The final product obtained from the annealing process consisted of ND-Fe_3O_4@mC nanorods.

The structure and morphology of the α-Fe_2O_3 nanorods and ND-Fe_3O_4@mC-2 nanorods were investigated using TEM. The precursor α-Fe_2O_3 nanorods were 141 nm ± 44.8 nm long with diameters of 14 nm ± 3.4 nm (Figure 6-2(A)). A representative HR-TEM image (Figure 6-2(A) inset) shows continuous lattice fringes along the nanorod long axis. The observed *d*-spacing of 0.25 nm agrees with the spacing of the (110) planes of trigonal, hexagonal α-Fe_2O_3.[358]

Following carbonization, the nanorod morphology is preserved (see Figures 6-2(B-C)). A distinct amorphous carbon shell (thickness 1.5 nm ± 0.2 nm) formed on α-Fe_2O_3 nanorods that had been exposed to dopamine for 2 h (i.e., ND-Fe_3O_4@mC-2). The thickness of the carbon shell depends on the polydopamine coating time; increasing the time to 4 h (ND-Fe_3O_4@mC-4) and 12 h (ND-Fe_3O_4@mC-12), while keeping other parameters fixed, resulted in thicker coatings (Figure 6-3). The carbon content for samples obtained from different PDA coating times was determined by

TGA (Figure 6-4). As expected, samples with the longest coating time (12 h) had the highest carbon content (38.3 wt %) and TEM analysis indicated a carbon layer thickness of 3.5 nm ± 0.5 nm. For the 2 h and 4 h coating time samples the carbon contents were 14.5 wt % and 20.8 wt %, with shell thicknesses of 1.5 nm ± 0.2 nm and 2.2 nm ± 0.5 nm, respectively.

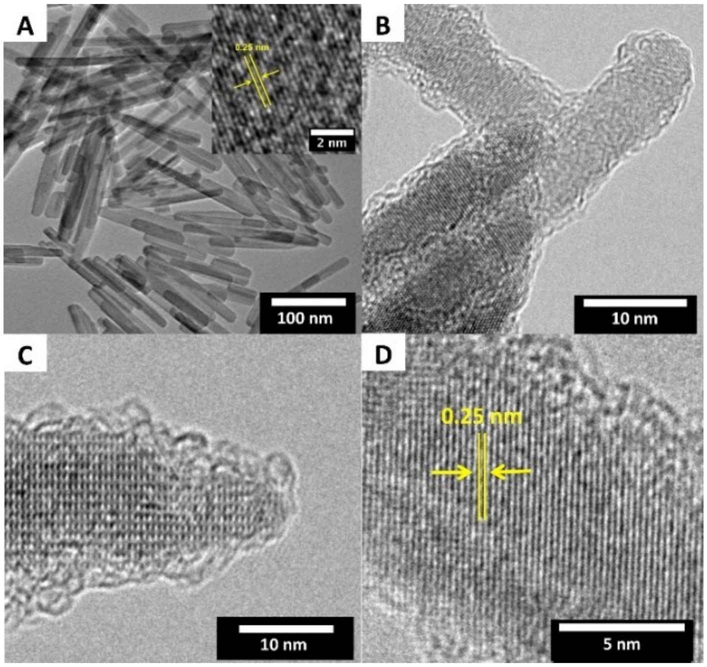

Figure 6-2 (A) Representative TEM BF image of α-Fe_2O_3 nanorods (inset is HR-TEM image of the sample shown in (A). (B-D) Representative HR-TEM images of ND-Fe_3O_4@mC-2 nanorods.

A representative HR-TEM image (Figure 6-2 (D)) shows regions with lattice fringes at different orientations indicating that the ND-Fe_3O_4@mC nanorods are polycrystalline. The lattice fringes have a *d*-spacing of 0.25 nm that corresponds to the (311) reflections for cubic Fe_3O_4[359]. Representative XRD patterns for ND-Fe_3O_4@mC-2 and α-Fe_2O_3 nanorods are shown in Figure 6-6.

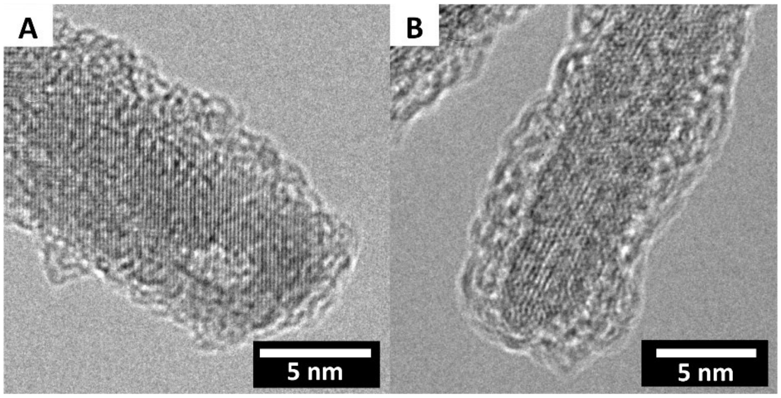

Figure 6-3 HR-TEM images of (A) ND-Fe_3O_4@mC-4 nanorods and (B) ND-Fe_3O_4@mC-12 nanorods.

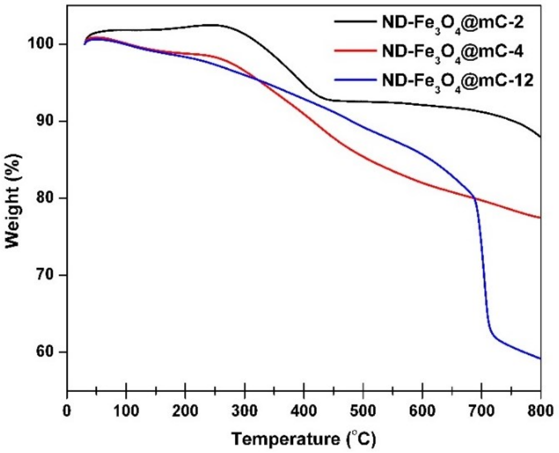

Figure 6-4 TGA curves for ND-Fe_3O_4@mC nanorods with different coating times.

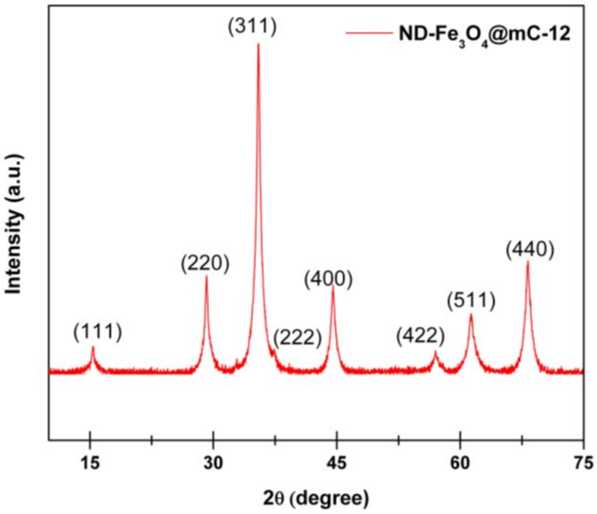

Figure 6-5 Representative XRD patterns for ND-Fe_3O_4@mC-2 and α-Fe_2O_3 nanorods.

The XRD pattern for the precursor nanorods can be indexed to α-Fe_2O_3 (JCPDS no. 89-8103).[318] In contrast, the patterns obtained for ND-Fe_3O_4@mC-2, ND-Fe_3O_4@mC-4 and ND-Fe_3O_4@mC-12 nanorods are consistent with pure Fe_3O_4 (JCPDS no. 65-3107). Clearly the precursor α-Fe_2O_3 nanorods transform into the face-centered cubic, inverse spinel phase of magnetite upon thermal treatment.[252] The conspicuous absence of reflections arising from graphite in the XRD pattern confirms that the carbon layer is amorphous, which is consistent with the HR-TEM (Figures 6-2 and 6-3).

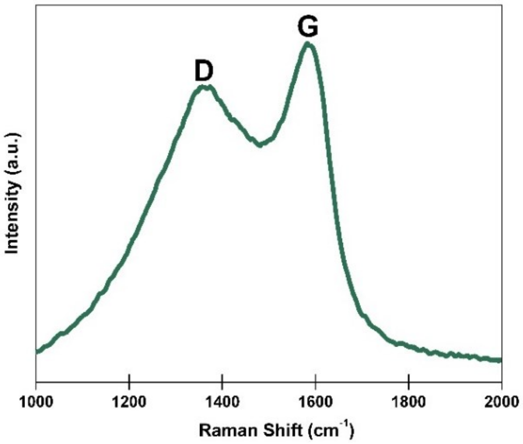

Figure 6-6 Raman spectrum for ND-Fe_3O_4@mC-2 nanorods.

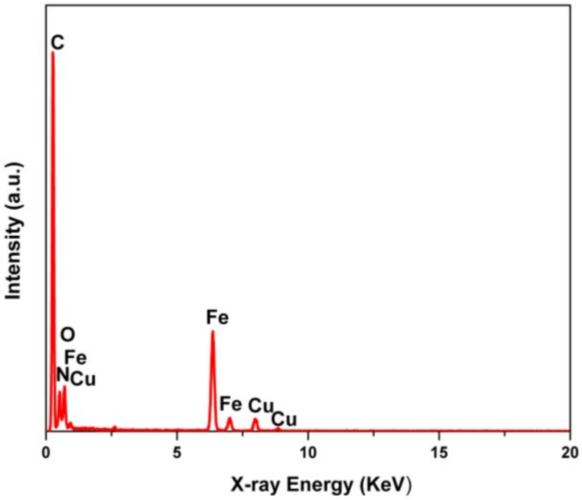

Figure 6-7 Representative TEM-EDX spectrum from ND-Fe_3O_4@mC-2 nanorods.

The Raman spectra (Figure 6-6) for all three samples show features at 1331 cm^{-1} and 1578 cm^{-1} that correspond to the D band and G band, respectively. The D band arises from the A_{1g} breathing mode from sp^3 carbon components, while the G peak corresponds to in-plane stretching of bonds involving sp^2 carbon atoms.[326] This further confirms that the carbon layer is amorphous, which is consistent with the HR-TEM (Figures 6-2 and 6-3) and XRD results (Figure 6-5).

To gain insight into the nanorod composition, samples were analysed using EDX spectroscopy and XPS. Representative EDX (Figure 6-7) and a survey XPS spectrum (Figure 6-8(A)) of ND-Fe_3O_4@mC-2 indicate the nanorods only contain N, C, O and Fe at the sensitivity limit of these methods (The Cu signal arises from the sample support).

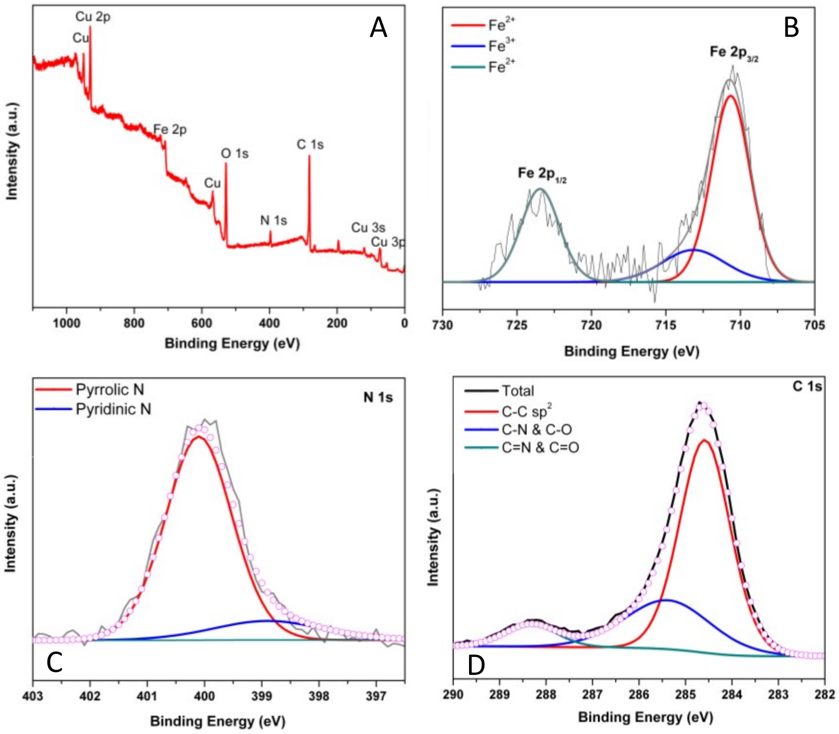

Figure 6-8 (A) Representative XPS survey spectrum for ND-Fe_3O_4@mC-2 nanorods. High resolution XPS spectra from ND-Fe_3O_4@mC-2 nanorods for the (B) Fe 2p and (C) N 1s (D) C 1s.

The Fe 2p region of the high-resolution XPS spectrum provides the oxidation states of the Fe atoms in the nanorods (Figure 6-8(B)). Peak deconvolution yields four components centred at 710.5 eV, 713.0 eV, 723.3 eV and 725.8 eV; these components are confidently assigned to Fe^{3+} $2p_{3/2}$, Fe^{2+} $2p_{3/2}$, Fe^{2+} $2p_{1/2}$ and Fe^{3+} $2p_{1/2}$, respectively.[360] Of note, the XPS spectrum confirms the partial reduction of Fe^{3+} to Fe^{2+}, due to thermal treatment, and is consistent with the formation of Fe_3O_4.[360] The N 1s region of the high-resolution XPS spectrum for ND-Fe_3O_4@mC-2 (Figure 6-8(C)) indicates there are two forms of nitrogen present - pyrrolic N (399.9 eV) and pyridinic N (398.1 eV).[361] Both nitrogen sites are catalytically active in oxygen reduction.[345] In addition, the C 1s region of the high-resolution XPS spectrum shows three main components (Figure 6-8(D)) that are attributed to sp^2 C-C (284.57 eV), C-O and C-N (285.45 eV) and C=N/C=O (288.2 eV ± 0.1 eV).[362]

Nitrogen sorption analysis was used to evaluate the porosity of the carbon shells for samples obtained with different coating times. The specific surface area, pore volume and average pore diameter of the carbon shells are summarized in Table 6-1. The corresponding isotherms (Figures 6-9(A-C)) show a distinct hysteresis loop at high relative pressure, consistent with the materials being mesoporous.[363] Evaluation of ND-Fe_3O_4@mC-2 nanorods indicates that they possess porosity consisting of uniform mesopores with diameters ~3.8 nm, a BET surface area of 121 $m^2\ g^{-1}$ and a pore volume of 0.54 $cm^3\ g^{-1}$.

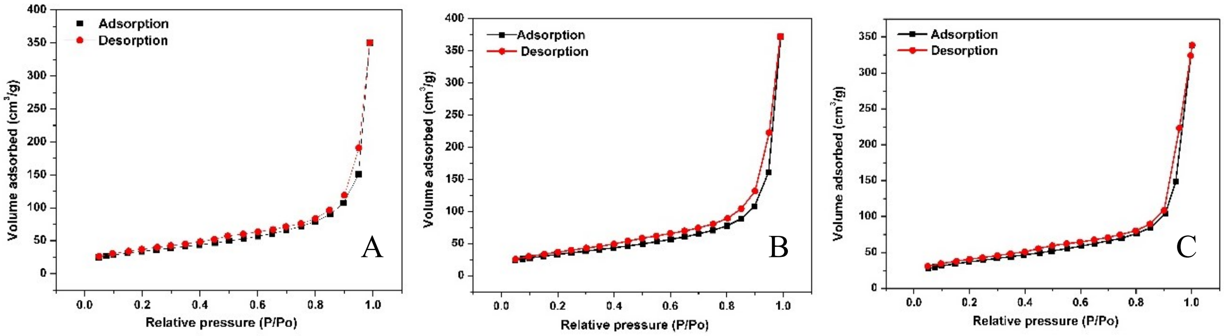

Figure 6-9 Nitrogen adsorption-desorption isotherms for (A) ND-Fe_3O_4@mC-2, (B) ND-Fe_3O_4@mC-4 and (C) ND-Fe_3O_4@mC-12.

Table 6-1 Textural properties of ND-Fe_3O_4@mC nanorods with different coating times.

Catalyst	BET surface area ($m^2\ g^{-1}$)	Pore radius (nm)	Pore volume ($cm^3\ g^{-1}$)
ND-Fe_3O_4@mC-2	121	1.9	0.54
ND-Fe_3O_4@mC-4	120	1.7	0.57
ND-Fe_3O_4@mC-12	130	1.7	0.52

To better understand the function of Fe_3O_4 nanorods and to clarify any synergistic ORR effects of combining a Fe_3O_4 core with a nitrogen doped carbon shell, "bare" Fe_3O_4 nanorods and hollow carbon shells were prepared. Bare Fe_3O_4 nanorods were prepared by heating ND-Fe_3O_4@mC-2 at 300 ˚C for 30 min in air to remove the carbon coating. HR-TEM images (Figures 6-10(A-B)) show no obvious carbon coating on the surface of the nanorods. The XRD pattern of the product obtained after heating in air (Figure 6-10(C)) shows features associated with α-Fe_2O_3 and Fe_3O_4, consistent with some oxidation of the nanorods; however, Fe_3O_4 remains the dominant phase. As expected, TGA shows that the carbon content (Figure 6-10(D)) for the bare Fe_3O_4 samples decreased substantially, i.e., 14.5 wt % for the ND-Fe_3O_4@mC-2 nanorods *vs*. 1.5 wt % for the bare Fe_3O_4 nanorods.

ND-Fe_3O_4@mC-2 nanorods were also treated with 6 M HCl to dissolve the Fe_3O_4 core to obtain hollow carbon nanorod shells. HR-TEM images of samples obtained from the acid treatment (Figure 6-11) reveal a collapsed structure. Still, the remaining carbon "shell" is an excellent reference material for comparison with other carbon coated samples during electrochemical testing.

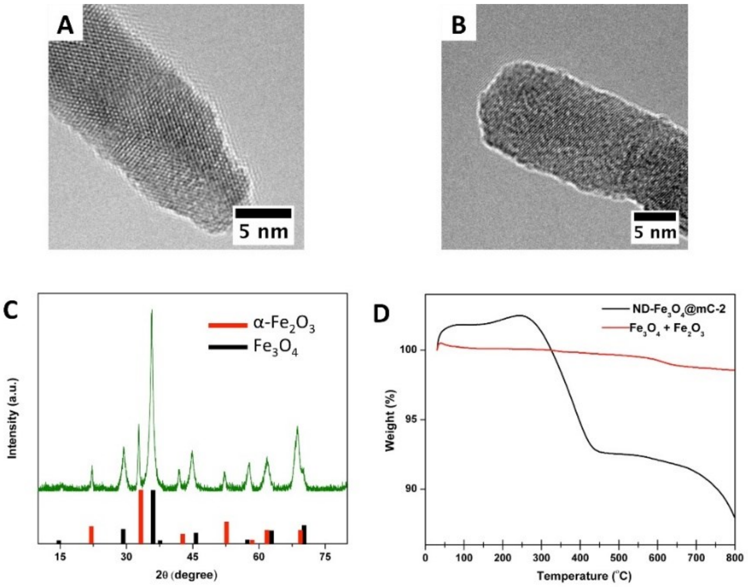

Figure 6-10 (A, B) HR-TEM images of Fe_3O_4 nanorods. (C) XRD pattern for Fe_3O_4 nanorods. (D) TGA curves for ND-Fe_3O_4@mC-2 nanorods (black) and Fe_3O_4 nanorods (red).

To evaluate the electrocatalytic activity of ND-Fe_3O_4@mC-2/CB, ND-Fe_3O_4@mC-4/CB and ND-Fe_3O_4@mC-12/CB, CV curves were recorded in Ar- and O_2-saturated 0.1 M KOH at a scan rate of 10 mV s^{-1}. CV curves for the potential range of -0.7 to 0.4 V *vs.* Hg/HgO are shown in Figure 6-13(A). Featureless voltammograms were obtained for all the analyses performed in Ar-saturated electrolyte. In contrast, an irreversible cathodic wave is present at ca. -0.26 V *vs.* Hg/HgO in O_2-saturated CV curves, which is consistent with ORR occurring for all the catalysts tested. The small peak appearing at ~-0.5 V *vs.* Hg/HgO for ND-Fe_3O_4@mC-2/CB corresponds to the reduction of ND-Fe_3O_4. This feature is not obvious for the other samples, presumably due to the thicker carbon shells. These observations are consistent with previous reports that carbon supports and/or coatings can hinder redox associated with degradation of Fe-based catalysts in alkaline conditions.[364] Closer examination of Figure 6-13(A) reveals that ND-Fe_3O_4@mC-2/CB displays a more positive peak potential (-0.246 V *vs.* Hg/HgO) and higher peak current density (-1.5 mA cm^{-2}) than the catalysts with thicker carbon coatings (ND-Fe_3O_4@mC-4/CB and ND-Fe_3O_4@mC-12/CB). The exact origin of this behavior is not completely clear. However, shorter coating times (1-1.5 h) result in non-uniform carbon deposits, whereas thicker coatings obtained at longer coating times may block ion access to the active sites of Fe_3O_4 nanorods. The optimal coating time for Fe_3O_4 nanorods, for the conditions examined, is 2 h.

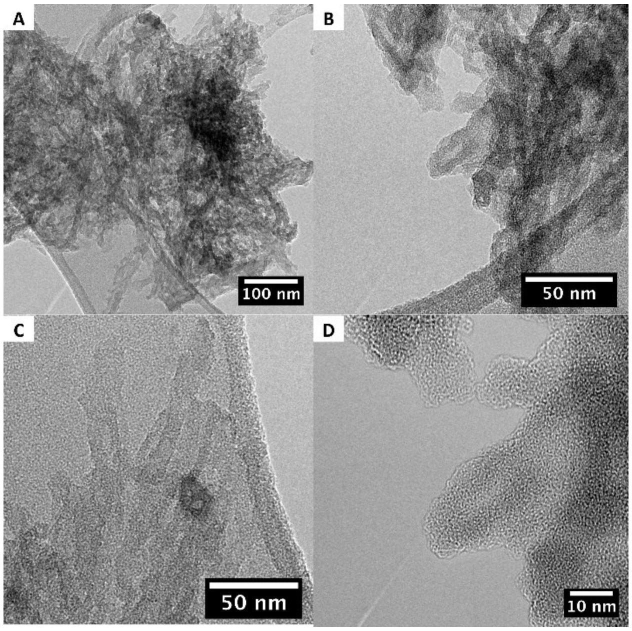

Figure 6-11 (A-D) Representative HR-TEM images of ND-C nanoshells.

6.3.2 Electrochemical characterizations

To further evaluate the ORR catalytic activity of the Fe_3O_4 nanorods coated with N-doped mesoporous carbon (ND-Fe_3O_4@mC), LSV was performed using standard RDE methods. Figure 6-12(B) shows the voltammograms obtained for samples in O_2-saturated, 0.1 M KOH at a scan rate and rotation speed of 10 mV s^{-1} and 1600 rpm, respectively. Consistent with the CV analysis (Figure 6-12), ND-Fe_3O_4@mC-2/CB shows the most positive onset potential (i.e., 0.024 V *vs.* Hg/HgO) and the highest diffusion-limited current density (i_l = -5.25 mA cm^{-2}) (Table 6-2). Tafel slope analysis of the three samples (*i.e.*, ND-Fe_3O_4@mC-2/CB, ND-Fe_3O_4@mC-4/CB and ND-Fe_3O_4@mC-12/CB) was performed. Figure 6-13 shows that ND-Fe_3O_4@mC-2/CB has a slightly smaller Tafel slope compared with the other samples. This confirms similar kinetic behavior for the samples (particularly in the low overpotential region). The Tafel slopes are also consistent with results reported for Fe_3O_4-based and Co_3O_4-based ORR catalysts.[352,365,366]

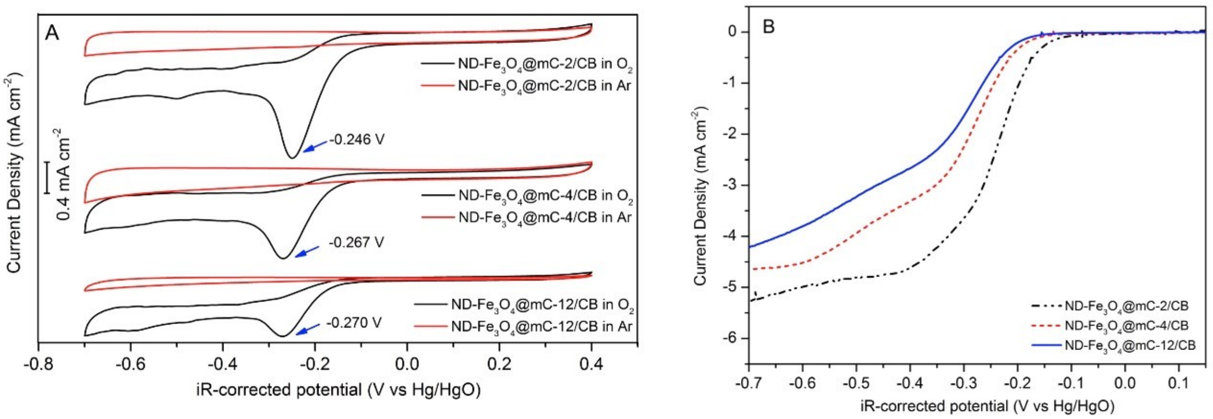

Figure 6-12. (A) CV curves for ND-Fe_3O_4@mC-2/CB, ND-Fe_3O_4@mC-4/CB, and ND-Fe_3O_4@mC-12/CB obtained at 10 mV s^{-1} in Ar- or O_2-saturated, 0.1 M KOH. (B) LSV curves for ND-Fe_3O_4@mC-2/CB, ND-Fe_3O_4@mC-4/CB, and ND-Fe_3O_4@mC-12/CB obtained at 1600 rpm and 10 mV s^{-1}.

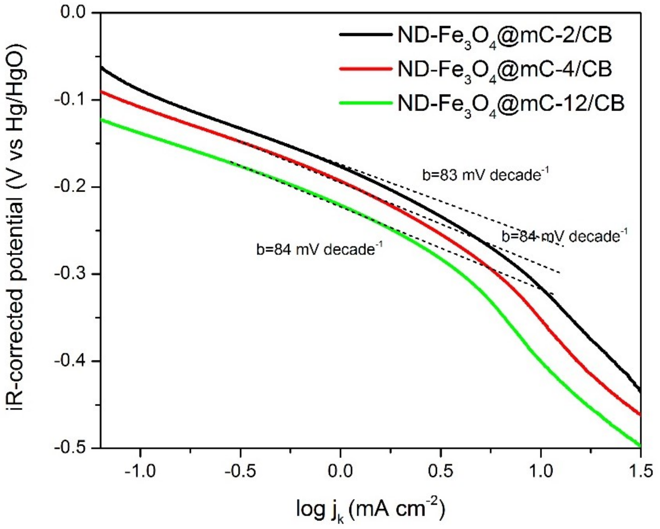

Figure 6-13 Tafel plots for ND-Fe_3O_4@mC nanorods obtained from the corresponding ORR LSV curves in the low current density region.

The kinetics of ND-Fe_3O_4@mC-2/CB catalyzed ORR were evaluated by comparing a series of LSV curves at 10 mV s^{-1} (Figure 6-14(A)) obtained at different electrode rotation rates. K-L plots for ND-Fe_3O_4@mC-2/CB are provided in Figure 6-14(B) at various potentials. Applying the K-L equations (Section 3.2.3) [4], the average number of electrons transferred (n) at different potentials was determined to be close to four for ND-Fe_3O_4@mC-2/CB. Table 6-3 summarizes the electrochemical data for ND-Fe_3O_4@mC-2/CB and similar Fe oxide-based catalysts from the literature.[351,361,364]

Table 6-2 Oxygen electrode catalyst activity.

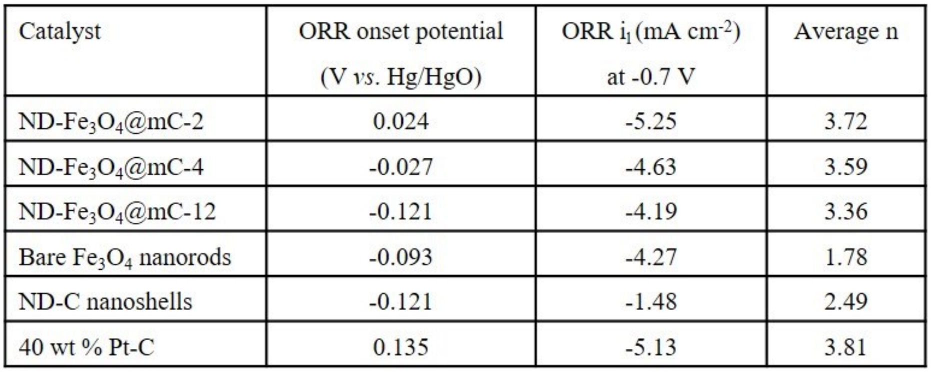

Catalyst	ORR onset potential (V *vs.* Hg/HgO)	ORR i_l (mA cm^{-2}) at -0.7 V	Average n
ND-Fe_3O_4@mC-2	0.024	-5.25	3.72
ND-Fe_3O_4@mC-4	-0.027	-4.63	3.59
ND-Fe_3O_4@mC-12	-0.121	-4.19	3.36
Bare Fe_3O_4 nanorods	-0.093	-4.27	1.78
ND-C nanoshells	-0.121	-1.48	2.49
40 wt % Pt-C	0.135	-5.13	3.81

Table 6-3 Comparison of ORR activities for ND-Fe_3O_4@mC-2/CB with various non-precious metal based catalysts in the recent literature.

Refs	**Materials**	**Onset potential (V *vs.* Hg/HgO)**	**i_l at 1600 rpm (mA cm^{-2})**	**Mass loading (mg cm^{-2})**	**Average *n***
This study	ND-Fe_3O_4@mC-2/CB	0.024	5.25	0.1	3.72
[364]	Fe_3O_4-CN_x	0.024	~4.00	ND	3.40
[351]	Fe@Fe_3O_4	0.136	5.79	0.2	2.50-3.50
[358]	Fe_3O_4/N-GA	-0.091	~4.50	ND	3.09-3.80
[350]	Fe_3O_4/graphene	-0.258	~4.00	ND	ND
[349]	Fe–Fe_2O_3/NGr	0.075	~7	ND	3.8
[367]	Fe_3O_4/N-GAs	-0.081	~5.5	ND	3.95
[354]	Nano-Fe_3O_4/CB	ND	ND	0.85	3.93
[368]	Fe_3O_4	0.026	~4.5	ND	3.8
[369]	Co_3O_4/rmGO	-0.046	~5	ND	~4

ND-Fe_3O_4@mC-2/CB has an onset potential (0.024 V vs Hg/HgO) that is either more positive or comparable to the other catalysts, with the exception of Fe–Fe_2O_3/N-doped graphene (NGr) (0.075 V *vs.* Hg/HgO).[349] The limiting current density observed for ND-Fe_3O_4@mC-2 (5.25 mA cm^{-2}) is very close to the limiting current density of the same catalyst (5.5 mA cm^{-2}). It should be noted, however, that the mass loading was not reported for this ORR catalyst.

To further investigate the ORR pathway and mechanism, the number of electrons transferred was determined using K-L plots for the other samples (Figures 6-14 and 6-15). As expected, for metal-free and non-precious metal ORR electrocatalysts, ORR occurs mainly via a two-electron transfer process when ND-carbon shell catalysts are employed.[370]

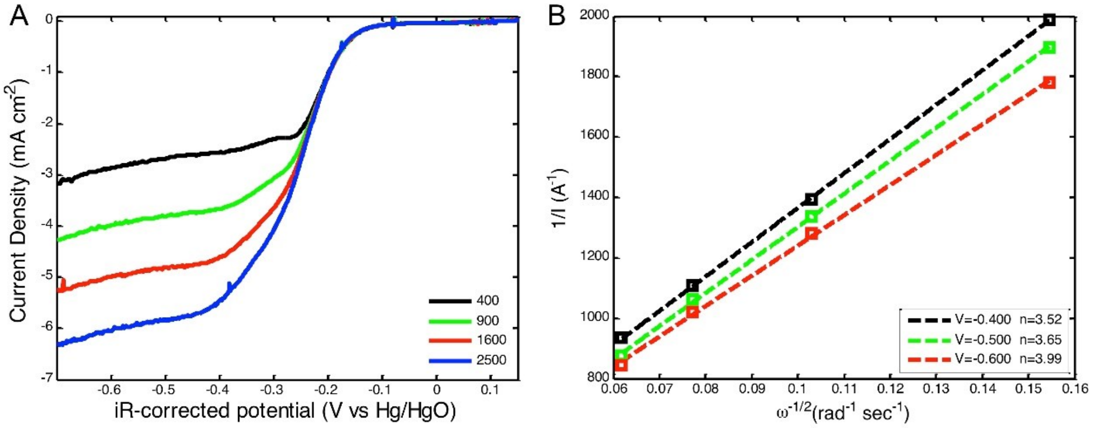

Figure 6-14 (A) LSV curves for ND-Fe_3O_4@mC-2/CB at electrode rotation speeds of 400, 900, 1600 and 2500 rpm at a scan rate of 10 mV s^{-1} in O_2-saturated 0.1 M KOH. (B) Corresponding K-L plots at -0.4, -0.5 and -0.6 V for ND-Fe_3O_4@mC-2/CB.

For ND-Fe_3O_4@mC/CB, the average number of electrons transferred during ORR (for the potential range of -0.4 to -0.7 V) increases with decreasing carbon coating time as presented in Table 6-2. To investigate the roles of the Fe_3O_4 and ND-C components for the ND-Fe_3O_4@mC-2 hybrid catalyst, bare Fe_3O_4 nanorods and ND-C shells were prepared (Sections 6.2.4 and 6.2.5). LSV measurements were performed to evaluate the catalytic activity for bare Fe_3O_4 nanorods, ND-C shells and 40 wt% Pt-C at different roation speeds; corresponding K-L plots were also obtained (Figure 6-15). The LSV response for these three materials (with identical mass loading) was also compared with the LSV response for the Fe_3O_4@mC-2/CB hybrid (Figure 6-16). The catalyzed electrochemical reduction of O_2 on ND-Fe_3O_4@mC-2/CB occurs at a more positive onset potential (0.024 V) than that for the ND-C nanorods (-0.121 V) and the Fe_3O_4 nanorods (-0.093 V). The ORR onset potential is 111 mV more negative than the value for 40 wt % Pt-C, which is consistent with other studies.[347,349,354] It is worth noting that the more negative onset potential for ND-Fe_3O_4@mC-2/CB relative to 40 wt% Pt-C can be tolerated when considering the abundance and lower cost of ND-Fe_3O_4@mC-2/CB.

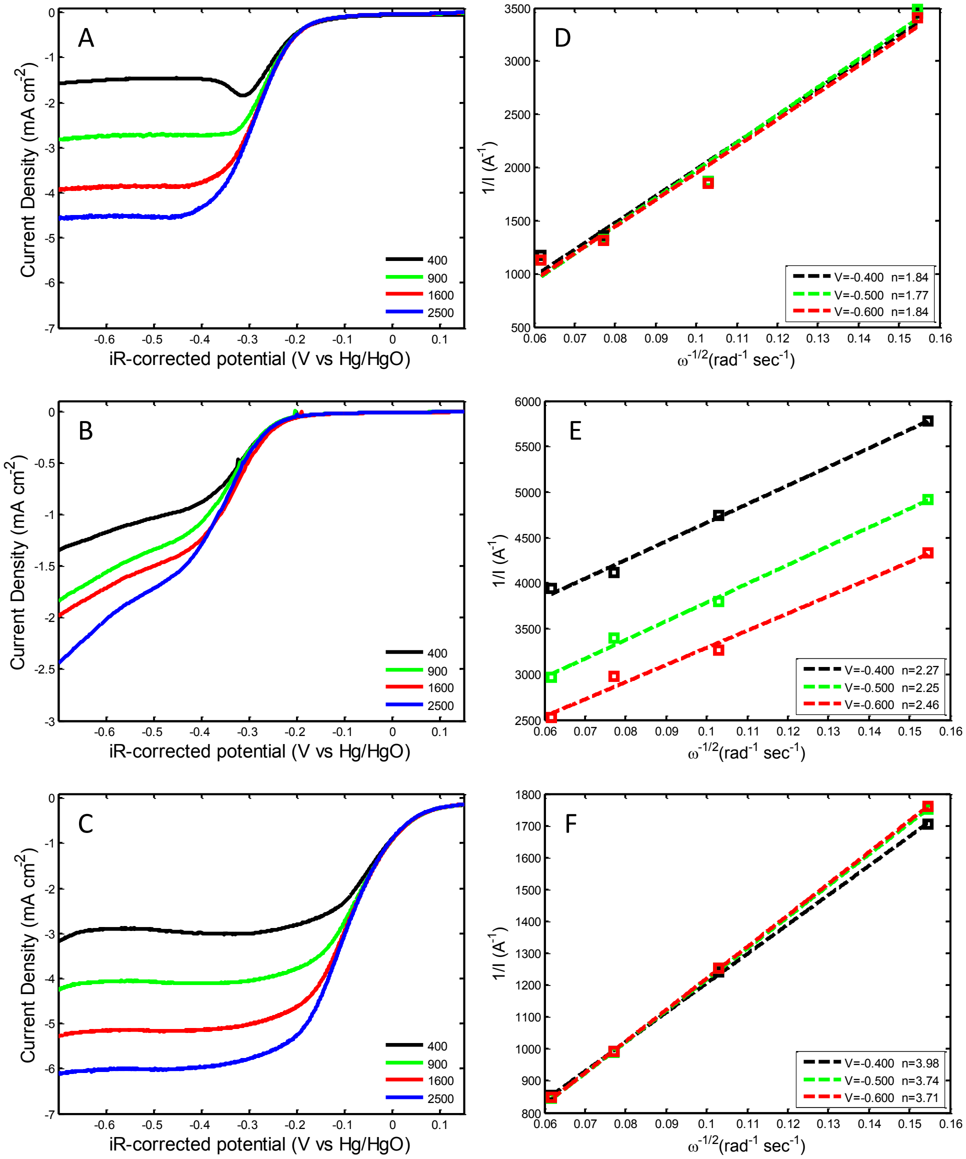

Figure 6-15 LSV curves for (A) Fe_3O_4 nanorods/CB, (B) ND-C shells/CB and (C) 40 wt% Pt-C in O_2-saturated, 0.1 M KOH at 10 mV s^{-1} for rotation speeds of 400, 900, 1600 and 2500 rpm. K-L plots for (D) Fe_3O_4 nanorods/CB, (E) ND-C nanoshells/CB and (F) 40 wt% Pt-C. The number of electrons transferred is calculated at -0.4, -0.5, and -0.6 V vs. Hg/HgO.

A comparison of the diffusion-limited current densities and the number of electrons transferred for ND-Fe_3O_4@mC-2/CB, Fe_3O_4 nanorods/CB, ND-C/CB and Pt-C is provided in Table 6-2. ND-Fe_3O_4@mC-2/CB exhibits a higher diffusion limiting current density (5.25 mA cm^{-2}) than both the Fe_3O_4 nanorods/CB (4.27 mA cm^{-2}) and ND-C/CB (1.48 mA cm^{-2}). Furthermore, the diffusion limiting current for ND-Fe_3O_4@mC-2/CB is superior to that of 40 wt% Pt-C (5.13 mA cm^{-2}). Table

6-2 also presents the number of electrons transferred during ORR based on K-L plots. There is a small variation in n, from 3.36 to 3.72, among ND-Fe_3O_4@mC-2/CB, ND-Fe_3O_4@mC-4/CB and ND-Fe_3O_4@mC-12/CB by varying the carbon shell thickness. The value of n follows the same trend as the limiting current density with n close to 4 for ND-Fe_3O_4@mC-2/CB.

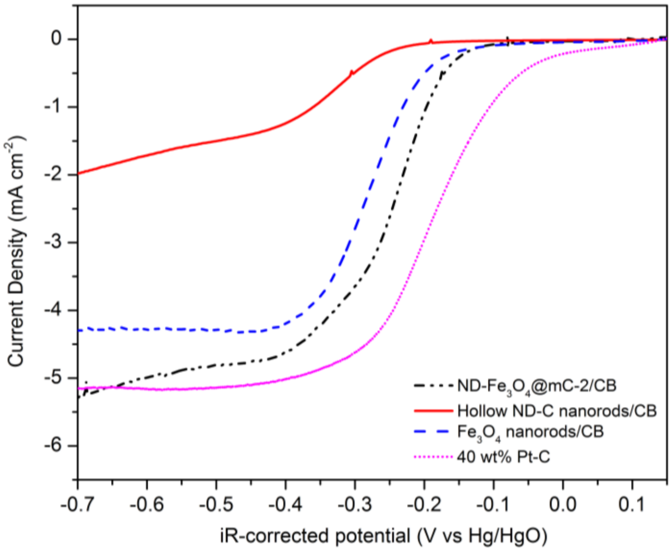

Figure 6-16 Representative LSV curves obtained for ND-Fe_3O_4@mC-2/CB, ND-carbon shells/CB, “bare” Fe_3O_4 nanorods/CB, and 40 wt% Pt-C at 1600 rpm and 10 mV s^{-1} in O_2-saturated, 0.1 M KOH.

The higher current density, more positive ORR onset potential and higher electron transfer number (~4) observed for ND-Fe_3O_4@mC-2/CB relative to the separate materials is attributed to the combined influences of the Fe_3O_4 core and ND-carbon shell. ND-C provides protection of the Fe_3O_4 nanorod surface, preserving the ORR active sites present on the surface of the nanorods. In addition, ND-C is a conductive surface modified with pyrrolic and pyridinic nitrogen, which explains the synergistic ORR effect of ND-C and Fe_3O_4 nanorods. Also, the larger pore radius of ND-Fe_3O_4@mC-2/CB (1.9 nm) compared with ND-Fe_3O_4@mC-4/CB and ND-Fe_3O_4@mC-12/CB, based on the BET results, may have a positive role by allowing more O_2 access to the active sites of the nanorods.

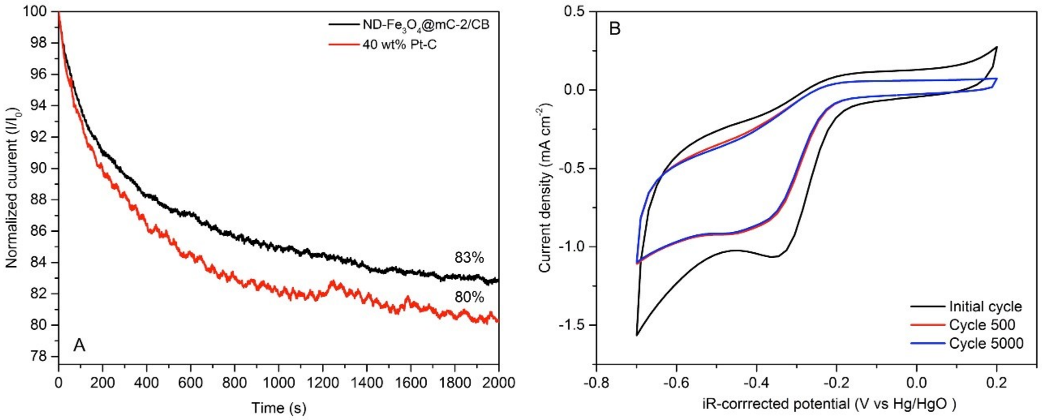

Figure 6-17 (A) Current–time (i-t) chronoamperometric responses for ND-Fe_3O_4@mC-2/CB and 40 wt% Pt-C at -0.3 V vs. Hg/HgO at 1600 rpm. (B) CV curves for ND-Fe_3O_4@mC-2/CB cycled in O_2-saturated, 0.1 M KOH at 100 mV s^{-1}.

To assess the short-term stability of ND-Fe_3O_4@mC-2/CB, the current-time chronoamperometric response was monitored in O_2-saturated, 0.1 M KOH at a scan rate of 1600 rpm and -0.3 V *vs.* Hg/HgO and compared with the response of the 40 wt% Pt-C catalyst (Figure 6-17(A)). Continuous O_2 reduction using ND-Fe_3O_4@mC-2/CB results in a 17% loss in the current density after 2000 s. Under identical conditions, the 40 wt% Pt-C catalyst showed a 20% decrease. Based upon these analyses, the short-term stability of ND-Fe_3O_4@mC-2/CB is slightly better than that for the 40 wt% Pt-C catalyst. To investigate the long-term performance of ND-Fe_3O_4@mC-2/CB, repetitive CV analysis was performed (-0.7 to 0.2 V *vs.* Hg/HgO in O_2-saturated, 0.1 M KOH) for 5000 cycles (25 h). A decrease in the ORR current density of ~30% at the peak potential (-0.34 V) occurs after 500 cycles (Figure 6-17(B)). However, the ORR current density and the onset potential do not change over the subsequent 4500 cycles, indicating excellent long-term ORR stability in the O_2-saturated alkaline solution It is generally accepted that the mechanisms and active sites associated with ORR behavior in Fe-oxide based catalysts is complex. We propose that the ORR activity of the ND-Fe_3O_4@mC system results from interplay between the properties of the Fe_3O_4 core and ND-C shell. While others have proposed that nitrogen centers on/in the nitrogen-doped carbon shell provide ORR active sites[364,371], our evaluation of the ND-C shells suggests otherwise. The ND-C shells are active towards ORR due to the pyrrolic and pyridic nitrogen sites. Also, they provide a conductive and high surface area hydrophilic catalytic surface.[99,364] Evaluation of the bare Fe_3O_4 nanorods indicates they are the primary catalytically active component of the present system. After etching the Fe_3O_4 core, the current density dropped by 71.8%, which explains the important role of Fe_3O_4 nanorods in oxygen chemisorption and the reduction of the ORR activation energy.[352]

The present study indicates that activity depends on the thickness of the ND-C coating. Thicker carbon layers (5 ± 0.5 nm and 2.2 ± 0.5 nm) diminish catalyst effectiveness, which is consistent with ORR active sites on the Fe_3O_4 surface being blocked. Very thin carbon layers ($< 1.5 \pm 0.2$ nm) increase the chance of Fe_3O_4 nanoparticle agglomeration, are non-uniform and have poor catalytic performance. For the present hybrid system, the optimal thickness is 1.5 nm obtained after 2 h; this is one of the thinnest layers reported.

6.4 Summary

A new microwave assisted method has been developed that provides well-defined α-Fe_2O_3 nanorods that are readily coated with controlled thicknesses of polydopamine via straightforward solution methods. Upon thermal treatment in flowing Ar, the polydopamine-coated nanorods are effectively converted to N-doped mesoporous carbon-coated (ND-C) Fe_3O_4 nanorods. Throughout the entire process the morphology of the nanorods is preserved. The resulting hybrid materials show promise as catalysts for ORR and provide insight into the synergistic impact of the Fe_3O_4/ND-C pairing and the importance of carbon shell thickness. Finally, the optimal system (ND-Fe_3O_4@mC-2 - 2 h of coating time) performed as well or better than commercial 40 wt% Pt-C catalysts with only 111 mV more negative ORR onset potential and superior limiting current density.

7 Conclusions and future directions

7.1 Conclusions

This thesis has presented efforts towards the development of non-precious metal bifunctional catalysts for zinc-air batteries (ZAB). A diverse selection of materials has been synthesized, each prepared using simple fabrication methods Three categories of catalytic materials, including transition metal oxide-based (Mn-Co mixed oxides and Fe_3O_4), transition metal nitride (Mn-N) and carbon-based materials (HMC), were developed and investigated as catalysts for air electrodes. Table 7-1 provides a summary and comparison of the half-cell ORR and OER performance and rechargeable ZAB tests for the best performing samples in each study, as well as the baseline catalysts. The electrocatalytic mechanism, influential factors for catalysis and electrode performance have been investigated in each study. These materials are promising alternatives to precious metal catalysts due to their low cost, simple fabrication methods and comparable ORR or OER activity vs. baseline and state-of-the-art bifunctional catalysts.

Table 7-1 Summary of oxygen electrochemistry and ZAB performance for the materials studied in this work.

	ORR onset V vs Hg/HgO	**ORR limiting current density (mA cm^{-2}) at -0.7 V vs Hg/HgO**	**OER onset V vs Hg/HgO**	**OER current density (mA cm^{-2}) at 0.7 V vs Hg/HgO**	**ZAB efficiency after 10 h cycling (%)**	**Battery load**
Mn-Co-PEDOT	-0.029	-3.79	0.350	6.00	ND	ND
Mn/Co:2.5-CB	0.076	-5.10	0.322	2.28	43.31	5 mA cm^{-2}
Mn-N-10/CB	-0.038	-3.52	0.330	2.81	52.68	7.5 mA cm^{-2}
HMC	-0.055	-4.95	0.365	4.53	55.39	2 mA cm^{-2}
ND-Fe_3O_4@mC-CB	0.024	-5.24	ND	ND	ND	ND
Pt/CB	0.086	-5.05	0.337	2.96	45.37	7.5 mA cm^{-2}
Ru-Pt/CB	0.140	-5.29	0.309	3.98	42.79	5 mA cm^{-2}

ND: not determined

The main achievements of this work include the following.

Mn-Co oxide work

i. The anodic electrodeposition process previously developed by our research group to synthesize high surface area Mn-Co mixed oxides has been optimized. The main advantage of this work is the use of a low cost technique to directly grow a non-precious metal catalyst on a carbon substrate without using post synthesis routes, such as spray coating and binders. For the optimized composition of Mn/Co:2.5, the catalyst (mixed with carbon black) has a bifunctional activity comparable to Pt/C and moderate stability in the alkaline solution. The bifunctional performance of the catalyst is attributed to the combined effect of high ORR activity Mn-oxide and high OER activity Co-oxide, as well as the high surface area of the fibrous rod-like structure, which provides more active sites for ORR/OER. ZAB results showed 43% battery efficiency after 10 h cycling at 5 mA cm^{-2}. Preliminary results for this work have been published in an MRS Proceedings.[115] The bulk of this work was reviewed and published in the Electrochimica Acta.[114]

Mn-nitride work

ii. Manganese nitride was fabricated as a bifunctional catalyst for ZABs for the first time via a simple route of nitridation of Mn powder in N_2 at 1100 °C. Detailed electrochemical and microstructural characterizations were performed on the synthesized powder. Phase quantification using Rietveld analysis showed that the sample heat treated for 10 h contained the largest fraction (~75%) of nitride phases (Mn_4N and $Mn_6N_{2.58}$). Interestingly, this sample exhibited more positive ORR onset potential and good long-term stability. The improved bifunctional activity corresponds to the active Mn-N phases which provides active sites for ORR/OER. This work has been submitted to ACS Applied Materials and Interfaces (November 10, 2016) and is under revision.

HMC and N-doped mesoporous carbon coated Fe_3O_4 nanorods work

iii. Carbonization of polymerized dopamine was used to synthesize a novel N-doped carbon mesostructured catalyst. The advantage of this work is the synthesis of a metal-free, high surface area bifunctional catalyst using a low cost technique. Electrochemical analysis showed improved long-term stability in comparison with the Pt/C baseline. Bifunctional activity of HMC particles is attributed to the high specific surface area (340 m^2 g^{-1}) and high concentration of pyridinic and pyrrolic nitrogen ORR active sites. This work has been published in the Nanoscale.[194] In order to enhance the activity of HMC, this structure is modified by incorporating Fe_3O_4 nanorods as a core material. A rapid low temperature microwave approach was used to generate Fe_2O_3 nanorods. Heating the PDA coated Fe_2O_3 nanorods leads to a new hybrid catalyst consisting of Fe_3O_4 nanorods coated with N-doped mesoporous carbon. The electrochemical results suggest that the N-doped carbon coating provides protection for the Fe_3O_4 nanorod surface, preserving the ORR active sites. In addition, HMC is a conductive surface, modified with pyrrolic and pyridinic nitrogen, which explains the ORR synergistic effect between the N-doped carbon coating and Fe_3O_4 nanorods. Shorter coating times (2 h) provide the optimum ORR performance, due to easy electrolyte access to the ORR active Fe_3O_4 core. Also, the 2 h coated sample showed stability up to at least 25 h in an alkaline solution. This work has been submitted to Nanotechnology and is under review (September 2, 2016).

7.2 Proposed future research

i. The anodic electrodeposition technique used in this work to deposit highly active bifunctional Mn-Co oxide catalysts is a simple and efficient technique to fabricate air electrodes for ZABs. However, changing the deposition parameters, such as concentration of the precursors, additives, pH, temperature and agitation results in a dramatic change in the physiochemical parameters of the deposits such as composition, valence state, structure, defects, morphology, surface area and conductivity. For example, as shown in Table 7-1, electrodepositing conductive polymer PEDOT enhances the OER current density significantly. However, PEDOT has poor stability in alkaline solutions and the layer dissolves in the electrolyte after long-term cycling. Modification of the fabrication process, such as depositing PEDOT as an intermediate layer between Mn oxide, may enhance performance, cyclability and stability.

ii. Mn-N was developed using a low cost technique. Good bifunctionally activity was shown in a ZAB. However, the catalyst surface area was low in comparison with the state-of-art bifunctional catalysts. Also, annealing in a SiO_2 crucible and N_2 atmosphere resulted in the formation of less active phases, such as MnO, and impurity phases. It may be beneficial to use a high surface area precursor (Mn nano-powder), an alternative non-reactive crucible and NH_3 atmosphere to form a single phase, high surface area catalyst.

iii. The activity of HMC particles depends heavily on the surface area and pyrrolic/pyridinic nitrogen active sites. Further investigation on the synthesis process to increase the density of active sites could be helpful to increase the bifunctional activity and stability of this structure.

iv. The performance of ZABs studied in this work can be dramatically increased by using an alternative, more corrosion resistant GDL. Currently, the performance of ZAB is limited to the cycle life of GDL, which is corroded at high battery loads during long term cycling. The corrosion of GDL results in the shifting of the three-phase boundary away from the catalytic layer, which degrades the charge-discharge performance. Developing hydrophobic, OER active and corrosion resistant Ni foam/plate could be a solution to this challenge.

v. ZABs are plagued by intrinsically limited power capability and rechargeability, mainly due to the slow kinetics and irreversibility of oxygen chemistry. A current possible approach could be using a hybrid battery with supercapacitors. ZABs can be used as the primary energy source during periods of light load, while supercapacitors can handle the peak powder requirements.

vi. A three electrode configuration, which uses a pair of air electrodes for ORR and OER separately, can provide better cycling performance as confirmed in an increasing numbers of studies.

vii. Other challenges such as Zn dendritic growth, carbonate precipitation and poor cycle life can be improved by using flowing electrolyte. The spent Zn particles, along with the KOH electrolyte, are replaced by circulating fresh material from an external tank.

References:

1 Y. Keho, *Energy Policy*, 2016, **91**, 233–246.

2 V. Caramia and B. Bozzini, *Mater. Renew. Sustain. Energy*, 2014, **3**, 28–40.

3 D. Linden and T. B. Reddy, *Linden's handbook of batteries*, McGraw-Hill, New York, Fourth., 2011.

4 L. R. Bard, Allen J and Faulkner, *Electrochemical Method*, John Wiley & Sons, New York, NY, 2nd edn., 2001.

5 F. Beck and P. Rüetschi, *Electrochim. Acta*, 2000, **45**, 2467–2482.

6 W. Tahil, *The Zinc Air Battery and the Zinc Economy : A Virtuous Circle*, 2007.

7 J. R. Owen, *Chem. Soc. Rev.*, 1997, **26**, 259–267.

8 V. Etacheri, R. Marom, R. Elazari, G. Salitra and D. Aurbach, *Energy Environ. Sci.*, 2011, **4**, 3243–3262.

9 J.-S. Lee, S. T. Kim, R. Cao, N.-S. Choi, M. Liu, K. T. Lee and J. Cho, *Adv. Energy Mater.*, 2011, **1**, 34–50.

10 Y. Li and H. Dai, *Chem. Soc. Rev.*, 2014, **43**, 5257–75.

11 M. Clark and D. G. Ivey, *Nanotechnology*, 2015, **26**, 1–9.

12 B. Babakhani and D. G. Ivey, *Electrochim. Acta*, 2011, **56**, 4753–4762.

13 K. M. Abraham and Z. Jiang, *J. Electrochem. Soc.*, 1996, **143**, 1–5.

14 T. Ogasawara, A. Débart, M. Holzapfel, P. Novák and P. G. Bruce, *J. Am. Chem. Soc.*, 2006, **128**, 1390–3.

15 Q. Xu and T. Kobayashi, *Advanced materials for clean energy*, Taylor a Francis Group, LLC, Boca Raton, 2015.

16 F. Cheng and J. Chen, *Chem. Soc. Rev.*, 2012, **41**, 2172–92.

17 Y. Feng and N. Alonso-Vante, *Phys. Status Solidi*, 2008, **245**, 1792–1806.

18 R. M. Dondelinger, *Biomed. Instrum. Technol.*, 2004, **38**, 100–110.

19 S. Amendola, *US Pat. 0021303 A1*, 2012.

20 B. Wang, *J. Power Sources*, 2005, **152**, 1–15.

21 P. Pei, K. Wang and Z. Ma, *Appl. Energy*, 2014, **128**, 315–324.

22 V. Neburchilov, H. Wang, J. J. Martin and W. Qu, *J. Power Sources*, 2010, **195**, 1271–1291.

23 L. Jörissen, *J. Power Sources*, 2006, **155**, 23–32.

24 D. U. Lee, P. Xu, Z. Cano, A. Ghorbani Kashkooli, M. G. Park and Z. Chen, *J. Mater. Chem. A*, 2016, **4**, 7107–7134.

25 T. Huh, G. Savaskan and J. W. Evans, *J. Appl. Electrochem.*, 1992, **22**, 916–921.

26 J. C. Salas-Morales and J. W. Evans, *J. Appl. Electrochem.*, 1992, **22**, 909–915.

27 K. Kinoshita, *Electrochemical Oxygen Technology*, Wiley, New York, 2nd edn., 1992.

28 K. Wang, P. Pei, Z. Ma, H. Xu, P. Li and X. Wang, *J. Power Sources*, 2014, **271**, 65–75.

29 K. Wang, P. Pei, Z. Ma, H. Chen, H. Xu, D. Chen and X. Wang, *J. Mater. Chem. A*, 2015, **3**, 22648–22655.

30 S. Siahrostami, V. Tripković, K. T. Lundgaard, K. E. Jensen, H. A. Hansen, J. S. Hummelshøj, J. S. G. Mýrdal, T. Vegge, J. K. Nørskov and J. Rossmeisl, *Phys. Chem. Chem. Phys.*, 2013, **15**, 6416.

31 D. Schröder, V. Laue and U. Krewer, *Comput. Chem. Eng.*, 2016, **84**, 217–225.

32 D. Schröder, T. Arlt, U. Krewer and I. Manke, *Electrochem. commun.*, 2014, **40**, 88–91.

33 K. Wang, P. Pei, Z. Ma, H. Chen, H. Xu, D. Chen and H. Xing, *J. Power Sources*, 2015, **296**, 40–45.

34 E. Deiss, F. Holzer and O. Haas, *Electrochim. Acta*, 2002, **47**, 3995–4010.

35 A. Latz, S. Clark, J. Stamm, T. Danner and B. Horstmann, *Theory-Based Development of Metal-Air Batteries*, 2016.

36 D. Wolfe, M. I. Us and P. B. Johnson, *US Pat. 0321970 A1*, 2012, 1–20.

37 Z. Yang, J. Zhang, M. C. W. Kintner-Meyer, X. Lu, D. Choi, J. P. Lemmon and J. Liu, *Chem. Rev.*, 2011, **111**, 3577–613.

38 T. Burchardt and M. Lanfranconi, *US Pat. 0027664 A1*, 2011.

39 T. Burchardt and M. Lanfranconi, *US Pat. 0027666 A1*, 2011.

40 T. Burchardt and R. F. Ngamga, *US Pat. 0199055 A1*, 2011.

41 G. Toussaint, P. Stevens, L. Akrour, R. Rouget and F. Fourgeot, *ECS Trans.*, 2010, **28**, 25–34.

42 M. Hilder, B. Winther-Jensen and N. B. Clark, *Electrochim. Acta*, 2012, **69**, 308–314.

43 J. F. Parker, E. S. Nelson, M. D. Wattendorf, C. N. Chervin, J. W. Long and D. R. Rolison, *ACS Appl. Mater. Interfaces*, 2014, **6**, 19471–19476.

44 J. F. Parker, C. N. Chervin, E. S. Nelson, D. R. Rolison and J. W. Long, *Energy Environ. Sci.*, 2014, **7**, 1117–1124.

45 M. N. Masri and A. A. Mohamad, *J. Electrochem. Soc.*, 2013, **160**, A715–A721.

46 X. G. Zhang, *J. Power Sources*, 2006, **163**, 591–597.

47 G.W. Heise, *US Pat. 1890178 A*, 1922.

48 Y. Takeshita, S. Fujimoto and M. Sudoh, *ECS Trans.*, 2013, **50**, 3–12.

49 D. B. Zhou and H. Vander Poorten, *Electrochim. Acta*, 1995, **40**, 1819–1826.

50 R. Schweiss, C. Meiser, T. Damjanovic, I. Galbiati and N. Haak, *SGL Gr.*, 2016, 1–10.

51 C. W. Lee, K. Sathiyanarayanan, S. W. Eom, H. S. Kim and M. S. Yun, *J. Power Sources*, 2006, **160**, 161–164.

52 C. W. Lee, K. Sathiyanarayanan, S. W. Eom and M. S. Yun, *J. Power Sources*,

2006, **160**, 1436–1441.

53 S. M. Lee, Y. J. Kim, S. W. Eom, N. S. Choi, K. W. Kim and S. B. Cho, *J. Power Sources*, 2013, **227**, 177–184.

54 Y. Da Cho and G. T. K. Fey, *J. Power Sources*, 2008, **184**, 610–616.

55 W. Gan, D. Zhou, J. Zhao and L. Zhou, *J. Appl. Electrochem.*, 2015, **45**, 913–919.

56 H. S. Kim, Y. N. Jo, W. J. Lee, K. J. Kim and C. W. Lee, *Electroanalysis*, 2015, **27**, 517–523.

57 R. Othman, W. J. Basirun, A. H. Yahaya and A. K. Arof, *J. Power Sources*, 2001, **103**, 34–41.

58 W. H. Zhu, B. A. Poole, D. R. Cahela and B. J. Tatarchuk, *J. Appl. Electrochem.*, 2003, **33**, 29–36.

59 M. G. Park, *Thesis, Univ. Waterloo*, 2015, 1–120.

60 Y. Xu, X. Xu, G. Li and Z. Zhang, *Int. J. Electrochem*, 2013, **8**, 11805–11813.

61 M. Maja, C. Orecchia, M. Strano, P. Tosco and M. Vanni, *Electrochim. Acta*, 2000, **46**, 423–432.

62 G. A. Somorjai, K. R. McCrea and J. Zhu, *Top. Catal.*, 2002, **18**, 157–166.

63 H. T. Chung, J. H. Won and P. Zelenay, *Nat. Commun.*, 2013, **4**, 1–5.

64 F. Calle-Vallejo, J. I. Martínez and J. Rossmeisl, *Phys. Chem. Chem. Phys.*, 2011, **13**, 15639–43.

65 M. Busch, N. B. Halck, U. Kramm, S. Siahrostami, P. Krtil and J. Rossmeisl, *Nano Energy*, 2016, **29**, 126–135.

66 J. Zhang, Z. Zhao, Z. Xia and L. Dai, *Nat. Nanotechnol.*, 2015, **10**, 444–452.

67 J. K. Nørskov, J. Rossmeisl, A. Logadottir, L. Lindqvist, J. R. Kitchin, T. Bligaard and H. Jónsson, *J. Phys. Chem. B*, 2004, **108**, 17886–17892.

68 R. J. Gilliam, J. W. Graydon, D. W. Kirk and S. J. Thorpe, *Int. J. Hydrogen Energy*, 2007, **32**, 359–364.

69 A. V Wolf, *Aqueous Solutions and Body Fluids*, Harper and Row, New York, 1966.

70 A. A. Mainar, O. Leonet, M. Bengoechea, B. Iker, I. de Meatza, A. Kvasha, A. Guerfi and J. A. Blázquez, *Int. J. energy Res.*, 2016, **40**, 1032–1049.

71 M. Sato, M. Ohta and M. Sakaguchi, *Electrochim. Acta*, 1990, **35**, 945–950.

72 D. Schröder, N. N. Sinai Borker, M. König and U. Krewer, *J. Appl. Electrochem.*, 2015, **45**, 427–437.

73 N. Vassal, E. Salmon and J. F. Fauvarque, *Electrochim. Acta*, 2000, **45**, 1527–1532.

74 C. C. Yang and S. J. Lin, *J. Power Sources*, 2002, **112**, 497–503.

75 C. C. Yang, S. J. Lin and S. T. Hsu, *J. Power Sources*, 2003, **122**, 210–218.

76 A. A. Mohamad, *J. Power Sources*, 2006, **159**, 752–757.

77 J. Fu, D. U. Lee, F. M. Hassan, Z. Bai, M. G. Park and Z. Chen, *Adv. Mater.*, 2015, **27**, 5617–5622.

78 J. Fu, J. Zhang, X. Song, H. Zarrin, X. Tian, J. Qiao, L. Rasen, K. Li and Z. Chen, *Energy Environ. Sci. Energy Enviro*, 2016, **9**, 663–670.

79 M. Kar, B. Winther-Jensen, M. Armand, T. J. Simons, O. Winther-Jensen, M. Forsyth and D. R. MacFarlane, *Electrochim. Acta*, 2016, **188**, 461–471.

80 M. Kar, B. Winther-Jensen, M. Forsyth and D. R. MacFarlane, *Phys. Chem. Chem. Phys.*, 2014, **16**, 10816–22.

81 M. Kar, B. Winther-Jensen, M. Forsyth and D. R. MacFarlane, *Phys. Chem. Chem. Phys.*, 2013, **15**, 7191–7.

82 T. J. Simons, P. C. Howlett, A. A. J. Torriero, D. R. Macfarlane and M. Forsyth, *J. Phys. Chem.*, 2013, **117**, 2662–2669.

83 M. Xu, D. G. Ivey, W. Qu and Z. Xie, *J. Power Sources*, 2014, **252**, 327–332.

84 M. Xu, D. G. Ivey, Z. Xie, W. Qu and E. Dy, *Electrochim. Acta*, 2013, **97**, 289–295.

85 M. Xu, D. G. Ivey, Z. Xie and W. Qu, *J. Power Sources*, 2015, **283**, 358–371.

86 E. Fabbri, A. Habereder, K. Waltar, R. Kötz and T. J. Schmidt, *Catal. Sci. Technol.*, 2014, **4**, 3800–3821.

87 M. Hamdani, R. N. Singh and P. Chartier, *Int. J. Electrochem. Sci.*, 2010, **5**, 556–577.

88 G. Liu, X. Li, J.-W. Lee and B. N. Popov, *Catal. Sci. Technol.*, 2011, **1**, 207–217.

89 A. Morozan, B. Jousselme and S. Palacin, *Energy Environ. Sci.*, 2011, **4**, 1238–1254.

90 G. Q. Zhang, X. G. Zhang and Y. G. Wang, *Carbon N. Y.*, 2004, **42**, 3097–3102.

91 F. P. Hu, X. G. Zhang, F. Xiao and J. L. Zhang, *Carbon N. Y.*, 2005, **43**, 2931–2936.

92 J.-J. Han, N. Li and T.-Y. Zhang, *J. Power Sources*, 2009, **193**, 885–889.

93 T. Wang, M. Kaempgen, P. Nopphawan, G. Wee, S. Mhaisalkar and M. Srinivasan, *J. Power Sources*, 2010, **195**, 4350–4355.

94 M. Chatenet, L. Genies-Bultel, M. Aurousseau, R. Durand and F. Andolfatto, *J. Appl. Electrochem.*, 2002, **32**, 1131–1140.

95 V. M. Dhavale and S. Kurungot, *ACS Catal.*, 2015, **5**, 1445–1452.

96 Z. Cui, H. Chen, M. Zhao and F. J. DiSalvo, *Nano Lett.*, 2016, **16**, 2560–2566.

97 X. Wu, F. Chen, Y. Jin, N. Zhang and R. L. Johnston, *ACS Appl. Mater. Interfaces*, 2015, **7**, 17782–17791.

98 Y. Jin, F. Chen, Y. Lei and X. Wu, *ChemCatChem*, 2015, **7**, 2377–2383.

99 Y. Jin and F. Chen, *Electrochim. Acta*, 2015, **158**, 437–445.

100 Z. Guo, C. Li, W. Li, H. Guo, X. Su, P. He, Y. Wang and Y. Xia, *J. Mater. Chem. A*, 2016, **4**, 6282–6289.

101 J. Suntivich, H. a Gasteiger, N. Yabuuchi, H. Nakanishi, J. B. Goodenough

and Y. Shao-Horn, *Nat. Chem.*, 2011, **3**, 546–50.

102 P. Li, C. Hu, T. Lee, W. Chang and T. Hai, *J. Power Sources*, 2014, **269**, 88–97.

103 P. Li, C. Hu, H. Noda and H. Habazaki, *J. Power Sources*, 2015, **298**, 102–113.

104 Z. Wei, W. Huang, S. Zhang and J. Tan, *J. Power Sources*, 2000, **91**, 83–85.

105 Q. Wu, L. Jiang, L. Qi, E. Wang and G. Sun, *Int. J. Hydrogen Energy*, 2014, **39**, 3423–3432.

106 T.-H. Yang, S. Venkatesan, C.-H. Lien, J.-L. Chang and J.-M. Zen, *Electrochim. Acta*, 2011, **56**, 6205–6210.

107 G. Q. Zhang and X. G. Zhang, *Electrochim. Acta*, 2004, **49**, 873–877.

108 Y.-J. Huang and W.-S. Li, *J. Inorg. Mater.*, 2013, **28**, 341–346.

109 Y. Huang, Y. Lin and W. Li, *Electrochim. Acta*, 2013, **99**, 161–165.

110 Z. Chen, A. Yu, R. Ahmed, H. Wang and H. Li, *Electrochim. Acta*, 2012, **69**, 295–300.

111 D. L. Liu, J. N. Cheng and J. J. Han, *Adv. Mater. Res.*, 2013, **724–725**, 808–812.

112 Y. L. Cao, H. X. Yang, X. P. Ai and L. F. Xiao, *J. Electroanal. Chem.*, 2003, **557**, 127–134.

113 J. Lee, G. S. Park, S. T. Kim, R. Cao and M. Liu, *Nano Lett.*, 2011, **11**, 5362–5366.

114 E. Davari, A. D. A. D. Johnson, A. Mittal, M. Xiong and D. G. Ivey, *Electrochim. Acta*, 2016, **211**, 735–743.

115 E. Davari and D. G. Ivey, *MRS Proc.*, 2015, **1777**, 1–6.

116 A. Sumboja, X. Ge, F. W. T. Goh, B. Li, D. Geng, T. S. A. Hor, Y. Zong and Z. Liu, *Chempluschem*, 2015, **80**, 1341–1346.

117 J.-S. Lee, T. Lee, H.-K. Song, J. Cho and B.-S. Kim, *Energy Environ. Sci.*,

2011, **4**, 4148–4154.

118 F. W. T. Goh, Z. Liu, X. Ge, Y. Zong, G. Du and T. S. A. Hor, *Electrochim. Acta*, 2013, **114**, 598–604.

119 Q. Wu, L. Jiang, L. Qi, L. Yuan, E. Wang and G. Sun, *Electrochim. Acta*, 2014, **123**, 167–175.

120 X. Xie, Z. Ma, X. Ma, Q. Ren and V. M. Schmidt, *J. Electrochem. Soc.*, 2007, **154**, 733–738.

121 J. Liu, L. Jiang, Q. Tang, E. Wang, L. Qi, S. Wang and G. Sun, *Appl. Catal. B Environ.*, 2014, **148–149**, 212–220.

122 Y. Zhan, G. Du, S. Yang, C. Xu, M. Lu, Z. Liu and J. Y. Lee, *ACS Appl. Mater. Interfaces*, 2015, **7**, 12930–12936.

123 Z. Jiang, Z.-J. Jiang, T. Maiyalagan and A. Manthiram, *J. Mater. Chem. A*, 2016, **4**, 5877–5889.

124 J. Song, C. Zhu, S. Fu, Y. Song, D. Du and Y. Lin, *J. Mater. Chem. A Mater. energy Sustain.*, 2016, **4**, 4864–4870.

125 X. Zhang, R. Liu, Y. Zang, G. Liu and G. Wang, *Chem. Commun.*, 2016, **52**, 5946–5949.

126 Z. Wang, B. Li, X. Ge, F. W. T. Goh, X. Zhang, G. Du, D. Wuu, Z. Liu, T. S. Andy Hor, H. Zhang and Y. Zong, *Small*, 2016, **12**, 2580–2587.

127 X. Liu, M. Park, M. G. Kim, S. Gupta, X. Wang, G. Wu and J. Cho, *Nano Energy*, 2016, **20**, 315–325.

128 M. Gong and H. Dai, *Nano Res.*, 2015, **8**, 23–39.

129 Y. Li, M. Gong, Y. Liang, J. Feng, J.-E. Kim, H. Wang, G. Hong, B. Zhang and H. Dai, *Nat. Commun.*, 2013, **4**, 1805–1822.

130 D. Kubo, K. Tadanaga, A. Hayashi and M. Tatsumisago, *J. Mater. Chem. A*, 2013, **1**, 6804–6809.

131 X. Liu, W. Liu, M. Ko, M. Park, M. G. Kim and P. Oh, *Adv. Funct. Mater.*,

2015, **25**, 5799–5808.

132 S. Chen, J. Duan, P. Bian, Y. Tang and R. Zheng, *Adv. Energy Mater.*, 2015, **5**, 1500936–1500943.

133 G. Nam, J. Park, C. Min, O. Pilgun, P. Suhyeon, K. Min Gyu, J. Cho, P. Neojung, J. Cho and J. Lee, *ACS Nano*, 2015, **9**, 6493–6501.

134 N. Ma, X. Yang, X. She, L. Zhang, Z. Peng, X. Yao and D. Yang, *J. Mater. Chem. A*, 2016, **4**, 6376–6384.

135 X. Liu, M. Park, M. G. Kim, S. Gupta, G. Wu and J. Cho, *Angew. Chemie Int. Ed.*, 2015, **54**, 9654–9658.

136 S. Luo and D. B. Zhou, *J. Electrochem. Soc.*, 2014, **161**, 23–27.

137 X. Li, A. L. Zhu, W. Qu, H. Wang, R. Hui, L. Zhang and J. Zhang, *Electrochim. Acta*, 2010, **55**, 5891–5898.

138 J. Zhang and W. Chen, *Adv. Mater. Res.*, 2012, **347**–**353**, 3621–3625.

139 M. Prabu, P. Ramakrishnan, H. Nara, T. Momma, T. Osaka and S. Shanmugam, *ACS Appl. Mater. Interfaces*, 2014, **6**, 16545–16555.

140 D. Wang, X. Chen, D. G. Evans and W. Yang, *Nanoscale*, 2013, **5**, 5312–5.

141 G. Du, X. Liu, Y. Zong, T. S. A. Hor, A. Yu and Z. Liu, *Nanoscale*, 2013, **5**, 4657–61.

142 M. Prabu, P. Ramakrishnan and S. Shanmugam, *Electrochem. commun.*, 2014, **41**, 59–63.

143 X. Ge, Z. Zhang, S. H. Lim, B. Li, X. Wang and Z. Liu, *ACS Appl. Mater. Interfaces*, 2014, **6**, 12684−12691.

144 T. Maiyalagan, K. A Jarvis, S. Therese, P. J. Ferreira and A. Manthiram, *Nat. Commun.*, 2014, **5**, 3943–3950.

145 F. Cheng, J. Shen, B. Peng, Y. Pan, Z. Tao and J. Chen, *Nat. Chem.*, 2011, **3**, 79–84.

146 K.-N. Jung, S. M. Hwang, M.-S. Park, K. J. Kim, J.-G. Kim, S. X. Dou, J. H.

Kim and J.-W. Lee, *Sci. Rep.*, 2015, **5**, 1–10.

147 F. Cheng, J. Shen, B. Peng, Y. Pan, Z. Tao and J. Chen, *Nat. Chem.*, 2011, **3**, 79–84.

148 C. Ma, N. Xu, J. Qiao, S. Jian and J. Zhang, *Int. J. Hydrogen Energy*, 2016, **41**, 9211–9218.

149 B. Li, X. Ge, F. W. T. Goh, T. S. A. Hor, D. Geng, G. Du, Z. Liu, J. Zhang, X. Liu and Y. Zong, *Nanoscale*, 2015, **7**, 1830–1838.

150 M. Prabu, P. Ramakrishnan and S. Shanmugam, *Electrochem. commun.*, 2014, **41**, 59–63.

151 M. Prabu, K. Ketpang and S. Shanmugam, *Nanoscale*, 2014, **6**, 3173.

152 L. Li, C. Liu, G. He, D. E. Fan and A. Manthiram, *Energy Environ. Sci.*, 2015, **8**, 3274–3282.

153 T. An, X. Ge, T. S. A. Hor, F. W. T. Goh, D. Geng, G. Du, Y. Zhan, Z. Liu and Y. Zong, *RSC Adv.*, 2015, **5**, 75773–75780.

154 D. U. Lee, M. G. Park, H. W. Park, M. H. Seo, X. Wang and Z. Chen, *ChemSusChem*, 2015, **8**, 3129–3138.

155 D. U. Lee, J. Scott, H. W. Park, S. Abureden, J. Y. Choi and Z. Chen, *Electrochem. commun.*, 2014, **43**, 109–112.

156 D. U. Lee, J. Y. Choi, K. Feng, H. W. Park and Z. Chen, *Adv. Energy Mater.*, 2014, **4**, 1–5.

157 S. K. Singh, V. M. Dhavale and S. Kurungot, *ACS Appl. Mater. Interfaces*, 2015, **7**, 21138–21149.

158 Y. Zhan, C. Xu, M. Lu, Z. Liu and J. Y. Lee, *J. Mater. Chem. A*, 2014, **2**, 16217–16223.

159 Y. Wang, X. Ma, L. Lu, Y. He, X. Qi and Y. Deng, *Int. J. Hydrogen Energy*, 2013, **38**, 13611–13616.

160 C. Li, X. Han, F. Cheng, Y. Hu, C. Chen and J. Chen, *Nat. Commun.*, 2015, **6**,

7345–7353.

161 G. Li, M. A. Mezaal, K. Zhang and L. Lei, *Int. J. Electrochem. Sci.*, 2015, **10**, 5395–5404.

162 J. F. Yuan, Xiao-Zi, Wie Qu, Xinge Zhang, Peter Yao, *ECS Trans.*, 2013, **45**, 105–112.

163 N. Li, X. Yan, Y. Jin, S. Li and B. Lin, *J. Appl. Electrochem.*, 1999, **29**, 1351–1354.

164 R. E. Carbonio, C. Fierro, D. Tryk, D. Scherson and E. Yeager, *J. Power Sources*, 1988, **22**, 387–398.

165 A. S. Bhalla, R. Guo and R. Roy, *Mater. Res. Innov.*, 2000, **4**, 3–26.

166 M. Yuasa, M. Nishida, T. Kida, N. Yamazoe and K. Shimanoe, *J. Electrochem. Soc.*, 2011, **158**, A605–A610.

167 H. Ma and B. Wang, *RSC Adv.*, 2014, **4**, 46084–46092.

168 S. Ahn, K. Kim, H. Kim, S. Nam and S. Eom, *Phys. Scr.*, 2010, **T139**, 1–4.

169 K.-N. Jung, J.-H. Jung, W. B. Im, S. Yoon, K.-H. Shin and J.-W. Lee, *ACS Appl. Mater. Interfaces*, 2013, **5**, 9902–9907.

170 J. Hu, L. Wang, L. Shi and H. Huang, *J. Power Sources*, 2014, **269**, 144–151.

171 J. Hu, L. Wang, L. Shi and H. Huang, *Electrochim. Acta*, 2015, **161**, 115–123.

172 G. Li, M. A. Mezaal, R. Zhang, K. Zhang, W. Liu and L. Lei, *Int. J. Electrochem. Sci.*, 2015, **10**, 8412–8422.

173 Y. Lee, P. Peng, W. Chang and C. Huang, *J. Taiwan Inst. Chem. Eng.*, 2014, **45**, 2334–2339.

174 X. Wang, P. J. Sebastian, M. A. Smit, H. Yang and S. A. Gamboa, *J. Power Sources*, 2003, **124**, 278–284.

175 A. Weidenkaff, S. G. Ebbinghaus and T. Lippert, *Chem. Mater.*, 2002, **14**, 1797–1805.

176 N. Wu, W. Liu and S. Su, *Electrochim. Acta*, 2003, **48**, 1567–1571.

177 C. Zhu, A. Nobuta, I. Nakatsugawa and T. Akiyama, *Int. J. Hydrogen Energy*, 2013, **8**, 13238–13248.

178 Z. Chen, A. Yu, D. Higgins, H. Li and H. Wang, *Nano Lett.*, 2012, **12**, 1946–1952.

179 S.-W. Eom, S.-Y. Ahn, I.-J. Kim, Y.-K. Sun and H.-S. Kim, *J. Electroceramics*, 2009, **23**, 382–386.

180 D. U. Lee, M. G. Park, H. W. Park, M. H. Seo, V. Ismayilov, R. Ahmed and Z. Chen, *Electrochem. commun.*, 2015, **60**, 38–41.

181 D. U. Lee, H. W. Park, M. G. Park, V. Ismayilov and Z. Chen, *ACS Appl. Mater. Interfaces*, 2015, **7**, 902–910.

182 S. W. Eom, S. Y. Ahn, C. W. Lee, Y. K. Sun and M. S. Yun, *Solid State Phenom.*, 2007, **124–126**, 1055–1058.

183 J. Jung, M. Risch, S. Park, M. G. Kim, G. Nam, H. Jeong, Y. Shao-horn and J. Cho, *Energy Environ. Sci.*, 2016, **9**, 176–183.

184 A. Vignesh, M. Prabu and S. Shanmugam, *ACS Appl. Mater. Interfaces*, 2016, **8**, 6019−6031.

185 M. Prabu, P. Ramakrishnan and P. Ganesan, *Nano Energy*, 2015, **15**, 92–103.

186 L. Dai, Y. Xue, L. Qu, H.-J. Choi and J.-B. Baek, *Chem. Rev.*, 2015, **115**, 4823–4892.

187 Q. Li, R. Cao, J. Cho and G. Wu, *Adv. Energy Mater.*, 2014, **4**, 1–19.

188 H.-W. Liang, X. Zhuang, S. Brüller, X. Feng and K. Müllen, *Nat. Commun.*, 2014, **5**, 4973.

189 Y. Sun, C. Li and G. Shi, *J. Mater. Chem.*, 2012, **22**, 12810–12816.

190 M. Wang, Z. Fang, K. Zhang, J. Fang, F. Qin, Z. Zhang, J. Li, Y. Liu and Y. Lai, *Nanoscale*, 2016, **8**, 11398–11402.

191 N. Gupta, T. Toh, M. W. Fatt, S. Mhaisalkar and M. Srinivasan, *J. Solid State Electrochem.*, 2012, **16**, 1585–1593.

192 Y. Liu, S. Chen, X. Quan, H. Yu, H. Zhao, Y. Zhang and G. Chen, *J. Phys. Chem. C*, 2013, **117**, 14992–14998.

193 S.-W. Eom, C.-W. Lee, M.-S. Yun and Y.-K. Sun, *Electrochim. Acta*, 2006, **52**, 1592–1595.

194 L. Hadidi, E. Davari, M. Iqbal, T. K. T. Purkait, D. G. Ivey and J. G. C. Veinot, *Nanoscale*, 2015, **7**, 20547–20556.

195 S. Müller, F. Holzer, H. Arai and O. Haas, *J. New Mater. Electrochem. Syst.*, 1999, 2, 227–232.

196 D. Higgins, Z. Chen, D. U. Lee and Z. Chen, *J. Mater. Chem. A*, 2013, **1**, 2639–2645.

197 D. U. Lee, H. W. Park, D. Higgins, L. Nazar and Z. Chen, *J. Electrochem. Soc.*, 2013, **160**, F910–F915.

198 B. J. Kim, D. U. Lee, J. Wu, D. Higgins, A. Yu and Z. Chen, *J. Phys. Chem. C*, 2013, **117**, 26501–26508.

199 G. Nam, J. Park, S. T. Kim, D. Shin, N. Park, Y. Kim, J.-S. Lee and J. Cho, *Nano Lett.*, 2014, **14**, 1870–6.

200 B. Li, D. Geng, X. S. Lee, X. Ge, J. Chai, Z. Wang, J. Zhang, Z. Liu, T. S. A. Hor and Y. Zong, *Chem. Commun.*, 2015, **51**, 8841–8844.

201 T. Y. Ma, J. Ran, S. Dai, M. Jaroniec and S. Z. Qiao, *Angew. Chemie - Int. Ed.*, 2015, **54**, 4646–4650.

202 M. Wu, J. Qiao, K. Li, X. Zhou, Y. Liu and J. Zhang, *Green Chem.*, 2016, **18**, 2699–2709.

203 G. S. Park, J.-S. Lee, S. T. Kim, S. Park and J. Cho, *J. Power Sources*, 2013, **243**, 267–273.

204 S. Zhu, Z. Chen, B. Li, D. Higgins, H. Wang and H. Li, *Electrochim. Acta*, 2011, **56**, 5080–5084.

205 Q. Liu, Y. Wang, L. Dai and J. Yao, *Adv. Mater.*, 2016, **28**, 3000–3006.

206 B. Li, D. Geng, X. S. Lee, X. Ge, J. Chai, Z. Wang, J. Zhang, Z. Liu, T. S. A. Hor and Y. Zong, *Chem. Commun.*, 2015, **51**, 8841–8844.

207 G. S. Park, J. S. Lee, S. T. Kim, S. Park and J. Cho, *J. Power Sources*, 2013, **243**, 267–273.

208 B. Li, Y. Chen, X. Ge, J. Chai, X. Zhang, T. S. A. Hor, G. Du, Z. Liu, H. Zhang and Y. Zong, *Nanoscale*, 2016, **8**, 5067–5075.

209 G. Girishkumar, B. McCloskey, A. C. Luntz, S. Swanson and W. Wilcke, *J. Phys. Chem. Lett.*, 2010, **1**, 2193–2203.

210 Y.-C. Lu, B. M. Gallant, D. G. Kwabi, J. R. Harding, R. R. Mitchell, M. S. Whittingham and Y. Shao-Horn, *Energy Environ. Sci.*, 2013, **6**, 750–768.

211 J. Goldstein, D. E. Newbury, D. C. Joy, C. E. Lyman, P. Echlin, E. Lifshin and L. Sawyer, *Scanning Electron Microscopy and X-ray Microanalysis*, Springer Science & Business Media, 3rd edn., 2013.

212 D. B. Williams and C. B. Carter, *The Transmission electron microscope*, Spriner Science and Business Media, 3rd edn., 2009.

213 B. D. Cullity, *Elements of X-ray Diffraction*, Addison-Wesley Publishing Company, 1978, 2nd edn., 1978.

214 P. van der Heide, *No X-ray photoelectron spectroscopy : an introduction to principles and practices*, Hoboken, N.J. : Wiley, 2012.

215 L. Van Vaeck, A. Adriaens and R. Gijbels, *Mass Spectrom. Rev.*, 1999, **18**, 1–47.

216 S. Brunauer, P. H. Emmett and E. Teller, *J. Am. Chem. Soc.*, 1938, **60**, 309–319.

217 A. W. Coats and J. P. Redfern, *Analyst*, 1963, **88**, 906–924.

218 J. Griffiths and J. A. De Haseth, *Fourier Transform Infrared Spectrometry*, John Wiley & Sons, 2007.

219 D. J. Gardiner and P. R. Graves, *Practical Raman Spectroscopy*, Springer

Berlin Heidelberg, 1989.

220 K. Baejung, *Thesis, Univ. Waterloo*, 2013, 1–97.

221 L. Jörissen, *J. Power Sources*, 2006, **155**, 23–32.

222 C. Song and J. Zhang, in *PEM Fuel Cell Electrocatalysts and Catalyst Layers*, ed. J. Zhang, Springer London, 2008, pp. 89–134.

223 Y.-M. Chang, P.-W. Wu, C.-Y. Wu and Y.-C. Hsieh, *J. Power Sources*, 2009, **189**, 1003–1007.

224 X. Wu and K. Scott, *J. Power Sources*, 2012, **206**, 14–19.

225 P. W. Menezes, A. Indra, N. R. Sahraie, A. Bergmann, P. Strasser and M. Driess, *ChemSusChem*, 2015, **8**, 164–171.

226 E. Rios, J.-L. Gautier, G. Poillerat and P. Chartier, *Electrochim. Acta*, 1998, **44**, 1491–1497.

227 J. Du, C. Chen, F. Cheng and J. Chen, *Inorg. Chem.*, 2015, **54**, 5467–5474.

228 A. Zhao, J. Masa, W. Xia, A. Maljusch, M. Willinger, G. Clavel, K. Xie, R. Schlo, W. Schuhmann and M. Muhler, *J. Am. Chem. Soc.*, 2014, **136**, 7551–7554.

229 E. M. Benbow, S. P. Kelly, L. Zhao, J. W. Reutenauer and S. L. Suib, *J. Phys. Chem. C*, 2011, **115**, 22009–22017.

230 F. Cheng, J. Shen, W. Ji, Z. Tao and J. Chen, *ACS Appl. Mater. Interfaces*, 2009, **1**, 460–466.

231 M. S. Burke, M. G. Kast, L. Trotochaud, A. M. Smith and S. W. Boettcher, *J. Am. Chem. Soc.*, 2015, **137**, 3638–3648.

232 T. Grewe, X. Deng, C. Weidenthaler, F. Schüth and H. Tüysüz, *Chem. Mater.*, 2013, **25**, 4926–4935.

233 T. W. Kim, M. A. Woo, M. Regis and K. Choi, *J. Phys. Chem. Lett.*, 2014, **5**, 2370–2374.

234 C. J. Clarke, G. J. Browning and S. W. Donne, *Electrochim. Acta*, 2006, **51**,

5773–5784.

235 E. Davari and D. G. Ivey, in *MRS Proceedings*, 2015, vol. 1777, pp. 1–6.

236 C. Han, X. Bo, Y. Zhang, M. Li and L. Guo, *J. Power Sources*, 2014, **272**, 267–276.

237 H. T. Chung, J. H. Won and P. Zelenay, *Nat. Commun.*, 2013, **4**, 1–5.

238 M. Ndjeri, S. Peulon, S. Bach and A. Chaussé, *Electrochim. Acta*, 2011, **56**, 8564–8570.

239 D. A. Bronson, *Interdiffus. Syst. (Nickel(X)-Oxide), Magnesium-Oxide*, 1972, 1–176.

240 W. D. Callister, *Materials Science and Engineering*, John Wiley & Sons, Inc, 7th edn., 2007.

241 Q. Tang, L. Jiang, J. Liu, S. Wang and G. Sun, *ACS Catal.*, 2014, **4**, 457–463.

242 M. Nakayama, K. Suzuki, K. Okamura, R. Inoue, L. Athouël, O. Crosnier and T. Brousse, *J. Electrochem. Soc.*, 2010, **157**, A1067–A1072.

243 M. S. El-Deab and T. Ohsaka, *Angew. Chemie*, 2006, **45**, 5963–5966.

244 J. S. Lee, G. S. Park, H. Il Lee, S. T. Kim, R. Cao, M. Liu and J. Cho, *Nano Lett.*, 2011, **11**, 5362–5366.

245 H.-Y. Su, Y. Gorlin, I. C. Man, F. Calle-Vallejo, J. K. Nørskov, T. F. Jaramillo and J. Rossmeisl, *Phys. Chem. Chem. Phys.*, 2012, **14**, 14010–22.

246 J.-S. Lee, S. T. Kim, R. Cao, N.-S. Choi, M. Liu, K. T. Lee and J. Cho, *Adv. Energy Mater.*, 2011, **1**, 34–50.

247 H. Ma and B. Wang, *RSC Adv.*, 2014, **4**, 46084–46092.

248 Q. Wu, L. Jiang, Q. Tang, J. Liu, S. Wang and G. Sun, *Electrochim. Acta*, 2013, **91**, 314–322.

249 E. Ríos, S. Abarca, P. Daccarett, H. Nguyen Cong, D. Martel, J. F. Marco, J. R. Gancedo and J. L. Gautier, *Int. J. Hydrogen Energy*, 2008, **33**, 4945–4954.

250 L. Hadidi, E. Davari, M. Iqbal, T. K. Purkait, D. G. Douglas and J. G. C.

Veinot, *Nanoscale*, 2015, **7**, 20547–20556.

251 J. Xi, Y. Xia, Y. Xu, J. Xiao and S. Wang, *Chem. Commun.*, 2015, **51**, 10479–10482.

252 D. Zhou, L. Yang, L. Yu, J. Kong, X. Yao, W. Liu, Z. Xu and X. Lu, *Nanoscale*, 2015, **7**, 1501–1509.

253 R. Yang, K. Stevens and J. R. Dahn, *J. Electrochem. Soc.*, 2008, **155**, B79–B91.

254 J. Chen, K. Takanabe, R. Ohnishi, D. Lu, S. Okada, H. Hatasawa, H. Morioka, M. Antonietti, J. Kubota and K. Domen, *Chem. Commun. (Camb).*, 2010, **46**, 7492–4.

255 Y. Wang, R. Ohnishi, E. Yoo, P. He, J. Kubota, K. Domen and H. Zhou, *J. Mater. Chem.*, 2012, **22**, 15549–15555.

256 C. Pozo-Gonzalo, O. Kartachova, A. a. J. Torriero, P. C. Howlett, A. M. Glushenkov, D. M. Fabijanic, Y. Chen, S. Poissonnet and M. Forsyth, *Electrochim. Acta*, 2013, **103**, 151–160.

257 P. He, Y. Wang and H. Zhou, *Chem. Commun.*, 2011, **47**, 10701–10703.

258 M. Liu, Y. Dong, Y. Wu, H. Feng and J. Li, *Chem. - A Eur. J.*, 2013, **19**, 14781–14786.

259 Y. Dong, Y. Wu, M. Liu and J. Li, *ChemSusChem*, 2013, **6**, 2016–21.

260 H. O. Pierson, *Handbook of Refractory Carbides and Nitrides*, William Andrew Publishing, 1996.

261 M. Meinert, *J. Phys. Condens. Matter*, 2016, **28**, 56006.

262 D. Xia, S. Liu, Z. Wang, G. Chen, L. Zhang, L. Zhang, S. (Rob) Hui and J. Zhang, *J. Power Sources*, 2008, **177**, 296–302.

263 R. Ohnishi, M. Katayama, D. Cha, K. Takanabe, J. Kubota and K. Domen, *J. Electrochem. Soc.*, 2013, **160**, F501–F506.

264 M. Chisaka, A. Ishihara, K. Suito, K. I. Ota and H. Muramoto, *Electrochim.*

Acta, 2013, **88**, 697–707.

265 Y. Du, Z. Dohnalek and I. Lyubinetsky, *J. Phys. Chem. B*, 2008, **112**, 2649–2653.

266 H. Zhong, H. Zhang, Y. Liang, J. Zhang, M. Wang and X. Wang, *J. Power Sources*, 2007, **164**, 572–577.

267 G. Xu, L. Zhang, C. Guo, L. Gu, X. Wang, P. Han, K. Zhang, C. Zhang and G. Cui, *Electrochim. Acta*, 2012, **85**, 345–351.

268 S. Dong, X. Chen, S. Wang, L. Gu, L. Zhang, X. Wang, X. Zhou, Z. Liu, P. Han, Y. Duan, H. Xu, J. Yao, C. Zhang, K. Zhang, G. Cui and L. Chen, *ChemSusChem*, 2012, **5**, 1712–5.

269 B. Avasarala and P. Haldar, *Electrochim. Acta*, 2010, **55**, 9024–9034.

270 A. Miura, C. Rosero-Navarro, Y. Masubuchi, M. Higuchi, S. Kikkawa and K. Tadanaga, *Angew. Chemie Int. Ed.*, 2016, **808**, 7963–7967.

271 Y. N. Miura, Norio, Horiuchi Hajime, Shimizu Youichi, *Chem. Soc. Japan*, **4**, 617–622.

272 W. J. Feng, N. K. Sun, J. Du, Q. Zhang, X. G. Liu, Y. F. Deng and Z. D. Zhang, *Solid State Commun.*, 2008, **148**, 199–202.

273 P.-Z. Si, W. Jiang, H.-X. Wang, M. Zhong, H.-L. Ge, C. Chul-Jin and L. Jung-Goo, *Chinese Phys. Lett.*, 2012, **29**, 128101–4.

274 H. Yang, H. Al-Brithen, E. Trifan, D. C. Ingram and A. R. Smith, *J. Appl. Phys.*, 2002, **91**, 1053–1059.

275 C. Li, Y. Yang, L. Lv, H. Huang, Z. Wang and S. Yang, *J. Alloys Compd.*, 2008, **457**, 57–60.

276 J.-W. Huang, J. Li and H. Peng, *Powder Metall.*, 2007, **50**, 137–141.

277 K. Suzuki, T. Kaneko, H. Yoshida, Y. Obi, H. Fujimori and H. Morita, *J. Alloys Compd.*, 2000, **306**, 66–71.

278 R. Yu, X. Y. Chong, Y. H. Jiang, R. Zhou, W. Yuan and K. Feng, *R. Soc.*

Chem., 2015, **5**, 1620–1627.

279 M. Meng, S. X. Wu, L. Z. Ren, W. Q. Zhou, Y. J. Wang, G. L. Wang and S. W. Li, *J. Appl. Phys.*, 2014, **116**, 173911–4.

280 J. C. Slater, *J. Chem. Phys.*, 1964, **41**, 3199.

281 B. Y. R. D. Shannon, M. H, N. H. Baur, O. H. Gibbs, M. Eu and V. Cu, *Acta Crystallogr. Sect. A*, 1976, **A32**, 751–766.

282 D. Vempaire, D. Fruchart, R. Gouttebarron, E. K. Hlil, S. Miraglia, L. Ortega and J. Pelletier, *Phys. A Stat. Mech. its Appl.*, 2005, **358**, 136–141.

283 T. Reier, M. Oezaslan and P. Strasser, *ACS Catal.*, 2012, **2**, 1765–1772.

284 X. Xu, C. Tan, H. Liu, F. Wang, Z. Li, J. Liu and J. Ji, *J. Electroanal. Chem.*, 2013, **696**, 9–14.

285 P. Serp, *Appl. Catal. A Gen.*, 2003, **253**, 337–358.

286 K. Lee, J. Zhang, H. Wang and D. P. Wilkinson, *J. Appl. Electrochem.*, 2006, **36**, 507–522.

287 Y. Shao, J. Sui, G. Yin and Y. Gao, *Appl. Catal. B Environ.*, 2008, **79**, 89–99.

288 C. Liang, Z. Li and S. Dai, *Angew. Chem. Int. Ed. Engl.*, 2008, **47**, 3696–717.

289 C. F. Lin, X. Zhang, H. Lin, N. Wang, J. B. Li and X. Z. Yang, *Adv. Mater. Res.*, 2006, **11**–**12**, 543–546.

290 X. Chen, K. Kierzek, Z. Jiang, H. Chen, T. Tang, M. Wojtoniszak, R. J. Kalenczuk, P. K. Chu and E. Borowiak-Palen, *J. Phys. Chem. C*, 2011, **115**, 17717–17724.

291 C. Liang, K. Hong, G. a Guiochon, J. W. Mays and S. Dai, *Angew. Chem. Int. Ed. Engl.*, 2004, **43**, 5785–9.

292 J. H. Knox, K. K. Unger and H. Mueller, *J. Liq. Chromatogr.*, 2006, **6**, 1–36.

293 S. Tanaka, N. Nishiyama, Y. Egashira and K. Ueyama, *Chem. Commun. (Camb).*, 2005, **16**, 2125–7.

294 R. Ryoo, S. W. Joo, M. Kruk and M. Jaroniec, *Adv. Mater.*, 2001, **13**, 652–

656.

295 R. Ryoo, S. H. Joo and S. Jun, *J. Phys. Chem. B*, 1999, **103**, 7743–7746.

296 B. W. Zhang, C. Liang, H. Sun, Y. Guan, P. Ying and C. Li, *Adv. Mater.*, 2002, **14**, 1776–1778.

297 Y. Meng, D. Gu, F. Zhang, Y. Shi, L. Cheng, D. Feng, Z. Wu, Z. Chen, Y. Wan, A. Stein and D. Zhao, *Chem. Mater*, 2006, **18**, 4447–4464.

298 T.-W. Kim, I.-S. Park and R. Ryoo, *Angew. Chem. Int. Ed. Engl.*, 2003, **42**, 4375–9.

299 C. Vix-guterl, S. Boulard, J. Parmentier and J. Werckmann, *Chem. Lett.*, 2002, **31**, 1062–1063.

300 T. Kyotani and A. Tomita, *Chem. Mater*, 1995, **7**, 1427–1428.

301 Y. Xia and R. Mokaya, *Chem. Mater*, 2005, **17**, 1553–1560.

302 C. H. Kim, D. Lee and T. J. Pinnavaia, *Langmuir*, 2004, **20**, 5157–5159.

303 Y. Oda, K. Fukuyama, K. Nishikawa, S. Namba, H. Yoshitake and T. Tatsumi, *Chem. Mater*, 2004, **16**, 3860–3866.

304 A. T. Rodriguez, M. Chen, Z. Chen, C. J. Brinker and H. Fan, *J. Ameriacan Chem. Soc.*, 2006, **128**, 9276–9277.

305 S.-S. Kim, T. R. Pauly and T. J. Pinnavaia, *Chem. Commun.*, 2000, **123**, 1661–1662.

306 M. Kaneda, T. Tsubakiyama, A. Carlsson and Y. Sakamoto, *J. Phys. Chem. B*, 2002, **106**, 1256–1266.

307 Z. Li and M. Jaroniec, *Chem. Mater*, 2003, **15**, 1327–1333.

308 Z. Li, M. Jaroniec, Y. J. Lee and L. R. Radovic, *Chem. Commun.*, 2002, 1346–1347.

309 B. J. Lee, S. Yoon and S. M. Oh, *Adv. Mater.*, 2000, **12**, 359–362.

310 H.-P. Lin, C.-Y. Chang-Chien, C.-Y. Tang and C.-Y. Lin, *Microporous Mesoporous Mater.*, 2006, **93**, 344–348.

311 C. Liang and S. Dai, *J. Am. Chem. Soc.*, 2006, **128**, 5316–5317.

312 V. V Strelko, V. S. Kuts and P. A. Thrower, *Carbon N. Y.*, 2000, **38**, 1499–1503.

313 B. M. Terrones, P. Redlich, N. Grobert, S. Trasobares, W. Hsu, H. Terrones, Y. Zhu, J. P. Hare, C. L. Reeves, A. K. Cheetham, M. Rühle, H. W. Kroto and D. R. M. Walton, *Adv. Mater.*, 1999, **11**, 655–658.

314 M. Terrones, *Annu. Rev. Mater. Res.*, 2003, **33**, 419–501.

315 R. A. Sidik, A. B. Anderson, N. P. Subramanian, S. P. Kumaraguru and B. N. Popov, *J. Phys. Chem. B*, 2006, **110**, 1787–1793.

316 C. Sun, L. Chen, M. Su, L. Hong, O. Chyan, C. Hsu, K. Chen, T. Chang and L. Chang, *Chem. Mater*, 2005, **17**, 3749–3753.

317 P. Matter, L. Zhang and U. Ozkan, *J. Catal.*, 2006, **239**, 83–96.

318 C. Lei, F. Han, D. Li, W.-C. Li, Q. Sun, X.-Q. Zhang and A.-H. Lu, *Nanoscale*, 2013, **5**, 1168–75.

319 M. Dasog, L. F. Smith, T. K. Purkait and J. G. C. Veinot, *Chem. Commun. (Camb).*, 2013, **49**, 7004–6.

320 Y. Ru, D. G. Evans, H. Zhu and W. Yang, *RSC Adv.*, 2014, **4**, 71.

321 H. Wang, X. Bo, A. Wang and L. Guo, *Electrochem. commun.*, 2013, **36**, 75–79.

322 R. Liu, D. Wu, X. Feng and K. Müllen, *Angew. Chem. Int. Ed. Engl.*, 2010, **49**, 2565–9.

323 Y. Su, Y. Zhu, H. Jiang, J. Shen, X. Yang, W. Zou, J. Chen and C. Li, *Nanoscale*, 2014, **6**, 15080–15089.

324 L. Yang, J. Kong, D. Zhou, J. M. Ang, S. L. Phua, W. A. Yee, H. Liu, Y. Huang and X. Lu, *Chem. - A Eur. J.*, 2014, **20**, 7776–7783.

325 K. Ai, Y. Liu, C. Ruan, L. Lu and G. M. Lu, *Adv. Mater.*, 2013, **25**, 998–1003.

326 X. Yu, H. Fan, Y. Liu, Z. Shi and Z. Jin, *Langmuir*, 2014, **30**, 5497−5505.

327 J. Liebscher, R. Mrówczyński, H. a Scheidt, C. Filip, N. D. Hădade, R. Turcu, A. Bende and S. Beck, *Langmuir*, 2013, **29**, 10539–10548.

328 Z. Yang, H. Nie, X. Chen and S. Huang, *J. Power Sources*, 2013, **236**, 238–249.

329 W. Yang, T.-P. Fellinger and M. Antonietti, *J. Am. Chem. Soc.*, 2011, **133**, 206–209.

330 J. Ozaki, T. Anahara, N. Kimura and A. Oya, *Carbon N. Y.*, 2006, **44**, 3358–3361.

331 Y. Shao, J. Liu, Y. Wang and Y. Lin, *J. Mater. Chem.*, 2009, **19**, 46-59.

332 E. Farjami, M. a. Rottmayer and L. Jay Deiner, *J. Mater. Chem. A*, 2013, **1**, 15501-15508.

333 Y. Zheng, Y. Jiao, L. Ge, M. Jaroniec and S. Z. Qiao, *Angew. Chemie - Int. Ed.*, 2013, **52**, 3110–3116.

334 D.-S. Yang, D. Bhattacharjya, S. Inamdar, J. Park and J.-S. Yu, *J. Am. Chem. Soc.*, 2012, **134**, 16127–16130.

335 Z. Zhang, X. Wang, G. Cui, A. Zhang, X. Zhou, H. Xu and L. Gu, *Nanoscale*, 2014, **6**, 3540.

336 J. Zhang, Z. Zhao, Z. Xia and L. Dai, *Nat. Nanotechnol.*, 2015, **10**, 444–452.

337 C. Song and J. Zhang, in *PEM Fuel Cell Electrocatalysts and Catalyst Layers*, 2008, pp. 89–134.

338 Y. Nie, L. Li and Z. Wei, *Chem. Soc. Rev.*, 2015, **44**, 2168–2201.

339 D. U. Lee, P. Xu, Z. P. Cano, A. G. Kashkooli, M. G. Park and Z. Chen, *J. Mater. Chem. A*, 2016, **4**, 7107–7134.

340 X. Cao, W. Yan, C. Jin, J. Tian, K. Ke and R. Yang, *Electrochim. Acta*, 2015, **180**, 788–794.

341 E. J. W. Verwey and E. L. Heilmann, *J. Chem. Phys.*, 1947, **15**, 174–180.

342 P. H. Klose, *J. Electrochem. Soc.*, 1970, **117**, 854-858.

343 H. Zhu, S. Zhang, Y. Huang, L. Wu and S. Sun, *Nano Lett.*, 2013, **13**, 2947–2951.

344 R. Wang, J. Jia, H. Wang, Q. Wang, S. Ji and Z. Tian, *J. Solid State Electrochem.*, 2013, **17**, 1021–1028.

345 K. Gong, F. Du, Z. Xia, M. Durstock and L. Dai, *Science*, 2009, **323**, 760–764.

346 Y. Shao, S. Zhang, M. H. Engelhard, G. Li, G. Shao, Y. Wang, J. Liu, I. A. Aksay and Y. Lin, *J. Mater. Chem.*, 2010, **20**, 7491–7496.

347 Y. H. Su, H. L. Jiang, Y. H. Zhu, X. L. Yang, J. H. Shen, W. J. Zou, J. D. Chen and C. Z. Li, *J. Mater. Chem. A*, 2014, **2**, 7281–7287.

348 Z.-L. Wang, D. Xu, J.-J. Xu and X.-B. Zhang, *Chem. Soc. Rev.*, 2014, **43**, 7746–86.

349 V. M. Dhavale, S. K. Singh, A. Nadeema, S. S. Gaikwad and S. Kurungot, *Nanoscale*, 2015, **7**, 20117–20125.

350 W. R. P. Barros, Q. Wei, G. Zhang, S. Sun, M. R. V. Lanza and A. C. Tavares, *Electrochim. Acta*, 2015, **162**, 263–270.

351 D. Huang, Y. Luo, S. Li, M. Wang and Y. Shen, *Electrochim. Acta*, 2015, **174**, 933–939.

352 Y. Zhu, B. Zhang, D.-W. Wang and D. S. Su, *ChemSusChem*, 2015, **8**, 4016–4021.

353 Z. Jiang, Z. J. Jiang, T. Maiyalagan and A. Manthiram, *J. Mater. Chem. A*, 2016, **4**, 5877–5889.

354 C. Shu, X. Yang, Y. Chen, Y. Fang, Y. Zhou and Y. Liu, *RSC Adv.*, 2016, **6**, 37012–37017.

355 G. Qui, H. Huang, H. Genuino, N. Opembe, L. Stafford, S. Dharmarathna and S. L. Suib, *J. Phys. Chem. C*, 2011, **115**, 19626–19631.

356 L. Hu, A. Percheron, D. Chaumont and C. H. Brachais, *J. Sol-Gel Sci. Technol.*, 2011, **60**, 198–205.

357 W. S. Rasband, *ImageJ*, U. S. National Institutes of Health, Bethesda, Maryland, USA, 1997, vol. ImageJ.

358 C. Wu, P. Yin, X. Zhu, C. OuYang and Y. Xie, *J. Phys. Chem. B*, 2006, **110**, 17806–17812.

359 S. M. Yuan, J. X. Li, L. T. Yang, L. W. Su, L. Liu and Z. Zhou, *ACS Appl. Mater. Interfaces*, 2011, **3**, 705–709.

360 K. Song, Y. Lee, M. R. Jo, K. M. Nam and Y.-M. Kang, *Nanotechnology*, 2012, **23**, 505401.

361 Z. Wu, S. Yang, Y. Sun, K. Parvez, X. Feng and K. Müllen, *J. Am. Chem. Soc.*, 2012, **134**, 9082–5.

362 Y. Dong, H. Pang, H. Bin Yang, C. Guo, J. Shao, Y. Chi, C. M. Li and T. Yu, *Angew. Chemie - Int. Ed.*, 2013, **52**, 7800–7804.

363 M. Kruk and M. Jaroniec, *Chem. Mater.*, 2001, **13**, 3169–3183.

364 H. Yang, H. Wang, S. Ji, V. Linkov and R. Wang, *Int. J. Hydrogen Energy*, 2014, **39**, 3739–3745.

365 C. Médard, M. Lefèvre, J. P. P. Dodelet, F. Jaouen and G. Lindbergh, *Electrochim. Acta*, 2006, **51**, 3202–3213.

366 J. Xu, P. Gao and T. S. Zhao, *Energy Environ. Sci.*, 2012, **5**, 5333–5339.

367 T. He, Z. Li, Z. Sun, S. Chen, R. Shen, L. Yi, L. Deng, M. Yang, H. Liu and Y. Zhang, *RSC Adv.*, 2015, **5**, 77296–77302.

368 X. Zhang, X. Wang, L. Le, A. Ma and S. Lin, *J. Mater. Chem. A*, 2015, **3**, 19273–19276.

369 Y. Liang, Y. Li, H. Wang, J. Zhou, J. Wang, T. Regier and H. Dai, *Nat. Mater.*, 2011, **10**, 780–786.

370 G. Jiang, H. Zhu, X. Zhang, B. Shen, L. Wu, S. Zhang and G. Lu, *ACS Nano*, 2015, **9**, 11014–11022.

371 C. W. B. Bezerra, L. Zhang, K. Lee, H. Liu, A. L. B. Marques, E. P. Marques,

H. Wang and J. Zhang, *Electrochim. Acta*, 2008, **53**, 4937–4951.

372 A. D. Chowdhury, N. Agnihotri, P. Sen and A. De, *Electrochim. Acta*, 2014, **118**, 81–87.

373 Y. Meng, W. Song, H. Huang, Z. Ren, S. Chen and S. L. Suib, *J. Am. Chem. Soc.*, 2014, **2**, 11452–11464.

374 X. Lin, Y. Shang, T. Huang and A. Yu, *Nanoscale*, 2014, **6**, 9043–9049.

375 Y. Liang, H. Wang, J. Zhou, Y. Li, J. Wang, T. Regier and H. Dai, *J. Am. Chem. Soc.*, 2012, **134**, 3517–3523.

376 X. Zhang, B. Li, C. Liu, Q. Chu, F. Liu, X. Wang, H. Chen and X. Liu, *Mater. Res. Bull.*, 2013, **48**, 2696–2701.

377 C. Li and T. Imae, *Macromolecules*, 2004, **37**, 2411–2416.

378 J. Jiang, Y. Li, J. Liu, X. Huang, C. Yuan and X. W. D. Lou, *Adv. Mater.*, 2012, **24**, 5166–80.

379 P. Simon and Y. Gogotsi, *Nat Mater*, 2008, **7**, 845–854.

380 R. Kötz and M. Carlen, *Electrochim. Acta*, 2000, **45**, 2483–2498.

381 G. Wang, L. Zhang and J. Zhang, *Chem. Soc. Rev.*, 2012, **41**, 797–828.

382 M. Toupin, T. Brousse and D. Bélanger, *Chem. Mater.*, 2004, **16**, 3184–3190.

383 W. Wei, X. Cui, W. Chen and D. G. Ivey, *Chem. Soc. Rev.*, 2011, **40**, 1697–1721.

384 J. Yang, L. Lian, H. Ruan, F. Xie and M. Wei, *Electrochim. Acta*, 2014, **136**, 189–194.

385 W. Chen, R. B. Rakhi, Q. Wang, M. N. Hedhili and H. N. Alshareef, *Adv. Funct. Mater.*, 2014, **24**, 3130–3143.

386 B. Babakhani and D. G. Ivey, *J. Power Sources*, 2010, **195**, 2110–2117.

387 B. Babakhani and D. G. Ivey, *J. Power Sources*, 2011, **196**, 10762–10774.

388 S. Pang, M. A. Anderson and T. W. Chapman, *J. Electrochem. Soc.* , 2000, **147**, 444–450.

389 M. J. Young, M. Neuber, A. C. Cavanagh, H. Sun, C. B. Musgrave and S. M. George, *J. Electrochem. Soc.* , 2015, **162**, A2753–A2761.

390 B. Babakhani and D. G. Ivey, *Electrochim. Acta*, 2010, **55**, 4014–4024.

391 S. Devaraj and N. Munichandraiah, *J. Electrochem. Soc.* , 2007, **154**, A80–A88.

392 O. Ghodbane, J.-L. Pascal and F. Favier, *ACS Appl. Mater. Interfaces*, 2009, **1**, 1130–1139.

393 D.-Y. Sung, I. Y. Kim, T. W. Kim, M.-S. Song and S.-J. Hwang, *J. Phys. Chem. C*, 2011, **115**, 13171–13179.

394 M. J. Young, A. M. Holder, S. M. George and C. B. Musgrave, *Chem. Mater.*, 2015, **27**, 1172–1180.

395 X. Zhao, B. M. Sanchez, P. J. Dobson and P. S. Grant, *Nanoscale*, 2011, **3**, 839–855.

396 L. Athouël, F. Moser, R. Dugas, O. Crosnier, D. Bélanger and T. Brousse, *J. Phys. Chem. C*, 2008, **112**, 7270–7277.

397 M. Schaffer and J. Wagner, *Microchim. Acta*, 2008, **161**, 421–425.

398 N. Otsu, *IEEE Trans. Syst. Man. Cybern.*, 1979, **9**, 62–66.

399 M. Guizar-Sicairos, S. T. Thurman and J. R. Fienup, *Opt. Lett.*, 2008, **33**, 156–158.

400 W. E. Lorensen and H. E. Cline, in *Proceedings of the 14th Annual Conference on Computer Graphics and Interactive Techniques*, ACM, New York, NY, USA, 1987, pp. 163–169.

401 R. C. Gonzalaz, R. E. Woods and S. L. Eddins, *Digital Image Processing Using MATLAB*, Pearson Prentice Hall, New Jersey, 2004.

402 M. Klingele, R. Zengerle and S. Thiele, *J. Power Sources*, 2015, **275**, 852–859.

Appendices

Appendix A: Mn-Co oxide/PEDOT as a bifunctional electrocatalyst for oxygen evolution and oxygen reduction reaction

A version of this Chapter has been published in the Proceedings of the Materials Research Society. **E. Davari**, and D. G. Ivey, Mn-Co oxide/PEDOT as a bifunctional electrocatalyst for oxygen evolution and oxygen reduction reaction, *MRS Proc., 2015,* **1777**, 1-6.

Abstract

Bifunctional electrocatalysts, which facilitate the oxygen reduction reaction (ORR) and oxygen evolution reaction (OER), are vital components in advanced metal-air batteries. Results are presented for carbon-free, nanocrystalline, rod-like, Mn-Co oxide/PEDOT bifunctional electrocatalysts, prepared by template-free sequential anodic electrodeposition. Electrochemical characterization of synthesized electrocatalysts, with and without a conducting polymer (PEDOT) coating, was performed using cyclic voltammetry (CV) and linear sweep voltammetry (LSV). In addition, microstructural characterization was conducted using SEM, TEM, STEM and XPS. Mn-Co oxide/PEDOT showed improved ORR/OER performance relative to Mn-Co oxide and PEDOT. On the basis of rotating disk electrode (RDE) experiments, Mn-Co oxide/PEDOT displayed the desired 4-electron transfer oxygen reduction pathway. Comparable ORR activity and superior OER activity relative to commercial Pt/C were observed.

A-1 Introduction

Rechargeable ZABs that utilize aqueous alkaline electrolytes have attracted interest due to their environmentally benign nature, low operation risks and high specific energy densities (470 Wh kg^{-1}).[2] ZABs are composed of three main parts: Zn metal as the anode, an air electrode as the cathode and a separator to divide the anode and cathode. The cathode utilizes oxygen from the atmosphere as the reactant rather than storing heavy materials as in other batteries. However, the round trip efficiency of ZABs is limited by sluggish kinetics for both the OER and the ORR. Platinum-based catalysts exhibit the lowest overpotentials for ORR but are less suitable for OER. Iridium oxides are the best OER catalysts, but they are not as active as Pt for ORR. Furthermore, the use of noble metal based catalysts pose challenges such as scarcity, prohibitive cost and declining activity.[10] Currently, there are no commercially available non-precious metal bifunctional catalyst materials with the necessary performance. Therefore, it is important to develop inexpensive, stable and active bifunctional catalysts suitable for both OER and ORR in ZABs.

Several strategies have been tried in the last several decades to design a multicomponent bifunctional catalyst by combining catalysts for ORR with those for OER.[178] Cobalt and Mn mixed oxides are presently being considered as promising electrocatalysts in alkaline solutions, because of their relatively high catalytic activity, availability, corrosion stability and lower cost compared with noble metals.[185] However, these oxides have high electronic resistance. To tackle this problem, the addition of conductive components, such as graphene and CNTs[185], or conductive polymers such as PEDOT($C_6H_6O_2S$) (~25 S cm^{-1}) and PPy[372], has been suggested.

A carbon-free Mn-Co oxide/PEDOT hybrid bifunctional catalyst has been fabricated in this work using simple, template-free, sequential anodic electrodeposition methods. The process utilized is similar to the one reported by Babakhani and Ivey[12] to fabricate similar structures for supercapacitor applications. The combination of a porous Mn-Co oxide rod-like structure and a conductive polymer (PEDOT) provides good electrochemical and electrical properties for electrochemical storage applications.

A-2 Experimental

Mn-Co oxide was anodically deposited sequentially from two solutions, one containing 0.01 M Mn acetate ($Mn(CH_3COO)_2$), 0.02 M ammonium acetate ($C_2H_4O_2.NH_3$) and 10% DMSO ($(CH_3)_2SO$) and one containing 0.01 M Co acetate ($Co(CH_3COO)_2$), 0.02 M ammonium acetate and 10% DMSO. The oxides were electrodeposited using a three electrode cell configuration onto the surface of GC (5.0 mm diameter) as the working electrode. Platinum coil was used as the counter electrode and Hg/HgO was used as the reference electrode. All potentials quoted are with respect to the reference electrode. The solution temperature was maintained at 60 ºC and agitated continuously during the deposition with a stirring bar at a speed of 300 rpm. Galvanostatic control, with a current density of 5 $mAcm^{-2}$ and deposition duration of 120 s, was applied using an SP-300 Bio-Logic® potentiostat for sequential anodic electrodeposition of Mn oxide and Co oxide. After electrodeposition, the GC working electrode was rinsed with DI water. Mn-Co oxide coaxial rods were subsequently coated with PEDOT by electropolymerization of a solution of 0.08 M PEDOT, 0.2 M lithium tetrafluoroborate ($LiBF_4$) and 0.14 M sodium dodecyl sulfate (SDS or $NaC_{12}H_{25}SO_4$). Electropolymerization was performed under potentiostatic control at 1 V for 45 s at room temperature in the three electrode cell described above. After electrodeposition the working electrode was rinsed with DI water and dried at 100ºC for 60 min in air to remove residual water and then stored in a desiccator.

Specifics of the electrochemical and microstructural analysis are explained in Section 3.2. ORR activity was measured by sweeping the potential from -0.8 to 0.3 V at a scan rate of 10 mV s^{-1}. For OER measurement, the potential range was 0.1 to 0.7 V with a rotation speed of 1600 rpm. Catalyst stability was evaluated by repeatedly scanning the potential from -0.7 to 0.2 V for 1000 cycles at 100 mV s^{-1} in an O_2-saturated 0.1 M KOH electrolyte.

A-3 Results and discussion

The as deposited material consists of fibrous, rod-like structures (about 10 µm long and 2 µm in diameter), which are orientated perpendicular to the surface and distributed uniformly across the substrate (Figure A-1(A) and 1(C)). The porous structure provides many active sites to facilitate adsorption and desorption of molecular oxygen for ORR and OER.[373] The rod-like structure is retained after cycling (Figure A-1(B)). Compositional mapping of the as deposited samples was done using EDX spectroscopy (Figure A-2). Manganese, Co and S (from the PEDOT) are uniformly distributed across the surface (i.e., no isolated Mn or Co oxides), and the average Mn:Co atomic ratio is ~2.1.

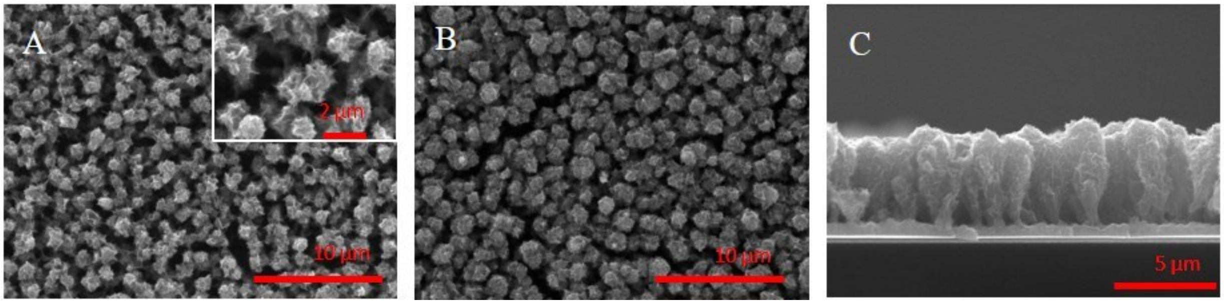

Figure A-1 SEM SE plan view images of a Mn-Co oxide/PEDOT sample on a GC substrate: (A) as-deposited and (B) after 50 cycles at 10 mV s^{-1} in O_2-saturated 0.1 M KOH. (C) Cross section SE image of as-deposited Mn-Co oxide/PEDOT.

As deposited Mn-Co oxide/PEDOT rods were examined in more detail by TEM. A TEM BF image of part of one rod is shown in Figure A-3(A). The rod is composed of thin sheets (~5 nm in thickness). The SAD pattern in (Figure A-3(B)) shows at least three diffuse rings, which indicate the nanocrystalline nature of the deposit. The d-spacings of the rings are 0.249, 0.206 and 0.146 nm, respectively, and can be indexed to a single phase $(Mn,Co)_3O_4$ spinel. This result is interesting, as Mn oxide and Co oxide were deposited separately, but sufficient interdiffusion has apparently occurred so that only one phase remains. No rings were attributed to the PEDOT layer, likely because of its thin and amorphous nature. X-ray line scans were done to examine the distribution of Mn, Co and S (from the PEDOT) (Figure A-3(C) and 3(D)). Manganese and Co are uniformly distributed across the surface and the X-ray intensity distribution for both is similar. This confirms the diffraction results and SEM results, i.e., Mn and Co interdiffuse during deposition to form a single phase. The X-ray intensity for S follows a similar distribution to that for Mn and Co, indicating uniform deposition of the PEDOT layer.

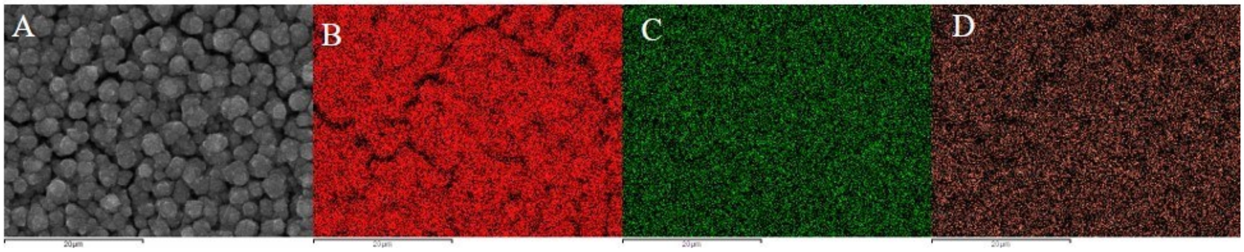

Figure A-2 (A) SEM SE image of a Mn-Co oxide/PEDOT sample on a GC substrate. EDX elemental maps showing (B) Mn, (C) Co and (D) S.

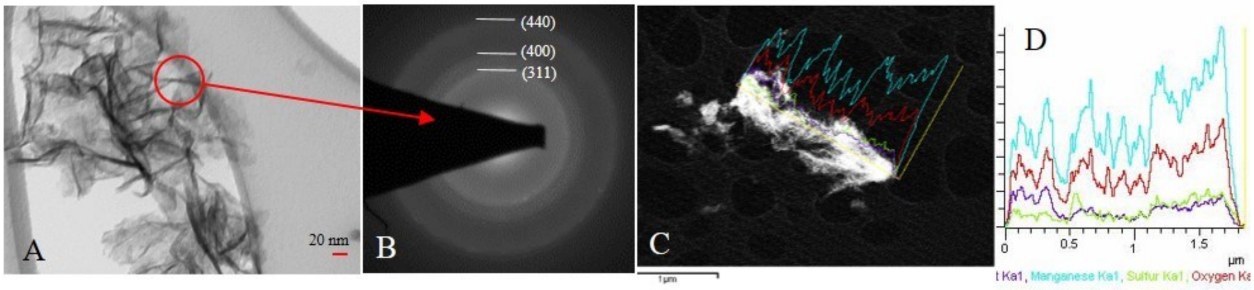

Figure A-3 (A) TEM BF image of Mn-Co oxide/PEDOT rod. (B) SAD pattern from (A). (C,D) X-ray line scan along part of a Mn-Co oxide/PEDOT rod.

XPS was employed to investigate the surface elemental composition and valence state of the Mn-Co oxide/PEDOT deposits. High resolution XPS spectra for the Mn 2p, Co 2p and O 1s regions of Mn-Co oxide/PEDOT before and after cycling (50 cycles) are shown in Figure A-4. The two main peaks at 642.8 and 654.4 eV in the Mn 2p spectra can be ascribed to Mn $2p_{3/2}$ and Mn $2p_{1/2}$, respectively, which are associated with both Mn^{2+} and Mn^{3+} species.[374] Also, the Co 2p spectra show a doublet containing a low energy band (Co $2p_{3/2}$) and a high energy band (Co $2p_{1/2}$) at 780.9 eV and 795.8 eV, respectively. The energy difference between the peaks is about 15 eV, which indicates the presence of both Co^{2+} and Co^{3+}.[141] These results are in good agreement with the TEM and SEM results, i.e., the Mn-Co oxide deposit has a spinel structure ($(Mn,Co)_3O_4$) with Mn:Co ratio of ~2.1. Weak 2p satellite features are also present with binding energies at 784.5 eV and 801 eV. As reported elsewhere, the weak satellite peaks indicate that 3+ cations occupy octahedral lattice sites and 2+ cations are in tetrahedral sites in the spinel structure.[375] The O 1s spectra for as deposited and cycled Mn-Co oxide/PEDOT exhibit three features. The most intense peak, located at 533.3 eV, corresponds to adsorbed molecular H_2O. The peak shoulders, located at 531.5 eV and 530.1 eV, can be assigned to oxygen species adsorbed on the surface, such as O_2^{2-} or O^- in the form of hydroxyl OH^- ions and lattice oxygen bonding with Mn and Co.[241] It has been suggested that O 1s peaks at higher energy are responsible for higher ORR activity for the catalyst.[376] The S 2p peaks located at 164.1 eV and 165.2 eV are attributed to thiophene S atoms in the PEDOT structure. The third component located at 169 eV is ascribed to the S atoms of the dodecyl sulfate (DS^-) anions trapped in the deposit during electrodeposition. All three S contributions show the successful incorporation of PEDOT over the surface.[377] The XPS results indicate that the oxidation state of the Mn- and Co-oxides oxidation state did not change after 50 cycles. The decrease in peak intensity of the O 1s and S 2p peaks at ~530.1 eV and 169 eV after cycling is due to PEDOT coating loss or degradation.

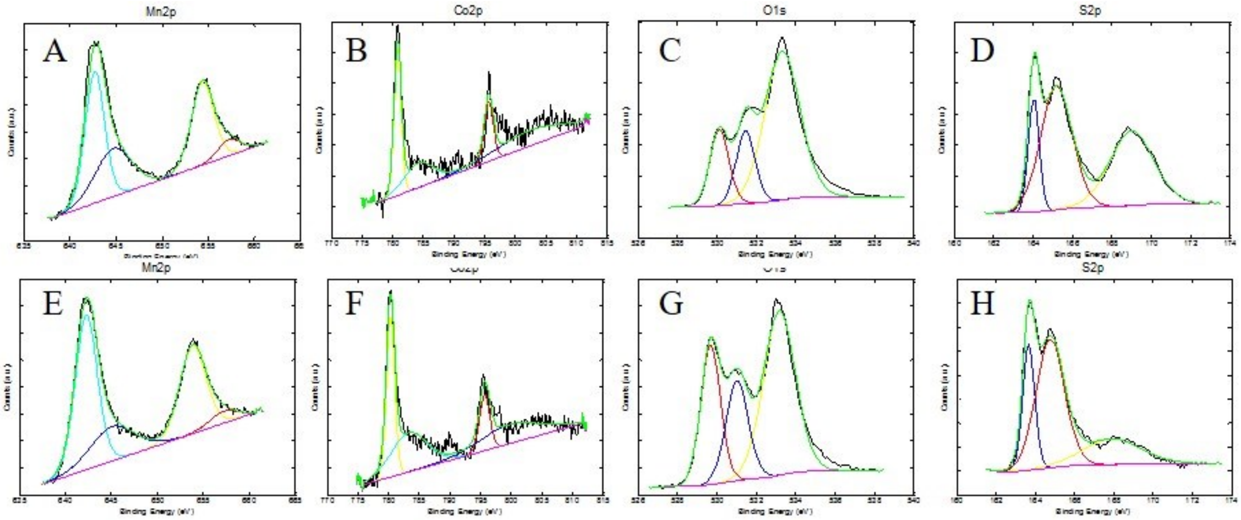

Figure A-4 XPS spectra for Mn 2p, Co 2p, O 1s and S 2p peaks in (A-D) as-deposited and (E-H) cycled (50 cycles at 10 mV s^{-1} in O_2-saturated 0.1 M KOH) Mn-Co oxide/PEDOT samples.

CV curves for Mn-Co oxide and Mn-Co oxide/PEDOT deposits in O_2-saturated and Ar-saturated KOH electrolytes are shown in Figure A-5. The CV curve in the O_2-saturated solution for Mn-Co oxide shows a cathodic peak at -0.3 V (Figure A-5(A)), which is not present for the Ar-saturated solution and is attributed to the electrocatalytic reduction of oxygen on the electrode. The oxygen reduction peak for Mn-Co oxide/PEDOT is shifted to a more positive potential than that for Mn-Co oxide (-0.05 V) (Figure A-5(B)). The two peaks located at -0.2 V and 0.03 V for Mn-Co oxide/PEDOT may be due to reduction and oxidation of the PEDOT coating, since the peaks are not present in the Mn-Co oxide CV curves. Figure A-5 also shows that Mn-Co oxide exhibits ORR activity, but with a more negative ORR onset potential and peak potential compared with Mn-Co oxide/PEDOT.

The ORR performance of the catalysts was also evaluated by calculating the electron transfer number (n). RDE current-potential curves were recorded for Mn-Co oxide/PEDOT at five different rotation speeds (100 to 2500 rpm) (Figure A-6(A)). The electrodes were cycled 20 times in O_2-saturated, 0.1 M KOH at 10 mV s^{-1} before voltammograms were recorded. When the potential was scanned cathodically, from 0.35 to -0.8 V, the current density increased and leveled off at the diffusion limiting current density (J_l). The current density increased at higher rotation speeds due to the faster flux of oxygen to the electrode surface (Figure A-6(A)).[4] The kinetics of ORR was analyzed using K-L plots (i^{-1} vs $\omega^{-1/2}$) (Figure A-6(B)) for the potential range of -0.3 to -0.7 V, where i is the current density and ω is the rotation speed. Parallel line fitting suggests first-order ORR kinetics. The electron transfer number for Mn-Co oxide/PEDOT was calculated from the slope of the K-L plots and a value close to 4 was obtained. This result suggests the desirable 4-electron transfer oxygen reduction pathway for Mn-Co oxide/PEDOT, which is similar to that for Pt/C catalysts. ORR kinetics for Mn-Co oxide/PEDOT catalysts was also compared with Mn-Co oxide, PEDOT and Pt/C catalysts (Figure A-6(C)). The PEDOT electrode was prepared by direct electrodeposition of PEDOT on GC. The Pt/C electrode was formed by pipetting 5 µl of a suspension of Pt/C powder on GC. The electrodes were cycled for 20 times in O_2-saturated 0.1 M KOH at 10 mV s^{-1} before voltammograms were recorded. The ORR onset potential for Mn-Co oxide/PEDOT is -0.029 V, which is only 700 mV more negative than that for the Pt/C catalyst. The onset potential for Mn-Co oxide/PEDOT is similar to the values reported for $MnCo_2O_4$/CNTs and $CoMn_2O_4$/PEDOT prepared by hypothermal and reductive routes, respectively.[143,372] The Mn-Co oxide/PEDOT composite improves the ORR onset potential by 236 mV and current density by two times compared with Mn-Co oxide alone. Also, the beneficial impact of the PEDOT coating is clearly evident by the shift from a 2-electron ORR mechanism for Mn-Co oxide to a one step, 4-electron pathway for Mn-Co oxide/PEDOT. The ORR activity of Mn-Co oxide/PEDOT is less than that of the Pt/C catalyst, but similar OER activity for the catalysts was also investigated to assess bifunctional activity (Figure A-6(D)). Mn-Co oxide/PEDOT showed a higher current density and earlier onset potential compared with the other catalysts (Table A-1). The high OER activity for Mn-Co oxide/PEDOT can be explained by the synergistic effect of integrating the OER active PEDOT layer onto the porous Mn-Co oxide rods, which promotes physical and electrical contact.[16]

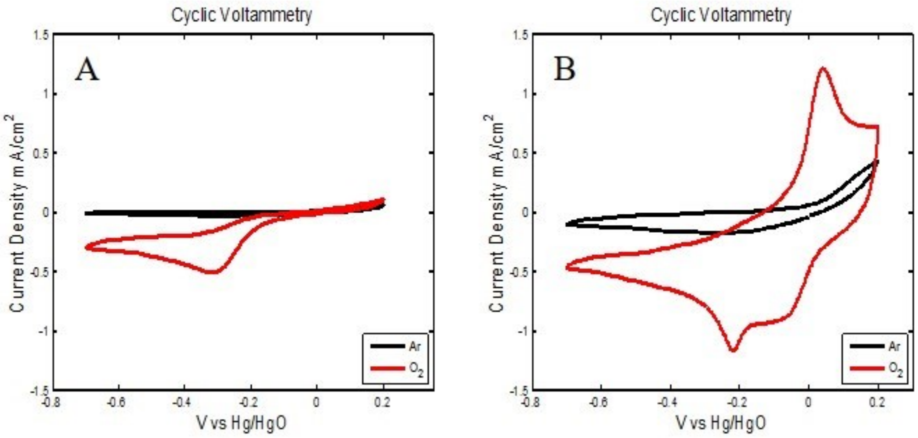

Figure A-5 CV curves (with a sweep rate of 10 mV s^{-1}) for (A) Mn-Co oxide and (B) Mn-Co oxide/PEDOT in O$_2$-saturated (red line) or Ar-saturated (black line) 0.1 M KOH.

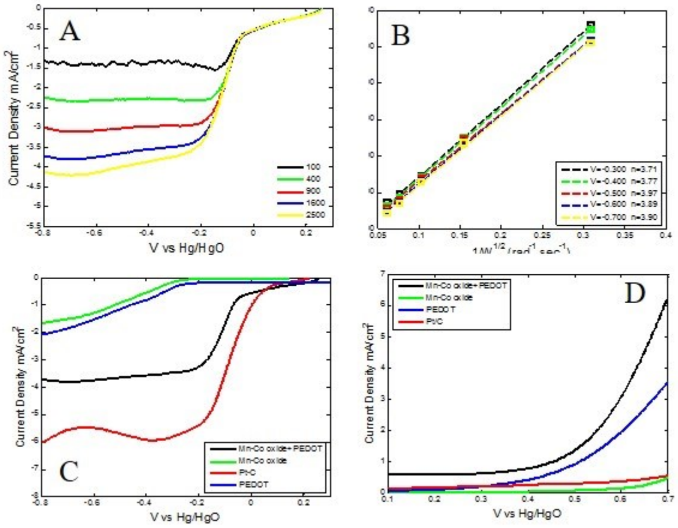

Figure A-6 (A) LSV curves for ORR performance of Mn-Co oxide/PEDOT in O$_2$-saturated alkaline electrolyte at different rotation speeds and a potential window of -0.8 to 0.3 V. (B) K-L plots for ORR of Mn-Co oxide/PEDOT at different rotation speeds (100-2500 rpm). (C) LSV curves for ORR of Mn-Co oxide/PEDOT along with Mn-Co oxide, PEDOT and Pt/C (O$_2$-saturated KOH at 1600 rpm). (D) OER curves (Ar-saturated 0.1 M KOH at 1600 rpm) for the electrocatalysts.

The higher bifunctional activity for Mn-Co oxide/PEDOT relative to Mn-Co oxide and PEDOT alone is attributed to the high specific surface area of the catalyst and the uniform distribution of the deposit across the substrate. More active sites are provided for both ORR and OER. The well-dispersed oxides and the conductive polymer provide synergetic improvements in both OER and ORR performance.

Table A-1 Electrochemical results for Mn-Co oxide/PEDOT, Mn-Co oxide, PEDOT and Pt/C.

	ORR onset potential (V)	**ORR current density at -0.7 V (mAcm^{-2})**	**OER onset potential (V)**	**OER current density at 0.7 V (mAcm^{-2})**	**n**
Mn-Co oxide/PEDOT	-0.029	-3.79	0.35	6.00	3.9
Mn-Co oxide	-0.265	-1.53	0.45	0.55	2.52
PEDOT	-0.264	-1.89	0.37	3.50	2.57
Pt/C	0.089	-5.54	0.60	0.60	4

Mn-Co oxide/PEDOT stability was tested using repetitive CV cycling between -0.7 V and 0.2 V. The ORR performance of the catalyst was tested after cycling using LSV (Figure A-7). The catalyst is not stable after long term operation. The current density decreased to -2.5 mA cm^{-2} and the ORR onset potential shifted to more negative potentials. The likely explanation for degradation is dissolution of the PEDOT layer. Poor mechanical stability of conducting polymers in aqueous solutions has been reported in other studies.[378] This is also apparent in the XPS results (Figure A-3 and Table A-1) for the O1s and S 2p peaks. After short term cycling (50 cycles) the intensity for the metallic adsorbed oxygen species increases, due to partial removal of PEDOT which exposes metal oxide underneath. Also, the S 2p peak, located at ~169 eV, is decreased in intensity after cycling due to the release of DS$^-$ anions in PEDOT.

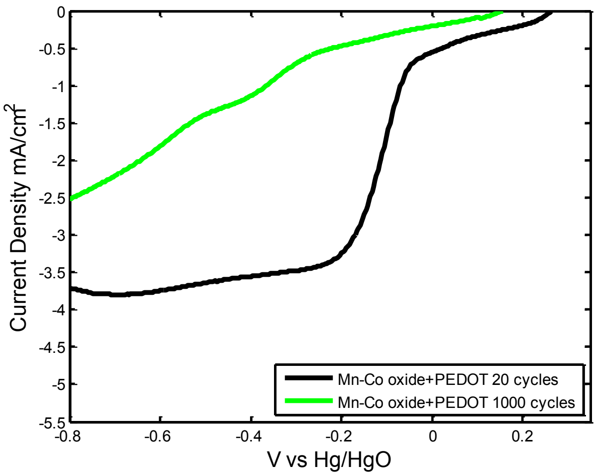

Figure A-7 LSV ORR curves for Mn-Co oxide/PEDOT after 50 and 1000 cycles. The scans were done from -0.7 to 0.2 V in O_2-saturated 0.1 M KOH at 100 mV s^{-1} and 1600 rpm.

A-4 Summary

Carbon-free, Mn-Co oxide/PEDOT bifunctional electrocatalysts have been successfully synthesized using anodic electrodeposition of Mn-Co oxide followed by deposition of the conducting polymer (PEDOT). A single metal oxide phase ($(Mn,Co)_3O_4$ spinel) was formed during electrodeposition. Comparable ORR activity and superior OER activity relative to commercial Pt/C catalysts were observed. The bifunctional activity of Mn-Co oxide/PEDOT is attributed to the high conductivity of PEDOT and the porous nature of the Mn-Co oxide. However, the catalyst is not stable during long-term operation in alkaline solutions due to degradation of the PEDOT coating. More work is needed to stabilize the coating.

Appendix B: Microstructural characterization of the cycling behavior of electrodeposited manganese oxide supercapacitors using 3D electron tomography

A version of this Chapter has been published in the Journal of Power Sources,
N. Dalili, M. P. Clark, **E. Davari**, D. G. Ivey, Microstructural characterization of the cycling behavior of electrodeposited manganese oxide supercapacitors using 3D electron tomography, *J. Power Sources*, 2016, **328**, 318-328.

Abstract

Manganese oxide has been investigated extensively as an electrochemical capacitor or supercapacitor electrode material. Manganese oxide is inexpensive to fabricate and exhibits relatively high capacitance values, i.e., in excess of 200 F g^{-1} in many cases; the actual value depends very much on the fabrication method and test conditions. The cycling behavior of Mn oxide, fabricated using anodic electrodeposition, is investigated using slice and view techniques, via a dual scanning electron microscope (SEM) and focused ion beam (FIB) instrument to generate three-dimensional (3D) images, coupled with electrochemical characterization. The initial as-fabricated electrode has a rod-like appearance, with a fine-scale, sheet-like morphology within the rods. The rod-like structure remains after cycling, but there are significant morphological changes. These include partial dissolution of Mn oxide followed by redeposition of Mn oxide in regions close to the substrate. The redeposited material has a finer morphology than the original as-fabricated Mn oxide. The Mn oxide coverage is also better near the substrate. These effects result in an increase in the specific capacitance.

B-1 Introduction

Electrochemical energy storage devices, such as batteries, fuel cells and electrochemical capacitors (or super capacitors), have generated an increasing amount of interest over the past several years. This interest is fueled largely by the development of hybrid and electric vehicles, as well as the emphasis on renewable energy sources. Electrochemical capacitors are characterized by high power densities, long cycle life and low cost. They are used in conjunction with other energy storage devices to provide a burst of power during periods of high load, such as acceleration of an electric vehicle. Some other applications for electrochemical capacitors are portable electronics, energy grids and emergency power supplies.[379,380]

Charge is stored in electrochemical capacitors through the accumulation of ions. The ions are stored either electrostatically in the electrochemical double layer or through Faradaic reactions in the bulk and at the surface. Depending on the electrode material, one of these mechanisms will typically dominate. Electrostatic charge storage allows for fast charge/discharge rates, but overall capacitance is limited by the electrostatic repulsion of the stored ions. Capacitance is typically higher for Faradaic capacitors, but the need for ion diffusion limits their rate capability. For both charge storage mechanisms, the electrode surface area plays an important role in overall capacitance. For double layer capacitors, the amount of charge that can be stored is directly related to the surface area. For Faradaic capacitors, a large surface area allows for easier ion access to the bulk of the material.[381]

Manganese oxide (MnO_2) is of particular interest as an electrochemical capacitor because it is inexpensive, environmentally benign and has a high theoretical capacitance (1380 Fg^{-1}).[382–384] Like many transition metal oxides, Mn oxide stores charge in two ways: electrostatically in the double layer and through Faradaic reactions at the surface as well as in the bulk of the electrode. Faradaic processes tend to dominate. The theoretical capacitance of Mn oxide is difficult to achieve because of its relatively poor electronic and ionic conductivity.

Manganese oxide electrodes can be fabricated by a number of ways; e.g., as powders via hydrothermal methods[385], thin films by dip coating and drop coating, electrodeposition[386–388]and atomic layer deposition (ALD).[389] Electrodeposition is commonly utilized, because it is inexpensive, simple and is able to conformally coat complex shapes. In fact, the oxide can be fabricated directly, without subsequent annealing, through anodic electrodeposition. Manganese ions are oxidized at the anode leading to oxide formation on the electrode. Deposition parameters such as temperature, time, current, electrolyte composition and agitation are easily modified and are used to control deposit morphology, structure and properties. Various Mn oxide morphologies have been achieved through electrodeposition, including sheets, rods, fibers and particles. Our group has developed a template-free process to electrodeposit rods with a diameter of ∼2 μm and lengths ranging from a few microns to greater than 10 μm.[11,386,387,390] The rods can be deposited on a variety of substrates, such as metallized semiconductors (e.g., Au/Si), Ni foam and carbon. The individual rods have a fibrous structure on the nanoscale, which increases the exposed surface area. The rods also have a "petal-like" shape, i.e., tapered at the base and spread out near the top. This petal shape leads to rod impingement for lengths exceeding 10 μm.

The capacitances for Mn oxide are high, with specific capacitances reaching or even exceeding 200 F g^{-1}. There are conflicting explanations in the literature as to the major factor(s) controlling capacitance, with specific surface area, the crystal structure of Mn oxide, ion conductivity and ion transfer all being cited. Devaraj and Munichandraiah[391] studied MnO_2 nanoparticles, fabricated in a microemulsion medium, that were subsequently annealed at temperatures up to 400 °C. The surface area of the Mn oxide decreased with increasing annealing temperature (from 190 m^2 g^{-1} at 70 °C to 119 m^2 g^{-1} at 400 °C). This correlated to a decrease in capacitance, from ∼300 F g^{-1} to

~250 F g^{-1}, over the same temperature range. Ghodbane et al.[392] examined several different allotropic forms of MnO_2 powders. They showed that the crystallographic structure of MnO_2 affects the capacitance. The best performance was achieved for the 3D spinel structure, followed closely by the 2D birnessite structure; both materials had capacitances in the 225-240 F g^{-1} range. They claimed that surface area had only a limited effect on performance, while capacitance could be correlated with ionic conductivity of the Mn oxide powder, i.e., capacitance increased as ionic conductivity increased. Sung et al.[393] also examined different MnO_2 powders, namely δ-MnO_2, α-MnO_2 and γ-MnO_2. They reported less of an effect of structure and more of a correlation with surface area. Capacitance values were highest for δ-MnO_2 nanoplates (up to 213 F g^{-1}), which also had the largest surface area (116 m^2 g^{-1}). The lowest capacitances were obtained for α-MnO_2 nanowires (110 F g^{-1}), with the smallest surface area (53 m^2 g^{-1}). Young and et al.[394] recently compared the capacitance behavior of two MnO_2 materials with vastly different capacitances, i.e., α-MnO_2 (~200 F g^{-1}) and β-MnO_2 (~10 F g^{-1}). A common explanation for the difference in behavior is related to the tunnel or channel sizes in the 3D structures; α-MnO_2 has larger tunnels and is therefore better able to accommodate positive ions during intercalation. Young et al. attributed the capacitance difference to the electronic properties. Specifically, the high capacity for α-$MnO_2$was attributed to cation induced charge-switching states in the band gap that overlap with the scanned potential allowed by the electrolyte. The charge switching states come from interstitial and substitutional cations (e.g., H^+, K^+, Na^+) that are incorporated in the material. For β-MnO_2 the scanned potential window does not overlap with its band gap, i.e., it is entirely in the conduction band, so there is no charge switching.

An important consideration when selecting an electrochemical capacitor is its cycling behavior. The electrode should be able to undergo thousands of cycles with little or no capacitance fading. Again, the literature is mixed on the cycling performance of Mn oxide. Our earlier work showed a 25% decrease in capacitance after 250 cycles and the loss was attributed to partial dissolution of Mn oxide.[386,387] Several other studies have shown a capacitance decrease on cycling.[388,395] Pang et al.[388] fabricated MnO_2 electrodes by electrodeposition and dip/drop coating and found that the amount of capacitance loss depended on the processing method with losses ranging from 10 to 38% (over 1500 cycles). They also attributed the loss to partial dissolution of MnO_2 on cycling. Sung et al.[393] observed an increase (<10%) in capacitance for the three different structural types of MnO_2 (δ-MnO_2, α-MnO_2 and γ-MnO_2). α-MnO_2 had the largest increase (~15–20% over 1000 cycles). They attributed the behavior to an improvement in ion transport near the surface of the electrode. Athouel et al.[396] examined Mg-doped MnO_2 Na-birnessite (δ-MnO_2) (original capacitance was ~145 F g^{-1}) over a limited number of cycles (50) and saw a slight increase in the first few cycles followed by stable behavior. The slight increase was attributed to stabilization of the electrode structure.

Chen et al.[385] have studied MnO_2 prepared by hydrothermal methods using electron tomography in a TEM/STEM. By varying the process time, they generated a variety of structures ranging from nanosheets to nanofibres to nanotubes. The nanosheets were δ-MnO_2, while the nanotubes were α-MnO_2. MnO_2 processed for 1 h (δ-MnO_2 nanosheets) had the highest capacitance (110 F g^{-1} at 0.5 A g^{-1}), while the 12 h sample (α-MnO_2 nanotubes) had the lowest capacitance (<30 F g^{-1} at 0.5 A g^{-1}). There was a very strong correlation between capacitance and surface area; the nanosheets had a surface area of ~200 m^2 g^{-1}compared with a surface area of ~40 m^2 g^{-1} for the nanotubes. The δ-MnO_2 nanosheets exhibited a 20% increase in capacitance on cycling (up to 5000 cycles), with the largest change occurring in the first 1000 cycles. Through their electron tomography work, the authors attributed the capacitance increase to an increase in porosity upon cycling leading to increased surface area and easier access for cations.

As mentioned above, our group has been able to fabricate high surface area Mn oxide rods through electrodeposition. In the original work[386,387,390], the deposits had a defective antifluorite (cubic) nanocrystalline structure and displayed high capacitances (~200 F g^{-1}). In our more recent work, additives have been included in the electrolyte to improve adhesion. Capacitance values were similar, but a different nanocrystalline structure (birnessite-type δ-MnO_2) was obtained. The rod-like morphology was retained, but the capacitance increased on cycling even with partial dissolution of Mn oxide. The purpose of this work is to utilize electron microscopy techniques to characterize the morphology and structure of Mn oxide electrodeposits in detail with the aim of developing an understanding of the capacitive behaviour with cycling. Conventional SEM, along with slice and view methods using a combination of SEM and FIB to generate three-dimensional (3D) images and quantitative surface area information, are utilized.

B-2 Experimental

B-2-1 Mn oxide deposition and electrochemical analysis

Manganese oxide deposits were obtained through anodic electrodeposition onto Au coated, Si substrates. Pieces of Au coated Si (1.6 cm × 0.8 cm) were sectioned from full wafers and then ultrasonically cleaned in acetone and ethanol for 10 min each to remove any surface contamination from handling and wafer dicing. A wafer piece was placed in the electrodeposition cell, 2 cm away from the Pt mesh counter electrode. The electrolyte was composed of Mn salt, i.e., Mn acetate (0.01 M $Mn(C_2H_3O_2)_2$), along with two additives, i.e., ammonium acetate (0.02 M $NH_4(C_2H_3O_2)$) and dimethyl sulfoxide or DMSO (10% C_2H_6OS). The additives help to improve deposit uniformity and reproducibility. The electrolyte was utilized at its natural pH of 7.5 and was heated to 60 °C and stirred at a rate of 250 rpm with a Teflon coated magnetic stir bar. Electrodeposition was done at a current density of 5 mA cm^{-2} for times ranging from less than 1 min to several minutes. The samples were rinsed in DI water after deposition and then dried in air at 100 °C for 1 h.

Electrochemical testing was done using a Biologic SP-300 potentiostat. All electrochemical tests were conducted using an electrolyte of 0.5 M Na_2SO_4, with a Pt counter electrode and a SCE as the reference; all reported potentials are with respect to SCE. CV was used to determine capacitive performance of Mn oxide deposits. All CV measurements were made between 0 and 0.9 V. Extended cycling was done using CV for up to 500 cycles at a scan speed of 20 mV s^{-1}.

The electrolyte utilized for capacitance cycling was analyzed for Mn, before and after cycling using atomic absorption spectroscopy (AAS), i.e., a Varian 220 FS system operating in flame mode. The electrolyte mass analyzed for each test was 10 ml.

B-2-2 Imaging and 3D tomography

Electrodeposited samples were imaged using SEM, either a thermionic electron source SEM (Tescan Vega-3) operated at 20 kV or field emission source SEMs (Hitachi S-4800 SEM and Zeiss Sigma SEM) operated at 3 kV. The latter instruments utilize in-lens SE detectors for imaging. Select samples were also examined using TEM with a JEOL 2010 TEM operated at 200 kV. TEM samples were prepared by scraping off some of the deposited material, forming a suspension with ethanol and placing one or two drops of the suspension on a holey C-coated Cu grid.

To prepare for FIB tomography, electrodeposited samples were first impregnated with photoresist (HPR504) to fill the pore volume between the rods. This eliminated the topography on the milled surface and ensured that a flat surface was imaged. The photoresist was spin-coated at 500 rpm for 10 s and at 3000 rpm for 40 s, followed by a soft bake at 115 °C for 90 s. The process was repeated 5 times to ensure that the photoresist infiltrated all the accessible porosity. To create a conductive top layer for initial SEM and ion imaging, a 50 nm thick layer of single bond Au-Pd was deposited on the top surface using a Gatan 682 precision etching and coating system with a 10 kV Ar ion beam at a base pressure of 5×10^{-5} torr and a deposition rate of 0.05 nm s^{-1}. The sample was then mounted onto an SEM stub and loaded in a Hitachi NB5000 dual beam FIB/SEM, which features a vertical Ga ion beam and an SEM electron beam oriented at 58° to the FIB column.

The block lift-out technique[397] was used to separate the area of interest for FIB tomography from the bulk sample. The block lift-out technique consisted of the following steps: The volume was milled free using a 40 kV, 10 nA Ga ion beam, on all 4 sides. The top and bottom sides were milled using two cascade-like patterns and the sides were milled free using two regular rectangular patterns. The trenches were milled deeper than twice the height of the Mn oxide coating. A bridge was left on the top left corner of the block, connecting the block to the bulk of the sample. The stage was then tilted 58° to cut underneath the block. The block was attached to an in-situ probe and mounted onto a standard TEM grid using ion-induced deposition of W. The side-entry stage was rotated 90°. This orientation allowed the ion beam to be parallel to the wafer/Mn oxide interface (x-y plane) and the electron beam to image the top of the Mn oxide rods (capped with photoresist at this stage). A schematic of the sample geometry relative to the ion and electron beams is shown in Figure B-1. Next, a protective W layer was deposited by ion induced deposition onto the x-z plane. Prior to deposition this surface was polished using a 40 kV, 0.79 nA ion beam to remove the defects introduced by the high current of the ion probe during the initial lift-out process. This step created a smooth surface for W deposition and reduced the curtaining effect during FIB tomography. Milling was started by removing the excess photoresist cap. A gentle 40 kV, 0.07 nA beam was used for this step to create a polished surface and to minimize the differential milling rates of Mn oxide rods and the photoresist.

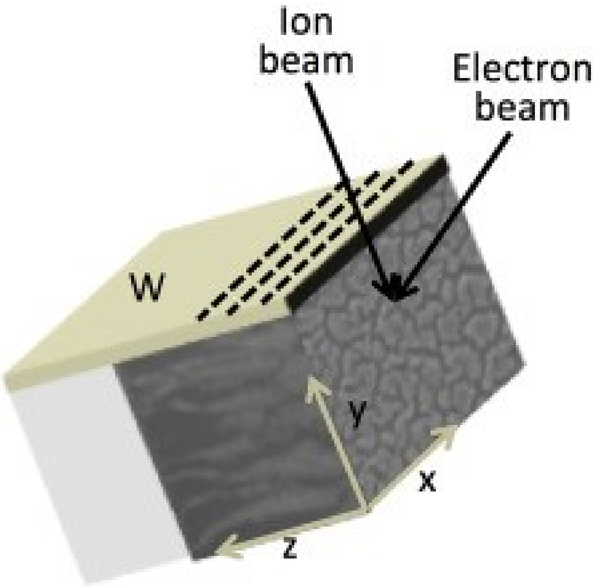

Figure B-1 Schematic showing sample orientation relative to the Ga ion beam and the electron beam. Note that the ion beam is perpendicular to the growth direction of the Mn oxide rods.

The prepared block was used for an automated FIB tomography procedure. A 40 kV, 0.07 nA ion beam was used to remove 10 nm of material at each step. During serial sectioning, the original sample surface (x-y plane) was kept parallel to the ion beam (Figure B-1). SEM imaging of the milled surface was performed in SE mode at an accelerating voltage of 3 kV to minimize the interaction volume of the SEs. SEM images of the x-y plane were taken from an angle of 32°. The Hitachi software automatically corrected for the oblique angle of imaging, beam focus and image shift. The SEM images were taken at a magnification of 20,000 times, yielding a voxel volume of 5 nm × 5 nm × 10 nm. A total area of 1220 pixels × 720 pixels was cropped from each image for further image processing. The number of slices was chosen based on the thickness of Mn oxide film, which was different for the as-deposited and cycled samples. The details of image processing are explained in the slice and view section.

B-2-3 Results and discussion

B-2-3-1 Electrochemical results

Manganese oxide samples, deposited for 2 min, were electrochemically tested. CV curves are shown in Figure B-2(A) for a range of cycles, i.e., from 10 cycles to 500 cycles. The plots are nearly rectangular, which is indicative of near ideal capacitive behavior. Redox peaks are visible, for both charging and discharging, and become more prominent with increased cycling. Capacitance values were calculated from the curves using the following equation.[3]

$$c = \frac{Q}{\Delta E}$$

where *C* is the capacitance, *Q* is the total anodic or cathodic charge transferred and *ΔE* is the potential window. To calculate the capacitance from a voltammogram, the charge transferred during a cathodic or anodic sweep is summed and divided by the potential window. An ideal capacitor experiences a linear relation between stored charge (*Q*) and the potential of the device (*ΔE*).

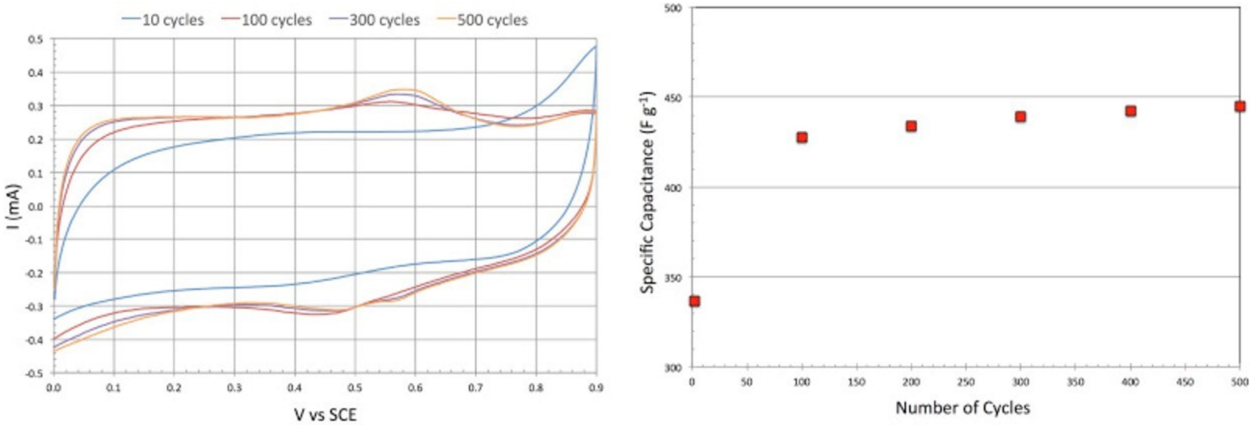

A

B

Figure B-2 (A) CV plots for Mn oxide sample for up to 500 cycles. (B) Plot of specific capacitance vs the number of cycles.

The capacitance values are shown in Figure B-2(B) as specific capacitance, i.e., normalized with respect to the initial mass of the deposit. There is an increase in capacitance with increasing cycling, with levelling off occurring for cycles exceeding 300. The capacitance for the as-fabricated material is 335 F g^{-1}, while the sample cycled 500 times has a capacitance of 445 F g^{-1}. Note that the capacitance does not deteriorate with further cycling; the high capacitance was maintained for at least 2000 cycles. As discussed in the Introduction, mixed results have been obtained in the literature for cycling behavior. We will show that for our electrodes partial dissolution of Mn oxide occurs, which should lead to a capacitance decrease not an increase. However, dissolution is accompanied by redeposition and a change in morphology, which has a beneficial effect on the capacitance.

SEM SE images of Mn oxide deposits, before and after cycling (300 cycles) are shown in Figure B-3. The morphology for both samples is similar, although the rods in the cycled sample are shorter in height, which suggests that some dissolution of Mn oxide has occurred.

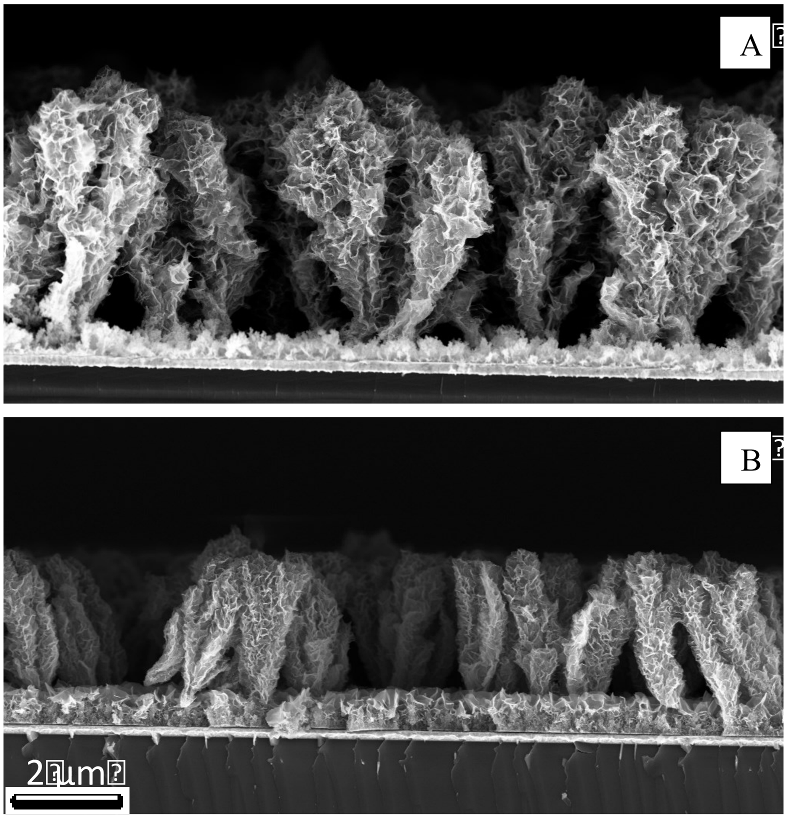

Figure B-3 SEM SE images of Mn oxide sample (A) before cycling and (B) after 300 cycles.

B-2-3-2 Slice and view

All samples for 3D imaging were prepared under the same deposition conditions, i.e., electrodeposited at 5 mA cm^{-2} at 60 °C for 2 min. SEM SE images acquired during FIB tomography were post-processed using a custom Matlab script. A 2D median filter was used to remove both the random, superimposed noise and the impulse noise from the individual images. Each pixel value was replaced by the median value of the neighboring pixels (3 pixels × 3 pixels). The contrast was enhanced using the contrast-limited adaptive histogram equalization method. This method breaks up the image into small regions of 3 pixels × 3 pixels and creates a custom transfer function required to achieve a uniform brightness histogram within the region. The image was then segmented into rods and voids using Otsu's thresholding method[398], which finds the value that minimizes the intra-class variance. 2D translation image registration and alignment were performed to correct for image shift during milling. This was accomplished using the algorithm developed by Guizar-Sicairos et al.[399], which is based on nonlinear optimization and discrete Fourier transforms.

Next, a representative sub-area of each image (1220 pixels × 720 pixels) was selected for further data processing and the 3D voxel data was created from the 2D images. Subsequent quantification and parameterization of the morphology was performed on this data volume. 3D visualization of the data was performed by importing the data to the TEMography Visualizer-Kai software. This software allows for easy manipulation and visualization of the 3D representation of the volume.

A series of SEM micrographs for the as-fabricated sample is shown in Figure B-4. Two types of images are shown; one set shows 2D views at various depths through the sample thickness and the other set shows reconstructed 3D images at the same depths as the 2D images. For the 2D images, the white regions correspond to Mn oxide while the black regions are photoresist, i.e., represent porosity or empty space. Useful quantitative information, such as surface coverage and specific surface areas were extracted from the images and will be discussed later in the paper.

The nucleation and growth process for the formation of Mn oxide rods has been studied previously[11] and is summarized here. Initially, Mn oxide nucleates uniformly across the surface of the substrate, although the surface is not completely covered. In fact, Mn oxide formation starts by the nucleation of thin sheets along Au grain boundaries and at triple points - not visible at the scale of this work, but observed in Ref.[11]

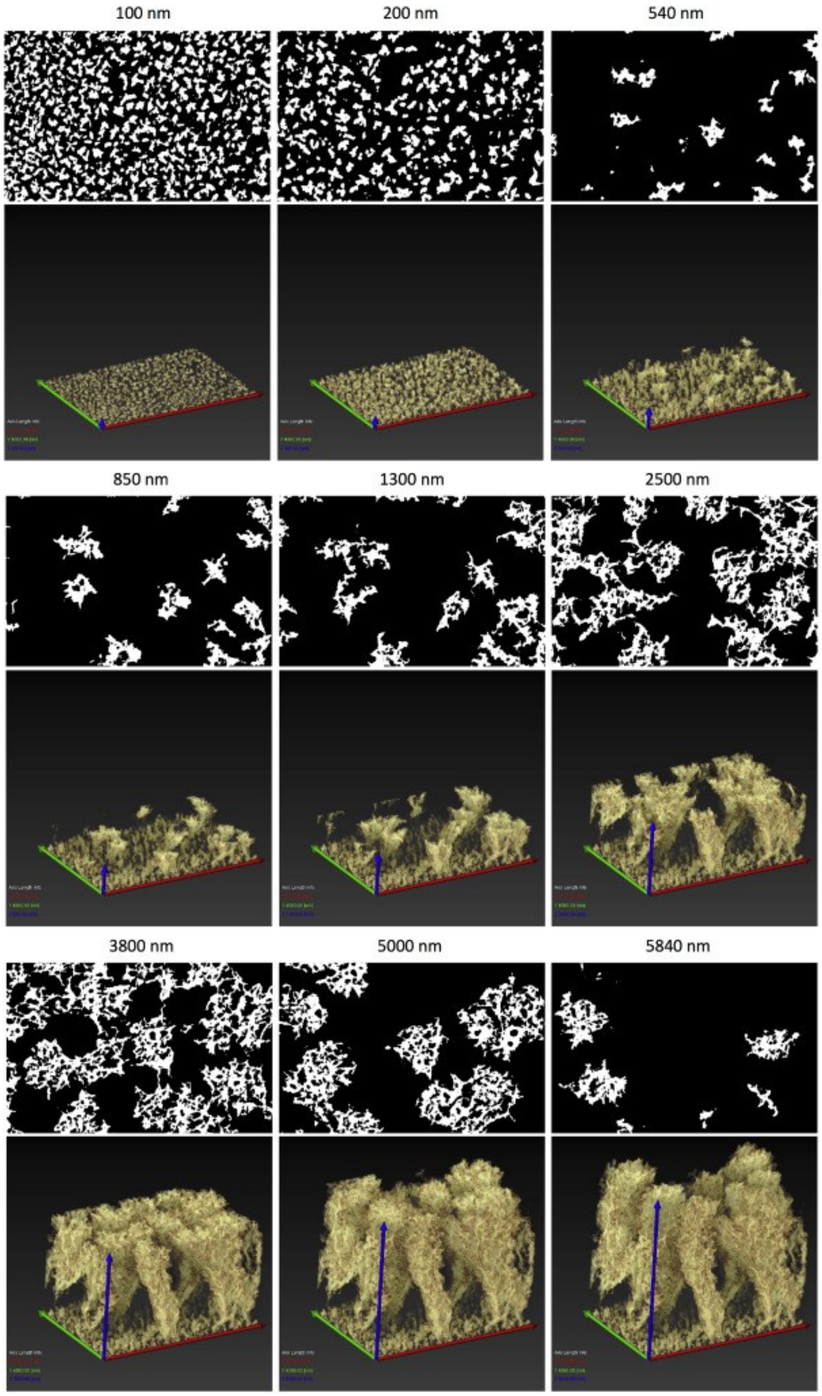

Figure B-4 Planar and reconstructed 3D images for as-fabricated Mn oxide sample. The 3D images correspond to the same depths as the 2D images. For the 2D images, the white regions correspond to Mn oxide while the black regions are photoresist, i.e., represent porosity or empty space. (The x and y are 6320 nm and 4060 nm in length, respectively).

As the initial nucleation sites are used up, nucleation spreads across the Au grains. Sheets in close proximity to one another agglomerate, forming rounded particles. Some of the rounded particles grow preferentially, initially in all directions and then primarily in the direction normal to the substrate surface, i.e., in the direction of the electric field. This accelerated growth leads to the formation of rods. As rods grow, the growth of other particles accelerates and they become rods as well. Eventually the entire sample surface is covered with rods, about 2 μm in diameter. The rods are tapered, expanding in width as they grow away from the substrate. The sheet-like morphology within the rods is retained at all stages of deposition. Cycled samples were also examined in the same manner as the as-fabricated one. Figure B-5 and Figure B-6 show a series of images for samples that have undergone 100 cycles and 300 cycles, respectively. The rod-like structure of the as-fabricated sample remains after cycling; however, there are significant morphological changes to the Mn oxide. There is a decrease in the height of the rods, which is evident by comparing the 3D reconstructions of the cycled samples in Figure B-5 and Figure B-6 with those for the as-fabricated sample in Figure B-4.

Quantitative measurements are shown in Figure B-7, which plots deposit coverage as a function of distance from the substrate surface. A simple pixel counting method was used to calculate the area fraction of the rods that intersect the x-y plane (see Figure B-1). The as-fabricated rods are almost 6 μm in height, while the samples tested for 100 cycles and 300 cycles have ~4.5 μm and ~3.5 μm long rods, respectively. Note that direct comparison of the as-fabricated and cycled samples cannot be made, since the same sample was not imaged for the three conditions because of the destructive nature of serial sectioning. There are also small height variations in different locations across the sample surfaces. Additionally, each sample was milled to expose the top of the rods before the serial sectioning process was initiated, which likely introduced small errors in height determination. Even with this uncertainty, the trends are valid and the rod heights correlate with those measured in the cross section SEM images (Figure B-3). The rod diameters have not changed appreciably, so the reduction in length is likely due to partial dissolution of Mn oxide during cycling.

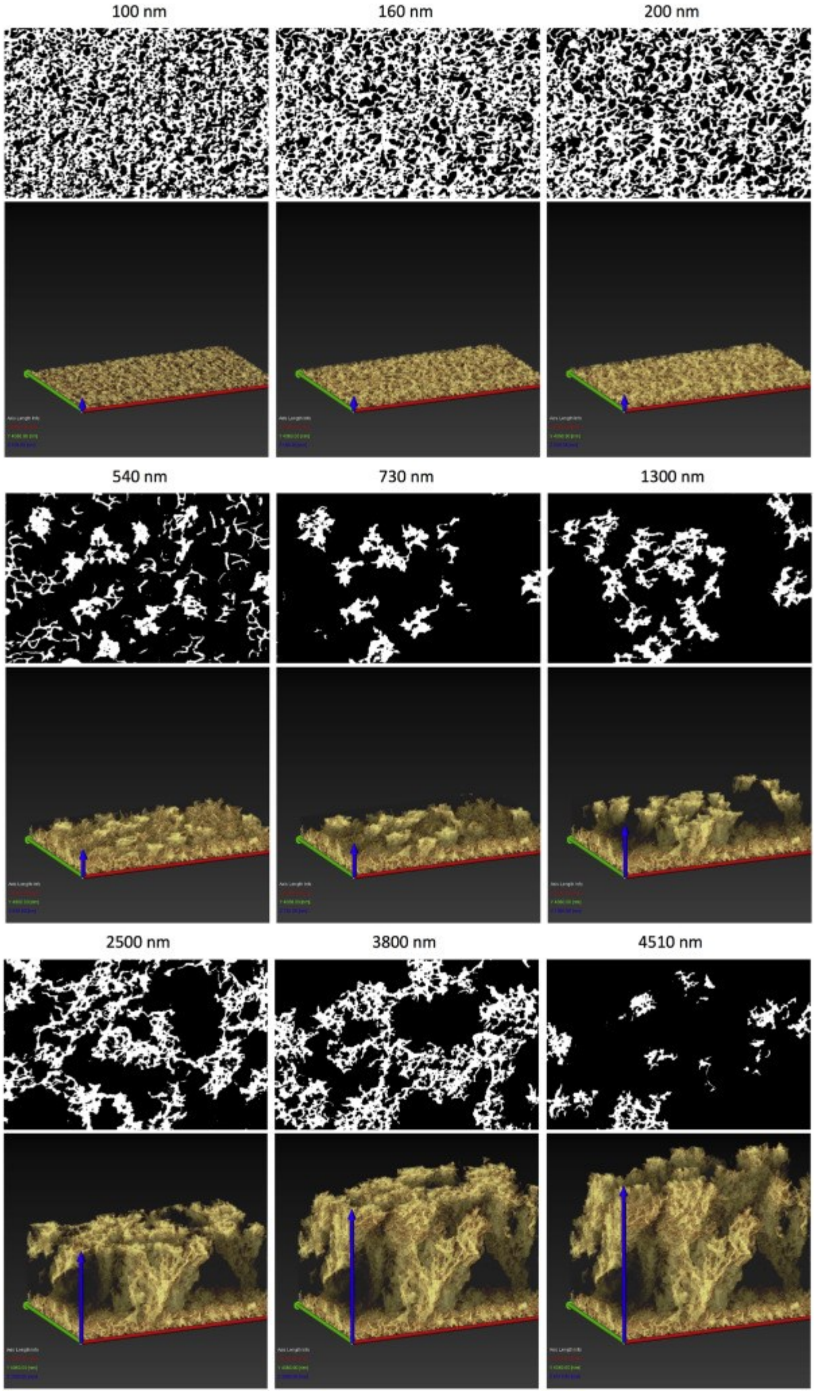

Figure B-5 Planar and reconstructed 3D images for Mn oxide sample after 100 cycles. The 3D images correspond to the same depths as the 2D images. For the 2D images, the white regions correspond to Mn oxide while the black regions are photoresist, i.e., represent porosity or empty space. (The x and y are 6320 nm and 4060 nm in length, respectively).

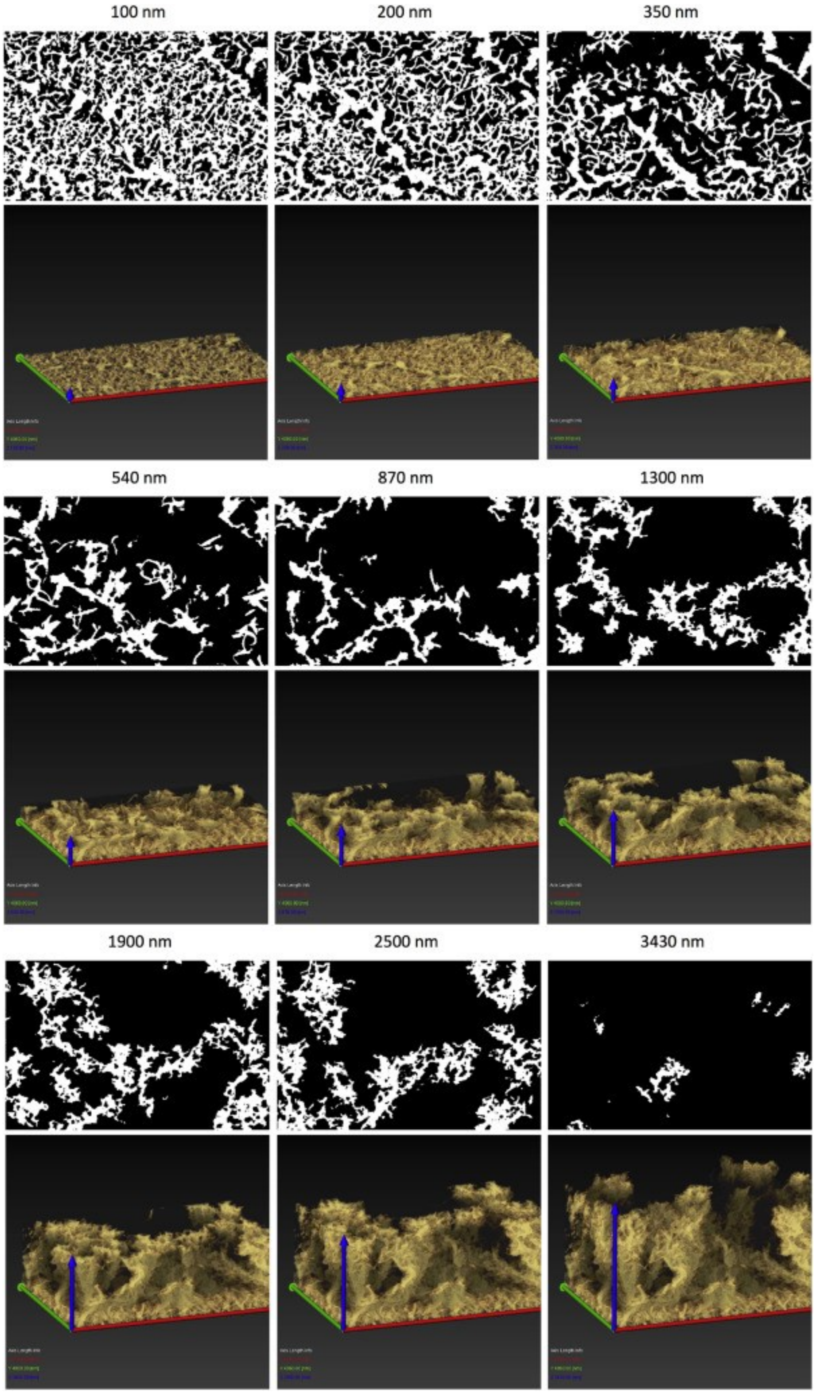

Figure B-6 Planar and reconstructed 3D images for Mn oxide sample after 300 cycles. The 3D images correspond to the same depths as the 2D images. For the 2D images, the white regions correspond to Mn oxide while the black regions are photoresist, i.e., represent porosity or empty space. (The x and y are 6320 nm and 4060 nm in length, respectively).

In order to confirm that dissolution was indeed occurring during cycling, AAS was utilized to analyze the electrolyte (0.5 M Na_2SO_4) before cycling, after 100 cycles and after 300 cycles. The amount of Mn in the pristine electrolyte (before cycling) was <0.07 ppm by weight (background level), while the concentrations after 100 cycles and 300 cycles were 1.66 ppm and 1.21 ppm, respectively. The AAS measurements were repeated for different samples and the same number of cycles. The actual amount of Mn dissolved was different, but the trends were the same. Clearly, Mn oxide dissolution occurred on cycling and accounts for the reduction in Mn oxide rod height. Also of note, is that there was more Mn dissolution for the sample after 100 cycles than after 300 cycles. This result will be discussed in the subsequent paragraphs.

As mentioned in the previous section, dissolution of Mn oxide would be expected to be accompanied by a reduction in the specific capacitance, which is not the case here (see Figure B-2(B)). In fact, there is an increase in capacitance with cycling. Note that the capacitance values reported in Figure B-2(B) are calculated based on the initial mass of the deposits.

Close examination of the three samples, particularly the first several hundred nanometers of the deposit, shows a significant change in morphology. The substrate surface coverage is higher for the cycled samples relative to the as-fabricated sample, as shown in Figure B-7. For the as-fabricated sample, the initial deposit coverage is about 0.4, which means that 40% of the substrate surface is covered with Mn oxide; the remaining 60% is bare Au. This is also apparent in the 2D image (100 nm thick) in Figure B-4. Note that the deposit coverage decreases with increasing deposit thickness to a value < 0.1 at a deposit thickness of ~500 nm, before increasing and peaking out at ~0.35 at a deposit thickness of ~4 μm and then dropping off again. This trend in the deposit density is a consequence of the formation process for the Mn oxide rods and their resultant morphology (petal shape). The high initial deposit density is due to nucleation of Mn oxide across the surface. The subsequent drop in deposit density is a consequence of the agglomeration of Mn oxide sheets to form the precursors to the rods. This is followed by an increase in deposit density, which reflects the vertical growth and lateral expansion of the rods. Finally, the peak in the deposit density corresponds to the rods laterally impinging upon one another.

The cycled samples show the same type of trends for the deposit density as that for the as-fabricated sample (Figure B-7). However, the cycled samples have significantly higher coverage for Mn oxide in close proximity to the substrate (~0.55). The higher deposit densities extend to deposit thicknesses up to ~2 μm. This behaviour is due to redeposition of Mn oxide during the charging portion of cycling. Redeposition occurs primarily at the base of the rods, close to the Au substrate, as opposed to on the rods themselves. The higher electronic conductivity in the vicinity of the Au substrate facilitates electrodeposition of Mn oxide. The redeposited material has a sheet-like morphology. Not all the dissolved Mn oxide is redeposited, as evident from the Mn detected in the electrolyte after cycling by AAS. More Mn oxide is redeposited as the number of cycles increases. Evidence for this claim comes from the AAS results, which show less Mn in the electrolyte for the 300 cycles sample compared with the 100 cycles sample. In addition, the deposit coverage fraction (Figure B-7) for the 100 cycles sample decreases to a lower level (~0.1) relative to the 300 cycles sample (~0.17). The thickness of the redeposited layer is also higher for the 300 cycles sample (Figure B-7).

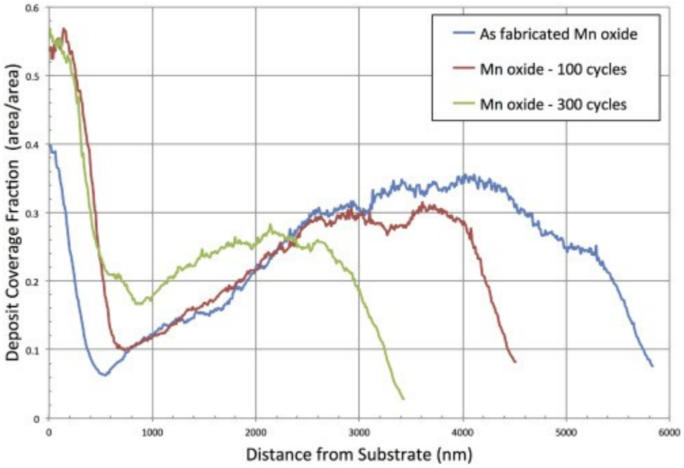

Figure B-7 Deposit coverage fraction as a function of distance from the substrate for the as-fabricated and cycled samples.

Two methods were used to calculate the surface area of the rods. In the first method, a triangulated mesh was calculated from the 3D voxel data by applying the well-known marching cube algorithm.[400] To calculate the surface area for various thicknesses of the film, 3D voxel data for each thickness was constructed. The surface area was calculated by summing the area of individual triangles in the mesh for each thickness (SA). In the second method, the interface between Mn oxide and the photoresist (empty space) was identified using the Moore-Neighbor tracing algorithm modified by Jacob's stopping criteria in Matlab.[401] The perimeter of the interface was then obtained from the chain code of the object boundary. This value was then multiplied by the slice width (10 nm) to give the total surface area for each volume interval. Both methods gave the same trends; however, the former method was deemed to be more accurate and, as such, the data presented below is based on this method. The volume of the rods in each interval was extracted from the binary data by pixel counting (V_{int}). The specific surface area (SSA_{int}) of each thickness was determined by dividing the surface area by the mass of the film (m).

$$\mathrm{SSA} = \frac{\mathrm{SA}}{\mathrm{m}}$$

$$\mathrm{m} = \sum \mathrm{V_{int}} \rho$$

The mass of the film for each thickness was estimated using the sum of the volume of the rods in each interval (V_{int}) over the entire thickness multiplied by the bulk density (ρ). The bulk density for the birnessite form of MnO_2 was chosen (5.05 g cm^{-3}), since Mn oxide was identified as birnessite in our previous work.[11] There is likely some error in using the bulk density, as thin films often have lower densities than the bulk material. However, any error should under predict the specific surface area, i.e., provide a more conservative estimate.

Specific surface area values for the as-fabricated sample and the two cycled samples are plotted as a function of deposit height from the substrate surface in Figure B-8. Distance from the substrate is plotted on a log scale to accentuate the surface area changes at small thicknesses. The calculated values for specific surface area include a number of errors: 1) Both models, mentioned above, assume that all the pores are accessible to liquid and do not exclude closed pores. 2) Image processing steps such as noise reduction, contrast enhancement and binarization threshold can dramatically affect the surface area values. 3) The small size of the sampled area (87.8 μm^2) may not be representative of the bulk samples. 4) The imaging resolution of the microscope limits the size of the features that can be resolved. As a result, the fibrous morphology of the rods is not fully resolved in the SE images and, therefore, the FIB slice and view process can significantly underestimate the surface area. Regardless of these errors, the trends are valid and can be used in comparing the as-fabricated and the cycled samples. For the as-fabricated sample, the highest specific surface area (41 m^2g^{-1}) occurs for the initial 100 nm of deposit, which correlates with deposit coverage. The surface area decreases continuously as the deposit thickness increases before levelling out at about 1000 nm. The same trend is followed for the cycled samples; however, it is clear that the specific surface areas for the cycled samples are higher than those for the as-fabricated sample, particularly in the regions closer to the substrate where redeposition has taken place. The sample with 300 cycles has a higher maximum specific surface area (~120 m^2 g^{-1}) than the 100 cycles sample (~59 m^2 g^{-1}), which is due to a higher amount of redeposition (compare Figure B-5 and Figure B-6. We believe that this increase in surface area is, at least partially, responsible for the increase in capacitance on cycling (see FigureB-2) and more than offsets the loss of Mn through dissolution during cycling.

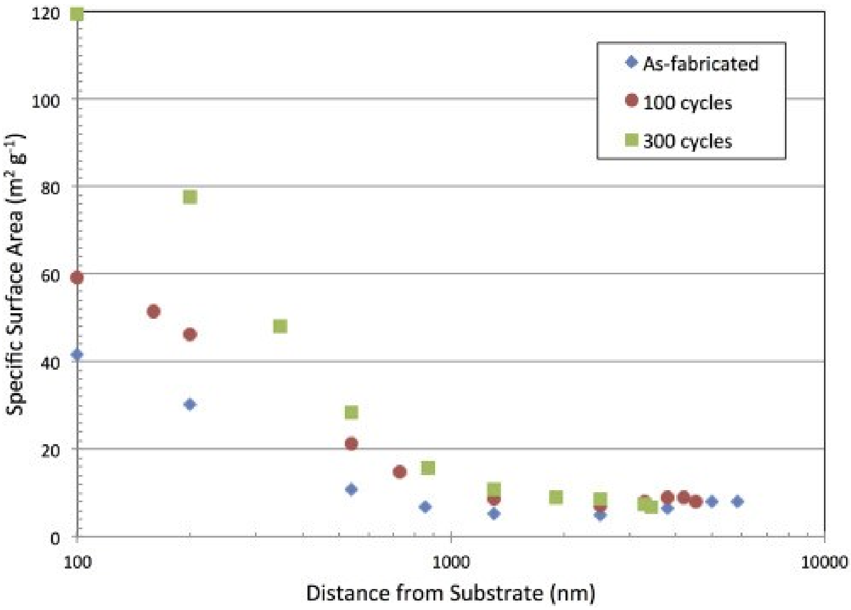

Figure B-8 Specific surface area as a function of distance from the substrate for the as-fabricated and cycled samples. The specific surface area clearly increases markedly with cycling in the near surface region.

In order to check the validity of the surface area measurements, particularly to determine whether the values obtained are of the correct order of magnitude, the specific surface area of the as-fabricated sample was determined using a more conventional method, i.e., the BET technique. Only one sample was evaluated, as multiple electrodepositions were needed to generate enough material for analysis. BET value of 143 m^2 g^{-1}was obtained. This value is similar to values for δ-MnO_2 reported in the literature[385,391,393], but higher than the maximum value obtained from serial sectioning (41 m^2 g^{-1}) and markedly higher than the overall specific surface area obtained from serial sectioning (~10 m^2 g^{-1}).

It is apparent that the method utilized in serial sectioning has significantly underestimated the specific surface area of the deposits. Even so, we believe that the trends are still valid. As mentioned above, the discrepancy is likely due to resolution limitations of the slice and view method. Klingele et al.[402] have quantified FIB artifacts associated with 3D tomography, primarily for fuel cell electrodes but the effects would be similar for supercapacitor electrodes, as both are porous. According to them, errors are caused by the FIB cutting distance (z-direction in Figure B-1), which is significantly larger than the SEM resolution. Because of this, morphological features, such as grain/particle size, pore size and surface area, can be significantly underestimated.

We explored the correlation between specific capacitance and specific surface area; the two parameters are plotted in Figure B-9(A). The calculated specific surface areas in the vicinity of the substrate surface (100 nm deposit height) were chosen. Specific capacitance increases with increasing specific surface area, but the increase is not linear. Similar dependencies were found for other deposit heights (200 nm and 400 nm), but the results are not shown here. Other effects likely play a role in capacitance as well; e.g., the Mn oxide structure and deposit electrical properties. As mentioned above, the improved electronic conduction on or near the Au surface facilitates MnO_2 redeposition. Because the redeposited material is localized to areas of good electronic conduction, electron transfer to the redeposited material during cycling occurs more easily, leading to higher specific capacitances for the redeposited material (compared with the as-fabricated rods). Specific capacitance was plotted against deposit coverage fraction; this was done for distances of 100 nm and 400 nm from the substrate surface (Figure B-9(B)). There is a linear relationship between the two parameters. This result suggests that capacitance may be limited by electron transfer, since Mn oxide has poor electron conductivity. Better surface coverage allows for more efficient transfer of electrons, needed for the intercalation (forward direction) and de-intercalation reactions (reverse reaction).

$(MnO_2) + C + e^- = (MnOOC)$ ($C^+ = Na^+$ or H^+ cations)

In order to determine any crystallographic effects on cycling behaviour, one of the cycled samples (300 cycles) was examined in the TEM. As mentioned previously, the as-fabricated material is poorly crystalline/nanocrystalline with a birnessite-type structure. The redeposited regions of the cycled sample were examined. The redeposited material was made up of agglomerated thin sheets (Figure B-10(A)) with a structure very similar to the as-fabricated one. The SAD pattern (Figure B-10(B)) had 3 diffuse rings, which is indicative of a poorly crystalline material. The pattern and d-spacings are similar to those for the as-fabricated sample and can be indexed to the birnessite structure.

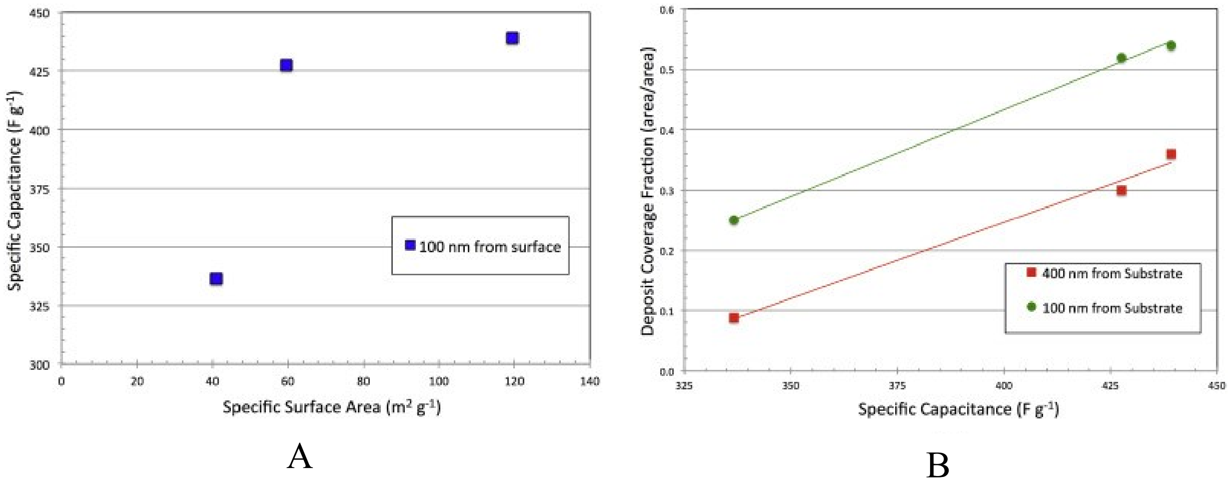

Figure B-9 (A) Plot of specific capacitance vs. calculated specific surface area in the vicinity of the substrate surface. (B) Plot of specific capacitance vs. deposit coverage fraction at distances of 100 nm and 400 nm from the substrate.

To summarize, the improved capacitance upon cycling of the Mn oxide electrode is due to a combination of effects, i.e., most notably increased surface area and increased surface coverage in the vicinity of the substrate. As such, much of the rod volume, particularly that forming further away from the substrate surface, likely contributes little to the overall capacitance. This explanation can also provide some insight into our earlier work, where the capacitance of electrodeposited Mn oxide rods decreased on cycling. In the earlier work[386,387], the rods were somewhat longer (~10 μm in length) because of longer deposition times (10 min). The tops of the rods tended to fuse together during cycling, inhibiting electrolyte access to the base of the rods and preventing redeposition of Mn oxide near the substrate surface. The crystal structure of the deposits was also different in the earlier work; a nanocrystalline, NaCl-type structure was generated, compared with the poorly crystalline birnessite structure for the current work. The different structure may be due to the additives in the current electrolyte for electrodeposition, which contains ammonium acetate and DMSO to improve deposit adhesion.

In order to provide further confirmation that redeposition occurs during cycling of the Mn oxide deposits, short term depositions (30 s) were performed and these samples were cycled. The time period of 30 s was chosen to represent the region of the as-fabricated rods near the Au substrate, where the rods are beginning to form (deposit heights of <200 nm).

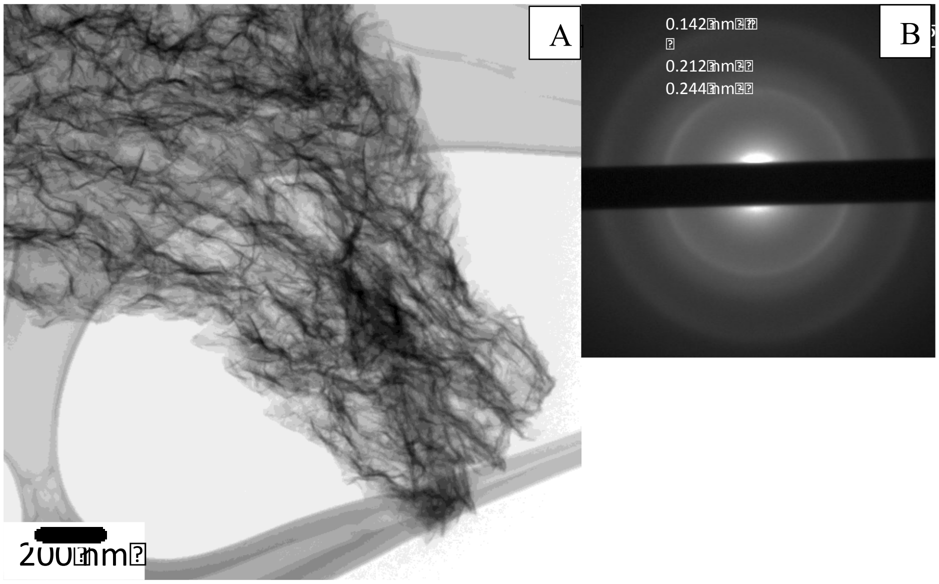

Figure B 10 (A) TEM BF image of redeposited material for the sample cycled 300 times. (B) SAD pattern from region in (A).

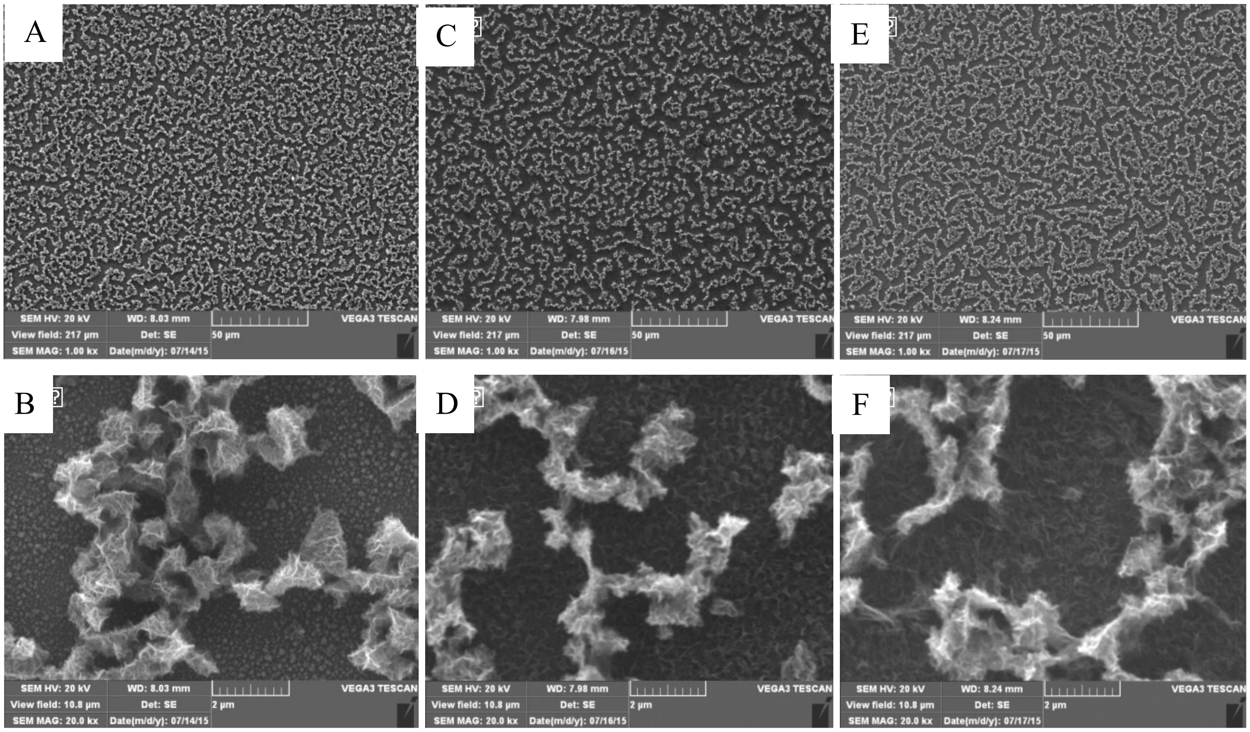

Figure B-11 SEM SE images of (A) and (B) Mn oxide sample fabricated by electrodeposition for 30 s; (C) and (D) fabricated sample cycled 100 times; (E) and (F) fabricated sample cycled 300 times.

A series of SEM SE images is shown in Figure B-11(A); a pair of images (low and higher magnification) are shown for each condition. The as-fabricated sample shows uniform coverage across the surface with a considerable fraction of uncovered or barely covered Au (Figures B-11(A-B)). This is very similar to the microstructure shown in Figure B-4 (100 nm thickness). The cycled samples (both 100 and 300 cycles - Figures B-11(C-D) and(E-F), respectively) look similar to the as-fabricated sample at lower magnifications (1,000x and 5,000x nominal magnifications), but differences are apparent at the higher magnifications. Additional deposited material, with a sheet-like morphology, is present between the protruding Mn oxide deposits. This material was confirmed to be Mn oxide by EDX analysis and is the result of redeposition during cycling Figures B-11(C-D) and(E-F) can be compared with the slice and view images in Figures B-5 and B-6; the microstructures are quite similar.

B-3 Summary

Slice and view techniques, using a dual SEM and FIB instrument, were used to generate three-dimensional (3D) images of Mn oxide supercapacitor electrodes in the as-fabricated condition and after cycling. The Mn oxide electrodes were fabricated using anodic electrodeposition on Au coated, Si substrates and had a rod-like appearance with a fibrous, sheet-like morphology within individual rods. The overall rod-like structure was retained after cycling, but the capacitance increased (from 335 F g^{-1} to 445 F g^{-1}). The tomography work clearly showed that cycling resulted in partial dissolution of the Mn oxide rods during discharge, reflected in a decrease in the overall rod height, followed by redeposition of Mn oxide during charging. The redeposited material formed at the base of the rods (adjacent to the substrate) producing a finer morphology, with increased specific surface area, and better surface coverage than the as-fabricated material. The combination of these effects led to the improved electrochemical performance with cycling.